Single-Source-Precursor Synthesis and Properties of SiMC(N) Ceramic Nanocomposites (M = Hf, Ta, HfTa)

M. Eng. Qingbo Wen

Prof. Dr. Ralf Riedel (Supervisor)

Dispersive Solids, Department of Materials and Earth Sciences

TECHNISCHE UNIVERSITÄT DARMSTADT

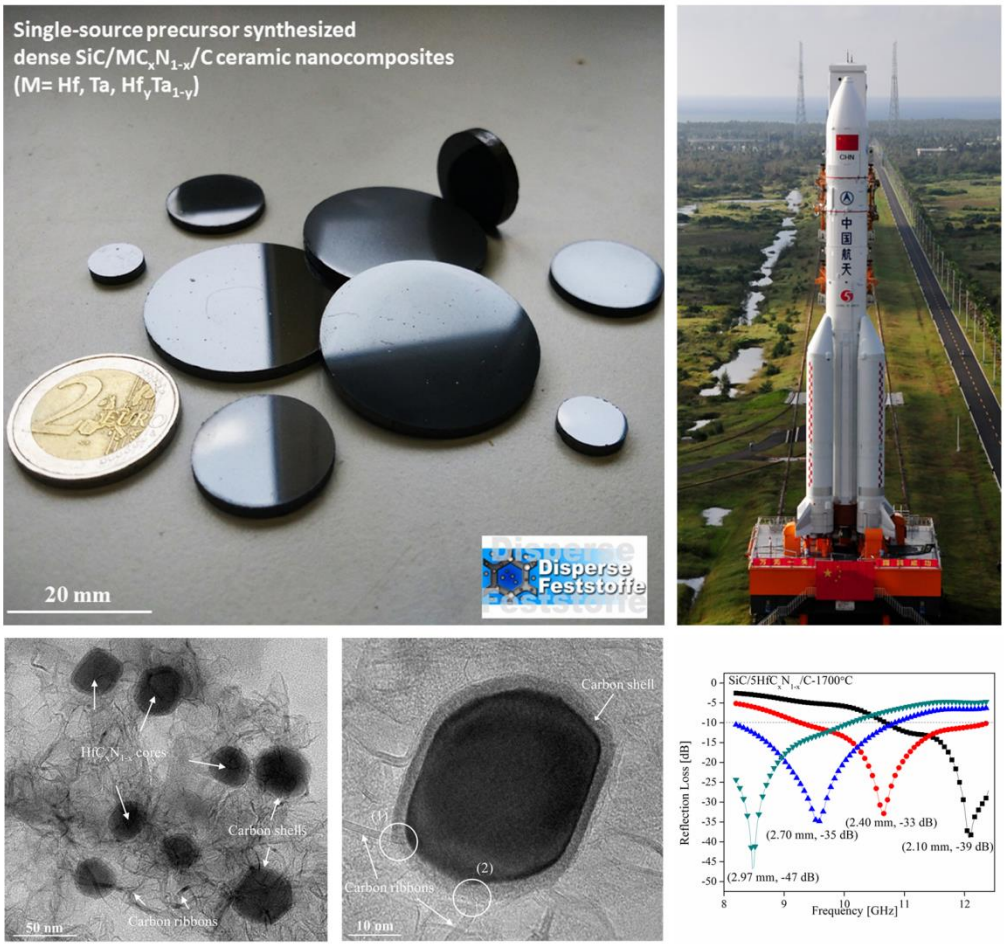

A Dissertation Approved by the Department of Materials and Earth Sciences in Fulfillment of the Requirements for the Degree of Doktor-Ingenieur (Dr.-Ing.)

Single-Source-Precursor Synthesis and Properties of SiMC(N) Ceramic Nanocomposites (M = Hf, Ta, HfTa)

M. Eng. Qingbo Wen

From Changsha, Hunan, China, Matrikel-Nr.: 1834026

TECHNISCHE UNIVERSITÄT DARMSTADT

Referee: Prof. Dr. Ralf Riedel

Co-referee: Prof. Dr. Zhaoju Yu

Fachbereich Material- und Geowissenschaften

Technische Universität Darmstadt

Date of submission: 10.01.2017

Date of oral examination: 23.02.2017

Darmstadt 2017

D 17

Dedicated to my parents (献予我的父母)

Declaration

M. Eng. Qingbo Wen

Nieder-Ramstädter-str. 11

64283 Darmstadt

Declaration

This work described in this thesis was carried out at the Department of Materials and Earth Sciences, Technische Universität Darmstadt during the period October 2012 to June 2016. This thesis represents the author's original work, except where otherwise stated, and no part of it has been submitted for a degree at any other university. Prior to the submission of this thesis, some work has been published as described in the relevant chapters herein.

Eidesstattliche Erklärung

Hiermit erkläre ich an Eides statt, dass ich die vorliegende Dissertation selbstständig und nur mit den angegebenen Hilfsmitteln angefertigt habe. Von mir wurde weder an der Technischen Universität Darmstadt noch einer anderen Hochschule ein Promotionsversuch unternommen.

Darmstadt, den 19.12.2016

M. Eng. Qingbo Wen (文青波)

Contents

List of Figures

List of Tables

List of abbreviations

PDCs	Polymer derived ceramics
UHTCs	Ultrahigh-temperature ceramics
NCs	Nanocomposites
UHTC-NCs	Ultrahigh-temperature ceramic nanocomposites
PDC-NCs	Polymer derived ceramic nanocomposites
CMCs	Ceramic matrix composites
SSPs	Single-source precursors
AHPCS	Allylhydridopolycarbosilane (SMP10)
PSE	Polysilaethylene
HBPSE	Hyper branched polysilaethylene
GPC	Gel permeation chromatography
TDMAH	Tetrakis(dimethylamino)hafnium (IV) [$Hf(NMe_2)_4$]
TDEAH	Tetrakis(diethylamido)hafnium (IV) [$Hf(NEt_2)_4$]
TDMAT	Pentakis(dimethylamino)tantalum(V) [$Ta(NMe_2)_5$]
BMS	Borane dimethylsulfide [$(CH_3)_2S{\bullet}BH_3$]
PIP	Polymer infiltration and pyrolysis
SPS	Spark plasma sintering
FT-IR	Fourier transformed infrared spectroscopy
ATR	Attenuated-total-reflectance
TGA	Thermogravimetric analysis
TG/MS	Thermogravimetric analysis coupled with mass spectrometry
NMR	Nuclear magnetic resonance
MAS NMR	Magic-angle spinning nuclear magnetic resonance
XRD	X-ray diffraction
TEM	Transmission electron microscopy
HRTEM	High-resolution transmission electron microscopy
SEAD	Selected Area Electron Diffraction

SEM	Scanning electron microscopy
EDX/EDS	Energy dispersive X-ray spectroscopy
BET	Brunauer-Emmett-Teller theory
MA	Microwave absorption
EMW	Electromagnetic wave
RL	Reflection loss
RT	Room temperature
EAB	Effective absorption bandwidth
EMI	Electromagnetic interference
SE	Shielding effectiveness
$\varepsilon'/\varepsilon''$	Real part of the permittivity/ Imaginary part of the permittivity
μ'/μ''	Real part of the permeability/ Imaginary part of the permeability
S_{ij}	Scattering parameters
σ	Electrical conductivity
Z_s	Intrinsic impedance of the shielding material
δ_s	Skin depth of the shielding material
f	Frequency of the electromagnetic wave
d	Thickness of the shielding material/microwave absorbing material
wt.% / vol.% / mol%	Weight percent/Volume percent/Mol percent
ρ_s/ρ_g	Skeletal density/Geometrical density
P	Open porosity

Abstract

Industrial and aerospace demands on future technologies have created an urgent need for new material properties that are beyond those of materials known today and that can only be fabricated by designing the respective microstructure at the nanoscale. Taking advantage of the correlation between the molecular structure of preceramic precursors and the microstructure of the derived ceramic materials, the single-source-precursor route offers possibilities to fabricate novel ceramic materials that are inaccessible by conventional synthesis.[1] The motivation of this Ph.D. work is to further develop the concepts for fabrication of novel ceramic nanocomposites with a tailor-made microstructure and versatile properties by molecular design of their precursors.

With this motivation, a series of dense monolithic SiMC(N) ceramic nanocomposites (M = Hf, Ta, HfTa) were fabricated using single-source-precursor synthesis plus spark plasma sintering. The chemical synthesis, polymer-to-ceramic transformation as well as high-temperature microstructural evolution was characterized using FT-IR, MAS solid NMR, TG/MS, XRD, Elemental analysis, SEM, TEM and Raman spectroscopy. Moreover, electrical conductivity, microwave absorption capability, electromagnetic interference shielding performance and laser ablation resistance of the as-prepared dense monoliths were investigated as well.

In the synthesis part, a series of M-containing single-source precursors were synthesized upon reactions between a commercially available allylhydridopolycarbosilane (SMP10) and metal compounds, including $Hf(NMe_2)_4$, $Hf(NEt_2)_4$ and $Ta(NMe_2)_5$. The polymer-to-ceramic transformation was characterized using FT-IR, ^{13}C and ^{29}Si MAS solid NMR as well as *in situ* TG/MS. The precursors synthesized using $Hf(NMe_2)_4$ and $Ta(NMe_2)_5$ lead to higher ceramic yield (≈ 80 wt.%) than that of $Hf(NEt_2)_4$ (≈ 71 wt.%), while the ceramic yield of the latter can be improved to ≈ 78 wt.% by introduction of $BH_3 \cdot SMe_2$.

Several thermal stable SiMC(N) ceramic nanocomposites (powders) were prepared upon high-temperature annealing of the amorphous SiMC(N) ceramics, including SiHfC(N), boron-doped SiHfC(N), SiTaC(N), SiHf7Ta3C(N) and SiHf2Ta2C(N). XRD, Raman and TEM results reveal that the ceramic nanocomposites mainly comprise β-SiC and MC_xN_{1-x} as well as free carbon (M = Hf, Ta, Hf_yTa_{1-y}). Rietveld refinement of XRD patterns and the TEM images confirm that the grain size of both β-SiC and MC_xN_{1-x} are less than 100 nm even after annealing at 1900 ºC for 5 h. The grain growth of β-SiC can be effectively suppressed by introducing M elements into the single-source precursors. $Hf_{0.7}Ta_{0.3}C_xN_{1-x}$ and $Hf_{0.2}Ta_{0.8}C_xN_{1-x}$ solid solutions with an expected Hf/Ta atomic ratio can be controlled precisely by adjusting the mole ratio of metal compounds during synthesis of the single-source precursors. It is worth emphasizing that a unique MC_xN_{1-x}-carbon core shell microstructure is observed within all the SiMC(N) ceramic nanocomposites, and the Hf-rich phase (*e.g.*, HfC_xN_{1-x} and $Hf_{0.7}Ta_{0.3}C_xN_{1-x}$) seems to facilitate the formation of the carbon shell more easily. The carbon shell on the MC_xN_{1-x} core is able to hinder the coarsening of MC_xN_{1-x} grains during high-temperature processing. Thus, dense monolithic SiMC(N)

ceramic nanocomposites are fabricated successfully upon spark plasma sintering of the amorphous SiMC(N) ceramics at 2200 ºC. The achieved maximum diameter is 35 mm, which is rarely reported in the literature.

Laser ablation behavior of the SiHfC(N) ceramics was investigated on dense monolithic SiHfC(N) ceramic nanocomposites and C_f-reinforced SiHfC(N) ceramic matrix composites. With addition of the HfC_xN_{1-x} phase, the rim of the ablation pit is covered by Hf-containing materials (*e.g.*, HfO_2), which are able to suppress the growth of the ablation pit. The dielectric properties and microwave absorption performance of the SiHfC(N) ceramics were investigated in the X-band (8.2 ~ 12.4 GHz) at room temperature. The minimum reflection loss and the maximum effective absorption bandwidth amount to -47 dB and 3.6 GHz, respectively. Free carbon, including graphitic carbon homogeneously dispersed in the SiC-matrix and less ordered carbon deposited as a shell on HfC_xN_{1-x} nanoparticles, accounts for the unique dielectric behavior of the SiHfC(N) ceramics. Electromagnetic interference (EMI) shielding performance of the dense monolithic SiHfC(N) ceramic nanocomposites were investigated in the X-band (8.2 ~ 12.4 GHz) at temperatures up to 600 ºC. At room temperature, the SiC/C-35mm and SiC/15HfC_xN_{1-x}/C-35mm exhibit an average total shielding effectiveness (SE_T) of ≈ 21 dB and ≈ 42 dB, respectively, and at 600 ºC, ≈ 22.6 dB and ≈ 40.2 dB, respectively. That means that with addition of a small amount of conductive HfC_xN_{1-x}, the SE_T is highly improved at both room and high temperatures.

In summary, the synthesis, ceramization, densification as well as microstructural evolution of SiMC(N) ceramic nanocomposites are deeply investigated in this work. With the addition of an M-containing phase, the as-prepared SiMC(N) ceramic nanocomposites exhibit enhanced electrical conductivity, microwave absorption capability, electromagnetic interference shielding performance and laser ablation resistance. Moreover, the correlations regarding to molecular design, microstructure and properties of the SiMC(N) ceramic nanocomposites are carefully discussed.

Zusammenfassung

Die Ansprüche von Industrie und Luftfahrt an zukünftige Technologien haben einen dringenden Bedarf an neuen Materialeigenschaften geschaffen, die die Eigenschaften der heutigen bekannten Materialien übertreffen und die nur durch die Gestaltung der jeweiligen Mikrostruktur im Nanobereich hergestellt werden können. Die Methode der Single-Source-Präkursoren eröffnet unter Ausnutzung der Korrelation zwischen der Molekülstruktur und der präkeramischen Präkursoren sowie der Mikrostruktur der abgeleiteten keramischen Materialien neue Möglichkeiten, neuartige keramische Materialien herzustellen, die durch konventionelle Synthesen nicht erreichbar sind. Das Ziel dieser Dissertation besteht darin, mit einer maßgeschneiderten Mikrostruktur und vielseitigen Eigenschaften durch das Moleküldesign der Präkursoren Ansätze für die Herstellung von neuartigen Keramik-Nanokompositen zu entwickeln.

Aus dieser Motivation heraus wurde eine Reihe von dichten monolithischen SiMC(N)-Keramik-Nanokompositen (M = Hf, Ta. HfTa) unter Verwendung der Einkomponenten-Präkursor-Synthese plus Spark-Plasma-Sintern hergestellt. Die chemische Synthese, Polymer-Keramik-Umwandlung sowie die Hochtemperatur-Mikrostrukturentwicklung wurde unter Verwendung von FT-IR, MAS Festkörper-NMR, TG/MS, XRD, Elementaranalyse, SEM, TEM und Raman-Spektroskopie etc. charakterisiert. Außerdem wurden die elektrische Leitfähigkeit, die Mikrowellen-Absorptionsfähigkeit, die Leistung bei der Abschirmung gegen elektromagnetische Störfelder und der Laserabtragungs-Widerstand der hergestellten dichten Monolithen untersucht.

Im Syntheseteil wurde eine Reihe von M-haltigen Einkomponenten-Präkursoren aus Reaktionen zwischen einem im Handel erhältlichen Allylhydridopolycarbosilan (SMP10) und Metallverbindungen einschließlich $Hf(NMe_2)_4$. $Hf(NEt_2)_4$ und $Ta(NMe_2)_5$ synthetisiert. Die Polymer-Keramik-Umwandlung wurde unter Verwendung von FT-IR, ^{13}C und ^{29}Si MAS-Festkörper-NMR sowie in situ TG/MS charakterisiert. Die unter Verwendung von $Hf(NMe_2)_4$ und $Ta(NMe_2)_5$ synthetisierten Präkursoren führen zu einem höheren Keramikertrag (≈ 80 Gew. %) als die von $Hf(NEt_2)_4$ (≈ 71 Gew. %), während der Keramikertrag der letzteren durch den Einsatz von $BH_3 \cdot SMe_2$ auf ≈ 78 Gew. % verbessert werden kann.

Mehrere thermisch stabile SiMC(N)-Keramik-Nanokomposite (Pulver) wurden durch das Hochtemperaturtempern der amorphen SiMC(N) Keramiken, einschließlich SiHfC(N), mit Bor dotiertem SiHfC(N), Sitac(N), SiHf7Ta3C(N) und SiHf2Ta8C(N) vorbereitet. XRD, Raman und TEM-Ergebnisse zeigen, dass die Keramik-Nanokomposite hauptsächlich β-SiC und MC_xN_{1-x} sowie freien Kohlenstoff enthalten (M = Hf, Ta, Hf_yTa_{1-y}). Die Rietveld-Verfeinerung des Röntgenbeugungsmusters und die TEM-Bilder bestätigen, dass die Korngröße sowohl von β-SiC als auch von MC_xN_{1-x} selbst nach dem Glühen bei 1.900 °C für 5 Stunden weniger als 100 nm beträgt. Das Kornwachstum von β-SiC kann erfolgreich durch Einbringen von M-Elementen in die Einkomponenten-Präkursoren unterdrückt werden. $Hf_{0,7}Ta_{0,3}C_xN_{1-x}$- und $Hf_{0,2}Ta_{0,8}C_xN_{1-x}$-Mischkristalle mit einem angenommenen Hf/Ta-Atomverhältnis können durch das Einstellen des Molverhältnisses von Metallverbindungen bei der Synthese der

Einkomponenten-Präkursoren genau gesteuert werden. Es ist erwähnenswert, dass eine einzigartige MC_xN_{1-x}-Kohlenstoff-Kern-Hülle-Mikrostruktur innerhalb aller SiMC(N)-Keramik-Nanokomposite beobachtet wird und, dass die Hf-reiche Phase (beispielsweise HfC_xN_{1-x} und $Hf_{0,7}Ta_{0,3}C_xN_{1-x}$) die Bildung der Kohlenstoffhülle zu erleichtern scheint. Die Kohlenstoffhülle auf dem MC_xN_{1-x} Kern ist imstande, die Vergröberung von MC_xN_{1-x} Körnern während der Hochtemperaturverarbeitung zu verhindern. Somit werden dichte monolithische SiMC(N)-Keramik-Nanokomposite bei 2.200 °C durch das Spark-Plasma-Sintern der amorphen SiMC(N)-Keramiken erfolgreich hergestellt. Der erreichte maximale Durchmesser beträgt 35 mm, was selten in der Literatur berichtet wird.

Das Laserabtragungs-Verhalten der SiHfC(N)-Keramiken wurde auf dichten, monolithischen SiHfC(N)-Keramik-Nanokompositen und C_f-verstärkten SiHfC(N)-Keramik-Matrix-Kompositen untersucht. Durch Zugabe der HfC_xN_{1-x}-Phase wird der Rand der Abtragungsvertiefung durch Hf-haltige Materialien abgedeckt (z.B, HfO_2), die die Ausdehnung der Abtragungsvertiefung verhindern soll. Die dielektrischen Eigenschaften und die Mikrowellen-Absorptionsleistungen der SiHfC(N)-Keramiken wurden im X-Band (8,2 ~ 12,4 GHz) bei Raumtemperatur untersucht. Der Mindest-Reflexionsverlust und die maximale effektive Absorptions-Bandbreite erreicht jeweils -47 dB und 3,6 GHz. Freier Kohlenstoff, einschließlich in der SiC-Matrix homogen verteilter graphitischer Kohlenstoff als auch weniger geordneter Kohlenstoff, der sich als Hülle auf den HfC_xN_{1-x}-Nanopartikeln abgeschieden hat, ist für das einzigartige dielektrische Verhalten der SiHfC(N)-Keramiken verantwortlich. Die Abschirmungs-Leistung der dichten monolithischen SiHfC(N)-Keramik-Nanokomposite gegenüber elektromagnetischer Interferenzen (EMI) wurde im X-Band (8,2 ~ 12,4 GHz) bei Temperaturen bis zu 600 ºC untersucht. Bei Raumtemperatur weisen SiC/C-35 mm und SiC/15HfC_xN_{1-x}/C-35 mm eine mittlere effektive Gesamt-Abschirmung (SE_T) von jeweils ≈ 21 dB und ≈ 42 dB und bei 600 ºC jeweils ≈ 22,6 dB und ≈ 40,2 dB auf. Das bedeutet, dass bei Zugabe einer geringen Menge an leitfähigem HfC_xN_{1-x} die SE_T sowohl bei Raumtemperatur als auch bei hohen Temperaturen starkverbessert wird.

Zusammenfassend kann gesagt werden, dass die Synthese, die Keramisierung, die Verdichtung sowie die mikrostrukturelle Entwicklung der SiMC(N)-Keramik-Nanokomposite in dieser Arbeit tiefgehend untersucht wurden. Mit der Zugabe einer M-haltigen Phase weisen die hergestellten SiMC(N)-Keramik-Nanokomposite eine verbesserte elektrische Leitfähigkeit, Mikrowellenabsorptionsfähigkeit, Laserabtragungs-Beständigkeit sowie eine verbesserte Abschirmung gegen elektromagnetische Interferenzen auf. Darüber hinaus werden die Korrelationen in Bezug auf das molekulare Design, die Mikrostruktur und die Eigenschaften der SiMC(N)-Keramik-Nanokomposite sorgfältig diskutiert.

1 Introduction

1.1 Background and motivation

Exploring our cosmos with a space shuttle and flying with a vehicle at hypersonic speeds is always a dream of many scientists and engineers. Generally speaking, the term "hypersonic" refers to speeds higher than Mach 5, *i.e.*, in excess of five times the speed of sound in the gas medium.[2] However, flying through the atmosphere at such a high speed is very challenging for materials used on these vehicles. One example is the sharp leading edges that are used to enable vehicle maneuverability during atmospheric exit and reentry. During the flight, the sharp leading edges must withstand ultrahigh temperatures in excess of 2000 ºC caused by aerothermal heating and also endure corrosive plasmas from the atmosphere. Thus, the challenges related to these hostile conditions including severe oxidation, extreme heat fluxes, strong shock-wave loading as well as high mechanical stresses are inevitable.[3] Moreover, other components on the space shuttle and hypersonic vehicles such as combustors and thermal protection systems (TPS) also require materials that can withstand similar harsh environments.[4]

Ultrahigh-temperature ceramics (UHTCs) are currently the only possible materials that are able to meet these extremely tough requirements, in spite that the rather rare, expensive and heavy iridium coated rhenium metals have been proved to show outstanding strength and oxidation resistance at ultrahigh temperatures.[5, 6] The UHTCs are typically non-oxides with melting/decomposition temperatures higher than 3000 °C. The refractory carbides, nitrides and borides of Group IV to Group V elements in the periodic table are the main choices. At the beginning, pure UHTCs (*e.g.*, HfC, ZrC, TaC, HfB_2, ZrB_2) are proposed to be used as the ultrahigh-temperature structural materials.[7, 8] However, high density, poor oxidation resistance and bad damage tolerance of these materials seriously limits their practical applications.[5, 9, 10]

UHTC composites, especially nanocomposites, thereby are considered as promising alternatives because their oxidation/ablation resistance and thermomechanical properties are possible to be improved by adjusting their chemical and phase compositions. Particularly, an enormous and even unexpected improvement in their properties can be achieved when reducing the grain size of the composites towards the nanoscale.[11-13] To date, several UHTC composites have been reported, including monoliths, ceramic matrix composites (CMCs) and multilayer coatings.[14-17] One typical monolith is the ZrB_2 with 20 vol.% of SiC prepared by hot pressing. With the addition of around 20 vol.% of SiC, the oxidation resistance is substantially improved by forming a protective borosilicate coating.[2] For the CMCs, numerous Carbon- or SiC- fiber reinforced CMCs containing HfB_2, HfC, ZrB_2 or TaC powders are prepared using pressure-assisted slurry impregnation.[5, 18] With the addition of UHTC powders, ablation resistance of the CMCs is significantly improved.[19] Moreover, multilayer coatings such as SiC/HfC/SiC or SiC/HfC/PyC are proven to be good choice for enhancing the ablation/oxidation resistance of C_f/C composites.[16, 17] During ablation test, the in situ formed a compact glassy HfO_2 layer effectively protected the C_f/C substrate from

erosion. Meanwhile, the SiC/HfC/SiC or SiC/HfC/PyC coatings with SiC as the outer layer showed excellent oxidation resistance due to the formation of glassy SiO_2 and $HfSiO_4$ scale.

From the literature we note that SiC is one of the best "partners" of UHTCs for fabricating UHTC composites because SiC is able to improve the oxidation resistance of the composites by forming protective scale (*e.g.*, SiO_2, $HfSiO_4$, $ZrSiO_4$) at 1200 - 2000 ºC, and the UTHC components (*e.g.*, HfC, HfB_2, TaC, ZrB_2) can enhance the ablation resistance of the composites at temperatures higher than 2000 ºC by forming dense metal oxide scale (*e.g.*, HfO_2 and ZrO_2). Therefore, fabrication of SiC/UHTCs-based composites has attracted much attention during the past decade. To date, several methods have been employed for fabrication of the SiC/UHTCs-based composites. For instance, hot pressing[2], pressureless sintering[20], spark plasma sintering[21] as well as reactive spark plasma sintering and reactive hot pressing[22] of mixed SiC and UHTC powders were used to prepared dense monoliths. Pressure-assisted slurry impregnation is usually used for preparation of CMCs.[5, 18] Chemical vapor deposition (CVD) is mainly used for multilayer coatings.[16, 17] However, each method has disadvantages. For sintering of the monoliths, high processing temperature is necessary and will lead to strong grain growth.[23] The application of slurry-impregnation for CMCs is highly limited by the homogeneous dispersion of UHTC powders, especially nano powders, within the slurry. The CVD method is expensive and time consuming, and it is hard to prepare UHTC solid solutions like Ta_4HfC_5 due to the different deposition kinetics of Ta and Hf atoms.[24] Thus, fabrication of SiC/UHTCs-based composites with expected chemical/phase composition and microstructure is quite difficult, and the preparation of ceramic nanocomposites with good homogeneity is particularly challenging. Therefore, some new preparative routes should be considered.

One of the most suitable preparative routes towards SiC/UHTCs-based ceramic nanocomposites is shown to be the single-source-precursor route.[13, 25] Firstly, the preceramic single-source precursors can be tailored at the molecular level to design ceramic nanocomposites with unique phase/chemical compositions and microstructures.[13, 25-27] Secondly, the dispersive UHTC phase is *in situ* generated by high-temperature processing, which guarantees excellent homogeneity of the nanocomposites.[28] Thus, in this Ph.D. work, the single-source-precursor route is employed to prepare dense monolithic SiMC(N) ceramic nanocomposites (M = Hf, Ta, HfTa). Moreover, most of the UHTCs are highly conductive ceramics that possess electrical conductivity of the order of $\sigma = 10^4$ S/cm (only 1 order of magnitude lower than silver and copper). Therefore, some functional properties and applications of the SiMC(N) ceramic nanocomposites including electrical conductivity, dielectric property, microwave absorption and electromagnetic interference shielding performance are also investigated. Furthermore, the correlations regarding to molecular design, microstructure and properties of the SiMC(N) ceramic nanocomposites are discussed in order to further develop the concepts of tailor-made molecular towards nanostructured ceramic nanocomposites with versatile properties.

1.2 Scope of the present work

With the motivation mentioned above, the whole thesis comprises 3 parts.

The first part is single-source-precursor synthesis and characterization of dense monolithic SiMC(N) ceramic nanocomposites (M = Hf, Ta, HfTa), including:

- SiHfC(N) ceramic nanocomposites and boron-doped SiHfC(N) ceramics;
- SiTaC(N) ceramic nanocomposites;
- SiHf7Ta3C(N) and SiHf2Ta8C(N) ceramic nanocomposites.

In this part, a series of SiMC(N) ceramic nanocomposites with a unique MC_xN_{1-x}-carbon core-shell microstructure are fabricated from M-containing single-source precursors. The characterization of chemical synthesis (section 3.1), polymer-to-ceramic transformation (section 3.2) as well as microstructure of the as-prepared ceramic powders (section 3.3) and dense monoliths (section 3.4) is conducted carefully in this part. FT-IR, MAS solid NMR, TG/MS, XRD, Elemental analysis, SEM, TEM and Raman spectroscopy are the main tools used for characterization.

The second part (section 3.5) describes the laser ablation resistance of bulk SiHfC(N) ceramics, comprising:

- Dense monolithic SiHfC(N) ceramic nanocomposites;
- C_f-reinforced SiHfC(N) ceramic matrix composites (*i.e.*, C_f/SiHfC(N)).

The samples are ablated by a CO_2 laser beam (10.6 μm) with a certain ablation time (0.5 ~ 1 s) and power (500 ~ 1000 W). The temperature of ablation center is higher than 3000 ºC. The intrinsic laser ablation behavior is characterized on the dense monolithic SiHfC(N) ceramic nanocomposites (section 3.5.1) using SEM coupled with EDX analysis. The C_f/SiHfC(N), as a case study for practical applications, is tested and compared with C_f/SiC (section 3.5.2).

The third part is functional applications of the SiHfC(N) ceramic nanocomposite, composed of the following:

- Microwave absorption of SiHfC(N) ceramic nanocomposites at room temperature;
- Electromagnetic interference (EMI) shielding performance of the dense monolithic SiHfC(N) ceramic nanocomposites at temperatures up to 600 ºC.

The dielectric properties and microwave absorption performance of the SiHfC(N) ceramic nanocomposites with different Hf content are investigated using a N5222A PNA-X Vector Network Analyzer in the X-Band (8.2 ~ 12.4 GHz). The correlation between the microstructure and dielectric properties of the SiHfC(N) ceramic nanocomposites is investigated and discussed with the aid of XRD, SEM, TEM and Raman spectroscopy. The unique HfC_xN_{1-x}-carbon core-shell structure is observed to play

an important role in their dielectric properties and microwave absorption performance (section 3.6). The EMI shielding performance of the dense monolithic SiHfC(N) ceramic nanocomposites at temperatures up to 600 ºC is investigated using a wave-guide method on a vector network analyzer (MS4644A; Anritsu, Japan) in the X-Band (8.2 ~ 12.4 GHz). The shielding mechanisms are discussed in terms of reflection loss and absorption loss. The variations of the shielding effectiveness as a function of temperature are discussed as well.

1.3 State of the Art

1.3.1 Polymer derived Si-based ceramics

Ceramics such as Al_2O_3, ZrO_2, HfO_2, TaC, SiC and Si_3N_4 are defined as inorganic, non-metallic materials that are typically crystalline in nature and possess some features (*e.g.*, brittleness and ductility) that are totally different from organic and metallic materials. Clay products, white ware, refractories, glasses, cements, abrasives, and advanced ceramics are main categories of ceramics used in industry.[29] Si-based advanced ceramics (*e.g.*, SiC, Si_3N_4) that provide a good combination of high strength, superior hardness, outstanding oxidation resistance as well as excellent thermal and chemical stability is one the most important kinds of ceramic materials. Conventionally, the Si-based ceramic parts are subsequently manufactured using powder synthesis (solid reaction), powder processing (*e.g.*, milling and mixing), shaping and sintering.[30] However, the powder technologies are impossible or not suitable for preparing ceramic fibers, crack-free coatings/films, ceramic matrix composites, ceramic nanocomposites as well as dense ceramic monoliths obtained at relatively low processing temperatures (*e.g.*, 1100 ~ 1300 ºC).

Around 40 years ago, preceramic polymers have been proposed for preparation of Si-based advanced ceramics, namely, polymer-derived ceramics (PDCs).[31] The PDC route typically comprises the following steps: *(1)* synthesis of preceramic precursors; *(2)* shaping and crosslinking; *(3)* polymer-to-ceramic transformation (*i.e.*, ceramization); and *(4)* crystallization. The transformation of polymer to ceramic upon pyrolysis provided an opportunity to develop several novel Si-based advanced ceramics, including crack-free coatings/films[32], small-diameter fibers[33, 34], dense monolithic ceramics obtained at low temperatures (1000 - 1300 ºC)[35] as well as non-oxide ceramics stable at temperatures up to 2000 ºC.[31, 36] Moreover, the PDC route enables producing of ternary (*e.g.*, SiCN, SiOC) and quaternary (*e.g.*, SiBCN) ceramics, which cannot be fabricated by other methods so far.[31, 37, 38] During the past several decades, significant technological breakthroughs were achieved by scientists, such as Ainger, Herbert, Chantrell, Popper, Verbeek, Fritz, Raabe, Yajima, Riedel, and others.[31] Recently, numerous novel ceramic nanocomposites with tailored microstructures and properties have been successfully synthesized using PDC routes. The structural and functional properties of the polymer derived ceramic nanocomposites can be controlled at the nano scale by molecular design of the preceramic precursors.[13, 39] Moreover, polymer derived porous ceramics, ceramic nanowires/nanobelts as well as ceramic microlattice and honeycomb cellular fabricated by 3D printing of preceramic precursors have been reported as well.[40-42] More details are summarized in Table 1. 1 in section 1.1.2. Figure 1. 1 provides an overview of different types of preceramic polymers that are suitable for Si-based advanced ceramics.[31, 43]

The oversimplified general formula in the center of the diagram can be modified or designed by adjusting either the group (X) on the polymer backbone or the substituents R_1 and R_2 attached to the silicon atom. The variations of group (X) result in different classes of organosilicon precursors, such as polysilanes, polycarbosilanes, polysiloxanes, polysilazanes, polyborosilanes and polysilylcarbodiimides with X =

R_1SiR_2, CH_2, O, NH, BR_3 and N=C=N, respectively. Moreover, polycarbosiloxanes, polyborosiloxanes, polyborosilazanes, etc. can be obtained as well if group (X) represents 2 elements in alternating arrangement. R_1 and R_2 at the silicon atoms are functional groups that can also be adjusted. Chemical and thermal stability, solubility and fusibility as well as electronic, optical and rheological properties of the organosilicon polymers can be modified by adjusting the R_1 and R_2 groups. Moreover, the carbon content within the PDCs can be affected by the R_1 and R_2 groups as well. Generally, the R_1 and R_2 can be hydrogen, aliphatic or aromatic groups.

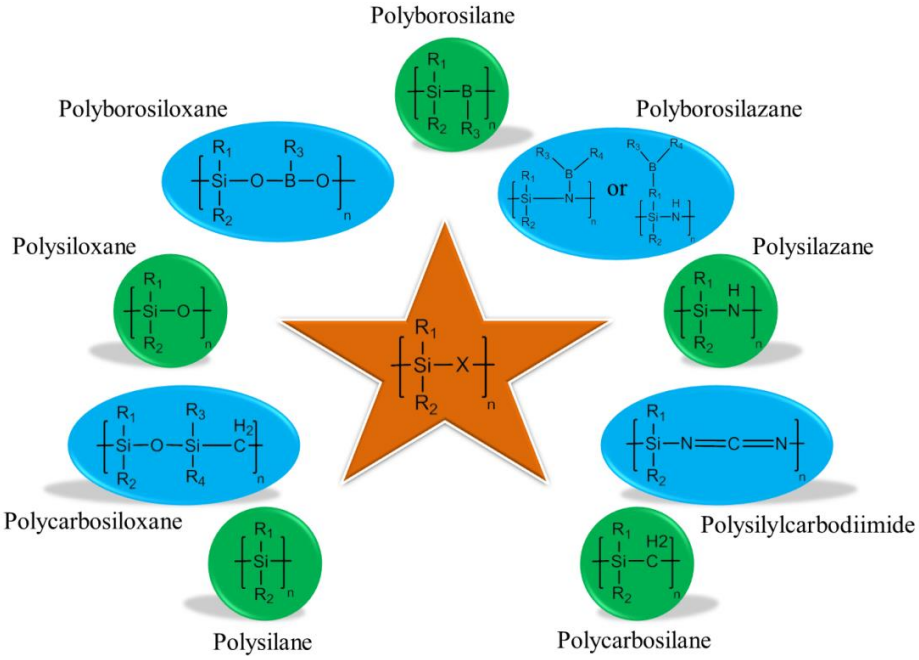

Figure 1. 1 Typical classes of organosilicon polymers for Si-based ceramics.

1.3.1.1 Synthesis of preceramic precursors

Synthesis of the preceramic precursors is a crucial step in fabrication of polymer derived ceramics (PDCs) because not only the chemical composition but also the phase composition and distribution as well as the microstructure of the finally produced ceramics are strongly affected by the molecular structure of the preceramic polymers. Thus, the chemical and physical properties of PDCs can be effectively adjusted by design of the precursors at the molecular level. In order to meet the requirements of practical applications, some properties of the polymers are quite important:

- high possibility for synthesis of ceramics with fitted stoichiometry, *e.g.*, SiC and Si_3N_4;
- suitable solubility or fusibility for processing/shaping;
- high molecular weight in order to avoid volatilization;
- no gelation, no uncontrolled polymerization or aging;
- high ceramic yield on pyrolysis.

Up to now, the synthesis of organosilicon precursors for advanced ceramics has been reported in numerous articles and books.[30, 31, 37] In this Ph.D. work, an allylhydridopolycarbosilane (SMP10, Starfire systems) is used for the synthesis of SiC-based ceramics. Thus, the introduction here focuses only on the synthesis of precursors for SiC. Figure 1. 2 is a simplified general formula of the organosilicon precursors for SiC. Group X on the backbone can be various arrangements according to the requirement of polymers and obtained ceramics.

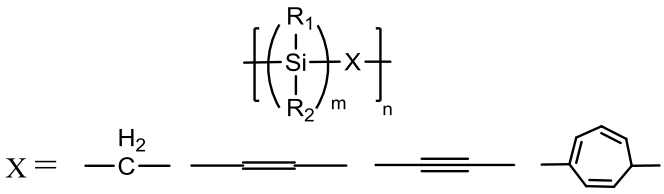

Figure 1. 2 Simplified general formula of typical polycarbosilanes used for SiC.[31]

Because of high ceramic yield, poly(methylcarbosilane) is one of the most important precursors for β-SiC and SiC-based fibers. Figure 1. 3 presents the synthesis process of the poly(methyl-carbosilane) from organic halides (*i.e.*, chlorosilanes). In the first step, polysilanes can be obtained by dehalogenation of chlorosilanes with Na at 110 ºC in toluene (Wurtz reaction). In the second step, the polysilanes convert into poly(methylcarbosilane) while undergoing a crucial rearrangement by heat treatment at 470 ºC (*i.e.*, the Kumada rearrangement), which can be accelerated by Lewis acid catalysts.[37]

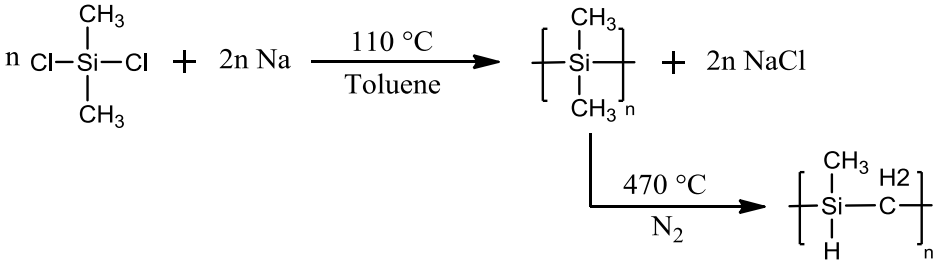

Figure 1. 3 Classical route for synthesis of poly(methylcarbosilane).

Preparation of SiC using poly(methylcarbosilane) has a problem of excess carbon, which limits the high-temperature properties (*e.g.*, oxidation resistance) of the ceramics.[37] Therefore, preparation of near stoichiometric SiC is always the target of the design and synthesis of suitable preceramic precursors. Among the polycarbosilanes[44-48], hydridopolycarbosilanes with essentially a "SiH_2CH_2" composition is one of the most promising precursors for near stoichiometric SiC ceramics with low excess carbon.[37] Two typical synthesis routes for the hydridopolycarbosilanes (HPCS) are shown in Figure 1. 4, including platinum-catalyzed ring-opening polymerization of 1,1,3,3-tetrachloro-1,3-disilacyclobutane *(a)* and Grignard coupling of chloromethyltrichloro-silane *(b)* followed by reduction with $LiAlH_4$.[37, 48]

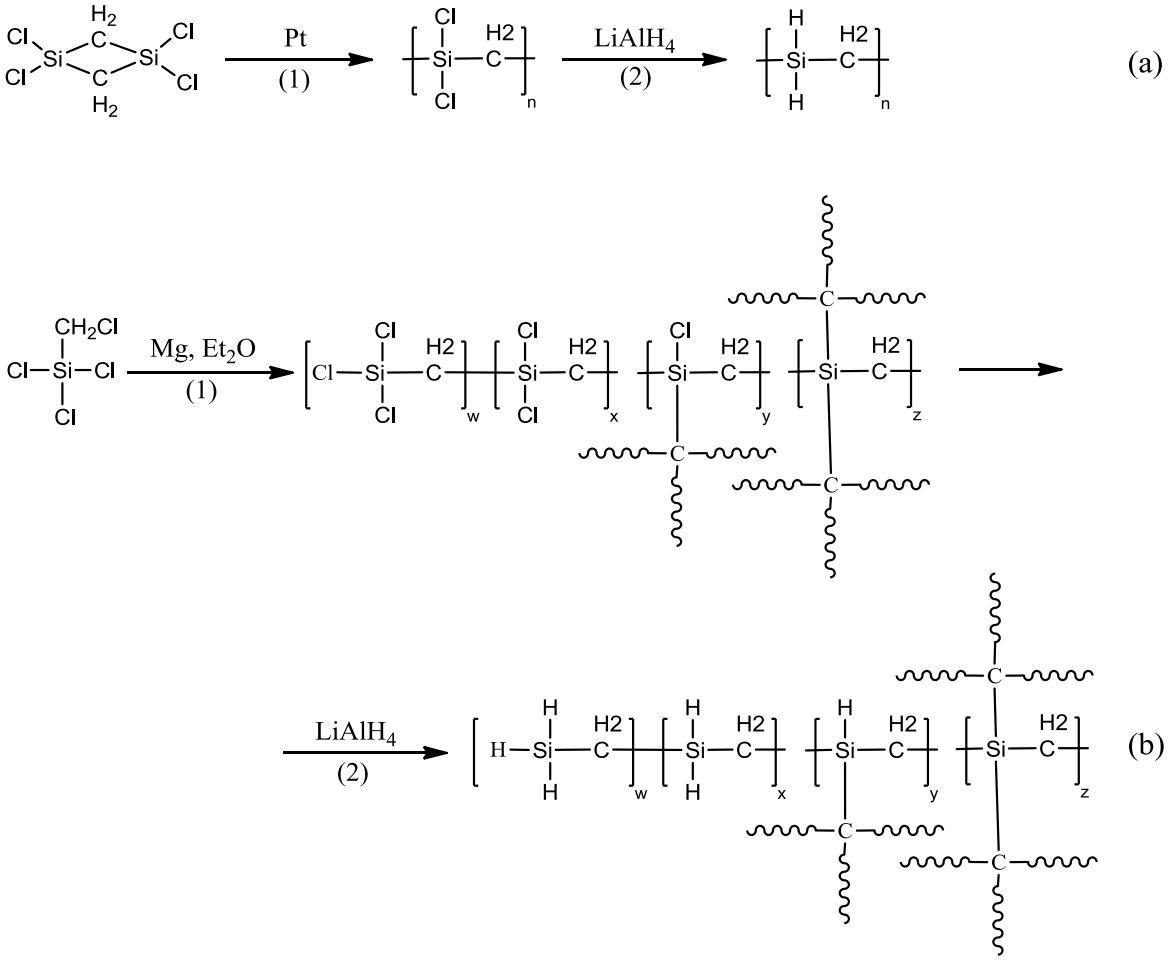

Figure 1. 4 Two typical routes for synthesis of hydridopolycarbosilanes.

Route *(a)* results in a linear polymer with repeat $[SiH_2CH_2]_n$ units, namely, polysilaethylene(PSE). This polymer is the monosilicon analog of polyethylene. However, different from the high density polyethylene, which has melting point at 135 °C, PSE is a liquid at room temperature. After pyrolysis at 1000 ºC, a stoichiometric β-SiC nanocrystalline with a quite high ceramic yield (up to 90% by thermogravimetric analysis) can be obtained from the PSE. However, due to the relatively high cost (*e.g.*, Pt catalysts) PSE is not suitable for practical applications. Because of its simple, highly regular and well-defined molecular structure, PSE is a useful model system for the investigation of the precursor-to-ceramic conversion process.

Route *(b)* results in a highly branched hydridopolycarbosilane, namely, hyper branched polysilaethylene (HBPSE, commercially known as HPCS). The HBPSE polymer has a $[H_3SiCH_2]_w[H_2SiCH_2]_x[HSiCH_2]_y[SiCH_2]_z$ structure with w/x/y/z ≈ 11:20:8:2 according ^{29}Si NMR and a typical M_w/M_n = 1000/600 (*i.e.*, polydispersity index ≈ 1.67) with an average degree of polymerization of about 13 according to the analysis of gel permeation chromatography (GPC) coupled with vapor-pressure osmometry.[49, 50] It thermosets at 200 ~ 400 °C (or at 100 °C with a catalyst) and gives near stoichiometric β-SiC with ceramic yield of ≈ 80% after pyrolysis at 1000 °C. Different from the PSE,

which at present is difficult and expensive to prepare and only available in small amount, HBPSE (or HPCS) and its allyl derivative (*i.e.*, AHPCS, A = allyl) are readily available in high yield from starting materials with a relatively low cost. Combined with its fluidity, ability to undergo thermal crosslinking, high ceramic yield and moderate stability in air, the HBPSE is a promising precursor for a β-SiC matrix of fiber-reinforced ceramic matrix composites fabricated via a vacuum polymer infiltration and pyrolysis (PIP) process.[48, 51]

One of the most successful commercially available AHPCS is SMP10 (Starfire Systems, USA) that is the precursor for all of the SiC-based ceramics in this Ph.D. work. It is an allyl derivative of the HBPSE (or HPCS) with ≈ 5 mol% allyl substituents. Figure 1. 5 is the general formula of SMP10. The SMP10 can be synthesized according to the reactions mentioned above. However, the specific techniques and reaction pathways employed to synthesize the SMP-10 is still unpublished because of confidential issues. Moreover, numerous synthesis routes of other representative preceramic precursors for Si_3N_4, SiCN, and SiOC are summarized in Ref.[30, 31, 37]

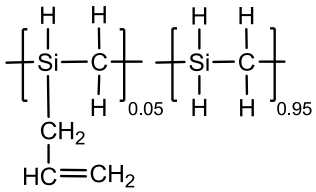

Figure 1. 5 Oversimplified general formula of a commercial AHPCS (SMP10, Starfire Systems).

1.3.1.2 Si-based ceramics synthesized in PDC route

Before crosslinking/curing and ceramization, the preceramic precursors are of polymeric nature. Taking advantages of the polymeric nature of preceramic precursors, numerous novel advanced ceramics have been developed. The adjustable solubility, fusibility and viscosity of the polymers enabled the preparation of several novel advanced ceramics that cannot be obtained by powder technology, including ceramic fibers, coatings/films, ceramic matrix composites as well as dense monoliths obtained at relatively low processing temperatures.[31, 52, 53] Furthermore, fabrication of porous ceramics, ceramic microparts, gas-turbine components as well as ceramic nanowires, nanotubes, etc. in PDC routes has been reported as well.[54-56] Table 1. 1 lists recently reported advanced ceramic synthesized in PDC routes. More details are presented in related literature.[31, 57]

Table 1. 1 Typical processing techniques and the as-prepared polymer derived ceramics.

Processing technique	Polymer derived ceramics
Casting/Freeze/Liquid/Tape casting	SiOC(N) ceramic tubes by centrifugal casting;[58] Porous SiC by freezing;[59] SiOC ceramic microparts via liquid casting;[60] Si-O-C-(N) tapes from preceramic polymers;[61]
Impregnation/infiltration/ Templating	Gas-turbine components (SiOC fiber reinforced SiCN composites) by impregnation;[62] Macroporous SiC by templating;[63]
Coating (spraying, dip- or spin-coating, CVD)	SiOC coatings by spraying;[64] SiC thin films from preceramic precursor;[65] SiCN alloys by remote plasma chemical vapor deposition;[66]
Cold/warm-uniaxial and cold-isostatic pressing	SiCN and SiBCN bulks by plastic forming and cold isostatic pressing;[67] Al_2O_3-SiC composites by warm pressing;[68]
Injection molding	Bulk SiC[69] and SiOC composites[70] by injection moulding;
Extrusion	Porous SiC parts by extrusion;[71] SiC microelectrodes by extrusion;[72]
Fiber drawing	Small-diameter SiC fibers;[73, 74]
Blowing/foaming	SiOC foams with gradient porosity;[75] SiOC microcellular by supercritical CO_2;[54]
Machining	Complex-shaped ceramic composites obtained by machining compact polymer-filler mixtures;[76]
Joining/seals	SiOC joining for SiC;[77] Non-oxide (SiC and Si_3N_4) seals;[78]
Rapid prototyping	SiOC/SiC parts by selective laser curing;[79]
Additive manufacturing (3D printing)	SiOC microlattice and honeycomb cellular by 3D printing;[41]
Ink jetting	Solid freeforming of SiC by inkjet printing;[80]
Electrohydrodynamic-spraying/spinning	Porous SiOC capsules by electrohydrodynamic forming;[81] B_4C/C nanofibers via electrostatic spinning;[82] Web-type SiC fibers by Electrospinning;[83] Superhydrophobic mats by SiCNO fibers;[84]
Self-assembly	Nano-ordered ceramics (BN and $B_4C_xN_{1-x}$/C) by self-assembly;[85, 86]
Microcomponent processing	SiCN microparts from x-ray lithography;[87]

(UV/X-ray lithography, etc.)	SiCN microfluidic channels and SiBCN MEMS microparts by a soft lithographic technique;[88, 89]
Emulsion processing	Porous SiOC bodies by emulsion processing;[90] SiC Whisker;[91]
In situ synthesis of nanotubes, nanowires, etc.	Ultra-long single-crystalline α-Si_3N_4 nanowires;[92] single-crystal Si_3N_4 nanowires/nanobelts;[42] Ultra-long SiCN nanowires and SiCN/SiO_2 nanocables;[93]

1.3.1.3 Polymer derived ceramic nanocomposites (PDC-NCs)

Recently, nanocomposites received increasing interest because an enormous or even unexpected improvement in their properties (*e.g.*, mechanical, electrical, optical) can be achieved when reducing the size of the components within the composite materials towards the nano scale.[11, 12, 94, 95] One of the most suitable preparative routes towards ceramic nanocomposites (NCs) was shown to be the PDC route relying on the pyrolytic conversion of polymeric single-source precursors.[13, 26, 28] The single-source precursors (SSPs) can be tailored at the molecular level in order to design ceramic nanocomposites with unique phase compositions and microstructures and consequently with improved properties.[27]

The formation of polymer derived ceramic nanocomposites (PDC-NCs) consists of 4 major steps: *1.)* preparation of suitable preceramic precursors via chemical modification of organosilicon polymers; *2.)* cross-linking at moderated temperatures (150 ~ 300 ºC) or under UV light to furnish an infusible organic/inorganic network (preceramic networks); *3.)* pyrolysis of the cross-linked precursors that can be converted into inorganic amorphous ceramics at temperatures from 1000 °C to 1300 °C; and *4.)* annealing of the as-pyrolyzed amorphous ceramics at elevated temperatures (≥1500°C) to prepare well crystallized PDC-NCs.

The PDC-NCs have been widely investigated and reported for structural and functional applications in the past few years.[13, 96] One example for structural application is the SiOC/ZrO_2 ceramic nanocomposite that is prepared upon pyrolysis and subsequent annealing of a single-source precursor synthesized by chemical reaction between commercially available zirconium tetra(n-propoxide) [$Zr(O^nPr)_4$] and polymethylsilsesquioxane (MK, Wacker, Germany). The experiments reveal that thermal stability of the SiOC/ZrO_2 ceramic nanocomposite with respect to crystallization and decomposition at temperatures higher than 1300°C is remarkably increased due to the incorporation of ZrO_2 into the SiOC matrix. This result emphasizes the enormous potential of the SiOC/ZrO_2 ceramic nanocomposite for high-temperature structural applications.[28] Another example is the SiCN/ZrO_2 ceramic nanocomposite. Compared with non-modified SiCN (derived from pure polysilazane HTT1800), the oxidation resistance of SiCN/ZrO_2 is improved significantly by chemical modification of the HTT1800 with zirconium isopropoxide. Moreover, a SiAlCN(O) ceramic nanocomposite that is prepared by chemical modification of Ceraset

Polysilazane (KiON Defense Technologies, Inc., Pennsylvania, USA) with aluminum isopropoxide exhibits an outstanding high-temperature stability in both oxidative and corrosive environment. The oxidation results show that the parabolic oxidation rates of SiAlCN(O) ceramic nanocomposites are 2 to 3 orders of magnitude (depending on Al content) lower than those of SiCN. The aluminium within the oxide scale on the surface of the SiAlCN(O) strongly suppresses the inward diffusion of oxygen.[97]

The functional applications of the PDC-NCs are involved in numerous research fields comprising electronics, sensors, batteries and other emerging areas.[13] For instance, a soft magnetic Fe_3Si-containing SiOC ceramic nanocomposite is synthesized upon pyrolysis of polymethylsilsesquioxane chemically modified with iron (III) acetylacetonate [$Fe(acac)_3$][98]; a stable SiOC/Sn nanocomposite anode used for Lithium-ion batteries with outstanding cycling stability is developed by chemical modification of polysiloxane (Polyramic RD-684a) with tin(II)acetate and subsequent pyrolysis at 1000 °C[99]; and a Cu@SiCN ceramic nanocomposite is prepared by pyrolysis of the aminopyridinato copper complex modified poly(organosilazanes) (HTT1800) to facilitate oxidation of hydrocarbons.[100] Moreover, the PDC-NCs used for microwave absorption[101], antibacterial application[102] as well as photo-degradation of organic dyes[103] have been reported as well.

1.3.1.4 PDC route towards UHTC nanocomposites (UHTC-NCs)

As mentioned in section 1.3.1.3, the PDC routes for ceramic nanocomposites should also be available for synthesis of ultrahigh-temperature ceramic nanocomposites (UHTC-NCs). The *in situ* formed UHTC nanocrystallines are able to disperse homogeneously within the ceramic matrix, which is rather difficult for other routes. Figure 1. 6 presents typical PDC routes used for synthesis of UHTC-NCs, including monoliths and CMCs. The monolithic UHTC-NCs can be directly obtained by route (I) or by annealing of amorphous samples obtained from route (II); the fiber reinforced UNTC-NCs can be obtained by annealing of amorphous sample fabricated by route (III). In route (II), the sequence of shaping and crosslinking can be arranged according to different requirements.

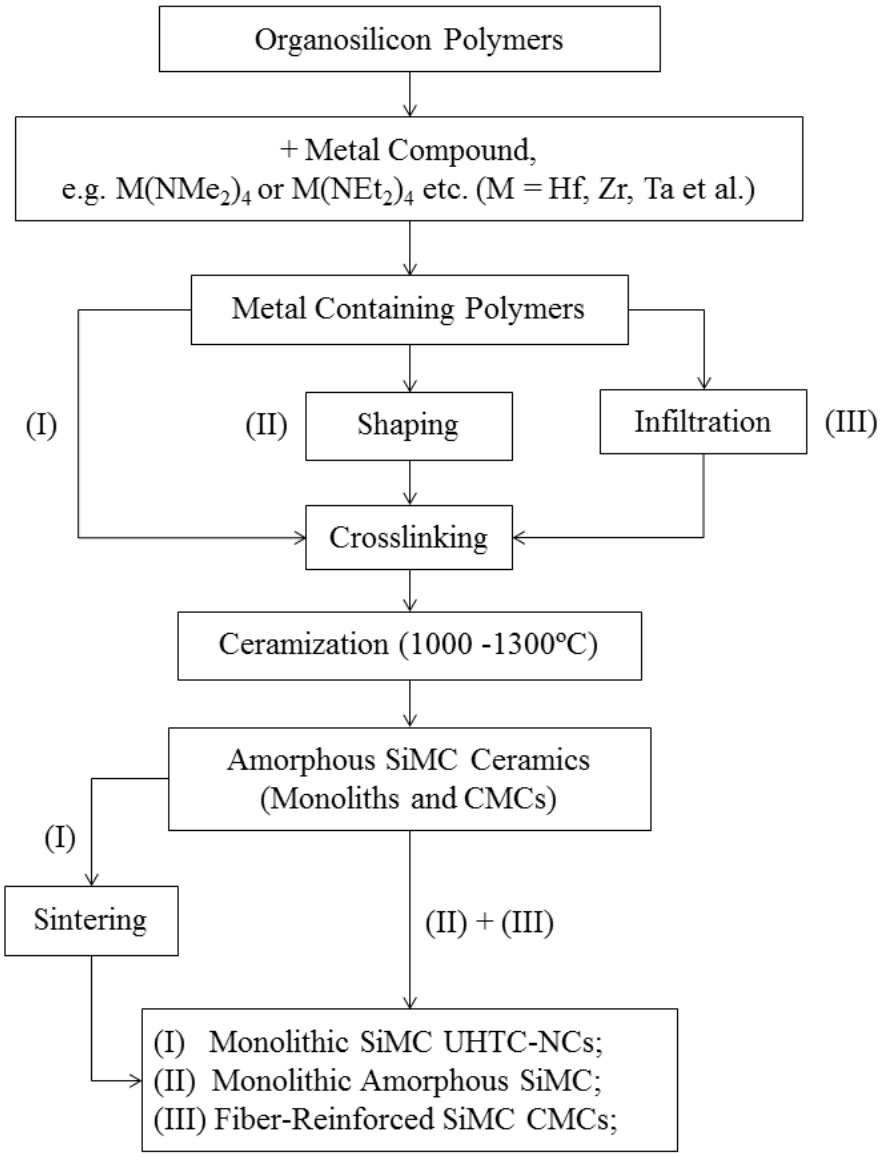

Figure 1. 6 Typical PDC routes used for synthesis of UHTC-NCs.[13, 25, 94]

One successful example is the SiHfBCN ceramic nanocomposites that were obtained by pyrolysis and subsequent annealing of a chemical modified polysilazane HTT1800.[25] The phase composition of the SiHfBCN ceramic nanocomposites can be adjusted by changing the annealing temperature and atmosphere. Various processing methods can be used to prepare different kinds of bulk SiHfBCN ceramics. For instance, the amorphous SiHfBCN ceramic powders can be densified by spark plasma sintering to prepare monolithic SiHfBCN UHTC-NCs, *i.e.*, route (I) in Figure 1. 6. The liquid preceramic precursor of the SiHfBCN can be infiltrated into carbon-fiber preforms to prepare ceramic matrix composites (*i.e.*, C_f/SiHfBCN), *i.e.*, route (III).[104, 105]

1.3.2 Microwave absorption (MA) materials

1.3.2.1 Absorption mechanisms and materials

Microwaves are a form of electromagnetic wave with wavelengths ranging from one meter to one millimeter and with corresponding frequencies between 300 MHz (1 m) and 300 GHz (1 mm). Microwave technology is extensively used for point-to-point telecommunication, TV, spacecraft communication, data transmission, radar technology, etc. because of their broad bandwidth, high data transmission rates and small antenna sizes.[106] However, the massive increase of high-frequency (in GHz range) electronic components and electronic systems, notably in telecommunication (0.8-1.5 GHz), LAN systems (2.45, 5.0, 19.0, 22.0, 60.0 GHz) and satellite broadcast systems (11.7-12.0 GHz) generate electromagnetic pollution and cause serious electromagnetic interference (EMI).[107, 108] Therefore, microwave absorption (MA) materials have attracted especial attention in the past decade. Generally, a MA material should be able to attenuate at least 90% of the electromagnetic wave, *i.e.*, the reflection loss (RL) should be lower than -10 dB. At RL < -20 dB, more than 99% of the waves are attenuated, and the material is said to have excellent microwave absorption capability.[109]

According to transmission-line theory, the microwave absorption for a single layer of absorber backed by a PEC (perfect electric conductor) can be evaluated by the reflection loss (RL):

$$RL = 20\log_{10}\left|\frac{\sqrt{\frac{\mu}{\varepsilon}}\tanh\left(j\frac{2\pi fd}{c}\sqrt{\mu\varepsilon}\right)-1}{\sqrt{\frac{\mu}{\varepsilon}}\tanh\left(j\frac{2\pi fd}{c}\sqrt{\mu\varepsilon}\right)+1}\right| \qquad (1\text{-}1)$$

where d, μ ($\mu=\mu'-j\mu''$) and ε ($\varepsilon=\varepsilon'-j\varepsilon''$) denote the thickness, complex permeability and complex permittivity of the absorber, respectively; c is the speed of light in the free space and f is the frequency of the incident electromagnetic wave. The terms ε' and μ' are the real parts of the complex permittivity and complex permeability, and the terms ε'' and μ'' represent the imaginary parts of the complex permittivity and complex permeability, respectively.[110-113]

To date, various MA materials used at room temperature have been developed, including ferrites, ferromagnetic metal particles (Fe, Co, Ni), intrinsically conductive polymers and ceramic composites with carbon nanotubes, graphene or ZnO nanotrees as fillers.[114-119] According to different attenuation mechanisms, the MA materials can be classified into 2 types: *1.)* magnetic-loss type, such as spinel ferrites (Fe_3O_4)[120], ferromagnetic metal particles (Fe/Co/Ni)[121, 122], Ba- and Sr-based hexaferrites[123, 124] and carbonyl iron[125] and *2.)* dielectric-loss type, such as ZnO[126], carbon black[127], CNTs[128], graphene[129], carbon fiber[130], SiC[131], $BaTiO_3$[132] and intrinsically conductive polymers like polyaniline[133] and polypyrrole.[134] Composite materials comprising both magnetic-loss type and dielectric-loss type MA materials were also widely investigated to obtain effective absorption in a wide frequency range.[135, 136]

When microwaves propagate into the magnetic-loss type MA materials, the energy will be attenuated by magnetic hysteresis, eddy current, magnetic domain-wall resonance, natural resonance, etc.[137, 138] Generally, the traditional magnetic-loss type MA materials are more suitable for low frequency microwave absorption because of a remarkable decrease of the complex permeability ascribed to the Snoek's limit (spinel ferrites) or eddy current phenomenon (ferromagnetic metal particles) in the GHz range.[114, 138] Ba- and Sr-based hexaferrites as well as carbonyl iron are able to be used in the GHz frequency range because a large value of the complex permeability can be obtained.[108, 121] Ferromagnetic metal particles are also found to be useful in GHz frequency range upon reducing the thickness/diameter of the particles to be less than skin depth.[121, 138] However, the Curie temperature limits the high-temperature application of magnetic-loss type MA materials.[139]

Within dielectric-loss type MA materials, the electric field of the microwave induces two types of electrical effects, *i.e.*, conduction current and displacement current.[140] The interaction with bound charge carries (displacement current) induces the polarization effect, which can be described by the real part of the permittivity (ε') according to the Debye theory:[130]

$$\varepsilon' = \varepsilon_\infty + \frac{\varepsilon_s - \varepsilon_\infty}{1 + [\omega\tau(\mathrm{T})]^2} \qquad (1\text{-}2)$$

where ε_s is static relative permittivity, ε_∞ is relative permittivity at high-frequency limit, ω is the angular frequency of incident electromagnetic wave and $\tau(T)$ is the temperature-dependent relaxation time of polarization. The effect arising from both free and bound charge carries gives rise to the imaginary part of the permittivity (ε''), which leads to the dielectric loss ($\varepsilon''/\varepsilon'$). From the Debye theory of dielectric materials, the ε''can be described as[130]

$$\varepsilon'' = \frac{\varepsilon_s - \varepsilon_\infty}{1 + [\omega\tau(T)]^2}\omega\tau(T) + \frac{\sigma(T)}{2\pi\varepsilon_0 f} \qquad (1\text{-}3)$$

where $\sigma(T)$ is temperature-dependent electrical conductivity, ε_0 is the permittivity of vacuum (8.854×10^{-12} F/m) and f is the frequency of incident electromagnetic wave.

In case of composites with carbon (or other highly conducting components) as a conductive filler, the electronic transport may be approximated by the free electron theory. Equation (1- 3) then reduces to[130, 140]

$$\varepsilon'' \approx \frac{\sigma(\mathrm{T})}{2\pi\varepsilon_0 \mathrm{f}} \qquad (1\text{-}4)$$

According to equation (1- 4), an increase/decrease of ε''(or dielectric loss) can be attributed to the increase/decrease of the electrical conductivity ($\sigma(T)$) of dielectric materials with conductive fillers. The value of $\sigma(T)$ can be affected by temperature, but there is no Curie temperature limit on the dielectric-loss type MA materials, which means this kind of MA materials can be considered to be used at high

temperature.

1.3.2.2 Microstructural design of the dielectric-loss type MA materials

In this Ph.D. work, we mainly focus on the dielectric-loss type MA materials, and hence only this kind of MA materials will be discussed here. As shown in Figure 1. 7a, the MA materials are generally composites comprising a matrix (denoted as *M* phase) with a low electrical conductivity (σ), a low real part of the permittivity (*ε′)* and a dielectric lossy phase (denoted as *L* phase) with a high electrical conductivity.[141, 142] The *M* phase with the *ε′* close to air is generally microwave transparent, which is good for the microwave propagating into the interior of the materials (*i.e.*, impedance match). For instance, polymers like paraffin[119], epoxy[140], polyethylene[143] and polyurethane[144] and ceramics like SiO_2, SiC and SiCN[145] are promising candidates for the *M* phase. The *L* phase disperses within the *M* phase and form effective percolation networks/domains to attenuate the microwave energy upon generating conduction currents.[146] Carbon materials (*e.g.*, carbon black, carbon fibers, CNTs, graphene, graphene oxide)[112], ZnO[147], MnO_2[148], YSZ[149] and TiC[150], etc. conductive/semi-conductive materials are good candidates for the *L* phase.

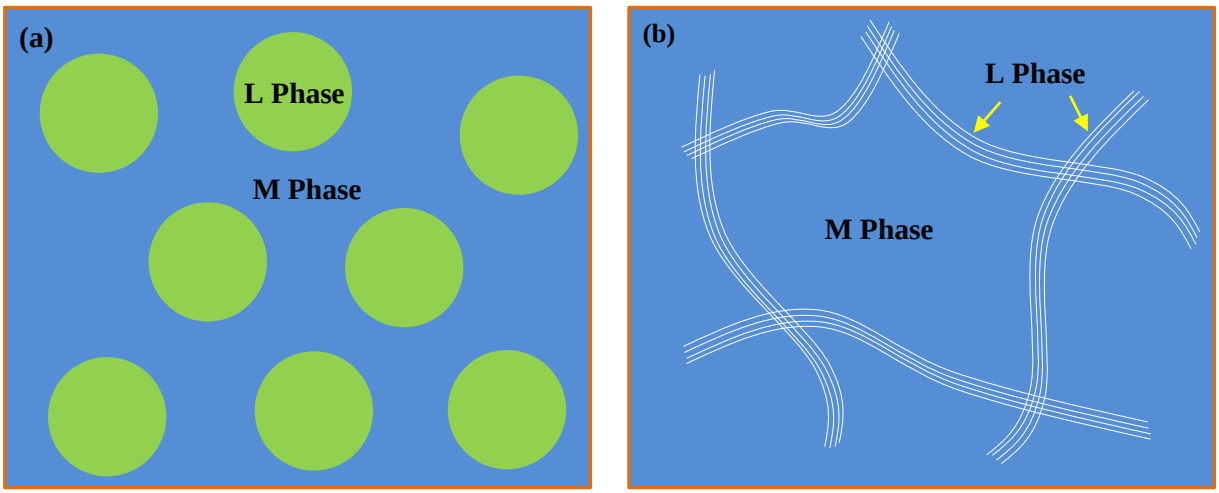

Figure 1. 7 Schematic illustration of the microstructural design of microwave absorption composite materials. The M phase is the matrix with low *σ and ε′*, while the L phase is the dielectric lossy phase with high *σ*.

However, according to the Maxwell Garnett mixing rule[151], with increasing content of the *L* phase, the *ε′* of the whole MA materials will be enhanced due to the high *ε′* of the *L* phase. More incident microwaves will be reflected by the surface of the MA materials because of the improved impedance mismatch between air and the MA materials. In addition, the volume percent of the *L* phase should not approach the vicinity of the percolation threshold because it will lead to significant enhancement of the *ε′* value.[152] Therefore, in order to obtain excellent microwave absorption capability, it is necessary to design the microstructure of the MA materials appropriately with an improved *ε″*value but also with a low *ε′*

value.[146]

According to equation (1- 4), an increase/decrease of ε''can be attributed to the increase/decrease of the electrical conductivity (σ) of the MA materials. The σ of composite materials can be predicted by the equation as follows:

$$\sigma = \sigma_L(x - x_c)^t, \ \ x > x_c \qquad (1\text{- }5)$$

$$\sigma = \sigma_M(x_c - x)^{-q}, \ \ x < x_c \qquad (1\text{- }6)$$

where σ_L and σ_M are electrical conductivity of the L phase and M phase, respectively; x and x_c are volume percent and percolation threshold of the L phase and t and q are critical exponents that are approximately 1.6 and 0.9, respectively.[153] Therefore, it is possible to tune the $\varepsilon''$by adjusting the x, x_c and σ_L of the L phase within the same M phase. As aforementioned, in the MA materials, the volume percent (x) of the L phase should be as low as possible to avoid high ε'. If the percolation threshold (x_c) of the L phase can be reduced, the required volume percent (x) will be decreased as well. Generally, the percolation threshold strongly depends on the particle size and shape (aspect ratio) of the L phase. For instance, the percolation threshold was predicted to be less than 5 vol.% when the aspect ratio of the conductive component exceeds 100.[154, 155] For spherical particles with a size below 50 nm, the percolation threshold will be lower than 10 vol.%.[156] Accordingly, reducing the particle size (nanocomposite formation) and increasing the aspect ratio of L phase (*e.g.*, nanotubes/nanonords and 2-dimentional materials, Figure 1. 7b) gives good opportunities to improve the σ or ε''value of the MA materials while keeping the ε' value low.

1.3.2.3 Microwave absorption at high temperature

In addition to sufficiently high microwave absorption capability in the required frequency range, an excellent MA material should also possess some other advantages such as structural lightweight, excellent thermal and chemical stability, superior oxidation and corrosion resistance to meet the requirement of application in harsh environment (*e.g.*, at high temperatures, in corrosive media). Recently, high-temperature MA materials have aroused increasing attention because of the demand for applications in high-temperature environments in the aerospace industry. As mentioned above, the application of most magnetic-loss type MA materials at high temperature is limited due to the Curie temperature.[157] The conductive polymer-based dielectric-loss type MA materials can only be used at temperatures lower than 300 °C due to their low melting/softening point and thermal stability.[158] Therefore, only a few dielectric-loss type MA materials are suitable for high-temperature microwave absorption, including YSZ/SiC[149], Ni/SiC[159], NiO/SiC[160], N-doped SiC[161], SiC powders[162], CNTs/SiO_2[158, 163], carbon fiber/SiO_2[130], TiC nanowire/SiO_2[150], ZnO/SiO_2[164], reduced graphene oxide/SiO_2[139], ZnO[147], ZnO/$ZrSiO_4$[165], MnO_2 nanonord[148] and Lithium Aluminum Silicate (LAS)/LAS-SiC double layer composite.[166] This shows that the most widely reported MA materials at high temperature are ceramic composites with SiC or SiO_2

as the *M* phase.[162] Especially, the dielectric properties of SiC at different temperatures reveal that increasing temperature has a positive effect on the microwave absorption capability of SiC in terms of the enhanced reflection loss value and widened effective absorption bandwidth.[162] In this Ph.D. work, β-SiC is also used as the matrix (*M* phase) of the MA materials.

As reported in previous studies, the MA performance of SiC-based ceramics at high temperature can be improved by decorating/coating with Ni[159] and NiO[160], and the minimum RL value and effective absorption bandwidth can be enhanced to ~ -30 to -50 dB and ~ 2.5 to 4.2 GHz in the X-band, respectively. However, the Ni and NiO phases are less chemically stable and might be easily corroded in a harsh environment. The YSZ/SiC reported in Ref.[149] is chemically and thermally stable. However, the MA capability at temperatures higher than 600 °C should be further improved. In order to fabricate a SiC-based MA material with excellent MA capability and high-temperature stability, a metallic component that is stable at high temperatures should be added. Ultrahigh-temperature ceramics such as MC as well as its solid solutions MC_xN_{1-x} (M = Zr, Hf, Ta) possess high electrical conductivity (σ) of the order of 10^4 S/cm, and they are well known for having ultrahigh melting points (> 3000 ºC), high hardness (20 ~25 GPa), wear resistance, thermal and chemical stability.[167] Therefore, in this Ph.D. work, HfC_xN_{1-x} will be used as *L* phase to prepare MA materials suitable for high-temperature microwave absorption.

1.3.2.4 PDC route towards microstructured MA materials

The fabrication of ceramic microwave absorption materials from preceramic precursors is a new technology reported only in the last 5 years. It has been applied so far for the fabrication of porous SiC[168], SiC/C[169], porous Si_3N_4/SiC composite[145], amorphous-SiBCN/SiC[170], amorphous-SiBCN/SiC nanoparticles[171] and SiOC/SiC-nanowire composite[172] MA materials. All of these MA materials are dielectric-loss type, and the corresponding parameters are listed in Table 1. 2.

The PDC-based MA materials have numerous advantages if compared with other MA materials. For instance, *i)* PDC-based composite MA materials possess amorphous ceramic matrix (M phase) exhibiting a low real part of the permittivity, which is preferable for impedance matching; *ii)* it is easy to homogeneously embed the dielectric loss phase (L phase) within the ceramic matrix by either *in situ* formation[170] or blending[171]; *iii)* the ceramic matrix with high melting point, excellent thermal and chemical stability as well as excellent resistance against decomposition and crystallization is especially useful for application in harsh environments[94, 173]; *iv)* the *in situ* precipitation of segregated carbon ribbon with high aspect ratio and electric conductivity is good dielectric loss phase[155]; *v)* due to the polymeric feature of the preceramic precursors, they can be subjected to a large variety of different shaping techniques to fabricate MA materials with various shapes (*e.g.*, monoliths, coatings, fibers and porous parts).[174]

Table 1. 2 Reported examples of Si-containing MA ceramics fabricated in PDC route.

Name	M phase	L phase	Optimum thickness (mm)	RL_{min} (dB)	EAB* (GHz)	Ref.
Porous SiC	SiC	Segregated carbon	2.75	-10.8	2.6	[168]
SiC/C	SiC	Carbon nanowires	2.85	-21	3.2	[169]
Porous Si_3N_4/SiC	Si_3N_4	SiC	3.35	-53	3.0	[145]
SiBCN/SiC	amorphous SiBCN	SiC-nanocrystals	2.31	-16.2	3.6	[170]
SiBCN/ nano-SiC	amorphous SiBCN	SiC-nanoparticles	14	-23.2	--	[171]
SiOC/SiC-nanowire	a-SiOC	SiC-nanowires	3.3	-20.0	1.8	[172]

* - EAB = Effective Absorption Bandwidth

1.3.3 Electromagnetic interference (EMI) shielding materials

Similar to microwave absorption materials, EMI shielding materials have attracted special attention in the past decade because of the massive increase of high frequency (in GHz) electronic components and electronic devices, notably in telecommunication, which cause serious electromagnetic interference. High shielding efficiency and light weight are two key factors for practical applications of EMI shielding materials. In addition, if they could be used in harsh environments (*e.g.*, at high temperatures, in corrosive media), the materials will be more attractive for a wide range of civil, commercial and aerospace applications.

1.3.3.1 Definition of EMI shielding effectiveness

The shielding effectiveness (SE) is usually defined as the ratio of the magnitude of the incident electric field (E_i) to the transmitted electric field (E_t):

$$SE = \left|\frac{E_i}{E_t}\right| \tag{1- 7}$$

$$SE(dB) = 20 \cdot log_{10}\left(\frac{E_i}{E_t}\right) \tag{1- 8}$$

This definition is sometimes referred to the electric field shielding effectiveness (ESE) because it involves the ratio of electric field amplitudes. In addition, the shielding effectiveness can be defined in terms of the ratio of the incident and transmitted magnetic field amplitudes, *i.e.*, the magnetic field shielding effectiveness (MSE). For plane waves and the same media (*e.g.*, air) on both sides of the shield, these two definitions are equivalent (*i.e.*, ESE = MSE). In this Ph.D. thesis, we mainly discuss the shielding of electromagnetic interference (EMI). Thus, here the SE represents the EMI shielding effectiveness.

Several factors are able to affect the SE values: (*a*) Frequency of the incident electromagnetic wave (EMW); (*b*) Properties (conductivity, permeability and permittivity) of shielding materials; (*c*) Thickness of shield; (*d*) Type of EMW source (plane wave, electric field or magnetic field); (*e*) Distance from the EMW source to the shield; (*f*) Shielding degradation caused by any shield apertures and penetrations and (*g*) Quality of the bond between shield surfaces.

1.3.3.2 EMI shielding theory

Assuming that the EMI shield is located in the far-field of the electromagnetic wave (EMW) source—thus the EMW can be considered as plane wave—the total shielding effectiveness (SE_T, in dB) can be expressed as the sum of an absorption loss (SE_A), a reflection loss (SE_R) as well as a multiple reflection correction term (SE_{MR}):

$$SE_T = SE_A + SE_R + SE_{MR} \quad (1\text{-}9)$$

EMI shielding processes are shown schematically in Figure 1. 8. An EMI shield has two boundaries where reflection and transmission of electromagnetic waves occur. An incident EMW is identified by "i" subscripts, a reflected EMW by "r" subscripts and a transmitted EMW by "t" subscripts. At each air/shield interface, a part of the EMW is reflected, and the remainder is transmitted. During transmission, part of the energy is absorbed by the shield. Reflection occurs due to an impedance mismatch, and absorption occurs due to energy losses within the shield.

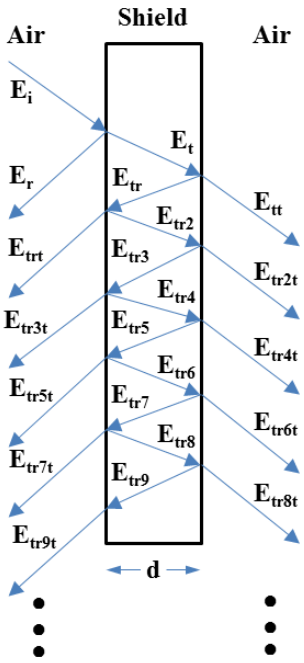

Figure 1. 8 Schematic illustration of reflection and transmission of electromagnetic wave.[175]

For a good EMI shield (*e.g.*, metal), a large part of the incident EMW (E_i) is reflected, and only a small part is transmitted (E_t). Thus, there is normally a large reflection loss (SE_R) at the first air/shield interface. The transmitted EMW experiences an absorption loss (SE_A) before encountering the second shield/air interface. Then, a small portion of this EMW (E_{tt}) transmits through the shield to the other air medium. If the absorption loss (SE_A) is large, this transmitted portion determines the total shielding effectiveness of the shield (*i.e.*, $SE_T = SE_A + SE_R$). However, if the absorption loss is small, multiple reflections within the EMI shield can lead to a reduction in the total shielding effectiveness (SE_T) due to the presence of

numerous significant higher order terms (*i.e.*, E_{tr2t}, E_{tr4t}, E_{tr6t}, E_{tr8t}, etc.) that add vectorially to the transmitted EMW (E_{tt}); see Figure 1. 8. Thus, the reduction in the SE_T due to multiple reflections manifests itself as a large, negative SE_{MR} term in equation (1- 9).

(1) Reflection Loss

Reflection loss at the interface between two media (*i.e.*, the air and the shield) can be considered as an impedance mismatch loss that is related to the ratio of the wave impedance to the intrinsic impedance of the shielding material. For electromagnetic waves in the far-field of the source (which can be considered as plane waves) and traveling through a homogeneous medium, the wave impedance is equal to the characteristic impedance of the propagation medium. The characteristic impedance (Z_0, Ω) of free space (and, in close approximation, of air) is given by:

$$Z_0 = \sqrt{\frac{\mu_0}{\varepsilon_0}} \approx 377\ \Omega \qquad (1\text{- }10)$$

where μ_0 is permeability of free space ($4\pi\times10^{-7}$ H/m), and ε_0 represents permittivity of free space (8.854×10^{-12} F/m). Thus, the wave impedance for the plane waves propagating in free space (and, in close approximation, of air) is ≈ 377 Ω. On the other hand, the intrinsic impedance of the shielding material (Z_s, Ω) is given by:

$$Z_s = \sqrt{\frac{j\omega\mu_s}{\sigma_s + j\omega\varepsilon_s}} \qquad (1\text{- }11)$$

where the terms μ_s, ε_s and σ_s are the magnetic permeability (H/m), electric permittivity (F/m) and electrical conductivity (S/m) of the shielding material, respectively. J is the imaginary unit ($j^2 = -1$), and ω is the angular frequency of the electromagnetic wave (rad/s). Typically, the shielding materials consist of highly conductive metal (σ_s is in order of 10^7 S/m), and the intrinsic impedance is considerably lower than that of free space (and air). Thus, equation (1- 11) can be simply written as the following:

$$Z_s = \sqrt{\frac{j\omega\mu_s}{\sigma_s}} \qquad (1\text{- }12)$$

Because of the large impedance mismatch, a large part of the incident electromagnetic wave (EMW) is reflected at the air/shield interface, and only a small part of the EMW is transmitted. According to transmission line theory, the total transmission coefficient can be described by:

$$T_{total} = \frac{E_{tt}}{E_i} = \frac{4Z_0Z_s}{(Z_s + Z_o)^2} \qquad (1\text{- }13)$$

The total reflection loss (SE_T) thus can be obtained by:

$$SE_T = -20log_{10}|T_{total}| = 20log_{10}\frac{|1+k|^2}{4|k|} \quad (1\text{- }14)$$

where $k=Z_s/Z_0$. For low impedance (highly conductive) shielding materials, k is very small, which results in a large reflection loss.

(2) Absorption Loss

Absorption loss occurs when the EMW penetrates the shield. The amplitudes of the electric and magnetic fields decay exponentially due to the induced currents and resultant ohmic losses within the shielding material. The propagation constant (γ_s) of the EMW in the highly conductive metal shield can be described as:

$$\gamma_s = \sqrt{j\omega\mu_s\sigma_s} \quad (1\text{- }15)$$

The real part of this propagation constant is the attenuation constant, and the reciprocal of the attenuation constant is defined as the skin depth (δ_s, m). Thus, the skin depth is the distance required for the EMW to be attenuated to *1/e* (or about 36.79%) of its initial amplitude. Solving for the real part of equation (1- 15) and then taking the reciprocal, the skin depth (δ_s) of metal shield can be described by:

$$\delta_s = \sqrt{\frac{2}{\omega\mu_s\sigma_s}} = \sqrt{\frac{1}{\pi f\mu_s\sigma_s}} \quad (1\text{- }16)$$

Therefore, the skin depth can be reduced by increasing the shield permeability and/or conductivity and is inversely proportional to the square root of frequency (*f, Hz*). Then, the absorption loss (SE_A, dB) can be calculated as:

$$SE_A = 20log_{10}\left(e^{d/\delta_s}\right) = 8.686\left(\frac{d}{\delta_s}\right) \quad (1\text{- }17)$$

where d is the thickness (m) of the EMI shield.

(3) Multiple Reflection Correction Term

The multiple reflection correction term (SE_{MR}) accounts for the reduction in shielding effectiveness for EMI shields with low absorption loss. This term can be calculated by:

$$SE_{MR} = 20log_{10}\left|1-\frac{(k-1)^2}{(k+1)^2}\times e^{\frac{-2d}{\delta_s}}\right| \quad (1\text{- }18)$$

where $k=Z_s/Z_0$. According to equation (1- 17), when the thickness of the shield is larger than the skin depth, the absorption loss will be large, and thus the SE_{MR} is negligible.[176]

1.3.3.3 PDC route towards microstructured EMI shielding materials

According to the shielding theory, the higher the SE_T value in dB, the less EMW passes through the

shielding materials.[177] Generally, the SE_T value of a commercially used EMI shielding material should be higher than 20 dB at the frequency of interest.[178] To date, investigations concerning EMI shielding materials used in the GHz range have been widely conducted. Various novel EMI shielding materials with SE_T value larger than 20 dB have been developed, such as metallic materials (*e.g.*, Titanium foams[179]), carbon materials (*e.g.*, graphene foam composites, reduced graphene oxides[139, 180]), polymer composites with conducting fillers (*e.g.*, carbon nanotube sponge, multiwall-CNT filled[181, 182]) or magnetic fillers (*e.g.*, Fe_3O_4 nanoparticles[183]), and ceramic composites (*e.g.*, PyC-Si_3N_4/Si_3N_4[184]). However, these materials cannot be used in harsh environments (*e.g.*, at high temperatures, in corrosive media) because of their poor corrosion/oxidation resistance and thermal/chemical stabilities. Ceramic composites with conductive phase/fillers enable the application in harsh environment due to their excellent corrosion, oxidation and decomposition resistance. Some ceramic composites (*e.g.*, C_f/SiO_2[130], SiC_f/SiC with Ti_3SiC_2 fillers[185]) exhibiting SE_T values higher than 20 dB at temperatures up to 600 °C have been reported. However, only few studies consider EMI shielding materials used in harsh environments.

Polymer derived ceramics (PDCs) are one of the most important kinds of advanced materials and are able to be used in harsh environments. The microstructure related functional properties of PDCs can be conveniently tailored at the molecular level upon chemical modification of the preceramic polymer. Moreover, the PDCs with low density are also suitable for light weight applications. As mentioned above, the EMI shielding materials tend to exhibit high electrical conductivity (σ), which is important for both reflection and absorption loss. Thus, polymer derived ceramic nanocomposites (PDC-NCs) with conductive nanofillers as a secondary phase should be a good choice for EMI shielding materials, especially for application in harsh environments.

The PDC-NCs have numerous advantages concerning EMI shielding applications. For instance, *i*) it is easy to homogeneously embed the conductive phase within the ceramic matrix either by *in situ* formation[94] or blending[171]; *ii*) the *in situ* formed nano-sized conductive phase will highly reduce the percolation threshold of the composite materials; *iii*) it is possible to improve the aspect ratio of the conductive phase within the ceramic matrix upon designing the architecture of preceramic precursors[27]; and *iv*) the *in situ* precipitated segregated carbon ribbons or simply blended conductive nanofillers with high aspect ratio and electrical conductivity are good for the enhancement of the overall electrical conductivity.[155] Therefore, the PDC-NCs enable the possibility of fabricating the state of the art EMI shielding materials.

A series of PDC-NCs with polymer derived ceramics (*e.g.*, SiC, SiOC and SiCN) as matrix and conductive nanofillers (*e.g.*, refractory carbides/nitrides/metals, carbon materials, conductive silicides) as the secondary phase is expected to exhibit promising EMI shielding performance in harsh environments. However, the publications about PDC-NCs used for EMI shielding are still limited, and the discussion is mainly focused on the enhancement contributed by free carbon.[169] In this Ph.D. work, a dense

monolithic SiHfC(N) ceramic nanocomposite was fabricated for EMI shielding application at temperatures up to 600 ºC using the PDC route (single-source-precursor synthesis). The SiHfC(N) ceramic nanocomposite with an *in situ* formed highly conductive HfC_xN_{1-x} phase is expected to exhibits excellent EMI shielding performance. To the best of my knowledge, the publications for single-source-precursor synthesized PDC-NCs used for EMI shielding (especially used in harsh environments) have never been reported so far.

2 Experimental procedures

2.1 Synthesis of single-source precursors

2.1.1 Synthesis of Hf-containing single-source precursors

The Hf-containing single-source precursors were synthesized upon reaction of allylhydridopolycarbosilane (AHPCS, SMP10, Starfire System Inc, USA) with tetrakis(dimethylamino)hafnium (IV) (TDMAH, Sigma-Aldrich, Germany) or tetrakis(diethylamido)hafnium (IV) (TDEAH, Sigma-Aldrich, Germany) with weight ratios of (TDMAH or TDEAH)/SMP10 5/95, 15/85 and 30/70. The reaction between TDMAH and SMP10 occurs at 80°C and the as-synthesized precursors can be denoted as 5Hf-SMP10_80, 15Hf-SMP10_80 and 30Hf-SMP10_80, respectively. The reaction between TDEAH and SMP10 occurs at 100 ºC and the as-synthesized precursors can be denoted as 5Hf-SMP10_100, 15Hf-SMP10_100 and 30Hf-SMP10_100, respectively. The synthesis of the Hf-containing single-source precursors was carried out in argon atmosphere (Schlenk Technique) in order to prevent the hydrolysis of the starting materials. Taking the synthesis of 30Hf-SMP10_80 using SMP10 and TDMAH for example, 1.500 g TDMAH was dissolved in 14.0 mL anhydrous toluene and then added dropwise to a solution of 3.500 g SMP10 in 20.0 mL anhydrous toluene with stirring at room temperature. The obtained solution was heated at 80 °C for 3 h and cross linking occurred very fast. Subsequently, the solvent was removed in vacuum (10^{-2} mbar) at 60 °C. After evaporation of the solvent, a brown solid (30Hf-SMP10_80) was obtained.[94] The synthesis of 30Hf-SMP10_100 using TDEAH and SMP10 is also conducted in the same way at 100 ºC, and the brown solid single-source precursor can be obtained as well.

2.1.2 Synthesis of boron doped Hf-containing single-source precursors

The boron doped Hf-containing single-source precursor (denoted as 30Hf-B-SMP10_100) was synthesized upon reaction among the SMP10, tetrakis(diethylamido)hafnium (IV) (TDEAH) and $BH_3 \cdot SMe_2$ (BSM, Sigma-Aldrich, Germany). The synthesis was carried out in argon atmosphere (Schlenk Technique). The weight ratio of TDEAH/SMP10 is 30/70 and the amount of $BH_3 \cdot SMe_2$ is calculated according to the mole ratio of Hf/B=1/2. Thus, 3.0 g TDEAH was dissolved in 5 mL anhydrous toluene and then added dropwise to a solution of 7.0 g SMP10 in 5 mL anhydrous toluene with stirring at ≈ -78 °C (dry ice/acetone). After 10 min, 0.976 g BMS dissolved in 5 mL anhydrous toluene was added dropwise into the mixture of SMP10 and TDEAH. The obtained solution was stirred at ≈ -78 °C for 2 h and then allowed to reach room temperature automatically. After that, the mixture was heated at 100 °C for 3 h and subsequently dried under vacuum (10^{-2} mbar) at 60 °C to obtain the solid 30Hf-B-SMP10_100.

2.1.3 Synthesis of Ta-containing single-source precursors

The Ta-containing single-source precursor was synthesized upon reaction of SMP10 with Pentakis(dimethylamino)tantalum(V) (PDMAT, Sigma-Aldrich, Germany) at 80°C with weight ratio of PDMAT/SMP10 30/70. The as-synthesized precursor was denoted as 30Ta-SMP10_80. The synthesis process was carried out in argon atmosphere (Schlenk Technique). Thus, 3.000 g PDMAT was dissolved in 15.0 mL anhydrous toluene and then added dropwise to a solution of 7.000 g SMP10 in 20.0 mL anhydrous toluene with stirring at room temperature. The obtained solution was heated at 80 °C for 3 h and subsequently the solvent was removed in vacuum (10^{-2} mbar) at 60 °C. After evaporation of the solvent, the black solid 30Ta-SMP10_80 was obtained.

2.1.4 Synthesis of HfTa-containing single-source precursors

The single-source precursors containing both Hf and Ta were synthesized upon reaction of SMP10 with tetrakis(diethylamido)hafnium (IV) (TDEAH) and Pentakis(dimethylamino)-tantalum(V) (PDMAT) at 100°C with weight ratio of (TDEAH+PDMAT)/SMP10 30/70. In this Ph.D. thesis, two precursors with mole ratios of Hf/Ta = 7/3 and = 1/4 were synthesized and denoted as 30Hf7Ta3-SMP10_100 and 30Hf2Ta8-SMP10_100, respectively. The synthesis of the single-source precursor was carried out in argon atmosphere (Schlenk Technique). Taking the synthesis of 30Hf2Ta8-SMP10_100 for example, 1.000 g PDMAT and 0.291 g TDEAH were dissolved in 10.0 mL anhydrous toluene together and then the brown and transparent liquid was added dropwise into a solution of 3.000 g SMP10 in 10.0 mL anhydrous toluene with stirring at room temperature. The obtained solution was heated at 100 °C for 3 h and subsequently the solvent was removed in vacuum (10^{-2} mbar) at 60 °C. After evaporation of the solvent, the black solid 30Hf2Ta8-SMP10_100 was obtained. Similarly, the 30Hf7Ta3-SMP10_100 can be obtained as well.

2.2 Pyrolysis of preceramic precursors

All the as-synthesized single-source precursors mentioned above were ground and pyrolyzed at 1100 or 1000 °C in argon for preparation of amorphous SiHfC(N), SiHfBC(N), SiTaC(N) and SiHfTaC(N) ceramics. For the sake of comparison, pure SMP10 was also pyrolyzed at 1000 ºC for 2h for the preparation of SiC. The heating program is illustrated in (Figure 2. 1). The quartz Schlenk tube and crucible were used for pyrolysis.

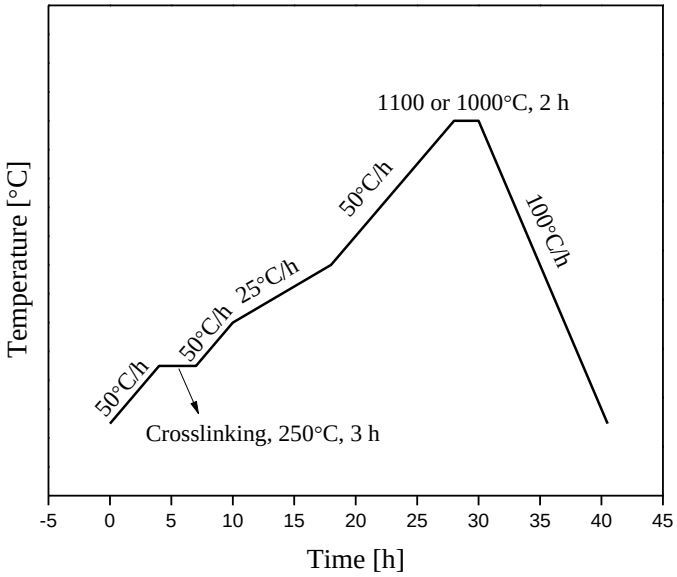

Figure 2. 1 The program of pyrolysis of single-source precursors.

2.3 Annealing of ceramic powders

After pyrolysis, the amorphous SiC, SiHfC(N), SiHfBC(N), SiTaC(N) and SiHfTaC(N) ceramics were ground and then annealed at elevated temperatures (1300 - 1900 ºC) for 5 h in argon atmosphere in a graphite furnace (GT Advanced Technologies, Merrimack, New Hampshire, USA, Figure 2. 2a) for preparation of SiC/C, SiC/HfC_xN_{1-x}/C, boron-doped SiC/HfC_xN_{1-x}/C, SiC/TaC_xN_{1-x}/C and SiC/$Hf_yTa_{1-y}C_xN_{1-x}$/C ceramic nanocomposites, respectively. The samples were placed in a SiC crucible with a SiC cab and then put in a larger graphite crucible with a graphite cab. The heating program is illustrated in Figure 2. 2b.

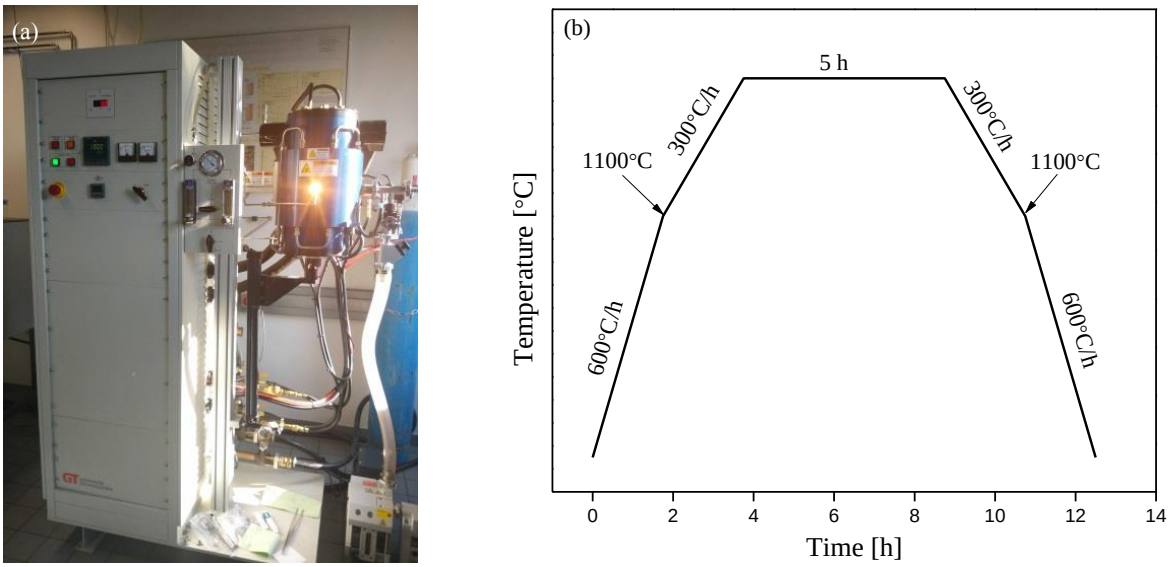

Figure 2. 2 *(a)* Photograph of the graphite furnace for high-temperature annealing; *(b)* Heating program of the annealing process.

2.4 Spark plasma sintering process

The spark plasma sintering (SPS) process, also called electric field-assisted sintering technique (FAST), was used to fabricate dense monolithic SiC/C, SiC/HfC_xN_{1-x}/C, boron doped-SiC/HfC_xN_{1-x}/C, SiC/TaC_xN_{1-x}/C and SiC/$Hf_yTa_{1-y}C_xN_{1-x}$/C ceramic (nano)composites. Take the SPS sintering of SiC/30HfC_xN_{1-x}/C ceramic nanocomposite for instance. The amorphous SiHfC(N) obtained by pyrolysis of 30Hf-SMP10_80 at 1100 ºC were milled into fine powders (<100 μm) and saved in argon atmosphere. Then, 3.0 g ceramic powders were filled into a graphite die with the inner diameter of 20 mm (Figure 2. 3b) and sintered by a SPS apparatus (FCT HP D 25/1, FCT Systeme GmbH, Frankenblick, Germany, Figure 2. 3a) in Forschungszentrum Jülich in Germany at 2200 ºC for 30 min under the pressure of 50 MPa. The sintering was conducted in vacuum atmosphere. The die and powders were separated by graphite paper. The sintering program is shown in Figure 2. 3c. The dense monolithic boron doped-SiC/30HfC_xN_{1-x}/C (SHBC) and SiC/30$Hf_yTa_{1-y}C_xN_{1-x}$/C can be successfully sintered as well and the sintering parameters were set as 2200 ºC, 50 MPa and 20 min. Besides, the dense monolithic SiC/C and SiC/15HfC_xN_{1-x}/C used for test of mechanical properties and EMI shielding performance were sintered on a SPS apparatus (Dr. Sinter 2050, Sumitomo Coal Mining Co. Ltd., Kawasaki, Japan) in Arrhenius Laboratory of Stockholm University in Sweden using a 35 mm die. The dense SiC/30TaC_xN_{1-x}/C monoliths were sintering by a SPS apparatus (SPS-1050, SPS Syntex Inc., Kawasaki, Japan) in national institute for materials science (NIMS) in Japan using a 10 mm die. All the sintering parameters were set as 2200 ºC, 50 MPa and 20 min.

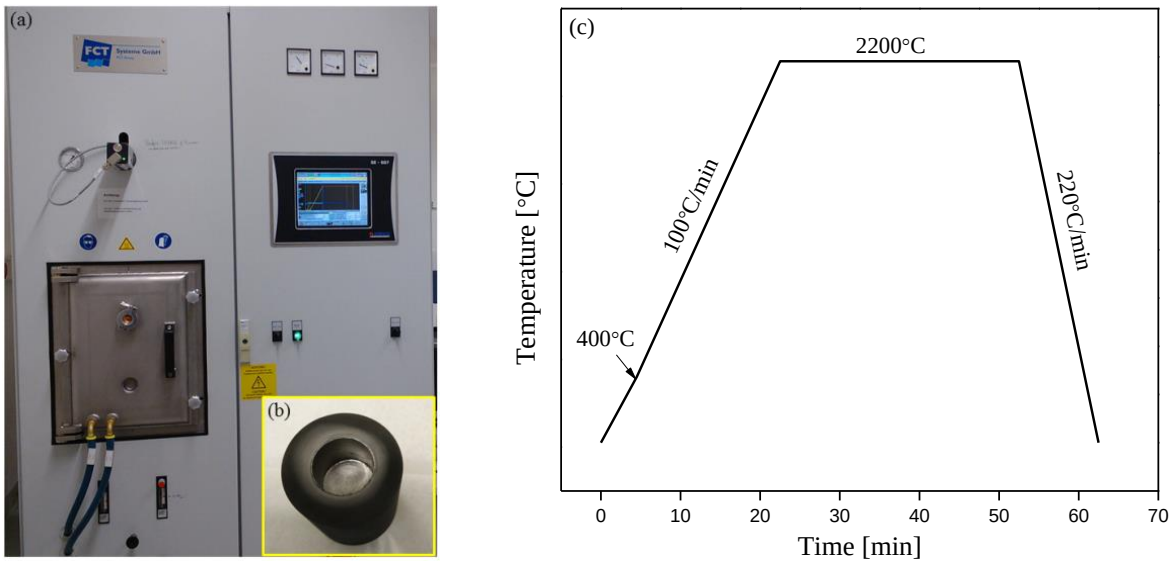

Figure 2. 3 *(a)* Photograph of SPS apparatus in Forschungszentrum Jülich; inset *(b)* is the graphite die filled with ceramic powders that are covered with a piece of graphite paper; *(c)* is the illustration of sintering program (the thermocouple is changed into pyrometer at 400 ºC).

2.5 Preparation of C_f-reinforced SiHfC(N) ceramic matrix composites (CMCs)

Polymer infiltration and pyrolysis (PIP) process was used to fabricate the C_f-reinforced SiHfC(N) CMCs. 2D carbon fabrics (T300, manufactured by Toray) were selected and cut into rectangular pieces with the

dimension of 44 mm × 16 mm (see Figure 2. 4a) for the preparation of C_f-reinforced CMCs. The $Hf(NEt_2)_4$ modified SMP10 (that was prepared as described in section 2.1.1) were used as preceramic precursors. The weight ratio of $Hf(NEt_2)_4$ to SMP10 was 3/7. A Teflon mold with the inner dimension of 44 mm × 16 mm ×3 mm (Figure 2. 4b) was designed to stack and fix the fabrics. After infiltration with the preceramic precursor (*i.e.*, 30Hf-SMP10), 16 pieces of infiltrated carbon fabrics were stacked on to each other within the Teflon mold to fabricate the preforms with thickness of ≈ 3.5 mm. After crosslinking at 250ºC for 3 h within the mode, the preform was taken out and subsequently pyrolyzed at 1100 ºC for 2 h in argon to prepare the C_f-reinforced SiHfC(N) CMCs. The pyrolysis program is the same as that for preparation of amorphous SiHfC(N) ceramics (Figure 2. 1). In order to reduce the porosity of the as-prepared CMCs, 10 times of infiltration and pyrolysis process were repeated. For the sake of comparison, the C_f-reinforced SiC CMCs were also prepared using the same PIP process.

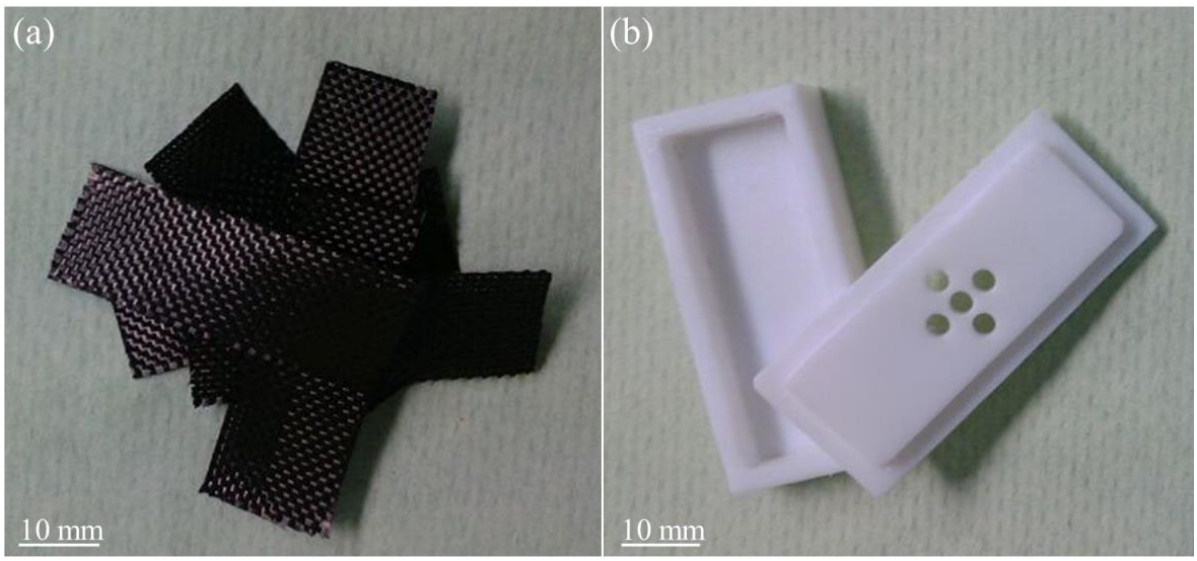

Figure 2. 4 Photographs of the 2D carbon fabrics *(a)* and Teflon mold *(b)* used for fabrication of the preforms of CMCs.

2.6 Characterization methods

2.6.1 Chemical and microstructural characterization

2.6.1.1 Preceramic precursors and ceramization process

The synthesis process was characterized by means of Fourier transform infrared spectroscopy (FT-IR) and nuclear magnetic resonance (NMR) spectroscopy including liquid NMR and solid-state magic-angle spinning NMR (MAS NMR). The polymer-to-ceramic transformation (ceramization) was investigated via solid-state MAS NMR as well as thermogravimetric analysis coupled with mass spectrometry (TGA/MS).

FT-IR spectra were recorded on a VARIAN 670-FTIR spectrometer (Agilent Technologies, Santa Clara, USA) from 400 cm^{-1} to 4000 cm^{-1} in attenuated-total-reflectance (ATR) mode. TGA/MS measurements

were carried out with a thermal analysis device (STA 449C Jupiter, Netzsch group, Hanau, Germany) coupled with a quadrupole mass spectrometer (QMS 403C Aëolos, Netzsch group, Hanau, Germany). The thermal analysis included heating under flowing argon with a rate of 5 °C/min, holding at 1400 °C for 2h and free cooling down to room temperature.

Liquid state NMR experiments of the starting materials (SMP10, TDMAH, TDEAH, PDMAT, etc.) were carried out on a Bruker AV 300 NMR spectrometer (Bruker BioSpin GmbH, Rheinstetten, Germany) with a 5.0 mm broad-band probe (PABBO BB-1H/D Z-GRD), operating at 300.13 MHz for ^{1}H, 75.46 MHz for ^{13}C (^{1}H-decoupling) and 59.63 MHz for ^{29}Si (^{1}H-decoupling), and the relaxation delay time was 1 ~ 2 s depending on different nuclei. The solvent for NMR was $CDCl_3$ (for SMP10) and C_6D_6 (for TDMAH, TDEAH, PDMAT, etc.). The chemical shifts of ^{1}H, ^{13}C, and ^{29}Si were all referred to tetramethylsilane (TMS) as external standard.

Solid state ^{11}B, ^{13}C and ^{29}Si MAS NMR measurements of preceramic precursors were performed on the Bruker AV 300 NMR spectrometer (Bruker BioSpin GmbH, Rheinstetten, Germany) using a 4.0 mm Bruker double resonance MAS probe (MAS 1H/BB) with a spinning speed of 5.0 kHz. The NMR spectra were measured using cross-polarization (CP) technique operating at 75.47 MHz for ^{13}C and using variable-amplitude cross-polarization (VACP) technique at 59.62 MHz for ^{29}Si. In order to suppress background signals coming from boron containing parts (NMR probe) near the coil and from also the borosilicate glass in the NMR tube, the ^{11}B spectra were measured at 96.29 MHz using a composite pulse technique (named “zgbs” in the Bruker pulse program library) that consists of a 90° and two 180° pulses with appropriate phase cycling.

2.6.1.2 Ceramic powders and monoliths

X-ray diffraction (XRD), elemental analysis, Raman spectroscopy and high-resolution transmission electron microscopy (HRTEM) were used to characterize the phase composition, chemical composition and microstructure of the as-prepared ceramics. The XRD patterns of ceramic powders were recorded using a STADI P powder diffractometer (STOE & Cie GmbH, Darmstadt, Germany) with a molybdenum $K\alpha_1$ radiation source (λ = 0.709300 Å). The XRD patterns of bulk materials were measured by a Bruker D8 system (Bruker Corporation, Billerica, Massachusetts, United States) with a copper $K\alpha_1$ radiation source (λ = 1.541874 Å). The carbon contents of the ceramics were measured using a combustion analysis method on a LECO C-200 analyzer (LECO Corporation, St. Joseph, Michigan, USA). The nitrogen and oxygen contents were measured by a hot gas extraction technique with a LECO TC-436 analyzer (LECO Corporation, St. Joseph, Michigan, USA). Hf, Ta, and Si content were measured at Mikroanalytisches Labor Pascher (Remagen, Germany) using Inductively Coupled Plasma-Atomic Emission Spectrometry (ICP- AES). Raman spectra were recorded from 400 to 4000 cm^{-1} employing a micro-Raman HR8000 spectrometer (Horiba JobinYvon, Bensheim, Germany) with a laser wavelength of 514.5 nm. TEM studies were conducted on ground powder samples using a JEM-2100 microscope (JEOL

Ltd., Tokyo, Japan) at an acceleration voltage of 200 kV (wavelength l52.51 pm) coupled with an electron diffraction spectroscope (EDS, EDAX, Mahwah, New Jersey, USA). The BET specific surface area and surface morphology of the ceramics were investigated by an Autosorb-3B Surface Area and Pore Size Analyzer (Quantachrome Instruments Corporation, Boynton Beach, Florida, USA) and a Philips XL30 FEG high-resolution scanning electron microscope (FEI Company, Hillsboro, Oregon, USA), respectively.

Moreover, ^{11}B, ^{29}Si and ^{13}C MAS NMR spectra of the as-synthesized ceramics obtained at 800, 1100, 1300, 1500 and 1700 ºC were measured selectively using different techniques on the Bruker AV 300 NMR spectrometer (Bruker BioSpin GmbH, Rheinstetten, Germany). ^{29}Si MAS NMR spectra were recorded using a single pulse (SP) technique with the pulse width of 4 μs and polarization delay of 60 s. ^{13}C spectra were recorded using a composite pulse technique (named "zgbs" in the Bruker pulse program library) with the pulse width of 4 μs and polarization delay of 60 s. ^{11}B spectra were also recorded using a composite pulse technique (named "zgbs" in the Bruker pulse program library) with the pulse width of 4.5 μs and polarization delay of 2 s. ^{29}Si and ^{13}C chemical shifts were determined relative to the external standards kaolin and adamantane, respectively, and are given with respect to the primary standard TMS (δ = 0 ppm). For the ^{11}B spectra, the chemical shifts were referenced with respect to trimethyl borate.

2.6.2 Density and open porosity characterization

The skeletal density (ρ_s), geometrical density (ρ_g) and open porosity (P) of the monolithic ceramic nanocomposites and CMCs were measured using the water immersion method (*i.e.*, the Archimedic method).[26] All the specimens used for this measurement were dried at 80 ºC for more than 24 h. Firstly, the weight of the dry specimens was measured (M_{dry}). Secondly, the specimens were boiled in water for 60 min and hence the open pores were filled with water. After cooling down to room temperature, the weight of the specimens immersed in water (M_{ww}) and the wet specimens (M_{wet}) were determined subsequently. The density (ρ_{water}) and temperature of the water used for measurements should be recorded as well. The skeletal density (ρ_s), geometrical density (ρ_g) and open porosity (P) of the specimens were calculated using the following equations:

$$\rho_s = \frac{M_{dry}}{M_{dry} - M_{ww}} \rho_{water} \quad (2 - 1)$$

$$\rho_g = \frac{M_{dry}}{M_{wet} - M_{ww}} \rho_{water} \quad (2 - 2)$$

$$P(\%) = \frac{M_{wet} - M_{dry}}{M_{wet} - M_{ww}} \quad (2 - 3)$$

$$P(\%) = 1 - \frac{\rho_g}{\rho_s} \qquad (2 - 4)$$

The relationship between the skeletal density (ρ_s), geometrical density (ρ_g) and open porosity (P) can be described using equation (2 - 4).

2.6.3 Flexural strength measurement

The flexural strength of the bulk samples including dense SiHfC(N) monoliths and C_f-reinforced SiHfC(N) CMCs was measured using a four-point bending flexural test. This test was conducted on a universal testing machine with a specified test fixture at room temperature (Z010, Zwick Roell Group, Ulm, Germany). The lower and upper span of the test fixture is 21.0 and 10.0 mm, respectively. The crosshead speed was set as 0.5 mm/min.

2.6.4 Laser ablation test

Laser ablation test was conducted on the dense monolithic SiHfC(N) ceramic nanocomposite (*i.e.*, SiHfC(N)-SPS) and the C_f-reinforced SiHfC(N) CMCs (*i.e.*, C_f/SiHfC(N)) as well as the C_f-reinforced SiC (*i.e.*, C_f/SiC). The as-prepared circular SiHfC(N)-SPS sample with the diameter of 20 mm and thickness of 1 mm were cut into 4 coupons for laser ablation test. The as-fabricated C_f/SiHfC(N) and C_f/SiC CMCs were machined into rectangular coupons with the dimension of 10 mm×15 mm for laser ablation test. A continuous wave CO_2 laser with wavelength 10.6 μm was used for the ablation test in air (DC 080W, ROFIN-SINAR Laser GmbH, Hamburg, Germany). Microstructure of the ablated specimens was characterized using a Philips XL30 FEG high-resolution scanning electron microscope (FEI Company, Hillsboro, Oregon, USA) coupled with an energy dispersive X-ray spectroscopy (EDX, EDAX, Mahwah, U.S.A.).

2.6.5 Electrical conductivity measurement

2.6.5.1 Four-point probe method.

The volume resistivity (or dc-electrical conductivity) of the monolithic ceramic samples was measured using the four-point probe method with square arrangement probes. Thus, a KEITHLEY 224 was used as a programmable current source, and a KEITHLEY 2010 multimeter was used for voltage measurement. The four-point probes were placed in the center of the monolithic samples that were polished with 1μm polycrystalline diamond on felt cloth. In this thesis, this method is mainly used for the measurements of the monolithic ceramic samples with high electrical conductivity.

2.6.5.2 Impedance Measurements.

The dc-electrical conductivity of the samples with low electrical conductivity (*e.g.*, the ceramic-paraffin wax composite) can be obtained using the impedance measurement that is conducted on a Solartron 1260 Impedance Analyser/1287 Electrochemical Interface within the frequency range 0.1Hz - 1 MHz. The ZView-software (Scribner Associates Inc., Southern Pines, North Carolina, USA) was applied to fit the data to equivalent circuits, and the dc-conductivity values were extracted from Nyquist- or Bode-plots.

2.6.6 Characterization of dielectric properties and microwave absorption (MA) performance

The ceramic powders were sieved and homogeneously mixed with molten paraffin wax (weight ratio ceramic/paraffin wax of 4:6) and pressed into hollow cylinder-shaped samples (inner diameter: 3.04 mm; external diameter: 7.00 mm; height: ≈ 2.5 mm, Figure 2. 5c). The complex permittivity of the composite samples was determined by the coaxial transmission/reflection method in the X-band (8.2-12.4 GHz). The paraffin wax is an insulator with the real and imaginary part of the permittivity of $\varepsilon' \approx 2.26$ and $\varepsilon'' \approx 0$ in the X-band, respectively.[186] The volume fraction of the ceramic powders within the composite samples is approximately 15 vol.%. The complex permittivity of the samples was calculated from the scattering parameters (S_{ij}) corresponding to transmission (S_{21} and S_{12}) and reflection (S_{11} and S_{22}) measured on a N5222A PNA-X Vector Network Analyzer (10 MHz to 26.5 GHz, Agilent Technologies Inc, Santa Clara, California, USA, Figure 2. 5). The schematic of the measurement is shown in Figure 2. 5d. Here, *i* and *j* represents the electromagnetic wave transmitting from port *j* to port *i* (*i, j*=1 or 2). The hollow cylinder-shaped samples were tightly fixed into the 50 Ω Airline (85051-60007, Agilent, Figure 2. 5b), and the measurements were calibrated using an electronic calibration module (N4696-60004, 300 kHz -18GHz, Agilent). All scattering parameters were determined with an experimental error less than 3%.

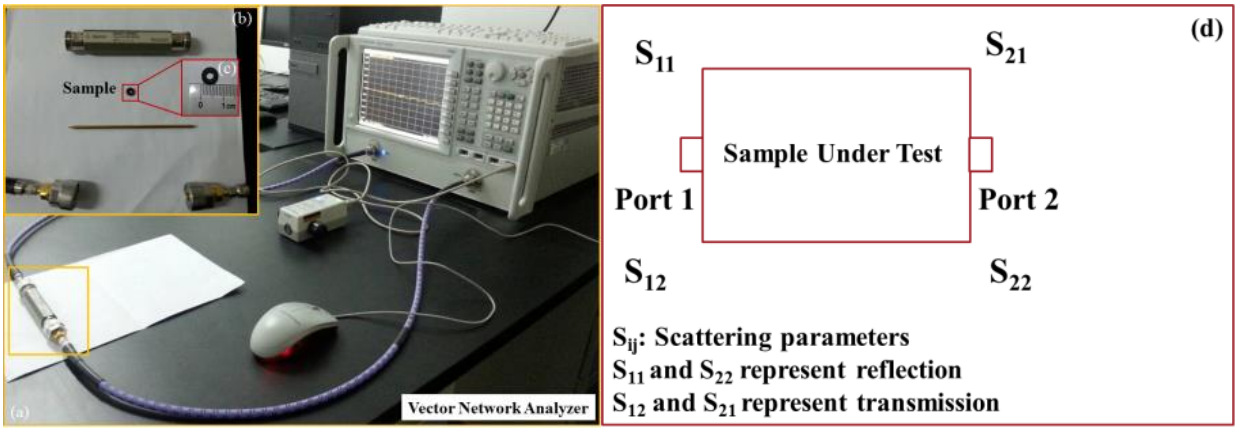

Figure 2. 5 *(a)* Photograph of the N5222A PNA-X Microwave Network Analyzer. Inset *(b)* is the enlarged view of measuring element with the hollow cylinder-shaped sample [inset *(c)*], and inset *(d)* is the schematic of measurements of scattering parameters.

According to the transmission-line theory, the microwave absorption performance for a single layer of absorber backed by a PEC (perfect electric conductor) can be evaluated by the reflection loss (RL),[110-113]

$$RL = 20log_{10}\left|\frac{\sqrt{\frac{\mu}{\varepsilon}}\tanh\left(j\frac{2\pi fd}{c}\sqrt{\mu\varepsilon}\right)-1}{\sqrt{\frac{\mu}{\varepsilon}}\tanh\left(j\frac{2\pi fd}{c}\sqrt{\mu\varepsilon}\right)+1}\right| \qquad (2-5)$$

where d, μ ($\mu=\mu'-j\mu''$) and $\varepsilon(\varepsilon=\varepsilon'-j\varepsilon'')$ denote the thickness, complex permeability and complex permittivity of the absorber, respectively; c is the speed of light in the free space, and f is the frequency of the incident electromagnetic wave. The terms ε' and μ' are the real parts of the complex permittivity and complex permeability, and the terms ε'' and μ'' represent the imaginary parts of the complex permittivity and complex permeability, respectively. In this thesis, μ' is taken as 1 and μ'' as 0 due to the weak magnetic properties of SiC/C and SiC/HfC_xN_{1-x}/C ceramic nanocomposites.[187, 188] In addition, another important parameter of MA materials, the effective absorption bandwidth (EAB), is defined as the frequency range in which the reflection loss is lower than -10 dB.[146, 189]

2.6.7 Characterization of EMI shielding performance at room and high temperatures.

The EMI shielding performance at room and high temperatures was measured on a vector network analyzer (MS4644A; Anritsu, Japan) in 8.2 to 12.4 GHz (X-band) using waveguide method.[176] The dimension of the bulk ceramic samples under test is 22.86×10.16×2.00 mm. Similarly, four scattering parameters (S_{ij}) corresponding to transmission (S_{21} and S_{12}) and reflection (S_{11} and S_{22}) were determined. With the measured S_{ij}, the shielding effectiveness (SE) values were calculated according to the equations as follows:

$$R = |S_{11}|^2 = |S_{22}|^2 \qquad (2-6)$$

$$T = |S_{12}|^2 = |S_{21}|^2 \quad (2 - 7)$$

$$R + A + T = 1 \quad (2 - 8)$$

$$SE_T = -10Log_{10}(T) \quad (2 - 9)$$

$$SE_R = -10Log_{10}(1 - R) \quad (2 - 10)$$

$$SE_T = SE_A + SE_R + SE_{MR} \quad (2 - 11)$$

$$SE_T = SE_A + SE_R \quad (2 - 12)$$

$$SE_A = SE_T - SE_R = -10Log_{10}(\frac{T}{1 - R}) \quad (2 - 13)$$

where R, A and T represent the reflected power, absorbed power and transmitted power of the incident electromagnetic wave, respectively. SE_R, SE_A, SE_{MR} and SE_T represent the reflection loss, absorption loss, multiple reflection correction term and total shielding effectiveness, respectively. If the thickness of the bulk sample is larger than its skin depth, the SE_{MR} value will be negligible due to the large absorption loss. Thus, the total shielding effectiveness (SE_T) can be described using equation (2 - 12).[176] Thus, SE_A can be calculated using equation (2 - 13). All scattering parameters were determined with an experimental error less than 3%. The high-temperature EMI shielding performance was measured at temperatures varying from 25 ºC to 600 ºC. By increasing temperature, the measurements were conducted at 100 ºC, 150 ºC, 200 ºC, 300 ºC, 400 ºC, 500 ºC and 600 ºC subsequently.

3 Results and discussion

3.1 Synthesis and characterization of single-source precursors

3.1.1 Hf-containing single-source precursors

Hf-containing single source precursors (5Hf-SMP10_80, 15Hf-SMP10_80 and 30Hf-SMP10_80) were synthesized by the reaction of TDMAH [$Hf(NMe_2)_4$] and SMP10 with the weight ratio of TDMAH/SMP10 5/95, 15/85 and 30/70. During the synthesis, samples were collected at different steps for FT-IR spectroscopy measurement, and the spectra of the precursors reacted at room temperature (RT) and at 80 °C are shown in Figure 3. 1 (taking the synthesis of 30Hf-SMP10_80 for example). For the sake of comparison, the spectra of pure SMP10 at room temperature (SMP10_RT) as well as heated at 80 °C for 3 h (SMP10_80) are also shown in Figure 3. 1. Upon TDMAH addition to pure SMP10 at room temperature, the absorption bands assigned to the allyl groups (C-H stretching at 3075cm^{-1} and C=C stretching at 1630 cm^{-1})[190] disappear, and the relative intensity of the Si-H band (Si-H stretching at 2115cm^{-1}) significantly decreases with respect to the intensity of the Si-CH_3 band (Si-C stretching at 747cm^{-1})[191], while new bands due to Hf-NCH_3 groups appear, including the characteristic vibrations of N-Si on the Hf-N-Si units at 945 cm^{-1}[192], NC-H stretching at 2788 cm^{-1} and bending at 1450 cm^{-1} as well as C-N stretching at 1287 $cm^{-1}$and 1178 cm^{-1}. After heating at 80 °C for 3 h, the relative intensity of the Si-H band at 2115cm^{-1} in the spectrum labeled (4) decreases further, while those of the Hf-NCH_3 bands change slightly.

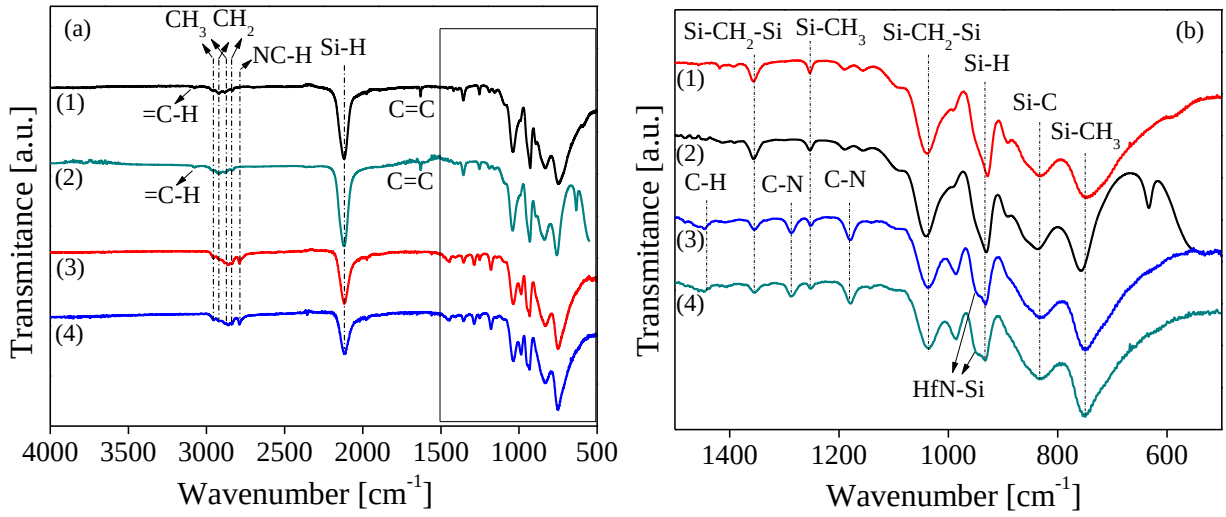

Figure 3. 1 FT-IR spectra of precursors before and after reaction are shown in *(a)*, and the region from 500 to 1500 cm^{-1} is shown magnified in *(b)*: *(1)* SMP10_RT, *(2)* SMP10_80, *(3)* 30Hf-SMP10_RT, *(4)* 30Hf-SMP10_80; RT = room temperature.

According to previous reports[39, 193], two reaction pathways occur during the synthesis of 30Hf-SMP10_80 (Figure 3. 2). The first one involves the hydrosilylation that explains the disappearance of

allyl groups and the decrease in the intensity of Si-H peaks. As the hydrosilylation process starts at temperatures of ca. 100-120 °C[13], the pure SMP10 heated at 80 °C (spectrum (2) in Figure 3. 1a) did not show significant changes of the intensities of the allyl and Si-H vibrations. However, the addition of TDMAH to SMP10 induces the disappearance of the absorption bands of the allyl groups even at room temperature (spectrum (3) in Figure 3. 1a), which indicates that the TDMAH acts as a catalyst for the hydrosilylation.[194, 195] The second reaction route involves the reaction of TDMAH with the Si-H groups of SMP10, which leads to the formation of Si-N-Hf linkages. Li, et al. calculated bond dissociation energies using density functional theory, and they roughly follow the order of Hf-N>C-H/Si-N>Si-H/Si-C>N-C/Hf-H>Hf-Si.[192] This information was corroborated with chemisorption experiments of TDMAH on Si substrates to suggest that the reaction between TDMAH and hydrogen terminated Si (100) surfaces occurs through the formation of Si-N bonds, which is more probable than that of Si-Hf bonds.

Based on the two reaction pathways, synthesis of the Hf-containing single source precursors from SMP10 and TDMAH can be described as depicted in Figure 3. 2: the allyl and Si-H groups of SMP10 are involved in hydrosilylation that leads to an increased cross-linking degree of the precursor; additionally, TDMAH reacts with the Si-H groups of SMP10 to form Si-N-Hf linkages and gaseous CH_4.

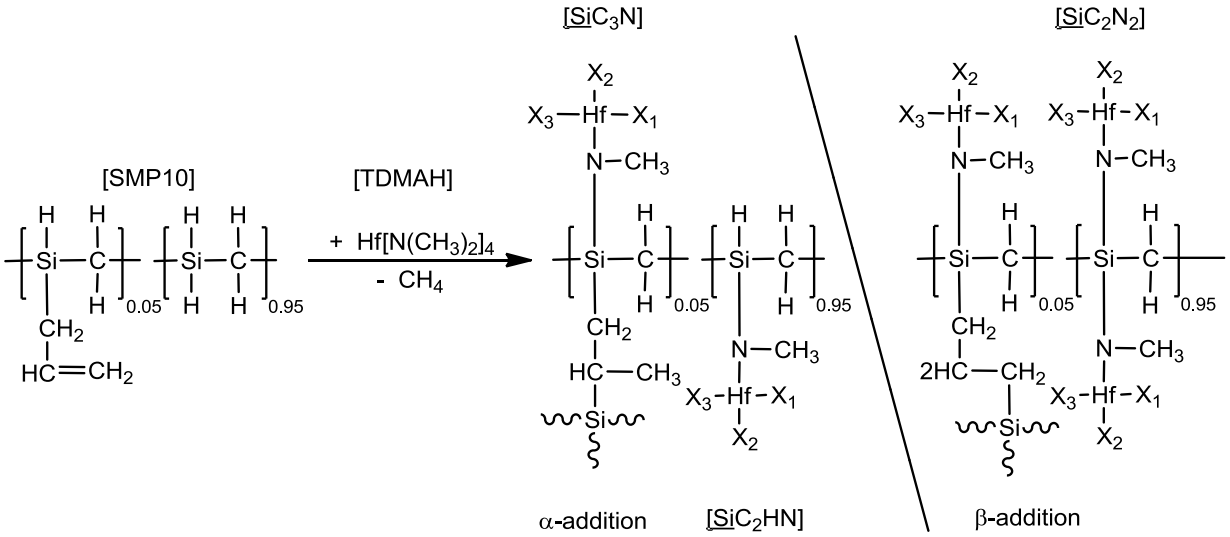

X_1, X_2, X_3 = {$N(CH_3)_2$, $NSi(CH_2)H_2$, $NSi(CH_2)(N)H$, $NSi(CH_2)(N)_2$, $NSi(CH_2)_2H$, $NSi(N)(CH_2)_2$, $NSi(CH_2)_3$ }

Figure 3. 2 Reaction pathways of synthesis of the single-source precursor from SMP10 and TDMAH.

According to the ^{29}Si NMR spectra, there are three kinds of hydrogen-bearing Si sites (hydrido silyl groups), as alternating groups of the polymer backbone of SMP10, *i.e.*, C<u>Si</u>H_3, <u>Si</u>C_2H_2 and <u>Si</u>C_3H.[196] Hence, different kinds of <u>Si</u>-$N(CH_3)$-Hf units including C<u>Si</u>H_2N, C<u>Si</u>HN_2, C<u>Si</u>N_3, <u>Si</u>C_2HN, <u>Si</u>C_2N_2 and <u>Si</u>C_3N can be generated upon reacting the corresponding Si-H groups with TDMAH. In order to further investigate the reaction between SMP10 and TDMAH in more detail and to confirm the molecular structure of the obtained precursors, ^{13}C and ^{29}Si NMR analysis was conducted on the pure SMP10, TDMAH as well as on 30Hf-SMP10_80, and the results are shown in Figure 3. 3.

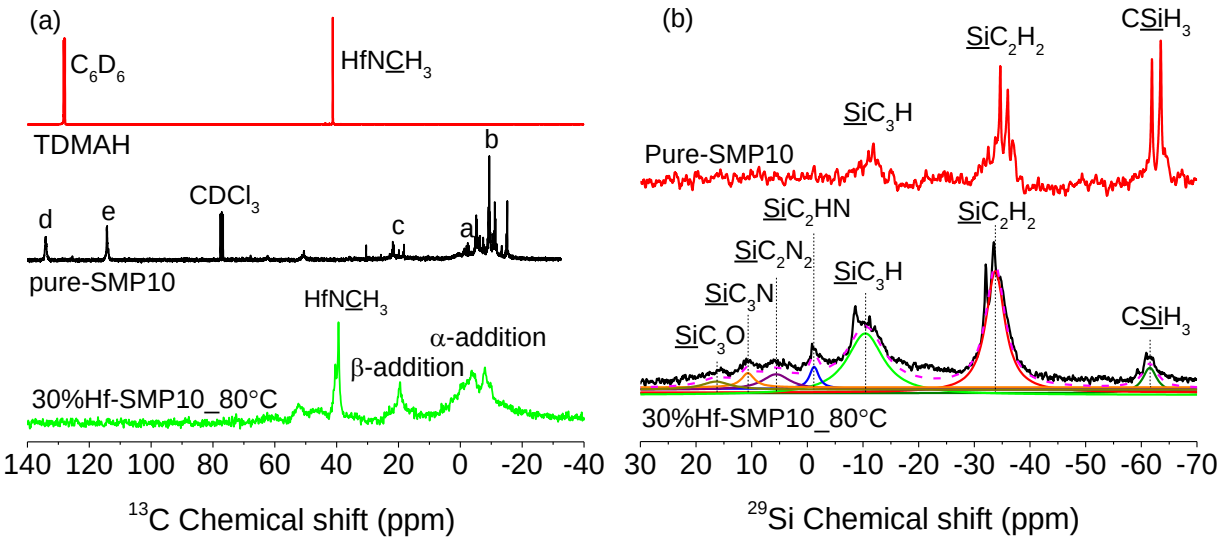

Figure 3. 3 NMR spectra of starting materials (TDMAH and SMP10) and MAS NMR spectra of 30Hf-SMP10_80: *(a)* ^{13}C and *(b)* ^{29}Si spectra.

In the ^{13}C NMR spectrum of SMP10 (Figure 3. 3a), the chemical shifts of 134.3 ppm and 114.7 ppm are assigned to the carbon sites of ≡Si–CH_2–$\underline{C}H$=CH_2 (d) and ≡Si–CH_2–CH=$\underline{C}H_2$ (e) of the allyl groups, respectively. Multiple chemical shifts in the region from 17.7 to 30.0 ppm are attributed to the ≡Si–$\underline{C}H_2$–CH=CH_2 (c) linkage between silicon and the allyl groups. The signal of the ≡Si-$\underline{C}H_3$ (a) groups was observed around 0 ~ 2.4 ppm, and the chemical shifts from -4.4 to -16.0 ppm were assigned to ≡Si–$\underline{C}H_2$–Si (b) linkages on the main chain.[190] Compared with the ^{13}C spectrum of pure SMP10, the allyl-carbon resonances (d and e) of the 30Hf-SMP10_80 disappeared due to the hydrosilylation process, which is consistent with the FT-IR results. A new broad resonance appeared in the region from 16 to 21 ppm, which was assigned to the carbon sites of ≡Si-CH_2-$\underline{C}H_2$-CH_2-Si≡ units derived from the β-addition product, while the resonance assigned to the methylene carbon of the ≡Si-CH_2-$\underline{C}H(CH_3)$-Si≡ units derived from the α-addition product was overlapped with those of the ≡Si-$\underline{C}H_3$ (a) units and ≡Si-$\underline{C}H_2$-Si≡ (b) groups from SMP10.[196] Concerning the hydrosilylation, the NMR results agree well with the reaction paths shown in Figure 3. 2. The spectrum of 30Hf-SMP10_80 shows one broad additional resonance around 41 ppm, which was assigned to =N-$\underline{C}H_3$ groups stemming from the Hf-N$\underline{C}H_3$ units of the precursor, thus supporting the reaction between SMP 10 and TDMAH.

The ^{29}Si NMR signals of pure SMP10 have been already published and are shown in Figure 3. 3b according to the references.[190, 197] If compared with pure SMP10, the integral of the peaks in the spectrum of 30Hf-SMP10_80 clearly show that the contents of C$\underline{Si}H_3$ and $\underline{Si}C_2H_2$ units are decreased, indicating that both the hydrosilylation of SMP10 and the reaction between SMP10 and TDMAH occurs. As aforementioned, new silicon units including C$\underline{Si}H_2N$, C$\underline{Si}HN_2$, C$\underline{Si}N_3$, $\underline{Si}C_2HN$, $\underline{Si}C_2N_2$ and $\underline{Si}C_3N$ are expected to form in the obtained 30Hf-SMP10_80 precursor. However, in the ^{29}Si MAS NMR spectrum of 30Hf-SMP10_80, only three new signals were analyzed and assigned to $\underline{Si}C_3N$, $\underline{Si}C_2N_2$ and $\underline{Si}C_2HN$

units, exhibiting site fractions of 1.9 , 2.1 and 4.4 %, respectively (Table 3. 1).[198] In conclusion, the NMR results clearly indicate that the reaction between TDMAH and SMP10 resulted in the formation of Hf-containing single-source precursors (*e.g.*, 30Hf-SMP10_80).

Table 3. 1 ^{29}Si MAS NMR chemical shifts and fractions of the silicon containing units in the precursors.

Temperature	$\underline{Si}C_3N$		$\underline{Si}C_2HN$		$C\underline{Si}H_3$		$\underline{Si}C_2H_2$	
[°C]	[ppm]	[%]	[ppm]	[%]	[ppm]	[%]	[ppm]	[%]
80	10.69	3.1	-1.22	3.4	-61.53	6.0	-33.78	38.8
Temperature	$\underline{Si}C_2N_2$		$\underline{Si}C_3H$		$\underline{Si}C_4$		$\underline{Si}C_3O$	
[°C]	**[ppm]**	**[%]**	**[ppm]**	**[%]**	**[ppm]**	**[%]**	**[ppm]**	**[%]**
80	5.59	7.2	-10.41	37.6	---	---	16.40	3.9

3.1.2 Boron doped Hf-containing single-source precursors

As mentioned above, the Hf-containing single-source precursor (30Hf-SMP10_100) was synthesized by the reaction of SMP10 and TDEAH [$Hf(NEt_2)_4$] at 100 ºC (section 2.1.1), and the boron doped Hf-containing single source precursor (30Hf-B-SMP10_100) was synthesized by adding borane dimethylsulfide (BMS) into the mixed SMP10 and TDEAH (section 2.1.2). FT-IR spectra of the as-synthesized 30Hf-B-SMP10_100 and 30Hf-SMP10_100 are shown in Figure 3. 4. Compared with the spectrum of pure SMP10, the highly increased intensity of the absorption peaks of alkyl groups on both 2 spectra at 2963 cm^{-1}, 2922 cm^{-1} and 2856 cm^{-1} (C-H stretching on NCH_2CH_3 groups) and the newly appeared peaks at 945 cm^{-1} (N-Si stretching on Hf-N-Si unites), 1453 cm^{-1} and 1375 cm^{-1} (C-H bending on NCH_2CH_3 groups), 1202 cm^{-1} (N-C bending on NCH_2CH_3 groups) as well as 1287 cm^{-1} and 1178 cm^{-1} (N-C stretching[199]) proved that the TDEAH ($Hf[N(CH_2CH_3)_2]_4$) is able to react with SMP10 by forming Hf-N-Si linkages.[94] On the FT-IR spectra of 30Hf-B-SMP10_100, the newly appeared absorption peaks at 2438 cm^{-1} (B-H vibrations[200, 201]) as well as the disappeared peaks at 1630 cm^{-1} (C=C stretching) and 3075cm^{-1} (=C-H stretching) indicates the occurring of hydroboration between $BH_3 \cdot SMe_2$ and SMP10 (B-H/C=C). Please note that self hydrosilylation reaction between the allyl and Si-H groups can also occur at 100°C with TDEAH as catalyst, thus the peaks for allyl groups on the spectra of 30Hf-SMP10_100 disappeared, and the intensity of the Si-H peaks at 2115 cm^{-1} decreased as well.[94] However, it is well accepted that the B-H groups are more active than Si-H groups, and the hydroboration reaction between the $BH_3 \cdot SMe_2$ and SMP10 can occur at room temperature or even lower.[202, 203]

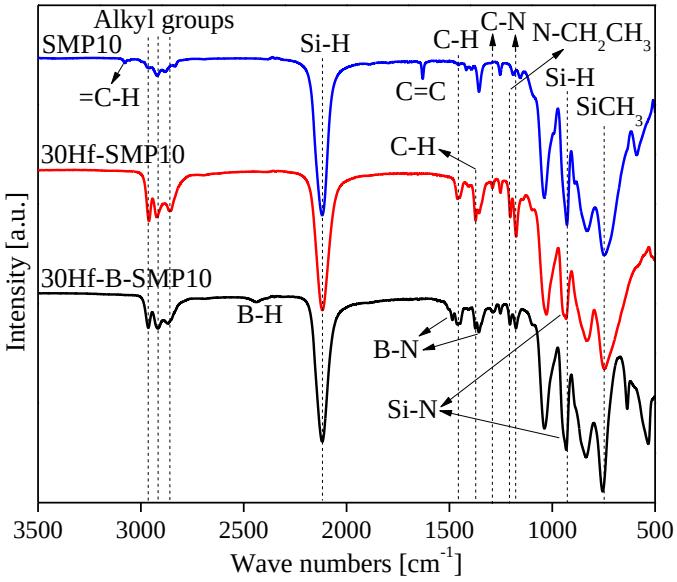

Figure 3. 4 FT-IR spectra of SMP10 and as-synthesized Hf -containing single-source precursors.

Based on the FT-IR spectra of 30Hf-SMP10_100 in Figure 3. 4 and investigations on reaction between SMP10 and TDMAH $[Hf(NMe_2)_4]$[94], the reaction routes between SMP10 and THEAH $[Hf(NEt_2)_4]$ can be proposed as Figure 3. 5.

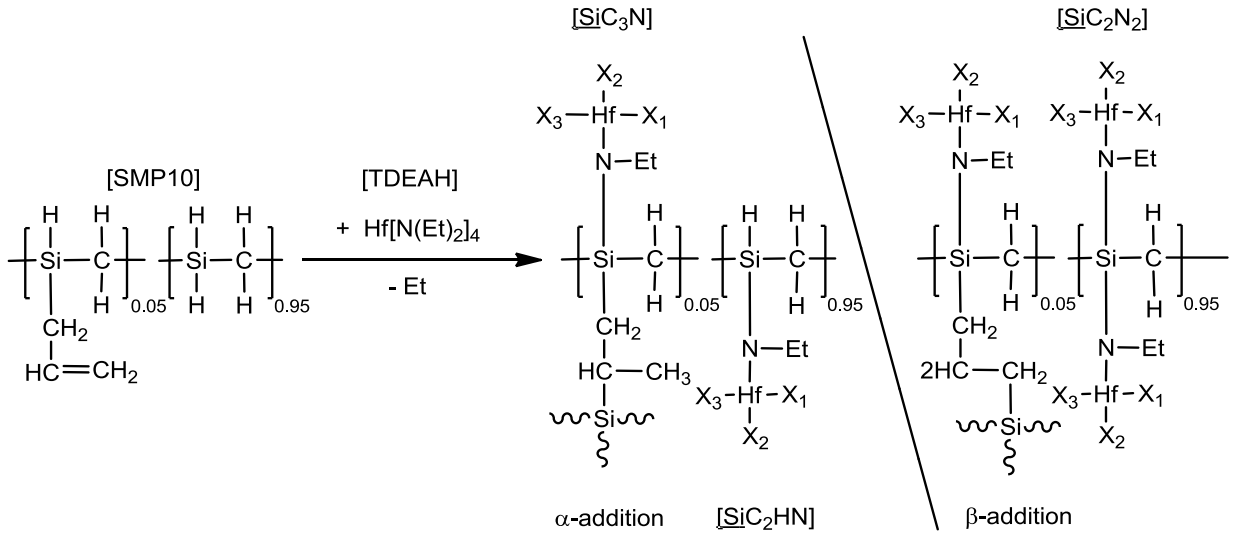

X_1, X_2, X_3 = {$N(Et)_2$, $NSi(CH_2)H_2$, $NSi(CH_2)(N)H$, $NSi(CH_2)(N)_2$, $NSi(CH_2)_2H$, $NSi(N)(CH_2)_2$, $NSi(CH_2)_3$ }

Figure 3. 5 Reaction routes with hydrosilylation during synthesis of the single-source precursor from SMP10 and TDEAH.

Solid state MAS NMR of the 30Hf-SMP10_100 and 30Hf-B-SMP10_100 is able to further prove the reactions. As mentioned above, the resonances with chemical shift at -61.2 ppm, -32.4 ppm and -10.4 ppm on the ^{29}Si NMR spectra of both precursors (Figure 3. 6a) can be assigned to C<u>Si</u>H_3, <u>Si</u>C_2H_2, and <u>Si</u>C_3H sites, respectively. The newly formed signals on the ^{29}Si NMR spectra with chemical shift at ~ -21.3, -5.8, 6.9 and 12.8 ppm are contributed by C<u>Si</u>HN_2, <u>Si</u>C_2HN, <u>Si</u>C_2N_2 and <u>Si</u>C_3N sites, respectively,

which proves that TDEAH reacts with SMP10 on the C<u>Si</u>H$_3$, <u>Si</u>C$_2$H$_2$ and <u>Si</u>C$_3$H sites by forming Si-N bonds.[204-206] However, the signals contributed by C<u>*Si*</u>H$_2$N and C<u>*Si*</u>N$_3$ sites have not been observed.

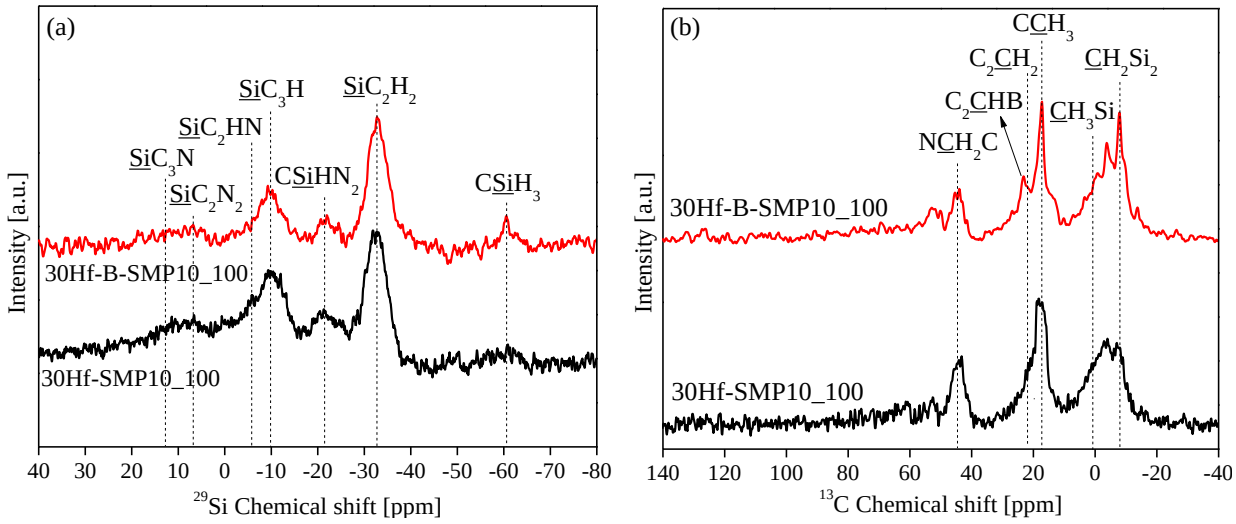

Figure 3. 6 NMR spectra of as-synthesized 30Hf-SMP10_100 and 30Hf-B-SMP10_100: *(a)* ^{29}Si and *(b)* ^{13}C spectra.

On the ^{13}C NMR spectra of both precursors (Figure 3. 6b), the signals at ~ 17.2 ppm (C<u>C</u>H$_3$ site) and ~ 44.5 ppm (N<u>C</u>H$_2$C site) are from the Hf-N-CH$_2$CH$_3$ groups, which further proves the reaction between the TDEAH and SMP10. The signals with chemical shift from 0 to 4 ppm and from -4.0 to -16.0 ppm were assigned to of the ≡Si-<u>*C*</u>H$_3$ units (<u>C</u>H$_3$Si) and ≡Si–<u>*C*</u>H$_2$–Si linkages (<u>C</u>H$_2$Si$_2$) on the main chain, respectively.[94, 190] The disappeared ^{13}C NMR resonances of allyl groups at 134.3 ppm (-<u>C</u>H=CH$_2$) and 114.7 ppm (-CH=<u>C</u>H$_2$) indicate the occurring of hydrosilylation and hydroboration. The resonances at 18.0 to 20.0 ppm on the ^{13}C NMR spectra of 30Hf-SMP10_100 is contributed by the C$_2$<u>C</u>H$_2$ sites on the ≡Si-CH$_2$-<u>*C*</u>H$_2$-CH$_2$-Si≡ unites (β-addition hydrosilylation products)[94], but the resonance assigned to the C$_2$<u>C</u>HSi sites on the ≡Si-CH$_2$-<u>*C*</u>H(CH$_3$)-Si≡ units derived from the α-addition products was overlapped with those of the ≡Si-<u>*C*</u>H$_3$ units coming from the original SMP10.[196] On the ^{13}C NMR spectra of 30Hf-B-SMP10_100, the signal intensity of the C$_2$<u>C</u>H$_2$ sites decreases, and a new resonance for hydroboration products (C$_2$<u>C</u>HB sites on ≡Si-CH$_2$-CHB-CH$_3$ unites, α-addition) appears at low-field 23.2 ppm, which further proved the hydroboration reaction between the BH$_3$·SMe$_2$ and SMP10.[207]

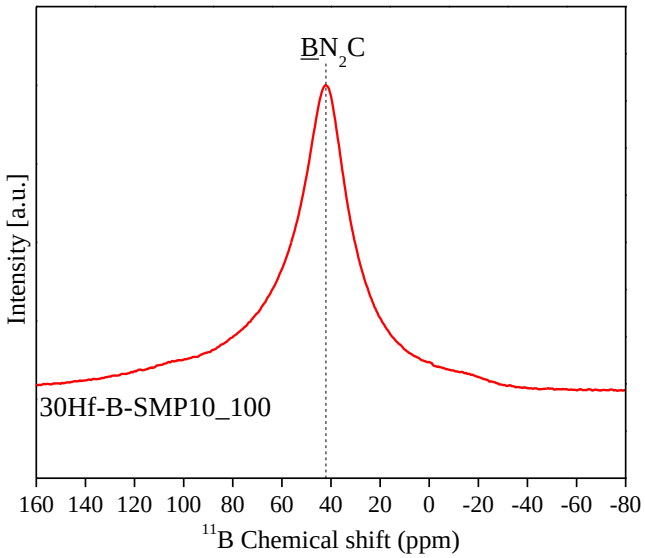

Figure 3. 7 ^{11}B NMR spectrum of as-synthesized 30Hf-B-SMP10_100.

On the ^{11}B NMR spectra of 30Hf-B-SMP10_100 (Figure 3. 7), it is interesting that a strong resonance with chemical shift at ≈ 42.6 ppm is observed, which can be assigned to $\underline{B}N_2C$ site.[208] That means, in addition to the hydroboration reaction with allyl groups, the B-H groups also react with the diethylamino groups by forming B-N bonds (Figure 3. 8), which is consistent with the newly appeared absorption peaks at 1350 and 1483 cm^{-1} (B-N vibrations) on the FT-IR spectrum of 30Hf-B-SMP10_100 (Figure 3. 4).[201] Figure 3. 8 illustrates the reaction routes during synthesis of 30Hf-B-SMP10_100: *(a)* describes the hydroboration process via α-addition; *(b)* presents the reaction between boron incorporated SMP10 and $Hf(NEt_2)_4$; *(c)* is the overall reaction routes during synthesis of the 30Hf-B-SMP10_100.

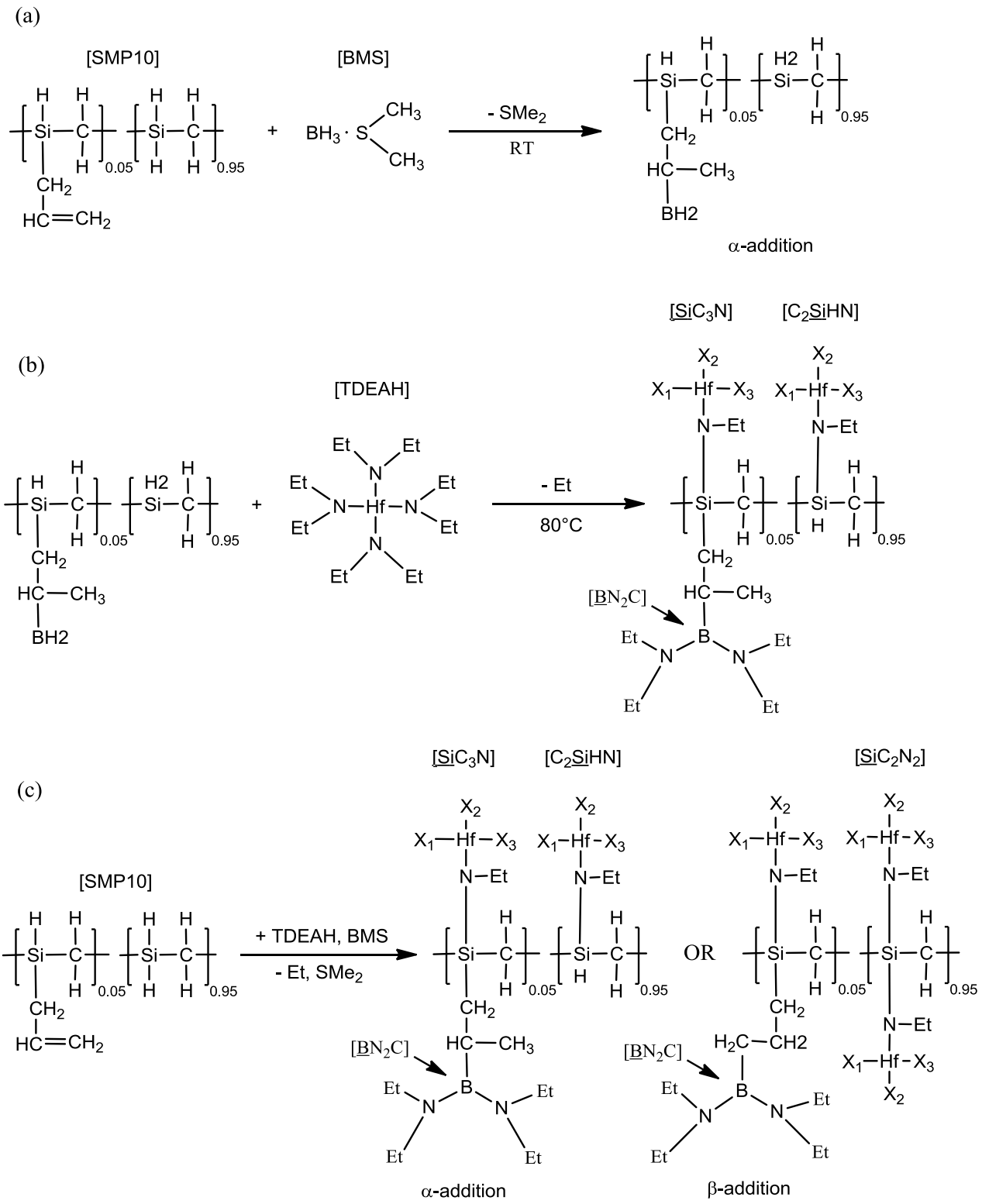

Figure 3. 8 Reaction routes during synthesis of the single-source precursor from SMP10, TDEAH and BMS (RT means room temperature).

3.1.3 Ta-containing single-source precursors

As mentioned in section 2.1.3, the Ta-containing single-source precursor (30Ta-SMP10_80) was synthesized by the reaction of SMP10 and PDMAT [$Ta(N(CH_3)_2)_5$] with the weight ratio of PDMAT/SMP10 30/70. After synthesis, the solid precursors were collected for FT-IR spectroscopy measurement, and the spectra of the precursors are shown in Figure 3. 9. The spectrum of pure SMP10 at room temperature is also shown for comparison. Compared with the spectrum of pure SMP10, the newly appeared absorption peaks on the 30Ta-SMP10_80 spectra at 945 cm^{-1} (N-Si stretching on Ta-N-Si unites)[192], 2788 cm^{-1} (C-H stretching on NCH_3 groups), 1453 cm^{-1} (C-H bending on NCH_3 groups) as well as 1287 cm^{-1} and 1178 cm^{-1} (N-C stretching[199]) proved that the PDMAT is able to react with SMP10.[94] Moreover, the highly increased the intensity of alkyl groups at 2956 cm^{-1}, 2882 cm^{-1}, 2922 cm^{-1} and 2860 cm^{-1} and significantly decreased intensity of Si-H band (2115 cm^{-1} and 930 cm^{-1}) with respect to the intensity of the Si-CH_3 band (747cm^{-1}) further confirm the reaction. The disappeared absorption bands of the allyl groups (C-H stretching at 3075cm^{-1} and C=C stretching at 1630 cm^{-1})[190] confirm the occurring of hydrosilylation.

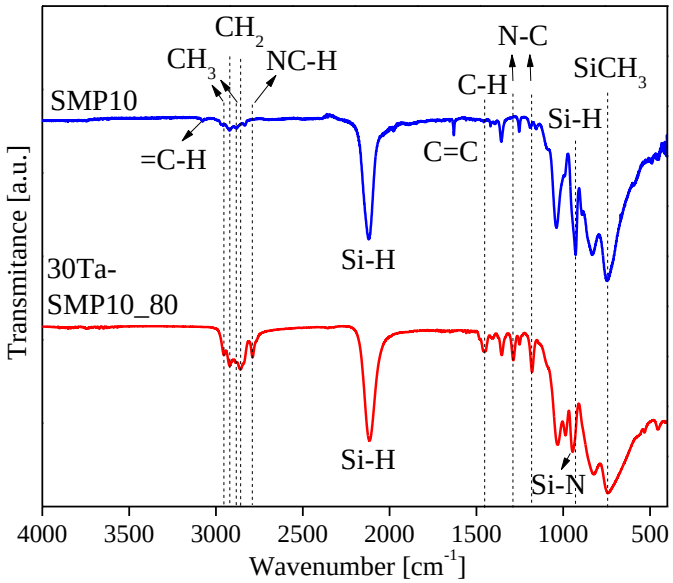

Figure 3. 9 FT-IR spectra of SMP10 and as-synthesized 30Ta-SMP10_80.

According to the FT-IR spectra and previously reported reaction between SMP10 and $Hf(NMe_2)_4$[94], two reactions are expected to occur during the synthesis of 30Ta-SMP10_80 (Figure 3. 10). The first one involves the hydrosilylation of the allyl groups, which explains the disappearance of allyl groups and the decrease in the intensity of Si-H peaks. Normally, the hydrosilylation process of pure SMP10 starts at temperatures of ca. 100-120 °C[13], the pure SMP10 heated at 80 °C (spectrum (2) in Figure 3. 1a) did not show significant changes of the intensities of the allyl and Si-H vibrations. However, the addition of PDMAT to SMP10 induces the disappearance of the allyl groups at 80ºC (Figure 3. 9), which indicates that the PDMAT acts as a catalyst for the hydrosilylation.[194, 195] The second reaction route involves the reaction of PDMAT with the Si-H groups of SMP10. Similar to $Hf(NMe_2)_4$, the reaction between the

PDMAT and Si-H groups occurs by forming Si-N bonds, which leads to the formation of Si-N-Ta linkages (Figure 3. 9).[94] Based on the two reaction pathways, synthesis of the Ta-containing single source precursors from SMP10 and PDMAT can be described as depicted in Figure 3. 10: the allyl and Si-H groups of SMP10 are involved in hydrosilylation that leads to an increased cross-linking degree of the precursor; additionally, PDMAT reacts with the Si-H groups of SMP10 to form Si-N-Ta linkages and release gaseous CH_4.

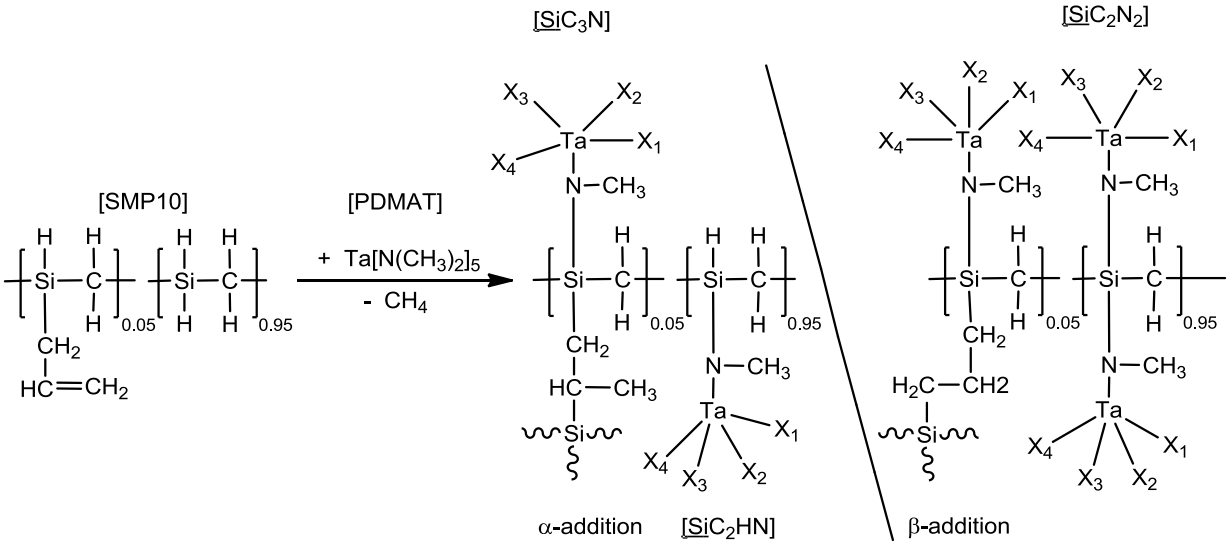

X_1, X_2, X_3, X_4 = {$N(CH_3)_2$, $NSi(CH_2)H_2$, $NSi(CH_2)(N)H$, $NSi(CH_2)(N)_2$, $NSi(CH_2)_2H$, $NSi(N)(CH_2)_2$, $NSi(CH_2)_3$ }

Figure 3. 10 Reaction pathways of synthesis of the single-source precursor from SMP10 and PDMAT.

The reactions can be further proved by MAS solid NMR of 30Ta_SMP10_80. As shown in Figure 3. 11a, if compared with the ^{29}Si spectrum of pure SMP10, the peaks in the spectrum of 30Ta-SMP10_80 clearly show that the contents of C*Si*H_3 and *Si*C_2H_2 units decrease, indicating the consuming of Si-H groups. The ^{29}Si NMR spectrum of pure SMP10 indicates that three kinds of hydrogen-bearing Si sites (hydridosilyl groups) exist as alternating groups of the polymer backbone of SMP10, *i.e.*, C<u>Si</u>H_3, <u>Si</u>C_2H_2 and <u>Si</u>C_3H.[190, 196, 197] Hence, different kinds of <u>Si</u>-N(CH_3)-Ta units including C<u>Si</u>H_2N, C<u>Si</u>HN_2, C<u>Si</u>N_3, <u>Si</u>C_2HN, <u>Si</u>C_2N_2 and <u>Si</u>C_3N can be generated upon reacting the corresponding Si-H groups with PDMAT. On the ^{29}Si MAS NMR spectrum of 30Ta-SMP10_80, 2 new signals were detected and assigned to *Si*C_3N and *Si*C_2HN units, respectively (Figure 3. 11a).

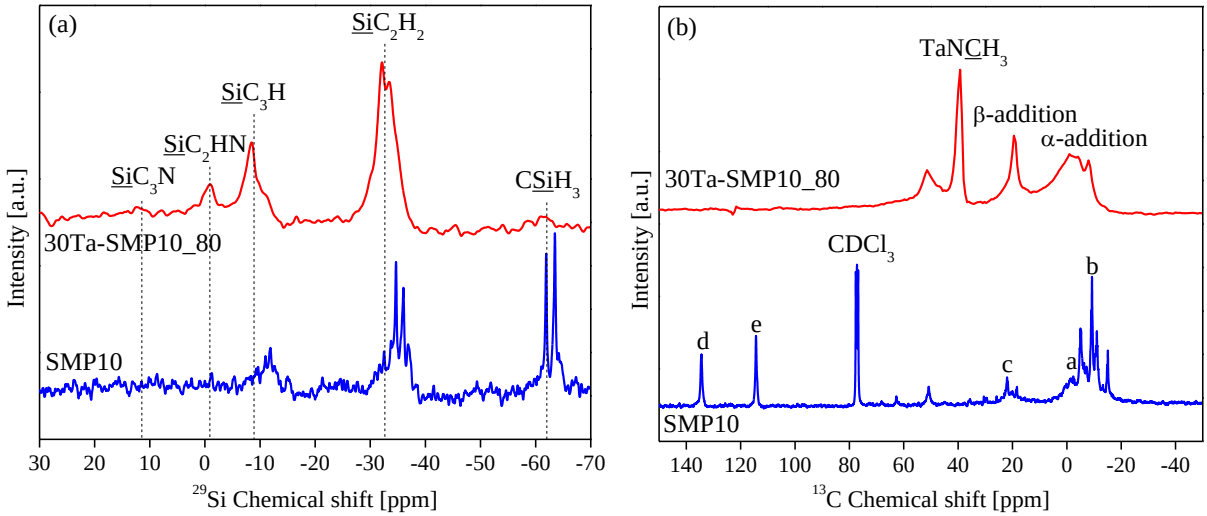

Figure 3. 11 NMR spectra of pure SMP10 and MAS NMR spectra of 30Ta-SMP10_80: *(a)* ^{29}Si and *(b)* ^{13}C spectra.

In the ^{13}C NMR spectrum of SMP10 (Figure 3. 11b), the chemical shifts of 134.3 ppm and 114.7 ppm are assigned to the carbon sites of ≡Si–CH_2–$\underline{C}H$=CH_2 (d) and ≡Si–CH_2–CH=$\underline{C}H_2$ (e) of the allyl groups, respectively. Multiple chemical shifts in the region from 17.7 to 30.0 ppm are attributed to the ≡Si–$\underline{C}H_2$–CH=CH_2 (c) linkage between silicon and the allyl groups. The signal of the ≡Si-$\underline{C}H_3$ (a) groups was observed around 0 ~ 2.4 ppm, and the chemical shifts from -4.4 to -16.0 ppm were assigned to ≡Si–$\underline{C}H_2$–Si (b) linkages on the main chain.[190] Compared with the ^{13}C spectrum of pure SMP10, the allyl-carbon resonances (d and e) of the 30Ta-SMP10_80 disappeared due to the hydrosilylation process, which is consistent with the FT-IR results. A new broad resonance appeared in the region from 16 to 21 ppm, which was assigned to the carbon sites of ≡Si-CH_2-$\underline{C}H_2$-CH_2-Si≡ units derived from the β-addition product, while the resonance assigned to the methylene carbon of the ≡Si-CH_2-$\underline{C}H(CH_3)$-Si≡ units derived from the α-addition product was overlapped with those of the ≡Si-$\underline{C}H_3$ (a) units and ≡Si-$\underline{C}H_2$-Si≡ (b) groups from SMP10.[196] Concerning the hydrosilylation, the NMR results agree well with the reaction paths shown in Figure 3. 10. The spectrum of 30Ta-SMP10_80 shows one broad additional resonance at around 39.2 ppm, which was assigned to =N-$\underline{C}H_3$ groups stemming from the Ta-N$\underline{C}H_3$ units of the precursor, thus strongly supporting the reaction between SMP 10 and PDMAT.

3.1.4 HfTa-containing single-source precursors

3.1.4.1 Synthesis of 30Hf7Ta3-SMP10_100

FT-IR spectra of the 30Hf7Ta3-SMP10_100 and pure SMP10 are shown in Figure 3. 12. Compared with the spectrum of pure SMP10, the newly appeared absorption peaks on the spectrum of 30Hf7Ta3-SMP10_100 at 945 cm^{-1} (N-Si stretching on Hf-N-Si and Ta-N-Si unites)[192], 2788 cm^{-1} (C-H stretching on NCH_3 groups), 1453 cm^{-1} and 1372 cm^{-1} (C-H bending on the -CH_3 of NCH_2CH_3 groups), 1205 cm^{-1} (C-N bending on NCH_2CH_3 groups) as well as 1287 cm^{-1} and 1178 cm^{-1} (N-C stretching[199]) proved that the SMP10 reacted with both PDMAT [$Ta(NMe_2)_5$] and TDEAH [$Hf(NEt_2)_4$].[94] Besides, the highly increased the intensity of alkyl groups at 2960 cm^{-1}, 2922 cm^{-1} and 2860 cm^{-1} and significantly decreased intensity of Si-H band (2115 cm^{-1} and 930 cm^{-1}) with respect to the intensity of the Si-CH_3 band (747cm^{-1}) further confirm the reactions. In addition, the disappeared absorption bands of the allyl groups (C-H stretching at 3075cm^{-1} and C=C stretching at 1630 cm^{-1})[190] confirm the occurring of hydrosilylation.

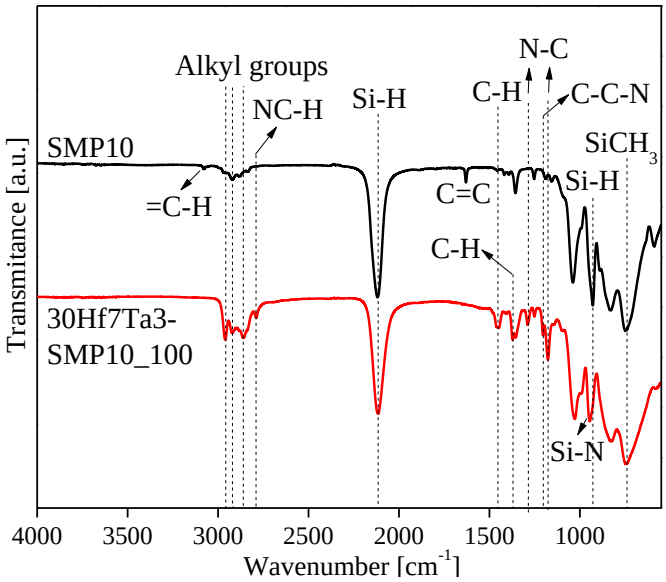

Figure 3. 12 FT-IR spectra of pure SMP10 and as-synthesized 30Hf7Ta3-SMP10_100.

3.1.4.2 Synthesis of 30Hf2Ta8-SMP10_100

FT-IR spectra of the 30Hf2Ta8-SMP10_100 and pure SMP10 are shown in Figure 3. 13. Compared with the spectrum of pure SMP10, the newly appeared absorption peaks on the spectrum of 30Hf2Ta8-SMP10_100 at 945 cm^{-1} (N-Si stretching on Hf-N-Si and Ta-N-Si unites)[192], 2788 cm^{-1} (C-H stretching on NCH_3 groups), 1453 cm^{-1} (C-H bending on CH_3 groups) as well as 1287 cm^{-1} and 1178 cm^{-1} (N-C stretching[199]) proved that the SMP10 reacted with both PDMAT and TDEAH.[94] Besides, the highly increased the intensity of alkyl groups at 2953 cm^{-1}, 2885 cm^{-1}, 2924 cm^{-1} and 2857 cm^{-1} and significantly decreased intensity of Si-H band (2115 cm^{-1} and 930 cm^{-1}) with respect to the intensity of the Si-CH_3 band (747cm^{-1}) further confirm the reactions. However, the peaks at 1372 cm^{-1} (C-H bending on the CH_3 of NCH_2CH_3 groups) and 1205 cm^{-1} (C-N bending on the NCH_2CH_3 groups) cannot be found due to the

small amount of TDEAH in feed. In addition, the disappeared absorption bands of the allyl groups (C-H stretching at 3075cm^{-1} and C=C stretching at 1630 cm^{-1})[190] confirm the occurring of hydrosilylation.

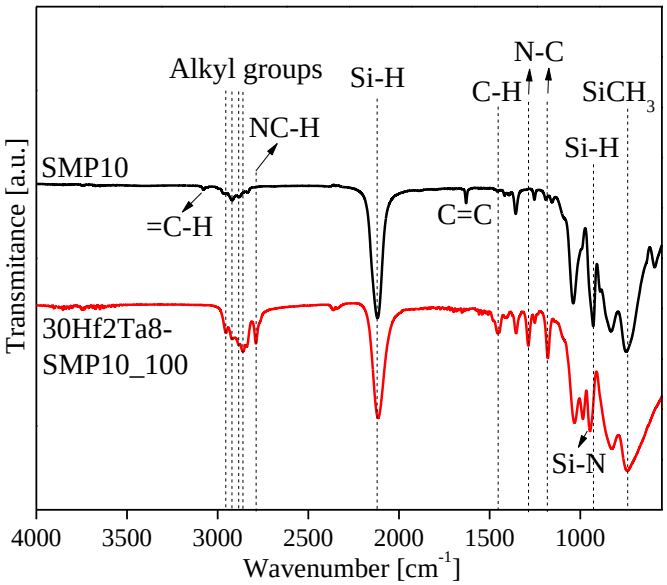

Figure 3. 13 FT-IR spectra of pure SMP10 and as-synthesized 30Hf2Ta8-SMP10_100.

3.1.5 Summary

In this part, a series of single-source precursors including 30Hf-SMP10_80, 30Hf-SMP10_100, 30Ta-SMP10_80, 30Hf7Ta3-SMP10_100 and 30Hf2Ta8-SMP10_100 were successfully synthesized upon reaction between SMP10 and metal compounds including TDMAH, TDEAH and PDMAT. The results of FT-IR and MAS solid NMR suggest that synthesis of the single-source precursors can be described as: the allyl and Si-H groups of SMP10 are involved in hydrosilylation that leads to an increased crosslinking degree of the precursors; additionally, the metal compounds react with the Si-H groups of SMP10 to form Si-N-M linkages (M = Hf or Ta) and release gaseous CH_4 or CH_3CH_3; moreover, the hydrosilylation process can be catalyzed by the metal compounds. Furthermore, a boron doped M-containing single-source precursor (30Hf-B-SMP10_100) was synthesized by reaction among SMP10, TDEAH and BMS ($BH_3 \cdot SMe_2$, borane dimethylsulfide). Hydroboration between B-H and allyl groups was observed, and the B-H groups were proved to react with diethylamino groups on the TDEAH by forming B-N bonds.

3.2 Polymer-to-ceramic transformation

The as-synthesized single-source precursors were pyrolyzed at 1000 ºC or 1100 ºC for 2 h in argon atmosphere in order to prepare single-phase amorphous SiHfC(N), SiHfBC(N), SiTaC(N), SiHf7Ta3C(N) and SiHf2Ta8C(N) ceramics. Taking the 30Hf-SMP10_80, 30Hf-B-SMP10_100, 30Hf-SMP10_100 and 30Ta-SMP10_80 for example, the polymer-to-ceramic transformation process was investigated by FT-IR, ^{13}C and ^{29}Si MAS NMR as well as *in situ* TGA/MS studies.

3.2.1 30Hf-SMP10_80

FT-IR characterization

As shown in Figure 3. 14, the intensities of the Si-H, NC-H and N-C vibrations have only slight changes with the temperature increasing from 80 °C to 200 °C. However, the intensity of the NCH_3 absorptions decreases significantly after pyrolysis at 400 °C due to the further reaction between the NCH_3 groups of TDMAH and the Si-H groups of SMP10 (NCH_3/Si-H). The bands of the Si-H vibration at 2115 cm^{-1} and 930 cm^{-1} also decrease due to dehydrocoupling (Si-H/Si-H) and further reactions between TDMAH and SMP10 (NCH_3/Si-H).

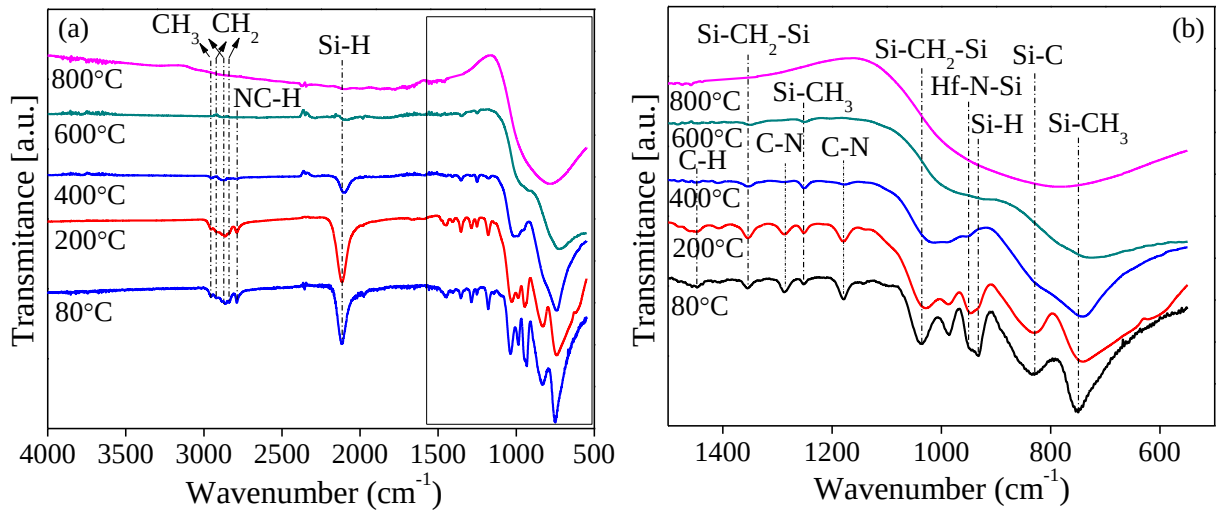

Figure 3. 14 *(a)* FT-IR spectra of 30Hf-SMP10_80 heat-treated at different temperatures; *(b)* magnification of the region from 500 to 1500 cm^{-1}.

At temperatures beyond 600 °C, the peaks for the NC-H stretching at 2788 cm^{-1} and bending at 1450 cm^{-1} as well as C-N stretching at 1287 cm^{-1} and 1178 cm^{-1} almost disappear, while the characteristic absorption band of Hf-N-Si at around 945 cm^{-1} still exists, overlapping with broad Si-C peaks (Figure 3. 14b). The intensities of the Si-CH_3 absorption bands at 750 cm^{-1} and 1250 cm^{-1} as well as that of the Si-CH_2-Si bands at 1035 cm^{-1} and 1353 cm^{-1} decrease to some extent because of the decomposition of the organic groups.

MAS NMR analysis

^{13}C and ^{29}Si MAS NMR analysis of pyrolytic residuals of the 30Hf-SMP10_80 at different temperatures was also performed, and the results are shown in Figure 3. 15 and Table 3. 2. As shown in Figure 3. 15a, the intensity of the carbon signal of the $HfN\underline{C}H_3$ units significantly reduces with the temperature increasing from 200 °C to 400 °C and disappears at 600 °C, indicating that the amido groups are consumed by the reaction between TDMAH and SMP 10 (NCH_3/Si-H), which is consistent with the FT-IR results.

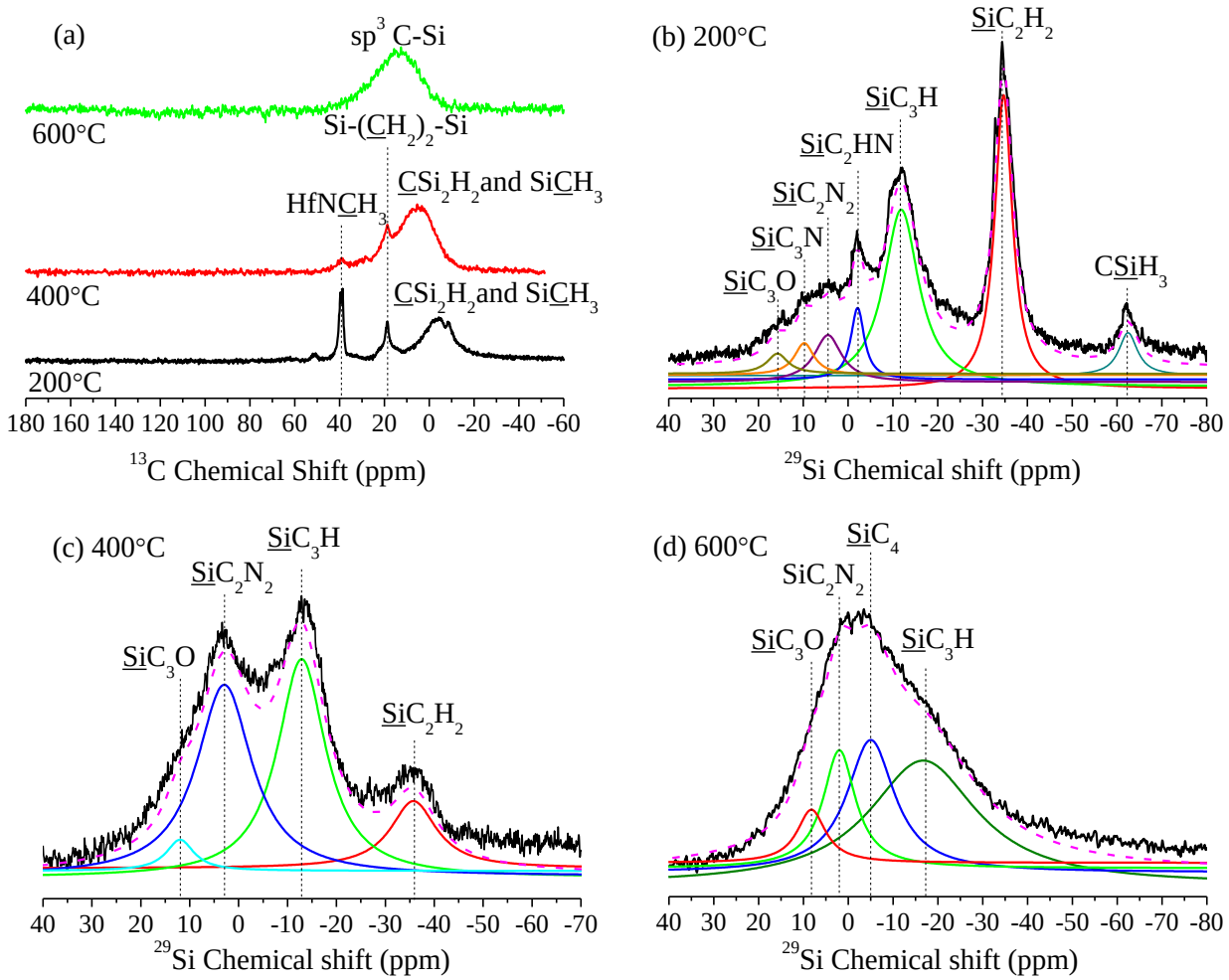

Figure 3. 15 ^{13}C and ^{29}Si MAS NMR spectra of 30Hf-SMP10_200, 30Hf-SMP10_400 and 30Hf-SMP10_600: *(a)* ^{13}C spectra; *(b)*, *(c)* and *(d)* ^{29}Si MAS NMR spectra. The black solid bold lines are the experimental spectra, the dashed lines represent the simulated spectra, and the colorful solid lines indicate the individually fitted components.

From 80°C to 200 °C, the chemical shifts of the ^{29}Si signals changed slightly, and the fractions of $\underline{Si}C_3N$, $\underline{Si}C_2HN$ and $\underline{Si}C_2N_2$ units increase owing to the progress of the reaction between TDMAH and SMP10 (NCH_3/Si-H) (Table 3. 2). With the temperature increasing from 200 °C to 400 °C, the $C\underline{Si}H_3$ units almost disappear, and the intensity of the $\underline{Si}C_2H_2$ signal decreases considerably, while those of the $\underline{Si}C_3H$ signals

increase (Table 3. 2, Figure 3. 15b and Figure 3. 15c), due to Si-H/Si-H dehydrocoupling reactions.[209] The signals of $\underline{Si}C_2HN$ and $\underline{Si}C_3N$ units disappear, and that of $\underline{Si}C_2N_2$ becomes stronger and broader with a fraction up to 42.2 %, indicating a significant reaction between NCH_3 and Si-H groups ($NCH_3/\underline{Si}C_2H_2$ and $NCH_3/\underline{Si}C_2HN$) upon generating additional $\underline{Si}C_2N_2$ units. Subsequently, after pyrolysis at 600°C, the signal related to $\underline{Si}C_2H_2$ units disappear, and a new peak assigned to $\underline{Si}C_4$ units (-5 ppm) appear due to Si-H/Si-H dehydrocoupling (Figure 3. 15d).[196]

Table 3. 2 ^{29}Si MAS NMR chemical shifts and fractions of the silicon containing units in the pyrolytic residues at different temperatures.

Temperature	$\underline{Si}C_3N$		$\underline{Si}C_2HN$		$C\underline{Si}H_3$		$\underline{Si}C_2H_2$	
[°C]	[ppm]	[%]	[ppm]	[%]	[ppm]	[%]	[ppm]	[%]
200	9.78	4.1	-2.12	6.2	-62.47	5.2	-34.80	33.6
400	---	---	---	---	---	---	-35.75	12.2
Temperature	$\underline{Si}C_2N_2$		$\underline{Si}C_3H$		$\underline{Si}C_4$		$\underline{Si}C_3O$	
[°C]	[ppm]	[%]	[ppm]	[%]	[ppm]	[%]	[ppm]	[%]
200	4.49	8.2	-11.86	40.1	---	---	15.76	2.7
400	2.93	42.2	-12.89	42.1	---	---	11.97	3.4
600	1.99	15.2	-16.70	53.6	-5.00	25.2	8.23	6.1
800	-5.73	19.0	---	---	-13.43	76.7	7.39	4.3
1100	-10.87	19.2	---	---	-16.56	79.1	3.97	1.7
1300	-22.60	2.3	---	---	-17.27	93.5	0.20	4.1

TG/MS analysis

The NMR and FT-IR spectroscopic results were further supported by the results of the *in situ* TG/MS analysis. As shown in Figure 3. 16, the TG and DTG curves (first time derivative of the TG) revealed that there are 3 main steps during the pyrolysis of 30Hf-SMP10_80. The first step started from ambient temperature to approximately 200 ºC with the DTG peak at 56.7ºC. During this step, a small mass loss was observed and slight release of CH_4 (Figure 3. 17a, m/z = 15) was detected, which relies on the reaction between TDMAH and SMP 10 (NCH_3/Si-H), leading to the decomposition of NCH_3 groups. However, the decomposition of the NCH_3 groups was not significant at these temperatures, as the intensity of $N\underline{C}H_3$ in the ^{13}C MAS NMR spectrum of 30Hf-SMP10_80 pyrolyzed at 200 ºC (Figure 3. 15a) is still very high. This behavior is different from that of the pure TDMAH, which fully decomposes at temperatures beyond 150 ºC.[192]

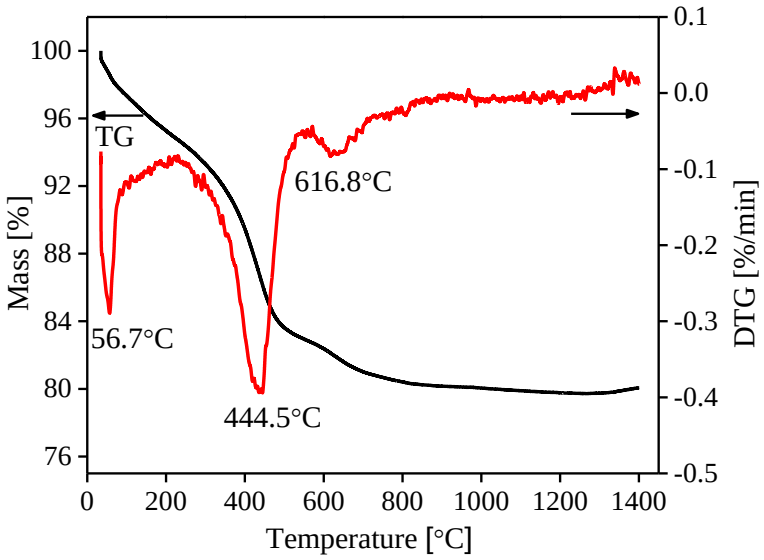

Figure 3. 16 TG and DTG (first derivative of the TG) curves of ceramization process of 30Hf-SMP10_80.

In the temperature range from 200 to 600 ºC, two evolution peaks of CH_4 were detected. At 490 ºC, the first release of CH_4 was observed, leading to the mass loss during ceramization process. The CH_4 is generated from the further reaction between TDMAH and SMP10 (reaction between NCH_3 and Si-H groups), which was substantiated by FT-IR and solid-state MAS NMR results. Moreover, the release of amines was also detected during the temperature range from 250 to 600 ºC (Figure 3. 17b and Figure 3. 17c), and ammonia was detected at temperatures from 340 to 780 ºC (Figure 3. 17a) as well, suggesting that transamination occurred during the ceramization process. This was further supported by *ex situ* FT-IR and MAS NMR investigations on the samples pyrolyzed at 200, 400 and 600 ºC. Furthermore, some fragments derived from hydrocarbons such as C_2H_6 (from 300 to 680 ºC, Figure 3. 17b), C_3H_8 (from 250 to 620 ºC, Figure 3. 17c) and C_4H_{10} (from 250 to 620 ºC, Figure 3. 17d) were detected as well; their release relies on the decomposition of the organic substituents in the single-source precursor decomposition. The ceramization process was found to be completed at approximately 900 °C (*i.e.*, beyond this temperature no mass loss was observed), leading to a ceramic yield of *ca*. 80 wt.%.

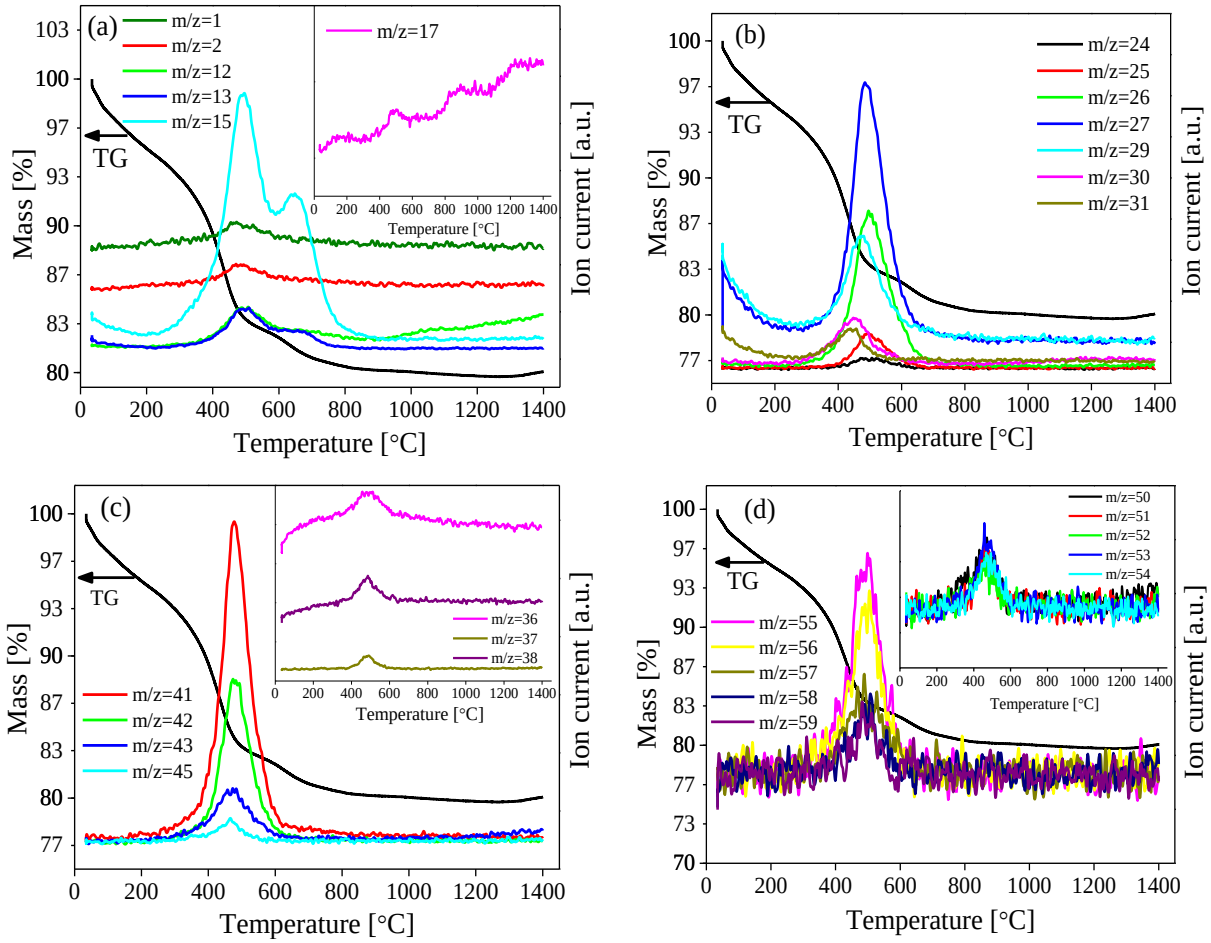

Figure 3. 17 TG and QMID ion current curves (QMID - quasi multiple ion detection) describing the evolution of volatile species during the polymer-to-ceramic transformation of Hf-SMP10_80 (*a*: hydrogen (*m/z* = 1 and 2), methane (*m/z* = 12, 13 and 15) and ammonia (*m/z* = 17); *b*: amines and C_2H_6 (*m/z* = 24, 25, 26, 27, 29, 30 and 31); *c*: amines and C_3H_8 (*m/z* =36, 37, 38,41, 42, 43 and 45); d: C_4H_{10}.

3.2.2 30Hf-B-SMP10_100 and 30Hf-SMP10_100

The polymer-to-ceramic transformation of the 30Hf-B-SMP10_100 and 30Hf-SMP10_100 was characterized using TGA coupled with *in situ* mass spectrometry (MS) from ambient temperature up to 1400 ºC (Figure 3. 18). Please note that, in this section, the Hf source is TDEAH [$Hf(NEt_2)_4$] instead of TDMAH [$Hf(NMe_2)_4$] as in section 3.2.1. The TG/MS results show that the polymer-to-ceramic transformation of both precursors almost finished at ≈ 900°C with around 3 steps, which results in ceramic yields of ≈ 78% for 30Hf-B-SMP10_100 and of ≈ 71% for 30Hf-SMP10_100, respectively. That means, with the addition of $BH_3{\cdot}SMe_2$, the ceramic yield is increased by ≈ 7%. The DTG and QMID ion current curves of 30Hf-SMP10_100 show that there are two strong mass-loss peaks at ≈ 290 and ≈ 400°C, respectively, with releasing of alkanes (C_nH_{2n+2}, n≤6), H_2 and amines (Figure 3. 18, a, b and c). The alkanes are coming from further reaction between the NCH_2CH_3 groups of TDEAH and the Si-H groups of SMP10 (NCH_2CH_3/Si-H) as well as the decomposition of NCH_2CH_3 groups and other organic

substituents of the polymers. H_2 is derived from dehydrocoupling of the Si-H groups of SMP10 (Si-H/Si-H). The release of amines is contributed by transamination during the ceramization process that mainly occurs at temperatures higher than 400°C (Figure 3. 18b).[94]

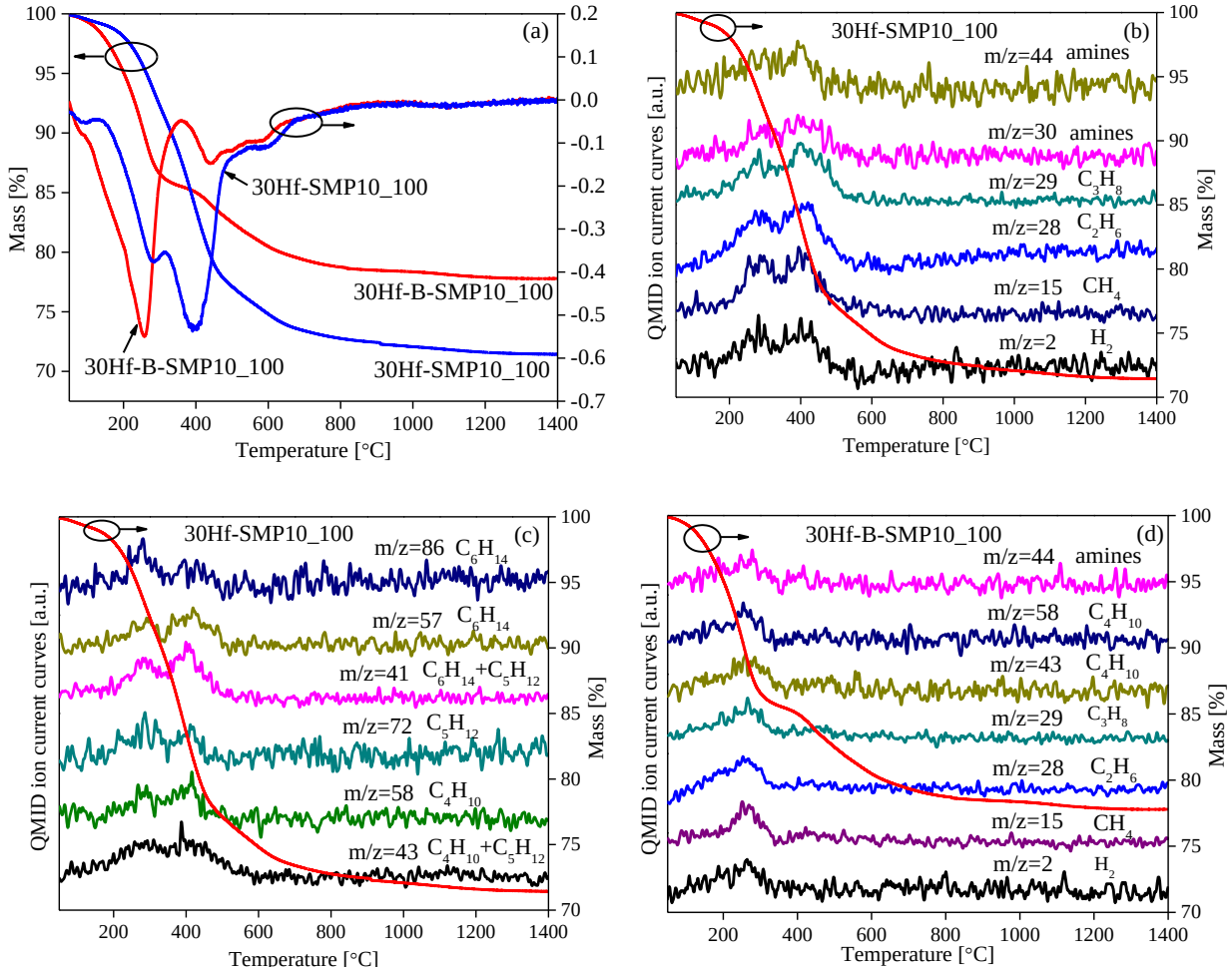

Figure 3. 18 *(a)* TG and DTG (first derivative of the TG) curves describing the polymer-to-ceramic transformation of the 30Hf-B-SMP10_100 and 30Hf-SMP10_100. *(b)*, *(c)* and *(d)* are TG and selected QMID ion current curves showing the evolution of volatile species during pyrolysis of the samples [*(b)* and *(c)* is for 30Hf-SMP10_100, *(d)* is for 30Hf-B-SMP10_100].

On the DTG and QMID ion current curves of the 30Hf-B-SMP10_100, there is only one strong mass-loss peak at ≈ 260°C (lower than that of 30Hf-SMP10_100) with releasing of H_2, small alkanes (C_nH_{2n+2}, n≤4) and amines (Figure 3. 18, a and d). The signals for fragments of larger alkanes (C_5H_{12} and C_6H_{14}) were not detected. Different from the 30Hf-SMP10_100, the second mass-loss step of 30Hf-B-SMP10_100 is rather weak, and the signals of fragments are negligible at temperatures higher than 400 ºC (Figure 3. 18d). This is because the BMS further enhanced the cross-linking of the precursors, which highly reduced the release of lager oligomers.[203] This is the reason why the ceramic yield of 30Hf-B-SMP10_100 is improved significantly.

3.2.3 30Ta-SMP10_80

As shown in Figure 3. 19, the TG and DTG curves (first time derivative of the TG) revealed that there are 3 main steps during the pyrolysis of 30Ta-SMP10_80. The first step started from ambient temperature to approximately 240 ºC with the DTG peak at 194.3 ºC. During this step, a small mass loss was observed, which should rely on the further reaction between PDMAT and SMP10 (NCH_3/Si-H) with release of CH_4. In the temperature range from 240 to 550 ºC (the second step), there is a large mass loss at around 460 ºC. This should be contributed by further reaction between NCH_3 and Si-H, decomposition of the organic substituents as well as transamination during the ceramization process.[94] In the third step, there is a DTG peak at around 590 ºC that should result from further decomposition of organic substituent. The ceramization process was found to be completed at approximately 900 °C (*i.e.*, beyond this temperature no mass loss was observed), leading to a ceramic yield of *ca*. 80 wt.%.

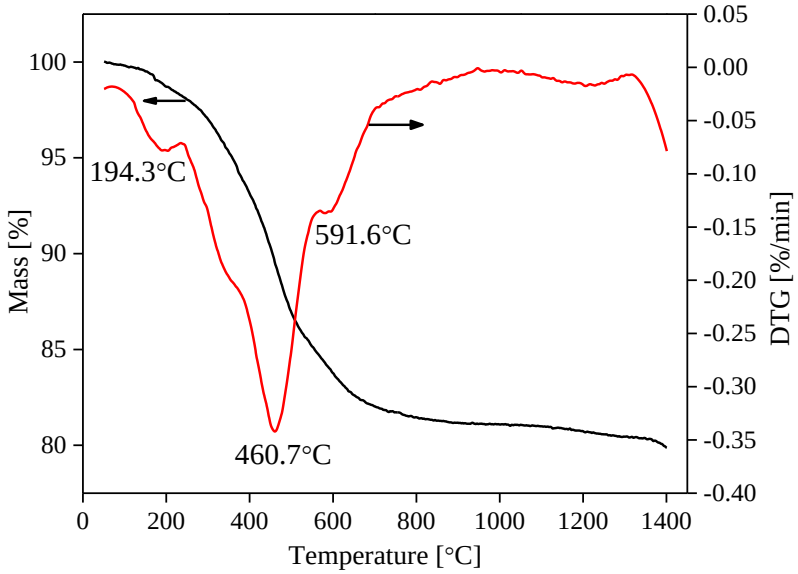

Figure 3. 19 TG and DTG (first derivative of the TG) curves describing the polymer-to-ceramic transformation of the 30Ta-SMP10_80.

3.2.4 Summary

In this section, the polymer-to-ceramic transformation of the as-synthesized single-source precursors was investigated using FT-IR, MAS solid NMR as well as *in situ* TG/MS. The TG curves indicate that the ceramic yield of all the precursors are higher than 70 wt.%. The precursors synthesized using TDMAH and PDMAT show higher ceramic yield (≈ 80 wt.%) than that of TDEAH (≈ 71 wt.%), while the ceramic yield of the later can be improved to ≈ 78 wt.% by introduction of borane dimethylsulfide. The TG and DTG curves suggest that there are several steps during the ceramization process. It can be figure out from the MS and MAS solid NMR spectra that, at lower temperatures (< 400 ºC), dehydrocoupling as well as reaction between the metal compounds and Si-H groups of SMP10 are the main reason for mass loss. At higher temperatures (≥ 400 ºC), transamination and decomposition of organic substituents contribute to further mass loss. All ceramization process was found to finish at ≈ 900 °C.

3.3 SiMC(N) ceramic nanocomposite powders

3.3.1 SiHfC(N) ceramic nanocomposites with HfC_xN_{1-x}-carbon core-shell microstructure

3.3.1.1 Chemical composition

After pyrolysis of the 30Hf-SMP10_80 at 1100 °C in argon atmosphere, a black ceramic was obtained (denoted as SHC-1100). The as-synthesized ceramic was subsequently annealed in argon atmosphere at 1300, 1400, 1500, 1700 and 1800 °C in order to investigate its high-temperature behavior with respect to decomposition, phase separation as well as crystallization. After annealing at different temperatures, the relative mass loss with respect to the sample SHC-1100 and the elemental contents of Hf, Si, C, N and O in the obtained ceramic materials were analyzed, and the results are listed in Table 3. 3. Considering that the SiC yield of pure SMP10 amounts 72-78 wt.%, the weight ratio of TDMAH:SMP10 is 30:70, and assuming that Hf segregates as HfC in the obtained ceramics, the HfC content can be estimated to be 23-24 wt.%, and it agrees well with the experimentally determined HfC contents (*e.g.*, 24 wt.% HfC in SHC-1700). Consequently, the loss of Hf during polymer-to-ceramic transformation of the single-source precursor and during the high-temperature annealing of the ceramic materials is considered to be negligible. The mole ratio of Hf to Si is calculated to be 0.07 in both SHC-1100 and SHC-1700, and it does not change during annealing as well. Thus, the Hf and Si concentration in the SHC-1300, SHC-1400, SHC-1500 and SHC-1800 can be estimated using the constant mole ratio of Hf to Si (Table 3. 3).

As shown in Table 3. 3, the mass loss of the ceramics annealed at temperatures below 1400 °C is low, and the contents of C, N and O are only slightly changed. A relatively obvious mass loss occurred at 1500 °C due to the loss of N and O.[210] After the release of N and O, the mass loss increases marginally, even upon annealing for 5 h at 1800 °C. This result suggests a promising high-temperature stability of the synthesized SiHfC(N) ceramic nanocomposites.

Table 3. 3 Mass loss and chemical composition of ceramics annealed at different temperatures.

Sample	Processing temperature	Mass loss (wt.%)	Elemental analysis (wt.%)					Empirical formula
			Si	Hf	C	N	O	
SHC-1100	1100 °C	-	45.80	20.00	25.14	3.86	3.89	$SiHf_{0.07}C_{1.28}N_{0.17}O_{0.15}$
SHC-1300‡	1300 °C	0.92%	46.58	20.72	25.26	3.78	3.66	$SiHf_{0.07}C_{1.27}N_{0.16}O_{0.14}$
SHC-1400‡	1400 °C	2.31%	46.77	20.80	24.98	3.96	3.49	$SiHf_{0.07}C_{1.25}N_{0.17}O_{0.13}$
SHC-1500‡	1500 °C	11.1%	48.94	21.77	25.80	1.97	1.52	$SiHf_{0.07}C_{1.23}N_{0.08}O_{0.05}$
SHC-1700	1700 °C	14.23%	51.00	22.90	24.94	0.28	0.14	$SiHf_{0.07}C_{1.13}N_{0.01}$
SHC-1800‡	1800 °C	14.76%	51.84	23.06	24.89	0.13	0.08	$SiHf_{0.07}C_{1.12}N_{0.005}$

‡ - Hf and Si content calculated according a constant mole ratio of Hf/Si.

3.3.1.2 Phase composition and microstructural evolution

MAS NMR analysis

In order to investigate the temperature evolution of the SiHfC(N) ceramics, ^{29}Si and ^{13}C MAS NMR spectra of the ceramics prepared at 800 °C, 1100 °C and 1300 °C were measured and deconvoluted using Lorentz fitting. As shown in Figure 3. 20, there is a broad ^{29}Si resonance in the spectra of the ceramics pyrolyzed at 800, 1100, and 1300 °C, indicating the heterogeneous amorphous nature of the local environment around the Si atoms.[196, 211]

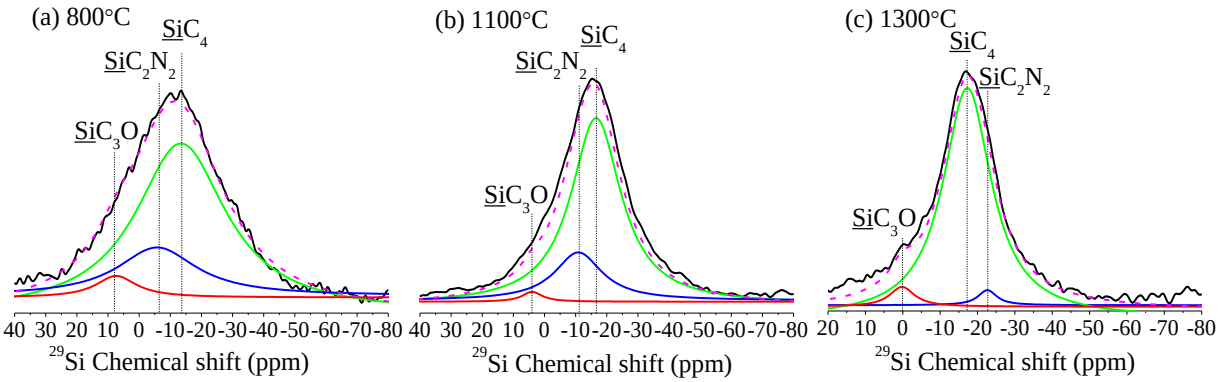

Figure 3. 20 ^{29}Si MAS NMR spectra of SiHfC(N) ceramics pyrolyzed at 800 °C *(a)*, 1100 °C *(b)* as well as annealed at 1300 °C *(c)*.

As aforementioned, the Hf atoms are connected to the polymeric backbone of the single-source precursor by Hf-N(CH_3)-Si units (Figure 3. 2). During the pyrolysis process, part of the nitrogen atoms at the Hf sites might be substituted by C atoms due to transamination processes.[192] Thus, in the ceramic pyrolyzed at 800 °C Hf atoms might be connected to the amorphous matrix by Hf-N and Hf-C bonds. This assumption is supported by the low-field shift of the ^{29}Si resonances of the $\underline{Si}C_2N_2$ and $\underline{Si}C_4$ sites (Figure 3. 15 and Figure 3. 20). It is known from literature that in SiCN samples obtained at 600 °C, the chemical shift of $\underline{Si}C_2N_2$ sites is ca. -7.5 ppm[209], while in our Hf-containing sample they exhibit a significant low-field shift to ca. 1.99 ppm. This is considered to rely on the presence of Hf in the proximity of the SiC_2N_2 sites. Analogous trends were also found in SiMOC materials (M = Zr[212], Hf[26]), in which the ^{29}Si chemical shifts SiO_4 sites were significantly low-field shifted due to the presence of Zr/Hf bonded to the SiO_4 tetrahedra. Also the resonances of $\underline{Si}C_2N_2$ and $\underline{Si}C_4$ sites (with chemical shifts of ca.-12 and -15 ppm, respectively)[209] are shifted to low field (*i.e.*, -5.73 and -13.43 ppm, respectively), due to the existence of Si-N-Hf and Si-C-Hf linkages.

As the heat-treatment temperatures increases (*e.g.*, to 1100 °C), HfC_xN_{1-x} starts to segregates [*i.e.*, phase separation of SiHfC(N) upon breaking of Si-N-Hf and Si-C-Hf linkages], which consequently leads to a high-field shift of the ^{29}Si resonances of the $\underline{Si}C_2N_2$ and $\underline{Si}C_4$ sites (Table 3. 2). The phase separation is not significant at 1100 °C, thus the $\underline{Si}C_2N_2$ sites are still significantly low-field shifted (-10.9 ppm) as compared to $\underline{Si}C_2N_2$ sites in Hf-free SiCN (-17 ppm). After annealing at 1300 °C, both $\underline{Si}C_2N_2$ (-22.6 ppm) and $\underline{Si}C_4$ sites (-17.3 ppm) show similar chemical shifts to those of Hf-free SiCN materials (see Table 3. 2).[213] The presence of small amounts of $\underline{Si}C_3O$ units (< 6%) in the investigated samples (Table

3. 2, Figure 3. 15 and Figure 3. 20) was explained as a consequence of some oxygen contamination during the processing of the single-source precursors.[210, 214]

The ^{13}C MAS NMR spectra in Figure 3. 21 show that the presence of segregated sp^2 carbon in the investigated materials is obvious. In Figure 3. 21a, the ^{13}C resonance at 138.07 ppm was assigned to sp^2 C-C with one or more Si nearest neighbors[215], indicating that the segregated carbon phase is connected to the SiHfC(N) matrix via C-Si bonds after pyrolysis at 800 °C. In the materials heat-treated at higher temperatures, two types of sp^2 carbon sites were found (Figure 3. 21b), namely one with a chemical shift of 164.10 ppm, which was assigned to nitrogen-containing sp^2 carbon, and a second resonance located at 127.49 ppm, which corresponds to turbostratic carbon (sp^2 C-C).[215, 216]

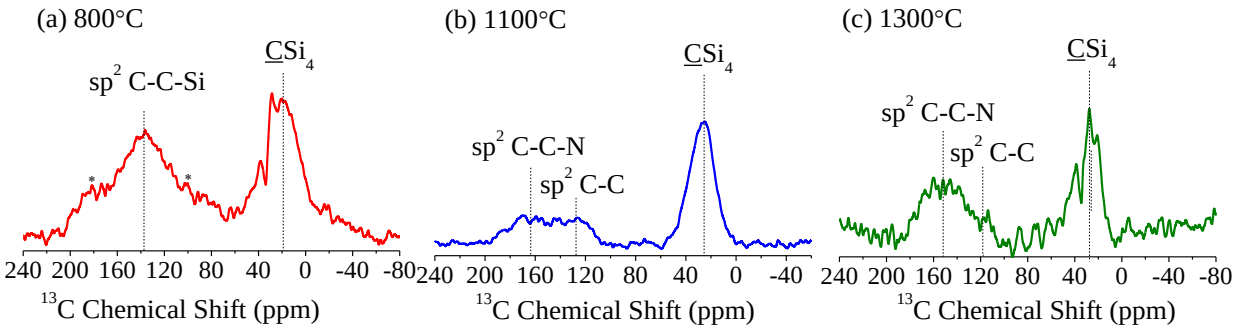

Figure 3. 21 ^{13}C MAS NMR spectra of ceramics prepared at 800 °C, 1100 °C and annealed at 1300 °C (the peaks denoted with asterisks are the spinning side bands).

After annealing at 1300 °C (Figure 3. 21c), the peak corresponding to the nitrogen-containing sp^2 carbon was found to shift to high-field (chemical shift at 151.44 ppm). Hence, from the NMR data it can be concluded that the ceramics pyrolyzed at 800 °C mainly comprise an amorphous SiHfC(N) single phase connected to carbon-rich domains, and that the phase separation of HfC_xN_{1-x} starts after pyrolysis at 1100 °C and is almost completed after annealing at 1300 °C.

X-ray diffraction patterns

In order to investigate the crystallization behavior of the SiHfC(N) ceramics, X-ray diffraction patterns (XRD) of the ceramic materials annealed at different temperatures were measured, and the results are shown in Figure 3. 22.

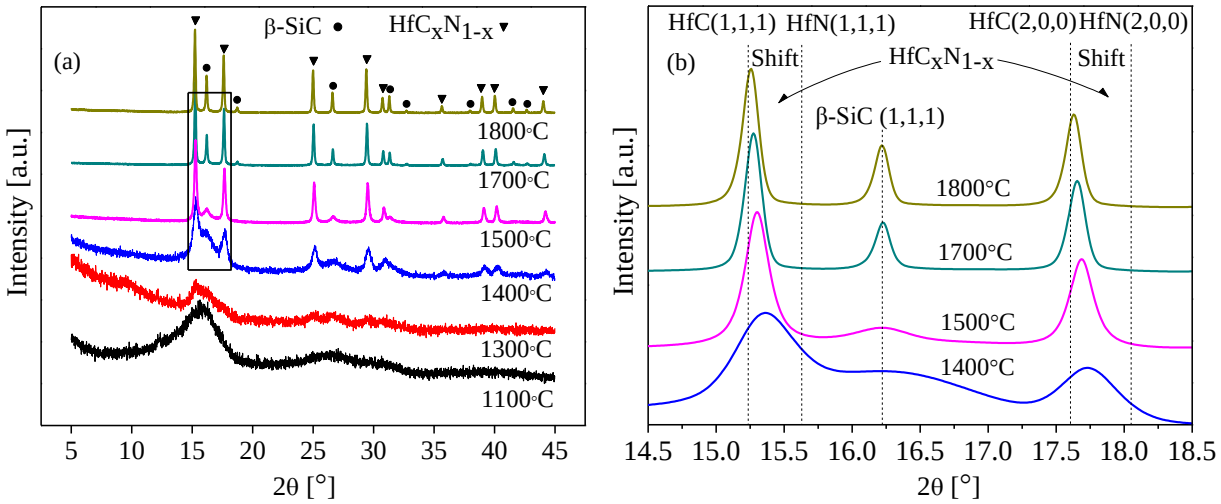

Figure 3. 22 (a) XRD patterns of the SiHfC(N) ceramics pyrolyzed and annealed at different temperatures. (b) the region in the rectangle is shown magnified.

Table 3. 4 Volume fractions, grain sizes and lattice parameters of HfC_xN_{1-x} and β-SiC as well as the estimated compositions of HfC_xN_{1-x} in the ceramics annealed at different temperatures.

Sample	Volume fraction (%)		Estimated grain size (nm)		Lattice Parameters, *a* (Å)		Estimated Composition
	HfC_xN_{1-x}	SiC	HfC_xN_{1-x}	SiC	HfC_xN_{1-x}	SiC	HfC_xN_{1-x}
SiHC-1400	1.71	98.29	5.61	1.63	4.6020	4.3445	$HfC_{0.68}N_{0.32}$
SiHC-1500	6.99	93.01	18.12	3.59	4.6132	4.3469	$HfC_{0.78}N_{0.22}$
SiHC-1700	11.01	88.99	45.11	33.41	4.6231	4.3519	$HfC_{0.87}N_{0.13}$
SiHC-1800	10.11	89.89	51.59	54.59	4.6309	4.3561	$HfC_{0.93}N_{0.07}$

XRD patterns reveal that the ceramic prepared at 1100 °C is mainly X-ray amorphous, while with increasing annealing temperatures, crystallization of both HfC_xN_{1-x} and β-SiC takes place. Interestingly, the Hf-containing phase was found to contain some amount of nitrogen (*i.e.*, HfC_xN_{1-x}). According to Hume-Rothery rules, cubic HfC and HfN are able to form complete quasi-binary solid solutions, as both of them are interstitial compound having Fcc structure, and the covalent radii of the C and N atoms differ by only 2.60 %.[217, 218] The volume fractions, grain sizes and lattice parameters of HfC_xN_{1-x} and β-SiC obtained by Full-Profile Rietveld refinement of the XRD patterns of the investigated samples, are listed in Table 3. 4.

As shown in Figure 3. 22b, the reflections of the HfC_xN_{1-x} phase shift towards low 2θ values upon increasing the annealing temperature, *i.e.*, the HfC_xN_{1-x} phase becomes enriched in carbon. As previously reported, the lattice parameter of HfC_xN_{1-x} is a linear function of its chemical composition, which obeys Vegard's law.[218, 219] Thus, the observed shift of the XRD reflections in Figure 3. 22b (as for the (111) and (200) reflections) was used to estimate the chemical composition of the HfC_xN_{1-x} phase in the ceramics prepared at different temperatures (Table 3. 4).[220] The composition of the HfC_xN_{1-x} phase can be estimated also from the chemical composition of the samples. For the sample SiHC-1700 (with the

chemical composition $SiC_{1.13}Hf_{0.07}N_{0.01}$), the composition of the HfC_xN_{1-x} phase is $HfC_{0.86}N_{0.14}$ and agrees very well with the composition estimated by the Vegard's law from the XRD pattern ($HfC_{0.87}N_{0.13}$,Table 3. 4).

Raman spectra

The Raman spectra of the ceramics pyrolyzed at 1100 ºC and annealed at different temperatures are shown in Figure 3. 23. It reveals the presence of segregated carbon at all temperatures.

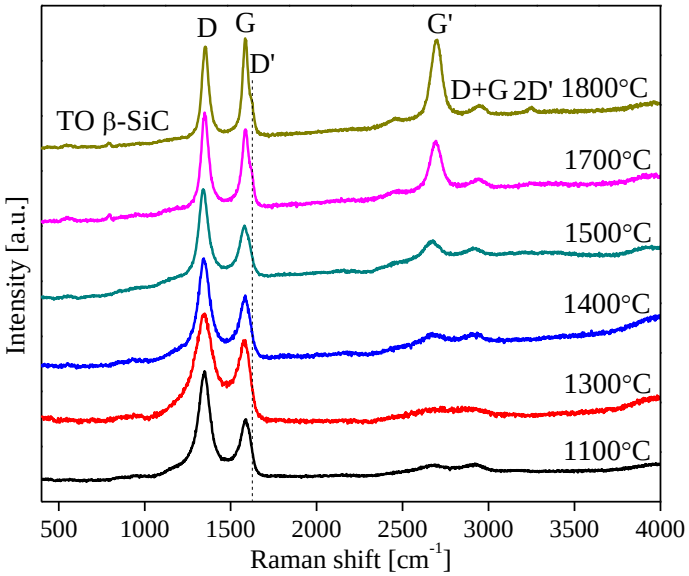

Figure 3. 23 Raman spectra of SiHfC(N) ceramics annealed at different temperatures.

In the Raman spectra of SiHfC(N) ceramics, the bands at 1350 cm^{-1} and 1620 cm^{-1} are assigned to the defect-induced D band and D' band, respectively, and the band at 1582 cm^{-1} are assigned to the G mode, representing the stretching vibrations of sp^2 carbon in the basal-plane of graphite.[221] The G' band at 2700 cm^{-1} is overtone of the D band, which is usually observed in defect-free graphite samples. The band appearing at 796 cm^{-1} after annealing at temperatures higher than 1500 °C is the transverse optical (TO) phonon mode of β-SiC.[222] At temperatures lower than 1300 °C, the D and G bands are broad and overlapped due to the high disorder of the segregated carbon phase.[223] With the increasing annealing temperature from 1400 ºC to 1800 ºC , the D and G bands become sharper, and the intensity of G' bands grows gradually indicating that the ordering of the segregated carbon phase increases. However, the high intensity of the D band in all recorded spectra indicates in all samples that the carbon phase should be considered as being highly disordered / turbostratic in its nature.

TEM characterization

The synthesized SiHfC(N) ceramics annealed at different temperatures ranging from 1100 to 1700°C were further studied by means of TEM in order to assess the evolution of their phase composition and

microstructure at high temperatures (Figure 3. 24 and Figure 3. 25).

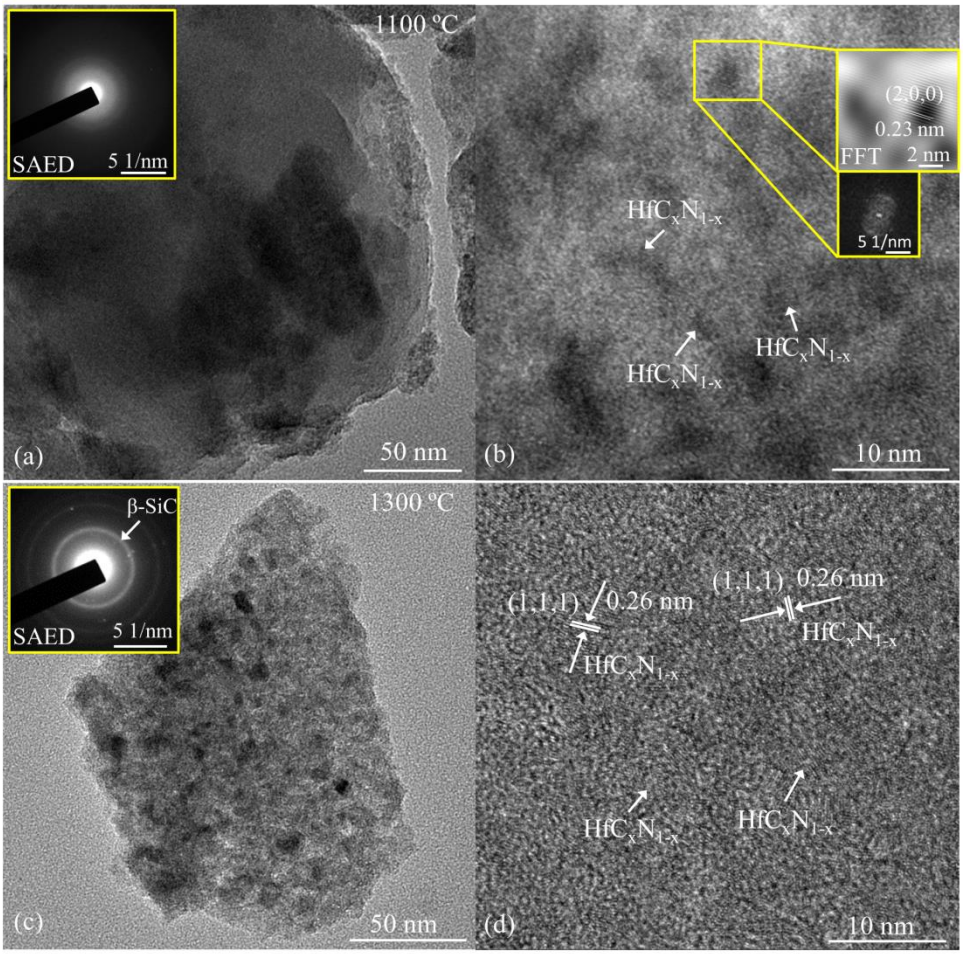

Figure 3. 24 TEM images of SHC-1100 (*a* and *b*) and SHC-1300 (*c* and *d*).

In Figure 3. 24a, the ceramic prepared at 1100 °C is amorphous, as revealed by the featureless selected area electron diffraction (SAED) patterns. However, contrast variations indicate that the phase segregation of HfC_xN_{1-x} occurred, as shown in the high-resolution micrograph in Figure 3. 24b, which shows small nuclei of HfC_xN_{1-x} with diameter less than 2 nm dispersed homogeneously throughout the matrix. After annealing at 1300 °C, HfC_xN_{1-x} precipitations (dark contrast) with an average particle size of ca. 2.5 nm were found to be homogeneously dispersed within a silicon carbide matrix (Figure 3. 24, c and d). In the high-resolution micrograph lattice fringes of the poorly crystallized HfC_xN_{1-x} nanoparticles can be observed. Although no β-SiC crystallites were visualized, the SAED pattern clearly indicates the crystallization of β-SiC and thus agrees with the XRD results.

The TEM micrographs of the ceramics annealed at 1400 and 1700 °C are shown in Figure 3. 25 and show the presence of HfC_xN_{1-x} embedded within a β-SiC matrix, as shown also by EDS analysis. After annealing at 1700 °C, β-SiC crystallites can be identified (see Figure 3. 25d). Interestingly, the sample annealed at 1400 °C is characterized by a unique microstructure. As depicted in Figure 3. 25a, the HfC_xN_{1-x} nanoparticles are encapsulated within a layer of carbon (thickness ca. of 2-4 nm) forming a

HfC_xN_{1-x}-carbon core shell microstructure. Moreover, the thickness of the carbon shell (CS) was found to increase from 1400 to 1700 °C. The high-resolution image (Figure 3. 25b) as well as Raman spectroscopy data (shown in Figure 3. 23) indicate that the encapsulating carbon phase has a rather highly disordered / turbostratic nature.[224]

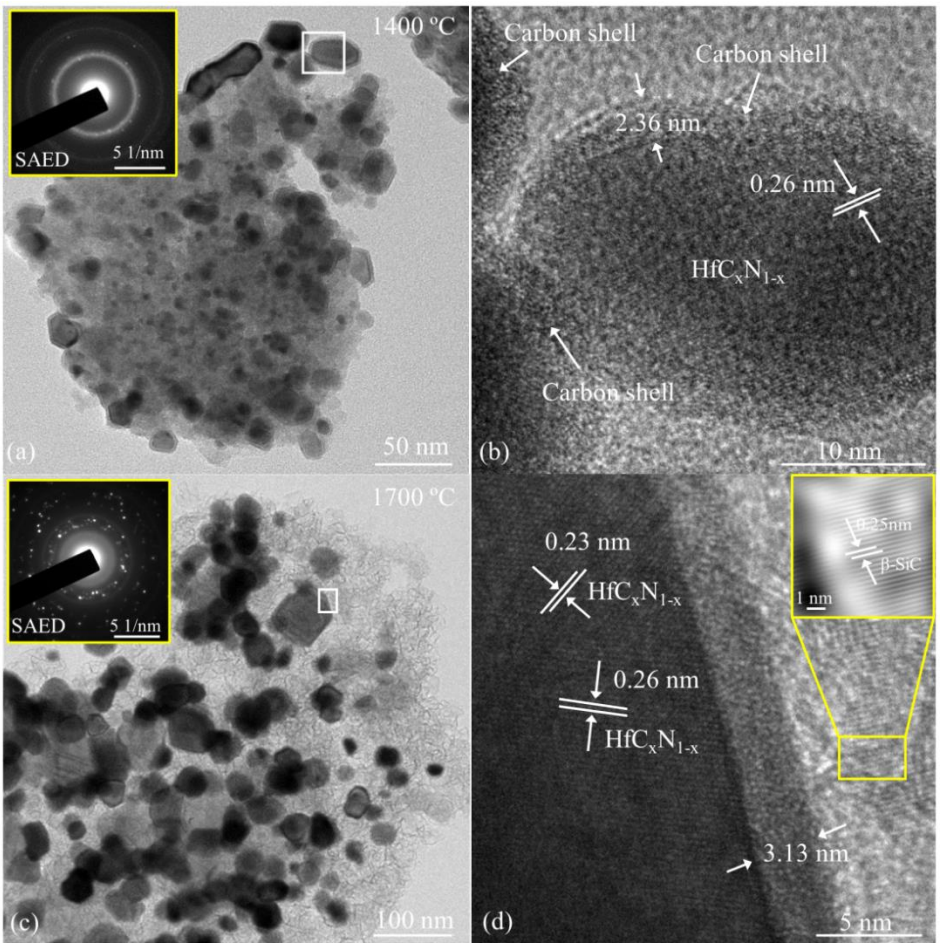

Figure 3. 25 TEM micrographs of SHC-1400 (*a* and *b* - *b* is a high-resolution image magnified from the white rectangular area in *a*) and SHC-1700 (*c* and *d* - *d* is a high-resolution image magnified from the white rectangular area in *c*).

Based on previous research reports, metal nanoparticles such as Fe encapsulated by carbon shell have been developed. The carbon shell is shown to act a diffusion barrier and thus to prevent the growth of the nanoparticles.[225, 226] In the present study, the HfC_xN_{1-x} particles are embedded in a 2-4 nm thick carbon shell, which effectively inhibits their coarsening even at very high temperatures. As can be taken from the TEM images, the average particle size of HfC_xN_{1-x} annealed at 1400 °C and 1700 °C amounts 8 and 37 nm, respectively. Thus, the HfC_xN_{1-x} precipitations do not increase significantly in size upon increasing the annealing the temperature. The average size of both HfC_xN_{1-x} and β-SiC was found to be less than 55 nm even after annealing at 1800 °C (Table 3. 4). This type of microstructure has also been reported in B_4C/SiC and SiC/Fe/C ceramic nanocomposites as well as ZrC-containing C/C composites.[39, 224, 227]

However, the mechanism of its formation is not clear yet.

3.3.2 Boron-doped SiHfC(N) ceramics nanocomposites

3.3.2.1 Chemical composition

After pyrolysis of 30Hf-B-SMP10 precursors at 1000 °C in argon atmosphere, the boron-doped SiHfC(N) ceramics was obtained (denoted as SHBC-1000°C). The as-synthesized ceramic was subsequently ground (150-mesh) and annealed in argon atmosphere at 1300, 1500, 1700 and 1900 °C for 5 h, respectively, in order to investigate its high-temperature behavior with respect to decomposition and phase separation as well as crystallization. The mass loss, chemical composition and empirical formula of the ceramics are list in Table 3. 5.

Table 3. 5 Mass loss and chemical composition of the boron-doped SiHfC(N) ceramics annealed at different temperatures.

Sample	Mass loss (wt.%)*	Elemental analysis (wt.%)						Empirical formula
		Si	Hf	C	N	B	O	
SHBC-1000°C	---	46.6	13.7	30.01	1.45	0.50	4.11	$SiHf_{0.05}B_{0.03}C_{1.51}N_{0.06}O_{0.15}$
SHBC-1300°C[a]	1.50	50.27	14.78	29.84	1.87	0.54	3.52	$SiHf_{0.05}B_{0.03}C_{1.41}N_{0.07}O_{0.12}$
SHBC-1500°C[a]	8.84	52.31	15.38	29.04	1.31	0.56	1.40	$SiHf_{0.05}B_{0.03}C_{1.30}N_{0.05}O_{0.05}$
SHBC-1700°C[a]	10.93	52.78	15.52	30.07	0.60	0.57	0.47	$SiHf_{0.05}B_{0.03}C_{1.33}N_{0.02}O_{0.02}$
SHBC-1900°C[a]	13.43	53.61	15.76	29.91	0.11	0.58	0.04	$SiHf_{0.05}B_{0.03}C_{1.30}$

* - mass loss with respect to the as-pyrolyzed ceramic (*i.e.*, SHBC-1000°C); [a] - Hf, Si and B content are estimated according a constant atomic ratio of Si/Hf/B.

Similar to previously reported SiHfC(N) ceramics (boron free)[94], a relatively obvious mass loss of the boron-doped SiHfC(N) occurred at 1500 °C due to carbothermal reduction with the release of N and O.[210] But the release of N is lower than that of the SiHfC(N) whose N content reduced by ≈ 50 wt.% after annealing at 1500 ºC and by 90 wt.% at 1700 ºC. That is the reason why the mass loss of boron-doped SiHfC(N) ceramics is less than that of the SiHfC(N) ceramics during annealing, suggesting improved thermal stability. After release of N and O, the mass loss increased marginally, even upon annealing at 1900 °C for 5 h in argon, indicating promising high-temperature stability.[94] The B and Hf content within the SHBC-1700 ºC sample is measured to be 0.57 wt.% and 15.30 wt.%, respectively, using ICP-AES, which is almost the same as the estimated value in Table 3. 5. That means no B and Hf loss during annealing, and variation of the mole ratio of Si/Hf/B is negligible.

3.3.2.2 Phase composition and microstructural evolution

X-ray diffraction patterns

XRD patterns of the boron-doped SiHfC(N) ceramics (denoted as SHBC-) are presented in Figure 3. 26. The information for SiHfC(N) ceramics (boron free, denoted as SHC-) is also provided for the sake of comparison. After pyrolysis at 1000 ºC, the SHBC-1000°C sample is X-ray amorphous. After annealing

at temperatures from 1300 to 1700°C, crystallization of β-SiC and HfC_xN_{1-x} is observed, but the crystallization of hexagonal HfB_2 [P6/mmm, a=3.1443(7), c=3.4843(2)] can be detected only after annealing at 1900°C. The average grain size, lattice parameters and weight fraction of crystallized HfC_xN_{1-x}, β-SiC and HfB_2 were determined by Rietveld refinement using the FullProf software (see Table 3. 6). The peak shapes were modeled using the Thompson-Cox-Hastings pseudo-Voigt function for average grain size and the pseudo-Voigt function for lattice parameters and weight fraction.[228]

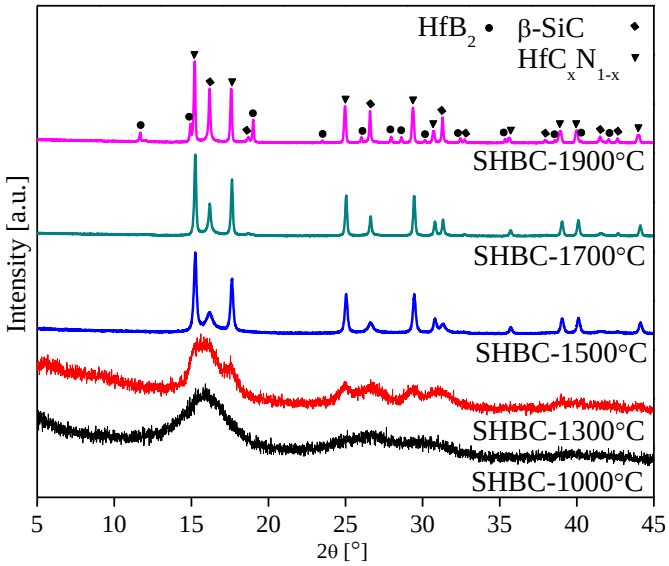

Figure 3. 26 XRD patterns of the boron-doped SiHfC(N) ceramics pyrolyzed and annealed at different temperatures.

Table 3. 6 Average grain size, lattice parameters, weight fractions of HfC_xN_{1-x} and β-SiC as well as the chemical composition of the crystallized HfC_xN_{1-x} within the boron-doped SiHfC(N) and SiHfC(N) ceramics.

Name	Average Grain Size (nm)			Lattice Parameter a (Å)		Weight Fraction (wt.%)		Chemical composition
	HfC_xN_{1-x}	HfB_2	β-SiC	HfC_xN_{1-x}	β-SiC	HfC_xN_{1-x}	HfB_2	HfC_xN_{1-x}
SHBC-1500°C	18.9	---	4.3	4.6250(4)	4.3549(6)	17.66	---	$HfC_{0.89}N_{0.11}$
SHBC-1700°C	42.9	---	15.6	4.6274(7)	4.3576(6)	21.36	---	$HfC_{0.91}N_{0.09}$
SHBC-1900°C	62.1	128.5	39.4	4.6323(2)	4.3532(6)	15.39	4.60	$HfC_{0.95}N_{0.05}$
SHC-1500°C	12.3	---	4.2	4.6211(7)	4.3526(4)	16.44	---	$HfC_{0.85}N_{0.15}$
SHC-1700°C	51.4	---	53.8	4.6265(6)	4.3564(8)	23.25	---	$HfC_{0.90}N_{0.10}$
SHC-1900°C	94.8	---	61.8	4.6330(8)	4.3543(2)	22.23	---	$HfC_{0.96}N_{0.04}$

As previously reported[94, 101], the reflections of the Hf-containing phase show slightly higher 2θ values than those of the stoichiometric cubic HfC phase, which indicates that the Hf-containing phase is a solid solution of cubic HfC and HfN (*i.e.*, HfC_xN_{1-x}). The observed shift of the XRD reflections in Figure 3. 26 [as for the (111) and (200) reflections] can be used to estimate the chemical composition of the HfC_xN_{1-x}

phase within the obtained ceramics via the lattice parameters according to Vegard's law (see Table 3. 6).[218, 219] The average grain size of the HfC_xN_{1-x} and β-SiC phase within the boron-doped SiHfC(N) annealed at temperatures ≤ 1900 ºC is less than 100 nm. Thus, it is possible to prepare SiC/HfC_xN_{1-x}/HfB_2/C ceramic nanocomposites upon annealing of the amorphous boron-doped SiHfC(N) ceramics (*i.e.*, SHC-1000ºC). Interestingly, compared with the SiHfC(N) ceramics without boron, the coarsening of β-SiC phase during annealing seems to be highly suppressed by boron, which is similar to previously reported polymer derived SiHfBCN ceramics.[25]

Raman spectra

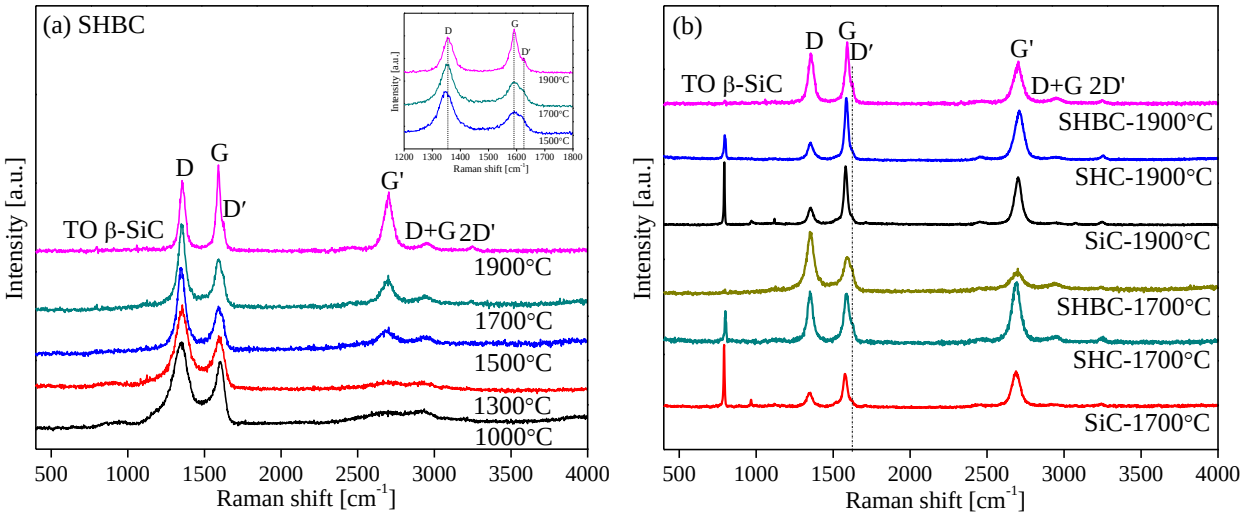

Figure 3. 27 Raman spectra of boron-doped SiHfC(N) ceramics annealed at different temperatures *(a)* as well as SiC and SiHfC(N) ceramics annealed at 1700 and 1900 ºC *(b)*.

Raman spectra (exciting laser wavelength: 514.5 nm) of the boron-doped SiHfC(N) ceramics pyrolyzed at 1000 °C and annealed at 1300-1900 °C are shown in Figure 3. 27a. Two characteristic peaks at ~1350 cm^{-1} (D band) and ~ 1580 cm^{-1} (G band) reveal the presence of segregated carbon at all temperatures.[221] The high intensity of the D band in the recorded spectra of the samples annealed at temperatures lower than 1900 °C indicates that the segregated carbon phase should be highly disordered in its nature. Compared with the SiHfC(N) ceramics without boron (Figure 3. 27b), the intensity of G and G' bands grow slowly even after annealing at 1700 °C, implying the slow graphitization process of segregated carbon within the boron-doped SiHfC(N) ceramics.[101] This is because the boron gets incorporated into the segregated carbon, which therefore highly suppresses the graphitization process.[203] Moreover, the intensity of defect-induced D' band (≈ 1620 cm^{-1}) on the spectra of SHBC-1500ºC, SHBC-1700ºC and SHBC-1900°C is significantly higher than that on the spectra of the SiC sample derived from pure SMP10 (Figure 3. 27b), which is directly correlated with the local structural distortion of the segregated carbon (d_{002} spacing) induced by N or B incorporation[203, 229-231], whereas the incorporation of N cannot be ruled out because the D' band is also relatively strong on the spectrum of SHC-1700°C. That means

the segregated carbon within the boron-doped SiHfC(N) ceramics might be incorporated by both B and N.

After annealing at 1900°C, the D and G bands on the spectrum of SHBC-1900°C (Figure 3. 27a) show a smaller line-width, and the intensities of the G and G' bands grow obviously, indicating remarkable graphitization (increasing structural ordering) of segregated carbon. The reduced intensity of the D' band can be observed as well. One reason is that after annealing at 1900 °C, part of the incorporated boron and nitrogen converted into HfB_2 and N_2, respectively, through a carbothermal reduction between HfC_xN_{1-x} and the boron and nitrogen containing segregated carbon[25], which can be proved by the newly apparent XRD peaks of HfB_2 (Figure 3. 26) and highly reduced nitrogen content (decreased by 80 wt.% with respect to the N content in the SHBC-1700ºC, Table 3. 5). However, compared with the SHC-1900ºC and SiC-1900ºC, the intensities of the D and D' bands on the spectrum of SHBC-1900ºC are still higher. This result indicates that part of the boron and nitrogen is still incorporated in the segregated carbon within the SHBC-1900ºC. The elemental analysis of the boron-doped SiHfC(N) shows that the atomic ratio of B to Hf is ≈ 0.60 (Table 3. 5). From the weight fraction of crystallized HfC_xN_{1-x} and HfB_2, that the atomic ratio of B to Hf is estimated within the crystallized phase to be ≈ 0.44 (Table 3. 5). That means part of the boron is still in the segregated carbon of the SHBC-1900ºC. The rest of the boron within segregated carbon will lead to more HfB_2 precipitations upon further high-temperature annealing of the nanocomposites.

The band appearing at 796 cm^{-1} after annealing at temperatures higher than 1500 °C is the transverse optical (TO) phonon mode of β-SiC.[222] At the same annealing temperature, the intensity of this signal varies in the order SiC>SHC>SHBC, indicating reduced crystallization degree of β-SiC in the boron-doped SiHfC(N), which is consistent with the XRD results (Figure 3. 26 and Table 3. 6).

TEM characterization

Figure 3. 28 are TEM images of the boron-doped SiHfC(N) ceramics annealed at 1700 °C for 5 h (*i.e.*, SHBC-1700°C). The SAED patterns reveal the existence of HfC_xN_{1-x} and β-SiC phase, which possesses dark and light contrast, respectively. Similar to the XRD patterns of the SHBC-1700°C, no signals for HfB_2 can be observed on the SAED patterns. Previously reported TEM images of the SiHfC(N) ceramics without boron reveal a unique microstructure, *i.e.*, the HfC_xN_{1-x} nano grains encapsulated by an amorphous carbon shell (core-shell structure) embedded homogeneously within the β-SiC matrix (Figure 3. 25).[94, 101] This unique microstructure can also be observed in the boron-doped SiHfC(N) ceramics. That means the doping of boron does not affect the formation of the core-shell structure. Two kinds of segregated carbon phase (carbon shell and carbon ribbon) within the β-SiC matrix can be observed as well (see inset in Figure 3. 28b). The carbon ribbons show much higher ordering than carbon shells, which is similar to the SiHfC(N) ceramics.[101] As calculated from Figure 3. 28a, except for a few large HfC_xN_{1-x} grains, the average grain size of HfC_xN_{1-x} within the SHBC-1700°C is around 40 nm, which is

consistent with the value (≈ 43 nm) estimated using Rietveld refinement (Table 3. 6).

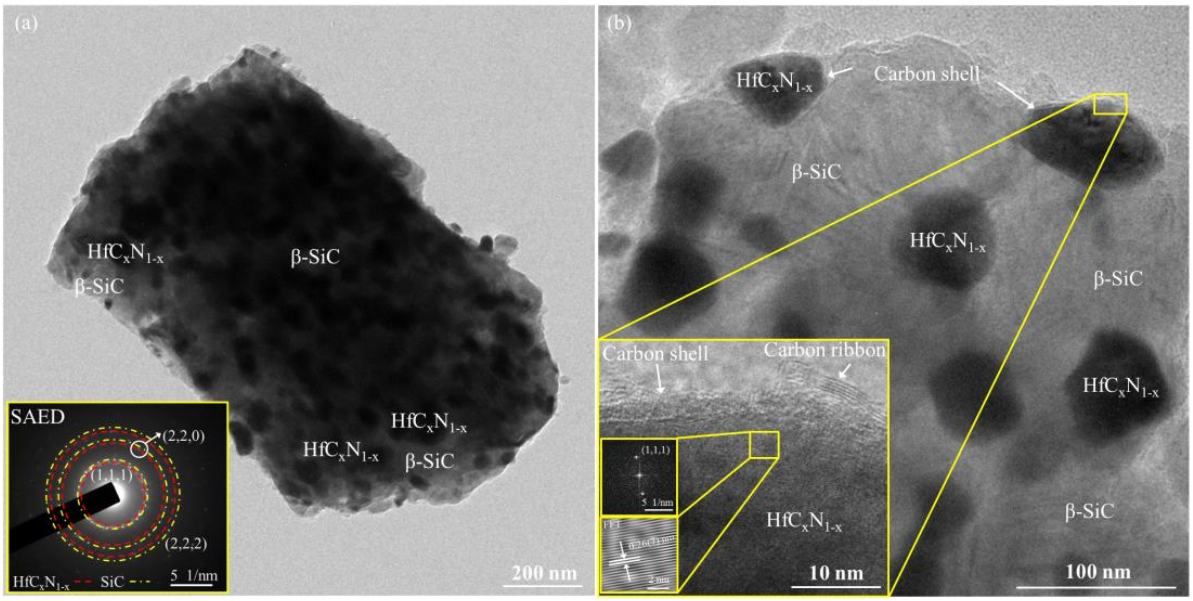

Figure 3. 28 TEM images (bright field) of boron-doped SiHfC(N) ceramics annealed at 1700 ºC for 5h.

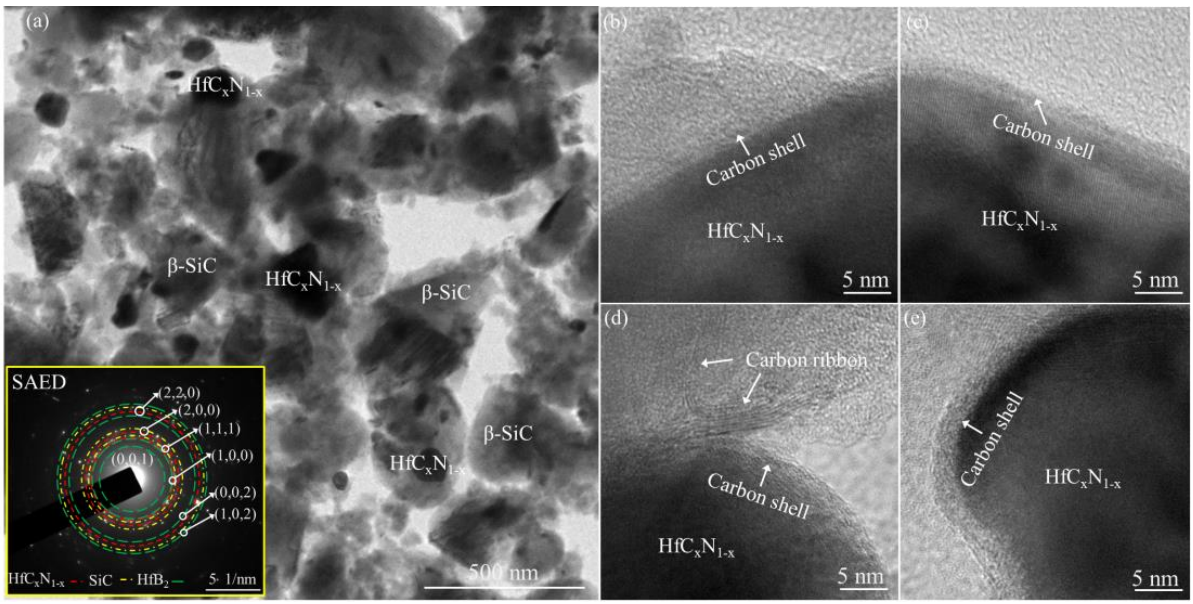

Figure 3. 29 TEM images (bright field) of boron-doped SiHfC(N) ceramics annealed at 1900°C for 5h.

TEM images of boron-doped SiHfC(N) ceramics annealed at 1900 °C for 5 h (SHBC-1900ºC) are shown in Figure 3. 29. The dark and light contrast is HfC_xN_{1-x} and β-SiC, respectively. Although no HfB_2 crystallites are visualized, the SAED patterns clearly indicate the crystallization of HfB_2 and thus agree with the XRD results (Figure 3. 26). The carbon shell on the surface of HfC_xN_{1-x} grains is still disordered (Figure 3. 29, b-e), which agrees with the relatively high intensity of D and D' on the spectrum of SHBC-1900°C. The disordered carbon shell highly suppressed the coarsening of HfC_xN_{1-x} grains, which exhibit the average diameter less than 100 nm even after annealing at 1900 °C for 5 h (Table 3. 6 and Figure 3.

29a).[94]

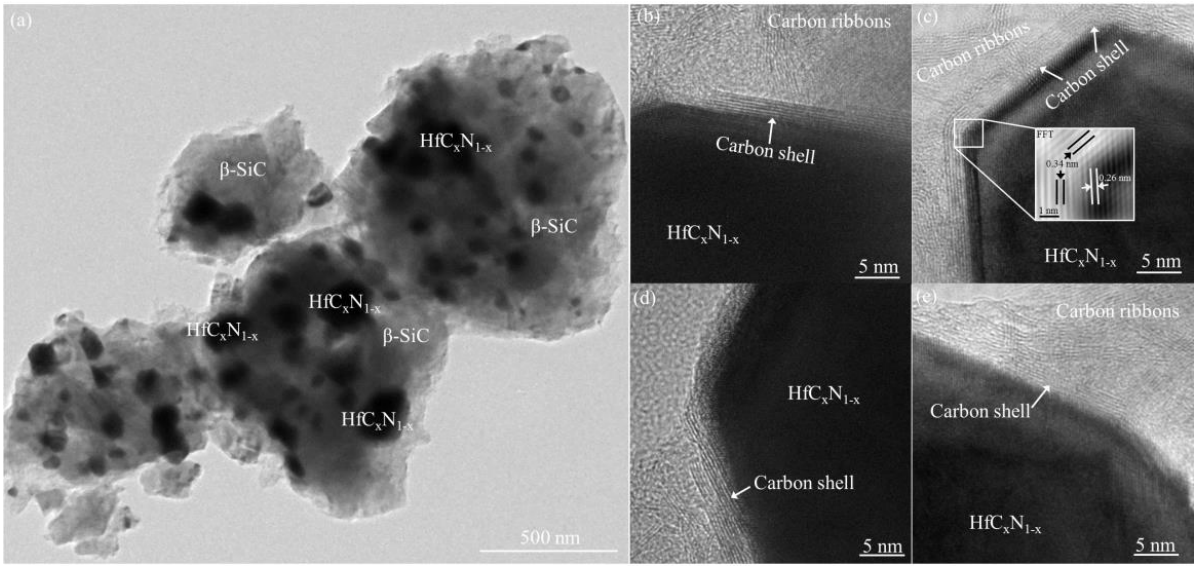

Figure 3. 30 TEM images (bright field) of SiHfC(N) ceramics annealed at 1900 °C for 5 h.

For comparison, TEM images of the SiHfC(N) ceramics (boron free) annealed at 1900 ºC for 5 h are shown in Figure 3. 30. Similarly, the dark contrast is HfC_xN_{1-x}, which homogeneously disperses within the β-SiC matrix. The carbon shell and carbon ribbons can be observed as well. It is interesting that the ordering of the carbon shell is highly improved, and thus some graphene-like layers can be observed on the surface of HfC_xN_{1-x} grains (Figure 3. 30, b-e), which is totally different from SHBC-1900ºC. This agrees with the highly increased G band and significantly reduced D band on the Raman spectrum of SHC-1900ºC. Moreover, the disappeared D' band indicates that the incorporated nitrogen was removed substantially by carbothermal reduction at 1900 ºC, which is consistent with the measured nitrogen content of SHC-1900ºC (≈ 0 wt.%). Compared with the carbon shell within the SiHfC(N) ceramics annealed at 1400 and 1700 ºC (Figure 3. 25) and the nitrogen content, it can be confirmed that the disordering of the carbon shell within the SiHfC(N) ceramics should be due to the incorporation of nitrogen. For the boron-doped SiHfC(N) ceramics, in addition to nitrogen, boron also incorporates into the carbon shell, which suppresses the ordering of carbon shell, even after annealing at 1900 ºC.

MAS NMR analysis of boron evolution

As discussed above, boron was incorporated into the SiHfC(N) ceramics by a hydroboration reaction between the B-H groups of BMS and the Allyl groups of SMP10. The boron is mainly in the $\underline{B}CN_2$ sites within the 30Hf-B-SMP10 precursor. After pyrolysis and annealing, the Raman spectra, XRD patterns and TEM images imply that, at the beginning, the boron probably located within the segregated carbon phase (particularly in the carbon shell) and then convert into HfB_2. The conversion of boron can be further confirmed using MAS NMR.

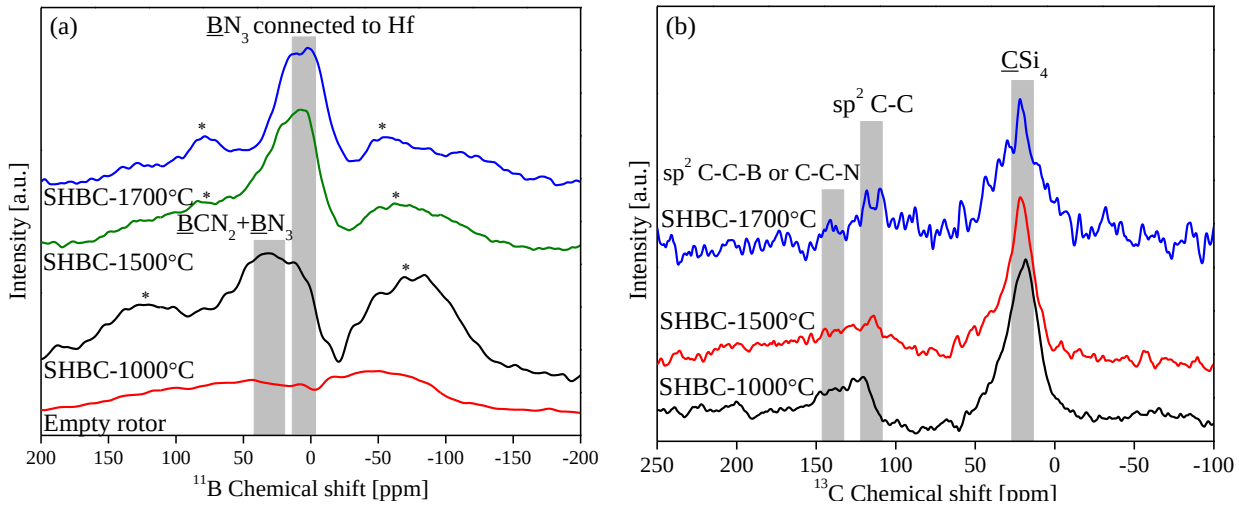

Figure 3. 31 MAS NMR spectra of boron-doped SiHfC(N) ceramics pyrolyzed at 1000 ºC as well as annealed 1500 ºC and 1700 ºC: *(a)* ^{11}B spectra (* are the side bands); *(b)* ^{13}C spectra.

As shown in Figure 3. 31a, the ^{11}B MAS NMR spectrum of SHBC-1000ºC shows one broad resonance with a chemical shift centered at 30 ppm, representing a boron atom bonded to three nitrogen atoms forming $\underline{B}N_3$ planar triangles as in hexagonal BN.[232] That means the $\underline{B}CN_2$ sites transformed into $\underline{B}N_3$ sites by rearrangement during pyrolysis. But the broad linewidth of the resonance suggests that part of $\underline{B}N_2C$ sites still exist. In Figure 3. 31b, the ^{13}C spectrum of SHBC-1000ºC proves that part of segregated carbon is connected to nitrogen or boron, forming a low-field shift of resonances at 140-150 ppm.[216] Thus, the boron incorporated segregated carbon always contain some nitrogen, and it can be approximated as a BC_yN_z phase (or domains) with mixed B-N and B-C bonds.[203] It is interesting that after annealing at 1500 and 1700 ºC, the ^{11}B resonances of the BC_yN_z phase exhibit high-field shift, and the resonances center at ≈ 11 and ≈ 7 ppm, respectively. The high-field shift might be due to the proximity of Hf atoms, which lead to the increase of electron density on the B atoms. That means a part of BC_yN_z phase (or domains) is in the carbon shell, which agrees well with the Raman spectra and TEM results discussed above. Moreover, the narrowed line width of the ^{11}B resonances at 1500 and 1700 ºC suggest that B-N bonds should be the main chemical bonds within the BC_yN_z phase (or domains). The incorporation of boron and nitrogen into the carbon shell makes it possible to connect the nitrogen-rich BC_yN_z phase (or domains) to the HfC_xN_{1-x} core, facilitating the formation of HfB_2.

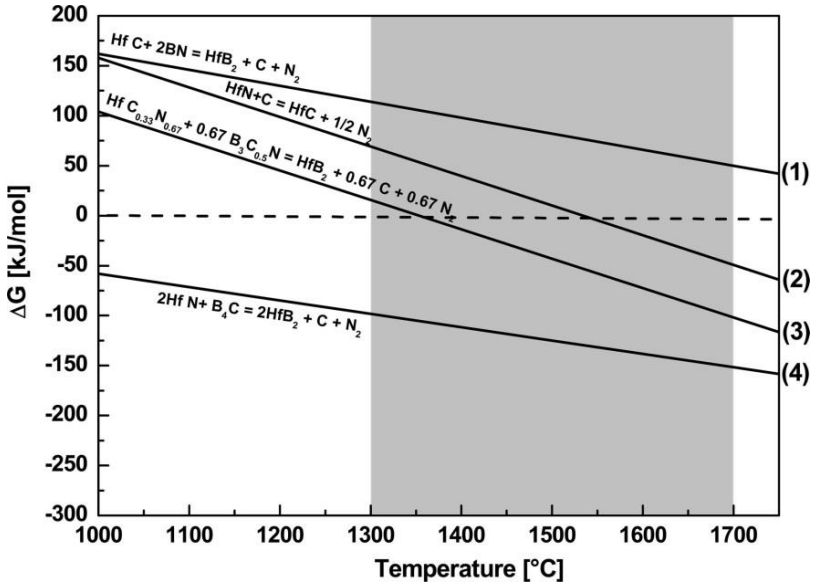

Figure 3. 32 Temperature dependence of the change in the Gibbs free energy (Ellingham diagram) of different possible reactions between BC_yN_z and HfC_xN_{1-x} phases during high-temperature annealing (data were taken from Ref.[233]). The ΔG value for reaction (3) in the figure was estimated upon combining reactions (1) and (4) in the figure [cf. (3) = 0.67(1) + 0.33(4)]. The gray shaded area indicates the temperature range of the high-temperature annealing experiments. Reprinted with permission from Ref.[25]

According to the Ellingham diagram of the reaction between the BC_yN_z and nitrogen-rich HfC_xN_{1-x} phase [reaction (3) in Figure 3. 32][25], the Gibbs free energy is < 0 when the annealing temperature is higher than 1400 ºC. However, the generation of HfB_2 by reaction between stoichiometric HfC and h-BN is favorable only at temperatures > 1700 ºC; see reaction (1) in Figure 3. 32. In the present system, the *x* value of the HfC_xN_{1-x} phase is higher than 0.85 (Table 3. 6), which is a carbon-rich HfC_xN_{1-x} phase similar to the stoichiometric HfC. Thus, the HfB_2 was detected only in the samples annealed at 1900 °C. Therefore, the high-temperature conversion of boron from segregated carbon into HfB_2 within the boron-doped SiHfC(N) ceramics is thermodynamically controlled, which allows for the preparation of $SiC/HfC_xN_{1-x}/HfB_2/C$ ceramic nanocomposites with tailored phase compositions.

3.3.3 SiTaC(N) ceramic nanocomposites

3.3.3.1 Chemical composition

After pyrolysis of the 30Ta-SMP10_80 at 1100 °C in argon atmosphere, a black SiTaC(N) ceramic was obtained (denoted as STC-1100ºC). The as-pyrolyzed ceramic was subsequently annealed in argon atmosphere at 1300, 1400, 1500, 1700 and 1900 °C in order to investigate its high-temperature behavior with respect to decomposition, phase separation as well as crystallization. After annealing at different temperatures, the relative mass loss with respect to the sample STC-1100ºC and the elemental contents of Si, Ta, C, N and O in the obtained ceramic materials were analyzed, and the results are list in Table 3. 7. The N and O contents reduced obviously due to the carbothermal decomposition at temperatures higher

than 1500 ºC, which is the main reason of the mass loss. Elemental analysis of Si and Ta contents of the STC-1100ºC and STC-1900ºC indicate that the mole ratio of Si/Ta does not change (near to 0.055). Therefore, the Si and Ta contents within the ceramics annealed at 1300, 1500 and 1700 ºC can be estimated according to the constant Si/Ta ratio (*i.e.*, 0.055).[101] After release of N and O, the mass loss increases marginally even after annealing at 1900 °C for 5 h. This result suggests a promising high-temperature stability of the as-synthesized SiTaC(N) ceramic nanocomposites.

Table 3. 7 Mass loss, chemical composition and empirical formula of the SiTaC(N) ceramics annealed at different temperatures.

Sample	Processing Temp.	Mass loss (wt.%)	Elemental analysis (wt.%)					Empirical formula
			Si	Ta	C	N	O	
STC-1100ºC	1100 °C	---	45.95	16.90	27.54	4.33	3.74	$SiTa_{0.055}C_{1.40}N_{0.19}O_{0.14}$
STC-1300ºC*	1300 °C	2.48	46.44	16.46	28.24	4.59	3.89	$SiTa_{0.055}C_{1.41}N_{0.20}O_{0.15}$
STC-1500ºC*	1500 °C	11.26	48.57	17.21	29.80	2.37	2.05	$SiTa_{0.055}C_{1.43}N_{0.10}O_{0.07}$
STC-1700ºC*	1700 °C	14.36	51.40	18.22	29.81	0.15	0.42	$SiTa_{0.055}C_{1.36}N_{0.01}O_{0.01}$
STC-1900ºC	1900 °C	15.82	52.45	18.05	30.62	0	0.27	$SiTa_{0.055}C_{1.37}O_{0.01}$

***** - Si and Ta estimated according to a constant mole ratio of Si/Ta.

3.3.3.2 Phase composition and microstructural evolution

MAS NMR analysis

In order to investigate the high-temperature evolution of the as-prepared SiTaC(N) ceramics, ^{29}Si and ^{13}C MAS NMR spectra of the ceramics prepared at 1100 °C and 1500 °C were measured, and the results are shown in Figure 3. 33. As shown in Figure 3. 33a, there is a broad ^{29}Si resonance in the spectra of the ceramics pyrolyzed at 1100 °C, indicating the heterogeneous amorphous nature of the local environment around the Si atoms.[94, 196, 211]

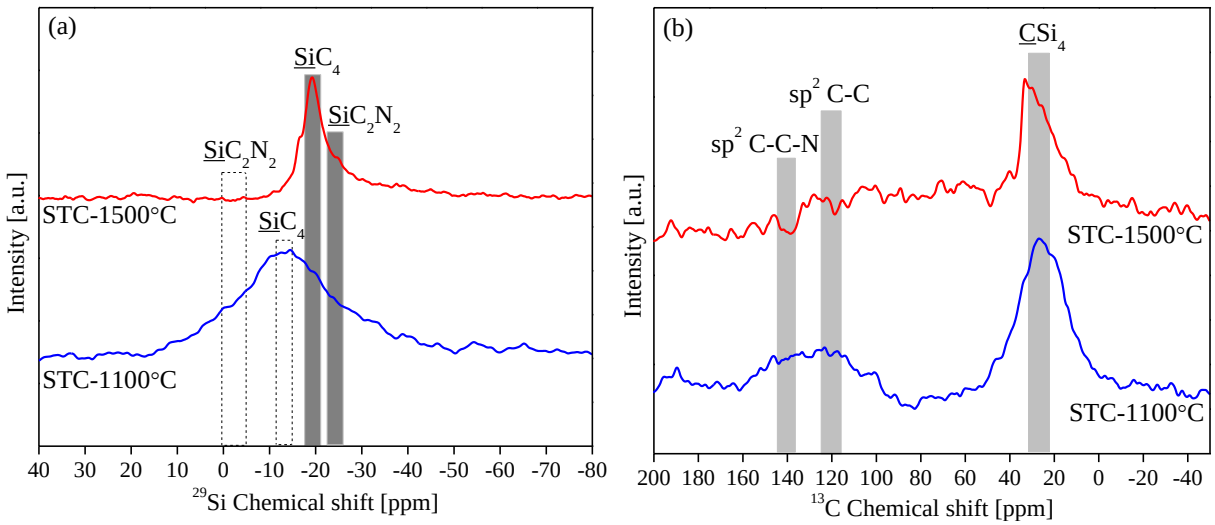

Figure 3. 33 MAS NMR spectra of SiTaC(N) ceramics pyrolyzed at 1100 °C and annealed at 1500 °C: *(a)* ^{29}Si and *(b)* ^{13}C. In *(a)* the dash-rectangular represent the ^{29}Si resonances of STC-1100ºC.

As aforementioned, the Ta atoms are connected of SMP10 by Ta-N(CH_3)-Si units to the polymeric backbone of the single-source precursor (Figure 3. 10). During the pyrolysis process, part of the nitrogen atoms at the Ta sites might be substituted by C atoms due to transamination processes.[192] Thus, in the ceramic pyrolyzed at 1100 °C Ta atoms might be connected to the amorphous matrix by Ta-N-Si and Ta-C-Si linkages, leading to the low-field shift of ^{29}Si resonances of $\underline{Si}C_2N_2$ and $\underline{Si}C_4$ sites (from ca.-12 and -15 ppm to ca. -2.14 and -13.33 ppm, respectively)[209]; see dash-rectangular in Figure 3. 33a. Analogous trends were also found in SiHfC(N) ceramics, in which the ^{29}Si chemical shifts of SiC_2N_2 and SiC_4 sites were significantly low-field shifted due to the presence of Hf bonded to the SiC_4 and SiC_2N_2 tetrahedra.[94] As the heat treatment temperatures increases (*e.g.*, to 1500 °C), TaC segregated (*i.e.*, phase separation of SiTaC(N) upon breaking of Si-N-Ta and Si-C-Ta linkages), which consequently leads to a high-field shift of the ^{29}Si resonances of the $\underline{Si}C_4$ and SiC_2N_2 sites (Figure 3. 33a). After annealing at 1500 ºC, the resonance of SiC_2N_2 sites almost vanished due to the carbothermal decomposition of N-containing phase.

The ^{13}C MAS NMR spectra in Figure 3. 33 show that the presence of segregated sp^2 carbon in the investigated materials is obvious. In Figure 3. 33b, two types of sp^2 carbon sites were found within the ceramics pyrolyzed at 1100 ºC, namely one with a chemical shift centered at 140 ppm, which was assigned to nitrogen-connected sp^2 carbon, and a second resonance located at 120-130 ppm, which corresponds to turbostratic carbon (sp^2 C-C) [215, 216]. After heat-treated at higher temperatures (*e.g.*, 1500 ºC), the signals of the nitrogen-connected sp^2 carbon sites reduce significantly, which agrees with the reduced nitrogen content within the STC-1500ºC sample (Table 3. 7).

X-ray diffraction *patterns*

The crystallization behavior of SiTaC(N) ceramics annealed at different temperatures were characterized using powder X-ray diffraction (XRD), and the results are shown in Figure 3. 34a. The XRD patterns reveal that the ceramic obtained at 1100 °C is mainly X-ray amorphous, while with increasing annealing temperatures, crystallization of both cubic TaC and β-SiC takes place. The Full-Profile Rietveld patterns of the SiTaC(N) ceramics annealed at 1500 - 1900 ºC are shown in Figure 3. 34(b-d). The weight fractions, grain sizes and lattice parameters of the TaC and β-SiC phase obtained by Full-Profile Rietveld refinement are listed in Table 3. 8.

As reported in literatures, the cubic TaC and TaN is able to form continuous solid solutions (*i.e.*, TaC_xN_{1-x}), and the relationship between the lattice parameters and *x* values obeys the Vegard's law with a small deviation, which is similar to the HfC_xN_{1-x}.[101, 234, 235] Therefore, the lattice parameters can be used to estimate the chemical composition (*i.e.*, *x* values) of the TaC_xN_{1-x} within the obtained ceramics. The lattice parameters of stoichiometric cubic TaC and TaN are 4.4547 Å (PDF 35-0801) and 4.3399 Å (PDF 49-1283), respectively, and thus the lattice parameters of cubic TaC_xN_{1-x} must vary in this range.[235, 236] Interestingly, the lattice parameters of the Ta-containing phase within the SiTaC(N) ceramics from STC-1500ºC to STC-1900ºC vary marginally (Table 3. 8), and they suggest that the Ta-containing phase within

the SiTaC(N) ceramics annealed at temperatures higher than 1500 ºC is almost stoichiometric TaC instead of TaC_xN_{1-x} solid solution. This is totally different from HfC_xN_{1-x} whose *x* value is still 0.93 even after annealing at 1800 ºC for 5 h. This can be explained by the Ellingham diagram (Figure 3. 35) of the reactions between the free carbon and HfN and TaC, respectively. It clearly shows that, at annealing temperatures lower than 2000 K, the Δ_rG_m value of reaction (2) is lower than that of reaction (1), which indicates that the nitrogen atoms within the lattice of HfN phase is more stable than that within the TaN phase under this condition. Therefore, hereafter the Ta containing phase within the SiTaC(N) ceramics is simply written as TaC.

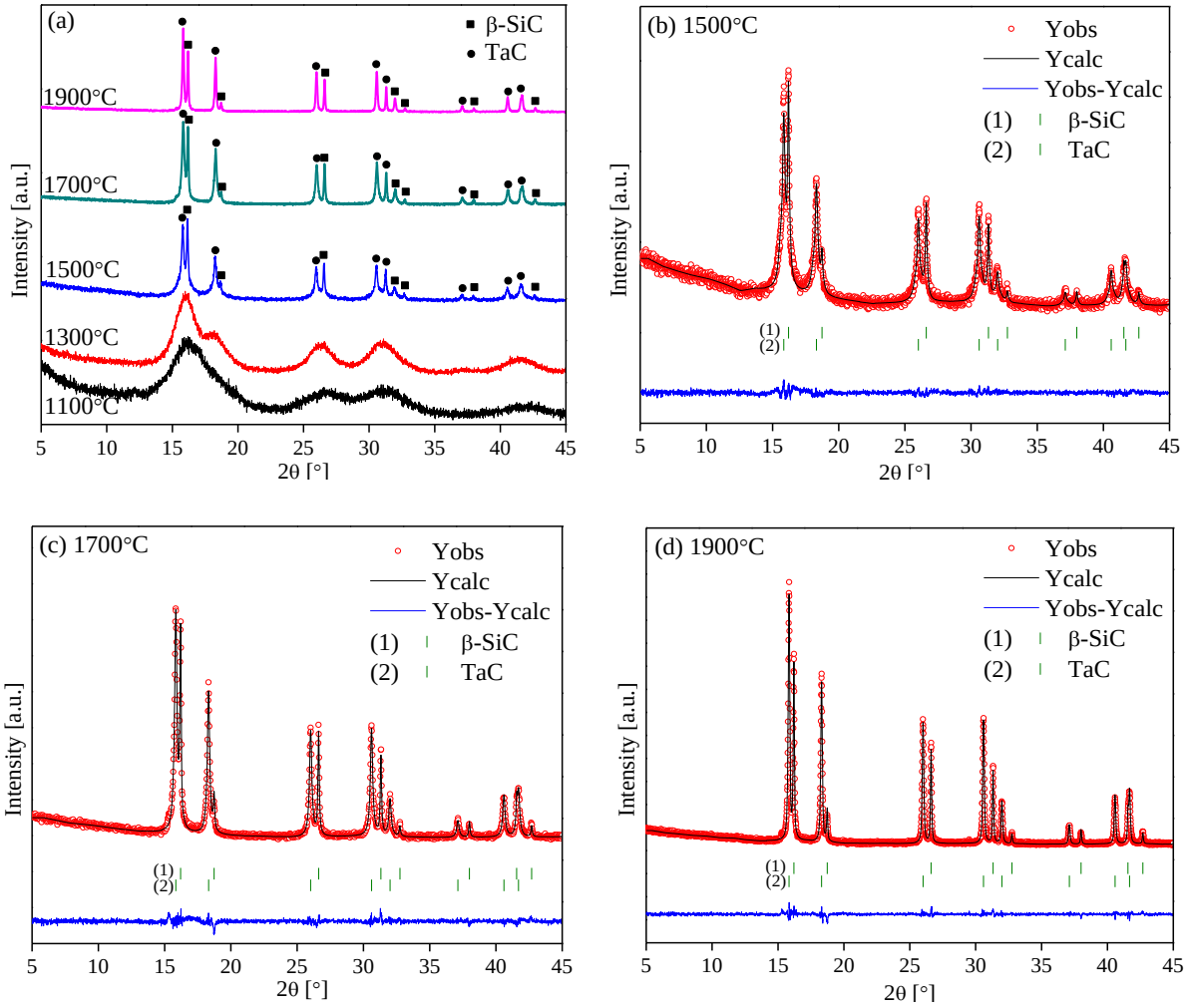

Figure 3. 34 XRD *(a)* and Rietveld *(b-d)* patterns of the SiTaC(N) ceramics obtained at different processing temperatures. Y_{obs} and Y_{calc} represents the observed and calculated profiles, respectively; the green sticks (1) and (2) are Bragg peak positions of related phase; the blue line at the bottom denotes the difference of the intensities between the observed and calculated profiles.

Table 3. 8 Weight fractions, grain sizes and lattice parameters of TaC and β-SiC within the ceramics annealed at different temperatures.

Sample	Weight fraction (wt.%)		Estimated grain size (nm)		Lattice Parameters, *a* (Å)	
	TaC	SiC	TaC	SiC	TaC	SiC
STC-1500ºC	23.72	76.28	9.9	25.2	4.4563(9)	4.3581(1)
STC-1700ºC	24.79	75.21	16.7	48.0	4.4556(7)	4.3572(1)
STC-1900ºC	23.01	76.99	46.4	111.6	4.4577(1)	4.3569(0)

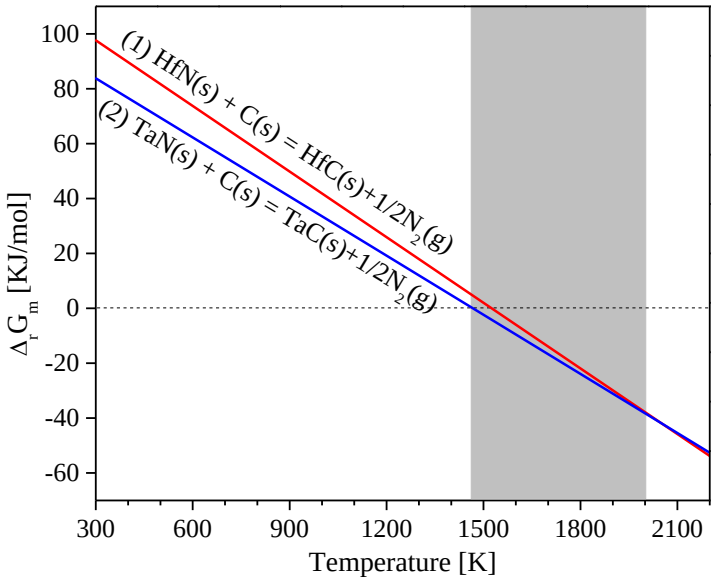

Figure 3. 35 Temperature dependence of the change in the Gibbs free energy (Ellingham diagram) of reactions between free carbon and HfN and TaN phases, respectively, during high-temperature annealing (data were taken from Ref.[237]).

Raman spectra

The Raman spectra of the SiTaC(N) ceramics pyrolyzed at 1100°C and annealed at different temperatures reveal the presence of segregated carbon at all temperatures (Figure 3. 36). In first-order Raman spectra of the SiTaC(N) ceramics, D, D' and G bands can be observed at ≈ 1350 cm^{-1}, 1620 cm^{-1} and 1580 cm^{-1}, respectively. Both D and D' bands are defect-induced bands, which represent the disordering of the segregated carbon. The G bands are contributed by stretching vibrations of sp^2 carbon in the basal-plane of graphite.[221] In the second-order Raman spectra, G', D+G and 2D' bands can be observed at ≈ 2700 cm^{-1}, 2945 cm^{-1} and 3245 cm^{-1}, respectively. G' band is overtone of the D band, which is usually observed in defect-free graphite samples.[238] Similar to the D and D' bands, the D+G band is also defect-induced. Moreover, the band appearing at 796 cm^{-1} after annealing at temperatures higher than 1700 °C is the transverse optical (TO) phonon mode of β-SiC.[222] At temperatures ≤ 1300 °C, the D and G bands are

broad and overlapped, and no G' band can be observed due to the high disorder of the segregated carbon phase.[223] With increasing annealing temperature from 1500 ºC to 1900 ºC , the D and G bands become sharper, and the intensity of G' bands grows gradually indicating that the ordering of the segregated carbon phase increases. However, the high intensity of the D band in all recorded spectra indicates in all samples that the segregated carbon phase should be considered as being highly disordered / turbostratic in its nature.

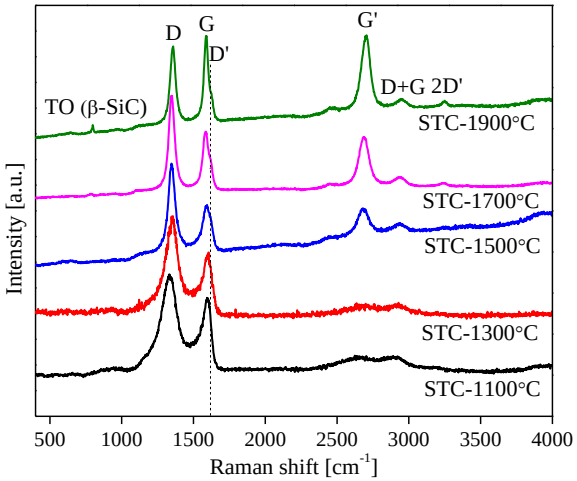

Figure 3. 36 Raman spectra of SiTaC(N) ceramics annealed at different temperatures.

Moreover, compared with the SiC sample derived from pure SMP10 (Figure 3. 27b), the intensity of the D' band of the SiTaC(N) ceramics annealed at the same temperature is much stronger. This is because a certain amount of N incorporates into the segregated carbon, inducing its local structural distortion.[203, 229-231] After annealing at 1900 ºC, the D' band decrease significantly, and the nitrogen content of the ceramics is ≈ 0 wt.%, which can further confirm this explanation.

TEM characterization

The SiTaC(N) ceramics annealed at 1700°C were further studied by means of TEM in order to assess the microstructure at high temperatures. As shown in Figure 3. 37, the TaC precipitations (dark contrast) with an average particle size of ca. 11 nm were found to homogeneously disperse within a β-SiC matrix, as shown also by EDS analysis. In the high-resolution micrograph, lattice fringes of the well crystallized TaC nanoparticles can be observed. The observed grain size of the TaC nanoparticles was similar as that estimated by Rietveld refinement (ca 16.7 nm, see Table 3. 8). The average grain size of TaC phase within the SiTaC(N) ceramics annealed at temperatures ≤ 1900 ºC is less than 50 nm, proving the possibility of preparing SiC/TaC/C ceramic nanocomposites upon annealing amorphous SiTaC(N) ceramics derived from a 30Ta-SMP10_80 single-source precursor. As mentioned above, the SiC/30HfC$_x$N$_{1-x}$/C/C-1700ºC is characterized by a unique microstructure, *i.e.*, the HfC$_x$N$_{1-x}$ nanoparticles are encapsulated within a layer of disordered carbon shell. However, within the STC-1700ºC sample, the carbon shell can only be observed on the lager TaC nanoparticles (see Figure 3. 37d), and no carbon shell can be observed on the

smaller TaC nanograins (Figure 3. 37b). That means, it is harder to form carbon shell on the TaC grains than on the HfC_xN_{1-x} grains. Nevertheless, the reason is not clear now.

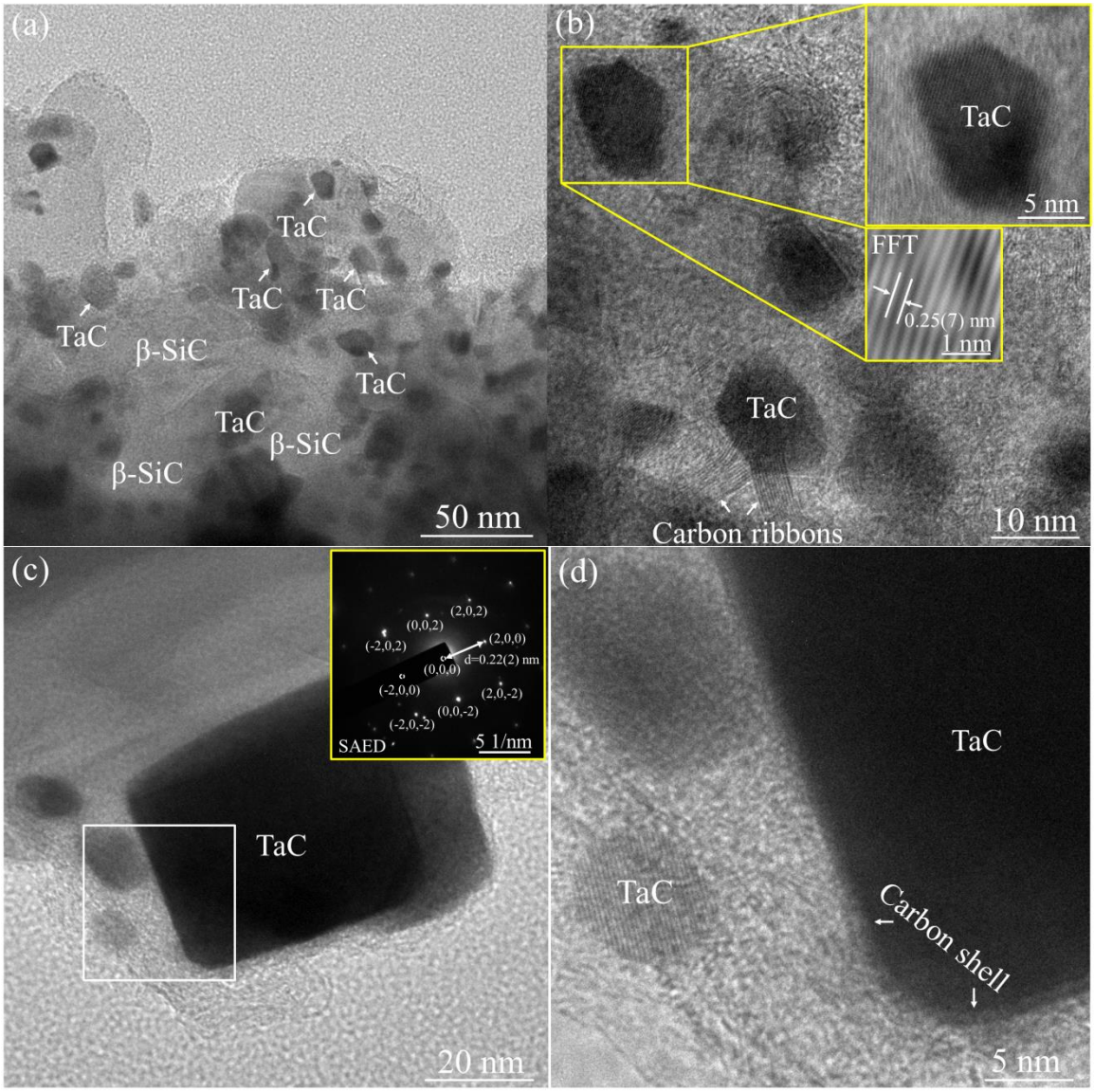

Figure 3. 37 TEM images (BF) of SiC/30TaC/C-1700ºC ceramic nanocomposite: inset in *(b)* is a high resolution image; inset in *(c)* is a SAED image of a larger TaC crystal; *(d)* is enlarged from the white square in *(c)*; the dark contrast is TaC phase, and bright contrast is β-SiC phase.

3.3.4 SiHfTaC(N) ceramics nanocomposites

3.3.4.1 Chemical composition

Two SiHfTaC(N) ceramics with different mole ratios of Hf to Ta were synthesized and denoted as SiHf7Ta3C(N) and SiHf2Ta8C(N), respectively. The ceramic yields of SiHf7Ta3C(N) and SiHf2Ta8C(N) are ≈ 76 wt.% and ≈ 79 wt.%, respectively. After pyrolysis at 1000 ºC, the elemental contents of Si, Ta, Hf, C, N and O in the obtained ceramic materials were analyzed, and the results are list in Table 3. 9.

Table 3. 9 Mass loss, chemical composition and empirical formula of the SiHfTaC(N) ceramics pyrolyzed at 1000 ºC and annealed at 1700 and 1900 ºC.

Sample	Mass loss (wt.%)	Elemental analysis (wt%)						Empirical formula
		Si	Hf	Ta	C	N	O	
SiHf7Ta3C -1000ºC*	---	45.95	12.20	5.50	27.98	4.40	3.97	$SiHf_{0.042}Ta_{0.018}C_{1.424}N_{0.192}O_{0.152}$
SiHf7Ta3C -1700ºC‡	12.79	51.17	13.59	5.90	28.69	0.14	0.51	$SiHf_{0.042}Ta_{0.018}C_{1.311}N_{0.005}O_{0.017}$
SiHf7Ta3C -1900ºC‡	14.90	51.81	13.76	5.98	28.17	<0.01	0.28	$SiHf_{0.042}Ta_{0.018}C_{1.271}O_{0.009}$
SiHf2Ta8C -1000ºC*	---	43.84	3.20	14.30	28.72	4.67	5.27	$SiHf_{0.012}Ta_{0.050}C_{1.532}N_{0.214}O_{0.211}$
SiHf2Ta8C -1700ºC‡	14.99	51.42	3.75	15.22	29.23	0.09	0.29	$SiHf_{0.012}Ta_{0.046}C_{1.329}N_{0.004}O_{0.010}$
SiHf2Ta8C -1900ºC‡	15.54	51.20	3.74	15.16	29.72	0	0.18	$SiHf_{0.012}Ta_{0.046}C_{1.357}O_{0.006}$

**- Si content is calculated by difference; ‡ - Si, Hf and Ta is estimated by a constant mole ratio of Si/Hf/Ta.*

The elemental analysis proves that it is possible to control the mole ratio of metallic elements within the synthesized ceramics upon controlling the ratio of starting materials (*i.e.*, metal compounds). As discussed in section 3.3.1 and 3.3.3, the variations of mole ratio of Si/Hf in SiHfC(N) ceramics and of Si/Ta in SiTaC(N) ceramics is negligible even after annealing at 1900 ºC for 5 h, and the Hf and Ta does not reduce during annealing. Thus, the Si, Hf and Ta content in the samples annealed at 1700 and 1900 ºC can be estimated according to the constant mole ratio of Si/Hf/Ta (Table 3. 9). The mass loss of both SiHf7Ta3C(N) and SiHf2Ta8C(N) ceramics after annealing at 1700 and 1900 ºC are similar to that of the SiHfC(N) and SiTaC(N) ceramics, indicating promising thermal stability at ultrahigh temperatures. The small deviation should come from the different oxygen contamination during the synthesis process.

3.3.4.2 Phase composition and crystallization behavior

X-ray diffraction *patterns*

(1) SiHf7Ta3C(N) ceramic nanocomposites

X-ray diffraction (XRD) patterns of the SiHf7Ta3C(N) ceramics annealed at different temperatures were measured, and the results are shown in Figure 3. 38a. The XRD patterns reveal that the ceramic prepared at 1000 °C is mainly X-ray amorphous, while with increasing annealing temperatures, crystallization of both cubic $Hf_{0.7}Ta_{0.3}C_xN_{1-x}$ and β-SiC takes place. As reported in previous studies, cubic HfC and TaC with rock-salt (NaCl) crystal structure is able to form continuous solid solution as their carbides and nitrides.[94, 167] Thus, the $Hf_{0.7}Ta_{0.3}C_xN_{1-x}$ is a solid solution with Hf and Ta atoms forming a cubic close-packed structure and with C and N atoms occupying the interstitial void spaces (*i.e.*, octahedral holes).

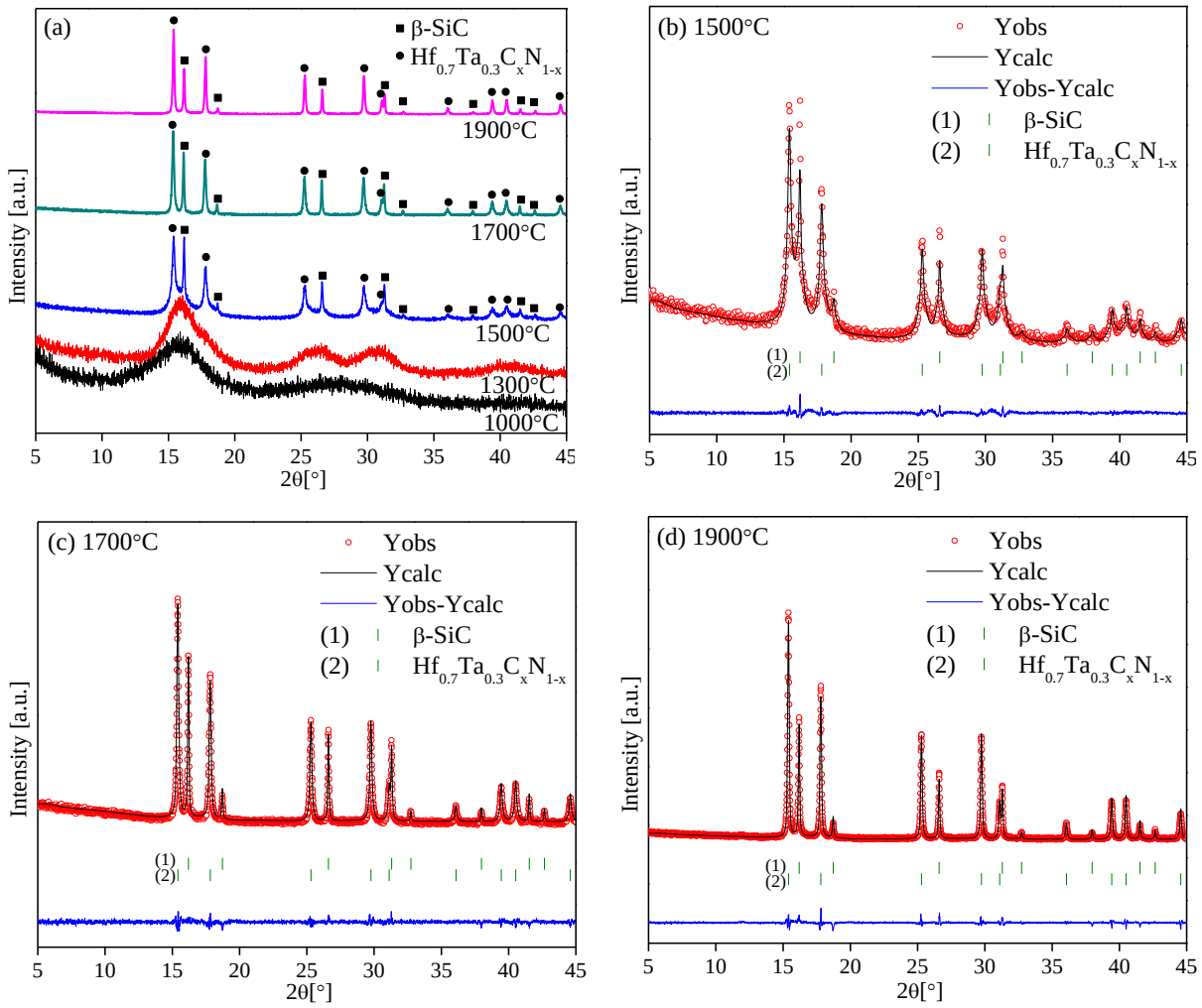

Figure 3. 38 XRD *(a)* and Rietveld *(b-d)* patterns of the SiHf7Ta3C(N) ceramics obtained at different processing temperatures. Y_{obs} and Y_{calc} represents the observed and calculated profiles, respectively; the green sticks *(1)* and *(2)* are Bragg peak positions of related phase; the blue line at the bottom denotes the difference of the intensities between the observed and calculated profiles.

The XRD results indicate that Hf and Ta atoms of the $Hf_{0.7}Ta_{0.3}C_xN_{1-x}$ solid solutions exhibit complete miscibility even after annealing at 1900 ºC for 5 h. The Full-Profile Rietveld patterns of the SiHf7Ta3C(N) ceramics annealed at 1500 - 1900 ºC are shown in Figure 3. 38(b-d). The weight fractions, grain sizes and lattice parameters of the $Hf_{0.7}Ta_{0.3}C_xN_{1-x}$ and β-SiC phase obtained by Full-Profile Rietveld refinement are listed in Table 3. 10. The peak shapes were modeled using the Thompson-Cox-Hastings pseudo-Voigt function for average grain size and the pseudo-Voigt function for lattice parameters and weight fraction.[228]

Table 3. 10 Weight fractions, grain sizes and lattice parameters of $Hf_{0.7}Ta_{0.3}C_xN_{1-x}$ and β-SiC within the ceramics annealed at different temperatures (HfTa represents $Hf_{0.7}Ta_{0.3}C_xN_{1-x}$).

Sample	Weight fraction (wt.%)		Estimated grain size (nm)		Lattice Parameters *a* (Å)		Chemical Composition
	HfTa	SiC	HfTa	SiC	HfTa	SiC	HfTa
SiHf7Ta3C-1500ºC	19.06	80.94	7.1	10.2	4.5802(3)	4.3608(4)	$Hf_{0.7}Ta_{0.3}C_{0.98}N_{0.02}$
SiHf7Ta3C-1700ºC	25.38	74.62	25.6	83.9	4.5796(8)	4.3597(4)	$Hf_{0.7}Ta_{0.3}C_{0.97}N_{0.03}$
SiHf7Ta3C-1900ºC	26.87	73.13	49.7	73.3	4.5826(5)	4.3600(8)	$Hf_{0.7}Ta_{0.3}C$

As we know that the *x* values of the TaC_xN_{1-x}, HfC_xN_{1-x} and $Ta_xHf_{5-x}C_5$ solid solutions can be estimated precisely according to the Vegard's law,[218, 235, 239] we can also try to estimate the *x* values of the $Hf_{0.7}Ta_{0.3}C_xN_{1-x}$ phase according to Vegard's law. The lattice parameter (*a*) of $Hf_{0.7}Ta_{0.3}C$ is calculated to be 4.5827(6) using the standard lattice parameters of stoichiometric HfC (PDF 39-1491) and TaC (PDF 35-0801), and the lattice parameter of $Hf_{0.7}Ta_{0.3}N$ is calculated to be 4.4696(8) using the standard lattice parameters of stoichiometric HfN (PDF 33-0592) and TaN (PDF 49-1283). The lattice parameter of the $Hf_{0.7}Ta_{0.3}C_xN_{1-x}$ within the SiHf7Ta3C-1900ºC sample is 4.5826(5) Å (Table 3. 10), which agrees well with the estimated lattice parameter of $Hf_{0.7}Ta_{0.3}C$. Thus, the *x* value of $Hf_{0.7}Ta_{0.3}C_xN_{1-x}$ phase within the SiHf7Ta3C-1900ºC sample should be 1. Considering the nitrogen content of the SiHf7Ta3C-1900ºC sample is ≈ 0 wt.% (*i.e.*, *x* must be 1), it can be confirmed that the *x* value can be estimated precisely according to Vegard's law. Therefore, the chemical composition of $Hf_{0.7}Ta_{0.3}C_xN_{1-x}$ phase within the SiHf7Ta3C-1500ºC and SiHf7Ta3C-1700ºC samples can be well estimated, and the results are listed in Table 3. 10. The *x* values reveal that the $Hf_{0.7}Ta_{0.3}C_xN_{1-x}$ phase within the three samples is almost stoichiometric carbide (*i.e.*, $Hf_{0.7}Ta_{0.3}C$).

(2) SiHf2Ta8C(N) ceramic nanocomposites

In order to investigate the crystallization behavior of the SiHf2Ta8C(N) ceramics, X-ray diffraction (XRD) patterns of the ceramic materials annealed at different temperatures were measured, and the results are shown in Figure 3. 39a. The XRD patterns reveal that the ceramic prepared at 1000 °C is mainly X-ray amorphous, while with increasing annealing temperatures, crystallization of both cubic $Hf_{0.2}Ta_{0.8}C_xN_{1-x}$ and β-SiC takes place. The $Hf_{0.2}Ta_{0.8}C_xN_{1-x}$ is a solid solution similar to the reported Ta_4HfC_5 (*i.e.*, $Hf_{0.2}Ta_{0.8}C$).[239, 240] XRD results indicate that the Hf and Ta atoms of $Hf_{0.2}Ta_{0.8}C_xN_{1-x}$ solid solutions within the β-SiC matrix exhibit complete miscibility, even after annealing at 1900 ºC for 5 h. The Full-Profile Rietveld patterns of the SiHf2Ta8C(N) ceramics annealed at 1500-1900 ºC are shown in Figure 3. 39(b-d). The weight fractions, grain sizes and lattice parameters of the $Hf_{0.2}Ta_{0.8}C_xN_{1-x}$ and β-SiC phase obtained by Full-Profile Rietveld refinement are listed in Table 3. 11. The peak shapes were modeled using the Thompson-Cox-Hastings pseudo-Voigt function for average grain size and the pseudo-Voigt function for lattice parameters and weight fraction.[228]

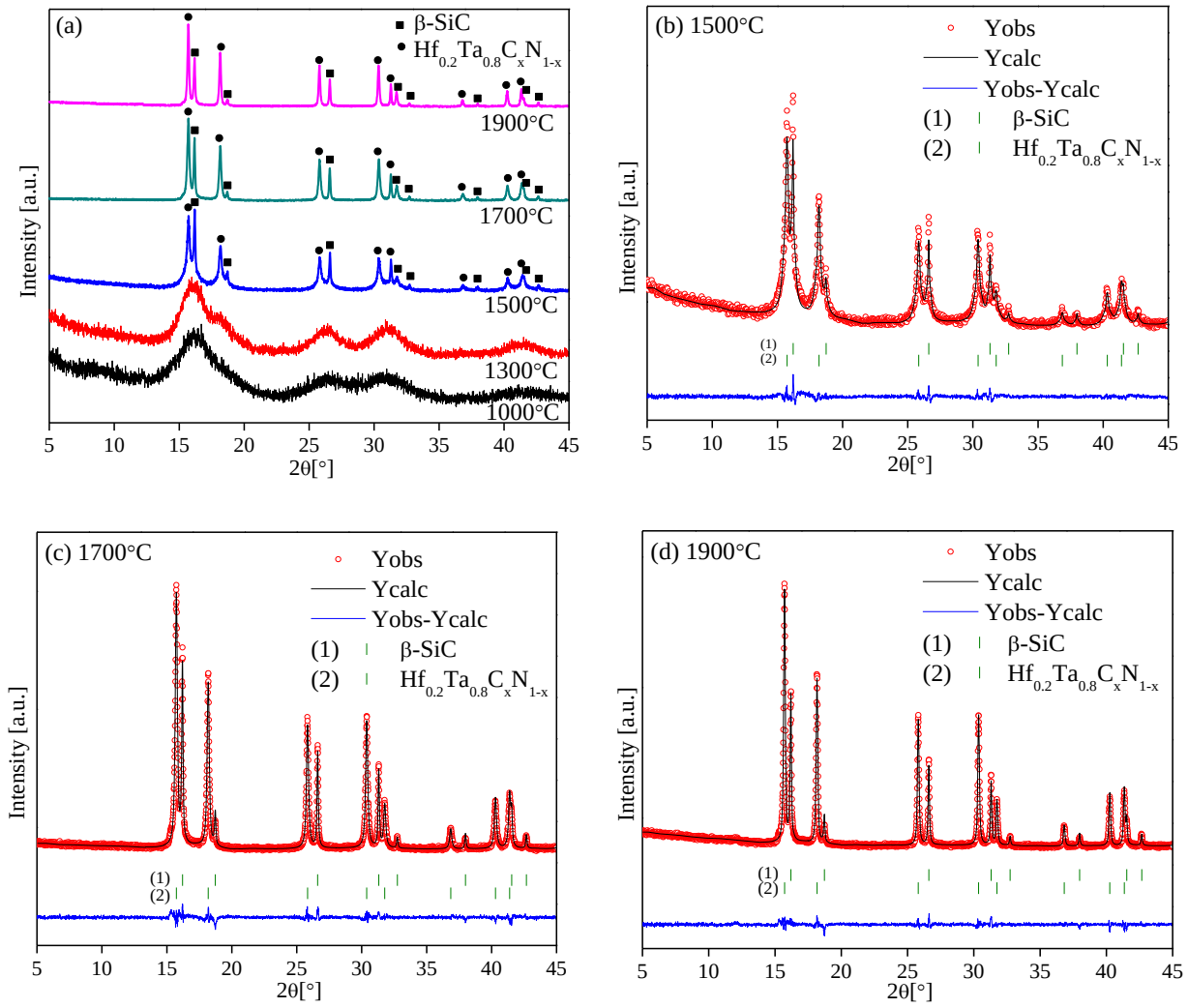

Figure 3. 39 XRD *(a)* and Rietveld *(b-d)* patterns of the SiHf2Ta8C(N) ceramics obtained at different processing temperatures. Y_{obs} and Y_{calc} represents the observed and calculated profiles, respectively; the green sticks (1) and (2) are Bragg peak positions of related phase; the blue line at the bottom denotes the difference of the intensities between the observed and calculated profiles.

Since the *x* values of the TaC_xN_{1-x} and HfC_xN_{1-x} and $Ta_xHf_{5-x}C_5$ solid solutions can be estimated precisely according to the Vegard's law,[218, 235, 239] we can try to estimate the *x* values of the $Hf_{0.2}Ta_{0.8}C_xN_{1-x}$ phase according to this law as well. The lattice parameter of $Hf_{0.2}Ta_{0.8}C_xN_{1-x}$ within SiHf2Ta8C-1900ºC sample is 4.4917(6) Å (Table 3. 11), which agrees with the reported lattice parameter of $Hf_{0.2}Ta_{0.8}C$ [*e.g.*, 4.4901(8) Å in Ref.[239] and 4.491 Å in Ref.[23]] as well as the theoretical value [4.4912(9) Å] calculated using the standard lattice parameters of stoichiometric HfC (PDF-39-1491) and TaC (PDF-35-0801). Thus, the *x* value of $Hf_{0.2}Ta_{0.8}C_xN_{1-x}$ within the SiHf2Ta8C-1900ºC sample should be 1 according to Vegard's law. The nitrogen content within SiHf2Ta8C-1900ºC sample is ≈ 0 wt.% (Table 3. 9); thus, the *x* value of the $Hf_{0.2}Ta_{0.8}C_xN_{1-x}$ phase must be 1 (*i.e.*, $Hf_{0.2}Ta_{0.8}C$). This means that the *x* value obtained by Vegard's law is consistent with that obtained by elemental analysis. Thus, it can be confirmed that the chemical composition of the $Hf_{0.2}Ta_{0.8}C_xN_{1-x}$ phase can be estimated according to Vegard's law, and the

results are presented in Table 3. 11. The lattice parameters of $Hf_{0.2}Ta_{0.8}C_xN_{1-x}$ within the SiHf2Ta8C-1500ºC and SiHf2Ta8C-1700ºC samples approach the reported lattice parameter of $Hf_{0.2}Ta_{0.8}C$ as well. Therefore, the $Hf_{0.2}Ta_{0.8}C_xN_{1-x}$ phase within the sample annealed at temperatures higher than 1500 ºC is almost stoichiometric carbide (*i.e.*, $Hf_{0.2}Ta_{0.8}C$) with rather low nitrogen content. Analogous phenomena were also observed in the SiTaC(N) and SiHf7Ta3C(N) ceramic nanocomposites discussed in section 3.3.3.

Table 3. 11 Weight fractions, grain sizes and lattice parameters of $Hf_{0.2}Ta_{0.8}C_xN_{1-x}$ and β-SiC within the ceramics annealed at different temperatures (TaHf represents $Hf_{0.2}Ta_{0.8}C_xN_{1-x}$).

Sample	Weight fraction (wt.%)		Estimated grain size (nm)		Lattice Parameters, *a* (Å)		Chemical composition
	TaHf*	SiC*	TaHf*	SiC	TaHf*	SiC	TaHf*
SiHf2Ta8C-1500ºC	22.41	77.59	8.3	19.5	4.4864(2)	4.3583(3)	$Hf_{0.2}Ta_{0.8}C_{0.96}N_{0.04}$
SiHf2Ta8C-1700ºC	26.87	73.13	21.2	58.2	4.4878(9)	4.3586(7)	$Hf_{0.2}Ta_{0.8}C_{0.97}N_{0.03}$
SiHf2Ta8C-1900ºC	24.92	75.08	40.8	61.2	4.4917(6)	4.3595(1)	$Hf_{0.2}Ta_{0.8}C$

Raman spectra

Raman spectra of SiHf7Ta3C(N) and SiHf2Ta8C(N) ceramics obtained at different temperatures are shown in Figure 3. 40. Similar to the SiHfC(N) and SiTaC(N) ceramics, the signals for segregated carbon can be observed within all the ceramics. In the first-order Raman spectra, D, D' and G bands can be observed at ≈ 1350 cm^{-1}, 1620 cm^{-1} and 1580 cm^{-1}, respectively.[221] In the second-order Raman spectra, G', D+G and 2D' bands can be observed at ≈ 2700 cm^{-1}, 2945 cm^{-1} and 3245 cm^{-1}, respectively. The evolution of segregated carbon as a function of temperature exhibits the same trend as SiHfC(N) and SiTaC(N) ceramics. At temperatures ≤ 1300 °C, the D and G bands are broad and overlapped and no G' band can be observed due to the high disorder of the segregated carbon phase.[223] By increasing the annealing temperature from 1500 ºC to 1900 ºC, the D and G bands become sharper, and the intensity of G' bands grows gradually, indicating that the ordering of the segregated carbon phase increases. However, the high intensity of the D band in all recorded spectra indicates in all samples that the segregated carbon phase should be considered as being highly disordered / turbostratic in its nature.

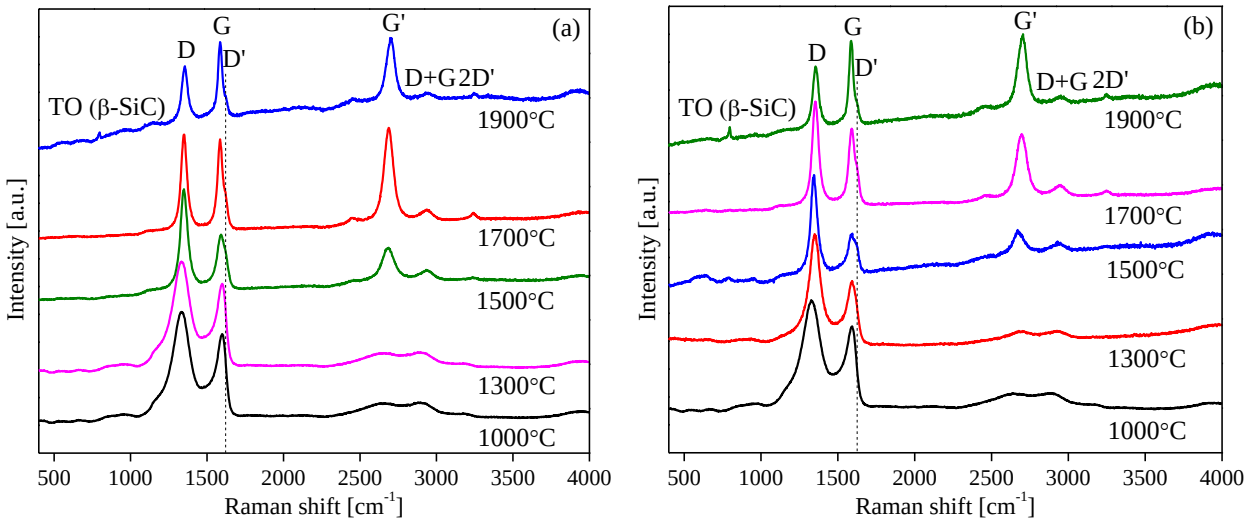

Figure 3. 40 Raman spectra of SiHf7Ta3C(N) *(a)* and SiHf2Ta8C(N) *(b)* ceramics annealed at different temperatures.

TEM characterization

Figure 3. 41 shows the TEM images of SiHfTaC(N) ceramics annealed at 1700 °C for 5 h. The $Hf_yTa_{1-y}C_xN_{1-x}$ phase as well as β-SiC phase that possesses dark and light contrast, respectively, can be observed. Previously reported TEM images of the SiHfC(N) ceramics reveal that the HfC_xN_{1-x} nano grains are encapsulated by an amorphous carbon shell (Figure 3. 25).[94, 101] Nevertheless, within the SiTaC(N) ceramics, the unique core-shell microstructure is rarely observed. Interestingly, within the SiHfTaC(N) ceramics annealed at 1700 ºC, this unique core-shell microstructure can be observed on both of the $Hf_{0.7}Ta_{0.3}C_xN_{1-x}$ and $Hf_{0.2}Ta_{0.8}C_xN_{1-x}$ nanograins. Therefore, according to the TEM observations of SiHfC(N), SiTaC(N) and SiHfTaC(N) ceramic nanocomposites, the Hf atoms seem to play a crucial role in the formation of the core-shell microstructure. Besides, a graphite layer was observed on the β-SiC crystals within the SiHf2Ta8C-1700ºC sample (Figure 3. 41d), which however is rarely observed in other samples.

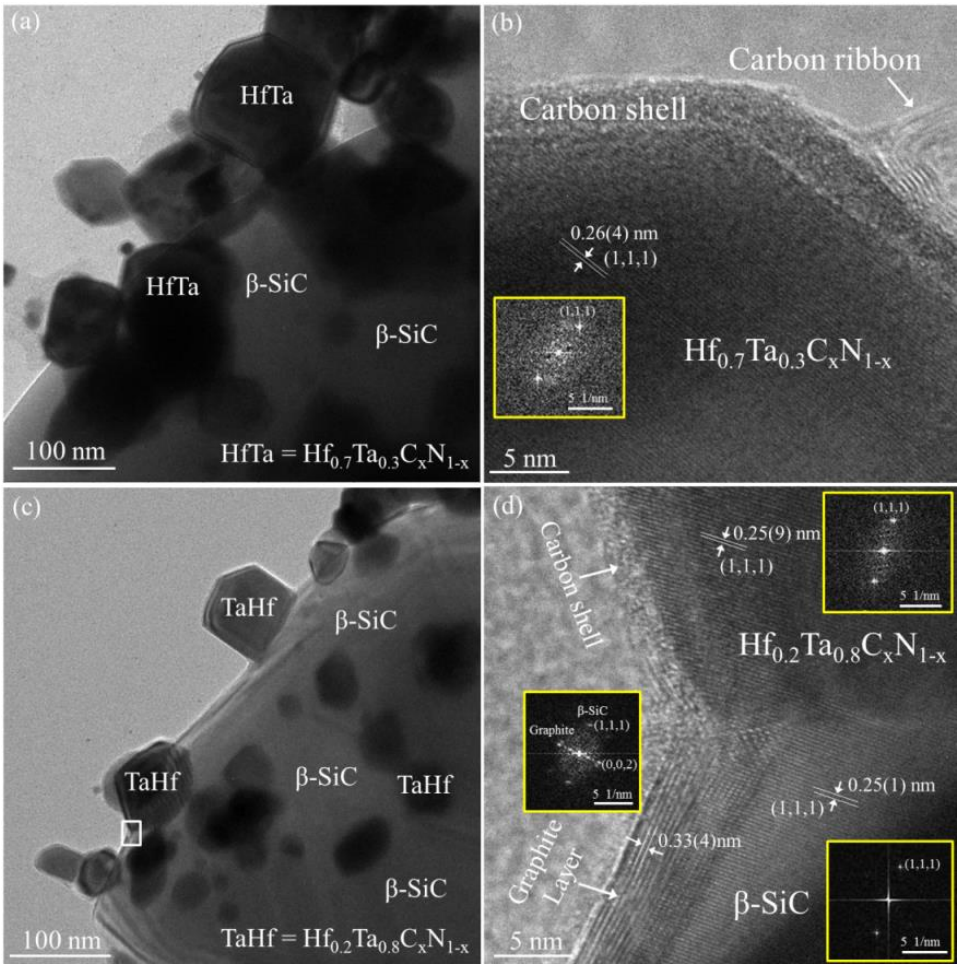

Figure 3. 41 TEM images (BF) of SiHf7Ta3C-1700ºC *(a and b)* and SiHf2Ta8C-1700ºC *(c and d)* ceramic nanocomposite (the dark contrast is HfTa-containing phase and bright contrast is β-SiC phase; the carbon shells were observed on the surface of both HfTa-containing nano grains).

3.3.5 Summary

In this section, several thermal stable ceramic nanocomposites were prepared upon high-temperature annealing of amorphous SiMC(N) ceramics obtained by pyrolysis of M-containing single-source precursors (M = Hf, Ta, HfTa), *i.e.*, SiHfC(N), boron-doped SiHfC(N), SiTaC(N), SiHf7Ta3C(N) and SiHf2Ta8C(N). XRD, Raman and TEM results reveal that the ceramic nanocomposites mainly comprise β-SiC and MC_xN_{1-x} as well as free carbon. The MC_xN_{1-x} and free carbon phases disperse homogeneously within the β-SiC matrix. Rietveld refinement of XRD patterns and TEM images confirm that the grain size of both β-SiC and MC_xN_{1-x} are less than 100 nm, even after annealing at 1900 ºC for 5 h. The grain growth of β-SiC can be effectively suppressed by introducing of M elements into the single-source precursors. Characterization of chemical and phase composition reveals that the $Hf_{0.7}Ta_{0.3}C_xN_{1-x}$ and $Hf_{0.2}Ta_{0.8}C_xN_{1-x}$ solid solutions with expected Hf/Ta atomic ratio can be controlled precisely by adjusting the mole ratio of metal compounds during synthesis of the single-source precursors.

After annealing at the same temperature, *x* values of the TaC_xN_{1-x}, $Hf_{0.7}Ta_{0.3}C_xN_{1-x}$ and $Hf_{0.2}Ta_{0.8}C_xN_{1-x}$

phases are obviously larger than that of the HfC_xN_{1-x}. Especially at temperatures ≥ 1500 ºC, the TaC_xN_{1-x}, $Hf_{0.7}Ta_{0.3}C_xN_{1-x}$ and $Hf_{0.2}Ta_{0.8}C_xN_{1-x}$ are almost stoichiometric carbides (*i.e.*, TaC, $Hf_{0.7}Ta_{0.3}C$ and $Hf_{0.2}Ta_{0.8}C$ with $x \approx 1$), whereas the x value of HfC_xN_{1-x} is only 0.96 even after annealing at 1900 ºC for 5 h. That means the N atoms within the lattice of HfC_xN_{1-x} grains should be more stable than those within the TaC_xN_{1-x}, $Hf_{0.7}Ta_{0.3}C_xN_{1-x}$ and $Hf_{0.2}Ta_{0.8}C_xN_{1-x}$ grains when annealing at high temperatures.

A unique MC_xN_{1-x}-carbon core shell microstructure was observed within all the ceramic nanocomposites. The carbon shell on the MC_xN_{1-x} core is able to hinder the coarsening of MC_xN_{1-x} grains during high-temperature annealing. Raman and TEM images suggest that the carbon shell is highly disordered in its nature. After annealing at the same temperature, the carbon shell on the HfC_xN_{1-x} core is thicker than that on the TaC core, whereas the thickness of the carbon shell on the $Hf_{0.7}Ta_{0.3}C_xN_{1-x}$ and $Hf_{0.2}Ta_{0.8}C_xN_{1-x}$ core is similar to that on the HfC_xN_{1-x} core. Thus, the Hf atoms seem to play a crucial role in the formation of the core-shell microstructure.

Within boron-doped SiHfC(N) ceramics, boron incorporates into free carbon, forming a BC_yN_z phase when the annealing temperature is < 1900 ºC. After annealing at 1900 ºC, the boron transferred into HfB_2 upon reaction between the BC_yN_z and HfC_xN_{1-x} phase. Therefore, the high-temperature conversion of boron is clearly thermodynamically controlled, which allows for the preparation of SiC/HfC_xN_{1-x}/HfB_2/C ceramics with tailored phase compositions.

3.4 Dense monolithic SiMC(N) ceramics

3.4.1 General information

In section 3.1, 3.2 and 3.3, a series of SiMC(N) ceramic nanocomposites (M = Hf, Ta, HfTa) were synthesized upon pyrolysis of chemically modified SMP10 and subsequent annealing of the obtained amorphous SiMC(N) ceramics. In this section, the as-pyrolyzed amorphous SiMC(N) powders were used to prepare dense monolithic SiMC(N) ceramics using spark plasma sintering (SPS). The maximum diameter achieved in this Ph.D. work is 35 mm, which is rarely reported in the literature. Photographs of the as-sintered monoliths are shown in Figure 3. 42.

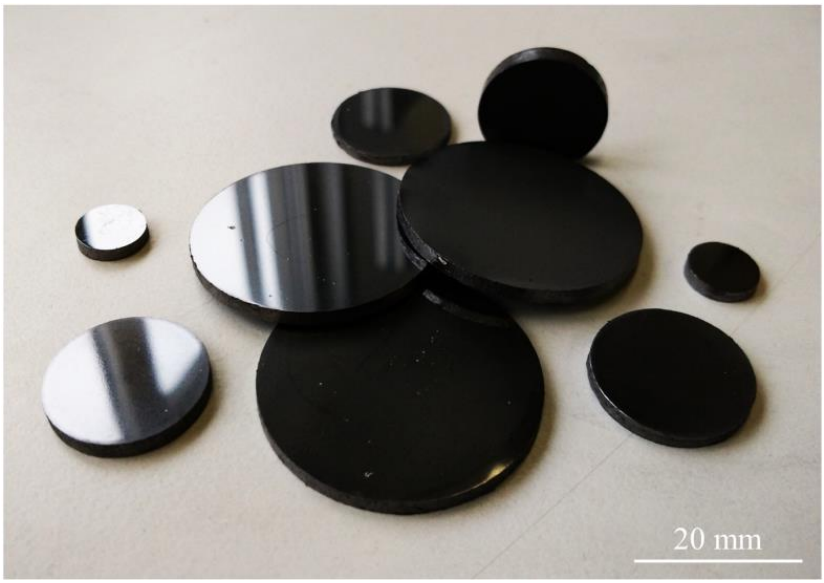

Figure 3. 42 Photographs of dense SiMC(N) monoliths prepared by Spark Plasma Sintering (M = Hf, Ta, HfTa).

Table 3. 12 Information of Spark Plasma Sintered (SPS) dense SiMC(N) monoliths (M = Hf, Ta, HfTa).

Name	Sintering conditions			Material parameters		
	Temp. (ºC)	Pressure (MPa)	Time (min)	Diameters (mm)	Density (g/cm^3)	Open porosity (%)
SiC/30HfC$_x$N$_{1-x}$/C*	2200	50	30	20	3.72	0.74
SiC/30HfC$_x$N$_{1-x}$/HfB$_2$/C	2200	50	20	20	3.50	0
SiC/30HfC$_x$N$_{1-x}$/C-35mm	2200	50	20	35	3.46	0.30
SiC/15HfC$_x$N$_{1-x}$/C-35mm	2200	50	20	35	3.16	0.26
SiC/30TaC/C	2200	50	20	10	3.57	0
SiC/30Hf$_{0.7}$Ta$_{0.3}$C$_x$N$_{1-x}$/C	2200	50	20	20	3.45	1.40
SiC/30Hf$_{0.2}$Ta$_{0.8}$C$_x$N$_{1-x}$/C	2200	50	20	20	3.51	1.14
SiC/C-35mm	2200	50	20	35	3.04	0.02

* - The Hf source is Hf(NMe$_2$)$_4$ and the others are Hf(NEt$_2$)$_4$;

Some general information for the dense monoliths is shown in Table 3. 12. The name of the monoliths are denoted as SiC/MC$_x$N$_{1-x}$/C in order to differentiate them from the powder SiMC(N) ceramic nanocomposites in section 3.3. The numbers “15” and “30” indicate the weight ratio of metal compounds

[*e.g.*, $Hf(NEt_2)_4$] to SMP10 in feed is 15/85 and 30/70, respectively. The "35mm" indicates that the diameter of this monolith is 35 mm. The density and open porosity were measured using the Archimedic method (see section 2.6.2), which reveals that the as-sintered monolithic ceramics are almost fully dense. The surface morphology, phase composition and microstructure were characterized using SEM, XRD and TEM.

3.4.2 Phase composition

X-ray diffraction *patterns and refinements*

XRD patterns as well as Full-Profile Rietveld XRD profiles of the as-sintered monoliths are shown in Figure 3. 43. The reflections of cubic MC_xN_{1-x} (M = Hf, Ta, Hf_yTa_{1-y}) and β-SiC as well as a small peak (at $2\theta = 12.16^{o}$) assigned to graphite can be observed in all monoliths. Within the SiC/30HfC$_x$N$_{1-x}$/HfB$_2$/C sample, some small peaks of HfB_2 can be observed as well (Figure 3. 43b). XRD results prove that all the MC_xN_{1-x} phases within the β-SiC matrix are very stable (no phase separation), even after sintering at 2200 ºC. The weight fractions, grain sizes and lattice parameters of the MC_xN_{1-x}, HfB_2 and β-SiC obtained by Full-Profile Rietveld refinement are listed in Table 3. 13. The peak shapes were modeled using the Thompson-Cox-Hastings pseudo-Voigt function for average grain size and the pseudo-Voigt function for lattice parameters and weight fraction.[228] The estimated average grain sizes reveal that except for the SiC/30HfC$_x$N$_{1-x}$/HfB$_2$/C sample all the other monoliths are ceramic nanocomposites. For the sake of comparison, the SiC/C-35mm monolith was also sintered using amorphous SiC powders derived from pure SMP10. The XRD pattern of the SiC/C-35mm monoliths (not shown) indicates that β-SiC and a small amount of α-SiC (Hexagonal, $P6_3mc$) formed during SPS sintering. The grain sizes and weight fractions of both phases are shown in Table 3. 13. The SiC/C-35mm monolith is not a nanocomposite because the grain size of β-SiC is around 180 nm (> 100 nm). The XRD results reveal that introduction of M elements (M = Hf, Ta) into the SiC-based composites using the PDC route can effectively reduce the grain size of β-SiC, which enables the preparation of dense monolithic SiC/MC_xN_{1-x}/C ceramic nanocomposites. Moreover, different from the SiC/HfC$_x$N$_{1-x}$/C monoliths, the *x* values of the SiC/TaC$_x$N$_{1-x}$/C, SiC/$Hf_{0.7}Ta_{0.3}C_xN_{1-x}$/C and SiC/$Hf_{0.2}Ta_{0.8}C_xN_{1-x}$/C monoliths approach 1, indicating that the Ta containing MC_xN_{1-x} phases are almost stoichiometric carbide (*i.e.*, MC).

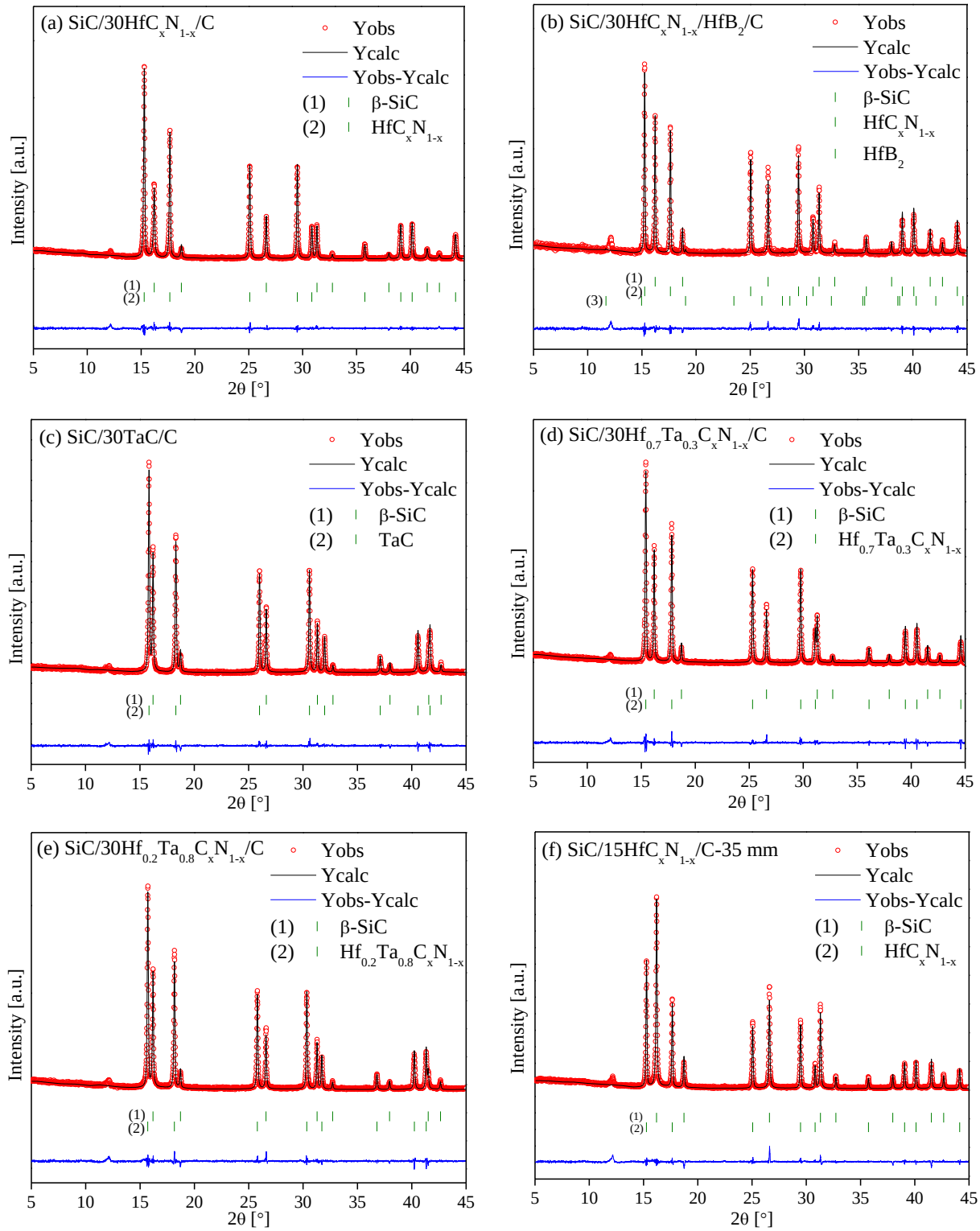

Figure 3. 43 Full-Profile Rietveld XRD patterns of the monolithic ceramics obtained by SPS sintering. Y_{obs} and Y_{calc} represents the observed and calculated profiles, respectively; the green sticks (1), (2) and (3) are Bragg peak positions of related phase; the blue line at the bottom denotes the difference of the intensities between the observed and calculated profiles.

Table 3. 13 Weight fractions, grain sizes and lattice parameters of MC_xN_{1-x} (M = Hf, Ta, Hf_yTa_{1-y}) and β-SiC within the as-prepared monolithic ceramics (MC represents the MC_xN_{1-x} phases).

Sample	Weight fraction (wt.%)		Estimated grain size (nm)		Lattice Parameters *a* (Å)		Chemical Composition
	MC	SiC	MC	SiC	MC	SiC	MC
SiC/30HfC$_x$N$_{1-x}$/C	26.30	73.70	80.9	36.6	4.6183(9)	4.3563(2)	$HfC_{0.83}N_{0.17}$
SiC/30HfC$_x$N$_{1-x}$/HfB$_2$/C‡	18.36	0.38	174.6	132.0	4.6275(4)	4.3530(2)	$HfC_{0.91}N_{0.09}$
SiC/30HfC$_x$N$_{1-x}$/C-35mm	18.64	81.36	79.8	63.4	4.6178(4)	4.3588(2)	$HfC_{0.82}N_{0.18}$
SiC/15HfC$_x$N$_{1-x}$/C-35mm	8.29	91.7	77.8	69.7	4.6239(6)	4.3598(6)	$HfC_{0.88}N_{0.12}$
SiC/30TaC/C	21.51	78.49	73.7	75.3	4.4584(4)	4.3570(2)	TaC
SiC/30Hf$_{0.7}$Ta$_{0.3}$C$_x$N$_{1-x}$/C	21.42	78.58	91.1	81.0	4.5792(8)	4.3608(8)	$Hf_{0.7}Ta_{0.3}C_{0.97}N_{0.03}$
SiC/30Hf$_{0.2}$Ta$_{0.8}$C$_x$N$_{1-x}$/C	20.30	79.70	72.3	73.0	4.4943(2)	4.3619(2)	$Hf_{0.2}Ta_{0.8}C$
SiC/C-35mmΨ	---	95.58	---	157.9	---	4.3600(6)	---

‡ - the grain size and weight fraction of HfB_2 is 97.5 nm and 0.38 wt.%, respectively; Ψ - the grain size and weight fraction of α-SiC is 20.8 nm and 4.42 wt.%.

Raman spectra

Raman spectra of the as-sintered monoliths are shown in Figure 3. 44. It clearly shows that sp^2-bonded segregated carbon exists within all the monoliths. In first-order Raman spectra of the monoliths, D, D' and G bands can be observed at ≈ 1350 cm^{-1}, 1620 cm^{-1} and 1580 cm^{-1}, respectively. Both D and D' bands are defect-induced bands which indicate the disordering of the segregated carbon. The G bands are contributed by stretching vibrations of sp^2 carbon in the basal-plane of graphite.[221] In the second-order Raman spectra, G', D+G and 2D' bands can be observed at ≈ 2700 cm^{-1}, 2945 cm^{-1} and 3245 cm^{-1}, respectively. The G' band is an overtone of the D band, which is usually observed in defect-free graphite samples. Similar to D and D' band, the D+G band is defect-induced as well. Except for the SiC/30HfC$_x$N$_{1-x}$/HfB$_2$/C sample, all of the D and G bands show small linewidth, and the intensities of the G and G' bands are significantly higher than those of the D band, indicating good graphitization of the segregated carbon (increased structural ordering). The intensities of the defect-induced D' and D+G bands are also rather low. This should be due to the high sintering temperature (2200 ºC). In the case of the SiC/30HfC$_x$N$_{1-x}$/HfB$_2$/C monolith, the graphitization of segregated carbon is suppressed by the incorporated boron; thus, the intensities of the D and D' bands are still quite high. This phenomenon is also observed on the boron-doped SiHfC(N) ceramic powders (see section 3.3.2).

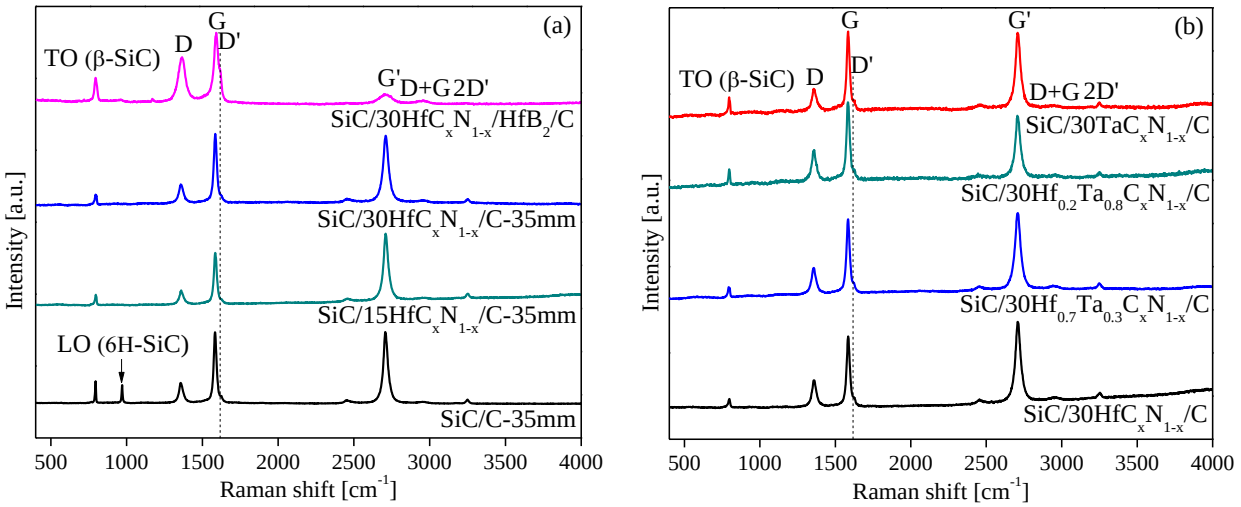

Figure 3. 44 Raman spectra of the as-sintered dense monolithic SiMC(N) ceramic nanocomposites (M = Hf, Ta, HfTa) and boron-doped SiHfC(N) ceramic monolith as well as SiC/C ceramic monoliths.

Moreover, a band appearing at ≈ 796 cm^{-1} can be observed on the Raman spectra of all the monoliths (Figure 3. 44), which is the transverse optical (TO) phonon mode of β-SiC.[222] The intensities of the TO bands on the spectra of SiMC(N) monoliths (M = Hf, Ta, HfTa) are obviously lower than those on the spectra of SiC/C monoliths, which further proves that the crystallization of β-SiC is suppressed by introduction of the M elements into the single-source-precursors. In the case of the SiC/30HfC$_x$N$_{1-x}$/HfB$_2$/C monolith, the TO band is stronger than those of the SiMC(N) monoliths, which is consistent with the larger grain size of β-SiC (Table 3. 13). This will be discussed later. Furthermore, on the spectrum of the SiC/C monolith, a band attributed to the longitudinal optical (LO) phonon mode of 6H-SiC (α-SiC) can be observed at ≈ 965 cm^{-1} (Figure 3. 44a), whereas the LO band of 6H-SiC has never been found on the spectra of other monoliths, which indicates that the M elements also prevent the phase transformation of β-SiC into α-SiC at ultrahigh temperatures. This is consistent with the XRD results presented in Figure 3. 43 and Table 3. 13.

3.4.3 Microstructural characterization

3.4.3.1 Dense monolithic SiC/30HfC$_x$N$_{1-x}$/C ceramic nanocomposites

SEM image of the dense monolithic SiC/30HfC$_x$N$_{1-x}$/C ceramic nanocomposites further proves that the monolithic sample is almost fully dense (Figure 3. 45). Two kinds of different areas [*i.e.*, area (1) and area (2) in Figure 3. 45a] can be observed. Area (1) is coming from the inside of ceramic particles used for sintering, and area (2) (the internal surface) is from the surface-near regions of the ceramic particles. Figure 3. 45c is a BSE image enlarged from the white square in area (1). Thus the homogeneously dispersed white phase should be the *in situ* formed HfC$_x$N$_{1-x}$ grains, and the matrix phase is β-SiC. The average diameter of the white phase is around 180 nm with the maximum and minimum diameters of ≈ 300 nm and ≈ 110 nm, respectively. The inset (b) shows a pronounced coarsening of the HfC$_x$N$_{1-x}$

crystallites in area (2), indicating a relatively fast diffusion rate of HfC_xN_{1-x} at the internal surfaces. This is due to a decrease of carbon content at the surface-near regions of the ceramic particles. As previously reported, the diffusion coefficient of hafnium in the carbon-depleted surface areas of SiOC particles was three orders of magnitude higher than that within the SiOC bulk.[241]

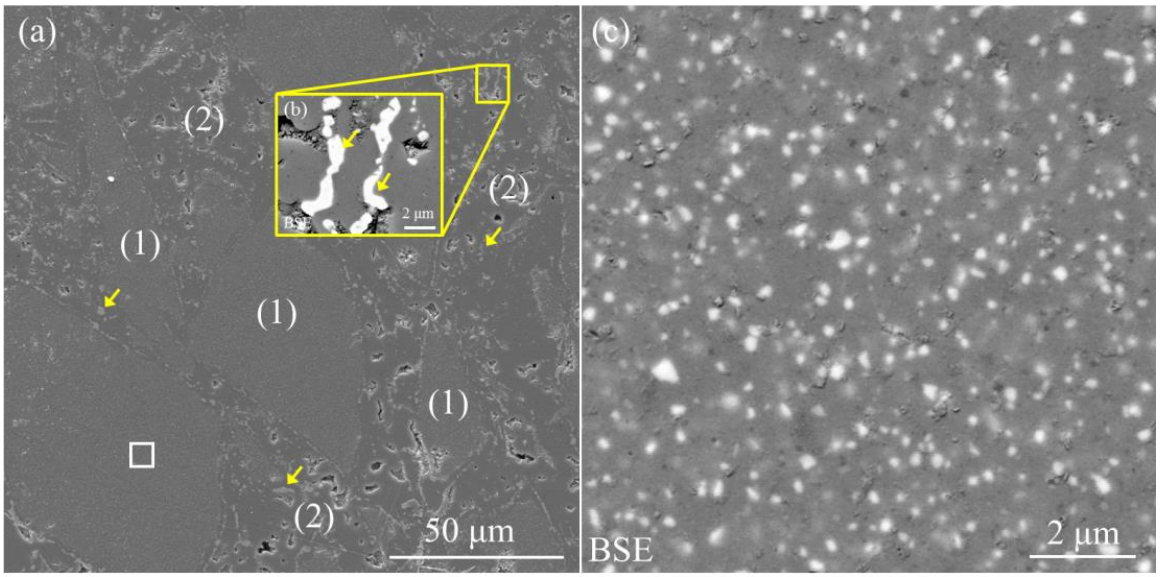

Figure 3. 45 SEM images of dense monolithic SiC/30HfC_xN_{1-x}/C ceramic nanocomposites: *(a)* is in SE mode, inset *(b)* and *(c)* are in BSE mode; *(c)* is magnified from the white square in (a).

Figure 3. 46 presents TEM images of the dense monolithic SiC/30HfC_xN_{1-x}/C ceramic nanocomposites. Confirmed by EDX and SAED, the particles with dark contrast are HfC_xN_{1-x} grains, and the matrix with bright contrast is β-SiC or amorphous SiHfC(N) phase.[25] The HfC_xN_{1-x} grains with different diameters from ≈ 270 nm to ≈ 25 nm (average ≈ 70 nm) can be observed. That is the reason why we observed many large HfC_xN_{1-x} grains in the SEM images, while we calculated the average diameters of HfC_xN_{1-x} grains to be ≈ 80 nm using XRD refinement (Table 3. 13). That means within the monolithic sample, the grain size of HfC_xN_{1-x} has a wide-range distribution from ≈ 20 nm to ≈ 300 nm, but the average value is less than 100 nm. Besides, another explanation is also possible. The larger HfC_xN_{1-x} grains observed in the SEM images might be polycrystalline HfC_xN_{1-x} with smaller grain size instead of larger HfC_xN_{1-x} single crystals. But this should be further proved. The gran size of β-SiC is not easy to be confirmed by TEM, but the XRD refinement indicate that the average grain size is also less than 100 nm (Table 3. 13). Therefore, the dense monolithic SiC/30HfC_xN_{1-x}/C is a ceramic nanocomposite.

Furthermore, the high resolution TEM images reveal that both large and small HfC_xN_{1-x} grains are encapsulated by a layer of disordered carbon, forming a core-shell structure similar to the powder samples annealed at 1400-1700 ºC(Figure 3. 25). The *in situ* formed carbon shell effectively suppressed the coarsening of HfC_xN_{1-x} grains at 2200 ºC.

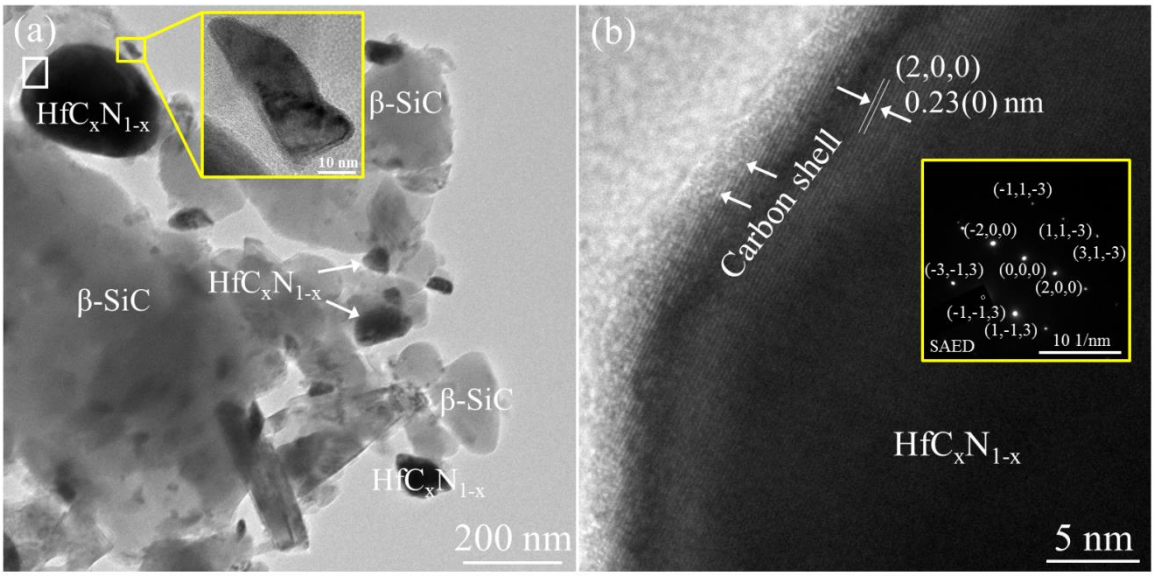

Figure 3. 46 Bright field TEM images of dense monolithic SiC/30HfC_xN_{1-x}/C ceramic nanocomposites [*(b)* is a high resolution TEM image taken from the white square in *(a)*].

3.4.3.2 Dense monolithic SiC/30HfC_xN_{1-x}/HfB_2/C ceramics

Figure 3. 47 shows SEM images of the dense monolithic SiC/30HfC_xN_{1-x}/HfB_2/C ceramics (SHBC-SPS). It shows a homogenous surface morphology that is totally different from the dense monolithic SiC/30HfC_xN_{1-x}/C ceramic nanocomposites (Figure 3. 45a). Figure 3. 47b is a high-resolution BSE image taken from the white square in Figure 3. 47a. Thus, the phase with white contrast is mainly HfC_xN_{1-x} [the amount of HfB_2 phase is rather low (< 0.4 wt.%) according to the results of XRD refinement], and the matrix is β-SiC. In Figure 3. 47a, the phase with white contrast is also the HfC_xN_{1-x} grains. The SEM images in SE mode are not sensitive to the atomic numbers of elements, but the contrast varies with the potential difference of the surface (voltage contrast). As we know that the HfC_xN_{1-x} grains show much higher electrical conductivity than β-SiC[101], the HfC_xN_{1-x} grains can also be identified in the SE mode due to a potential difference. Similar results can be observed in all the other M-containing nanocomposites in this thesis (*e.g.*, Figure 3. 45a). The average diameter of the white phase is around 1.5 μm with maximum and minimum value of ≈ 2.7 μm and ≈ 0.12 μm (see yellow arrows in Figure 3. 47b), respectively. This is quite larger than the dense monolithic SiC/30HfC_xN_{1-x}/C ceramic nanocomposites. Moreover, no pores can be found on the surface of the dense monolithic SiC/30HfC_xN_{1-x}/HfB_2/C ceramic sample. That means this monolithic sample is fully dense, which is consistent with its open porosity (≈ 0) measured by the Archimedic method (Table 3. 12).

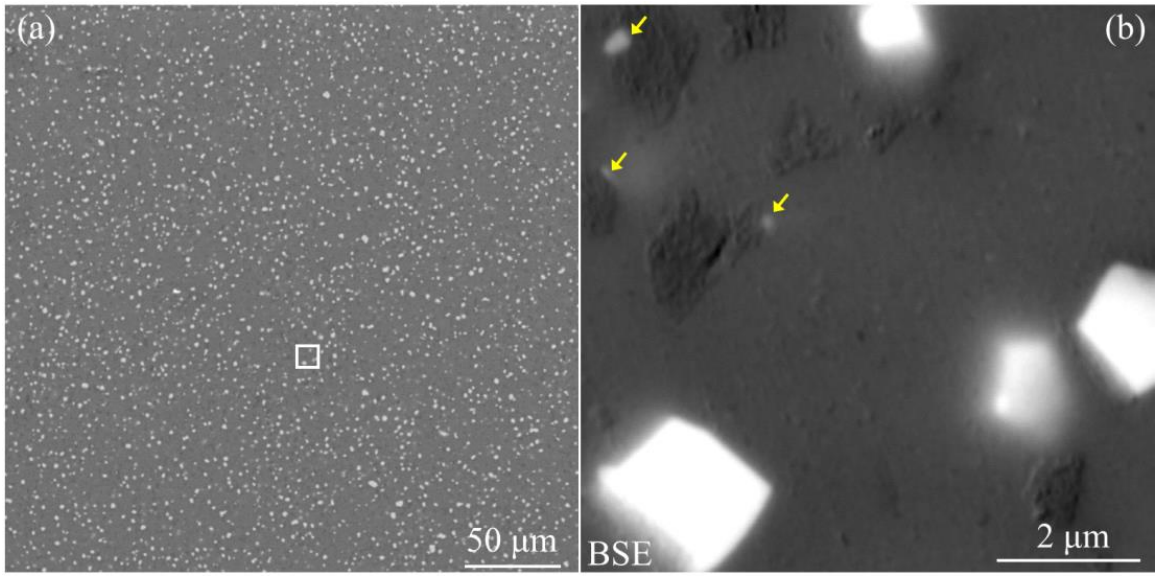

Figure 3. 47 SEM images of dense monolithic SiC/30HfC_xN_{1-x}/HfB_2/C ceramics (SHBC-SPS): *(a)* is in SE mode and *(b)* is in BSE mode, which is a high resolution image taken from the white square in *(a)*.

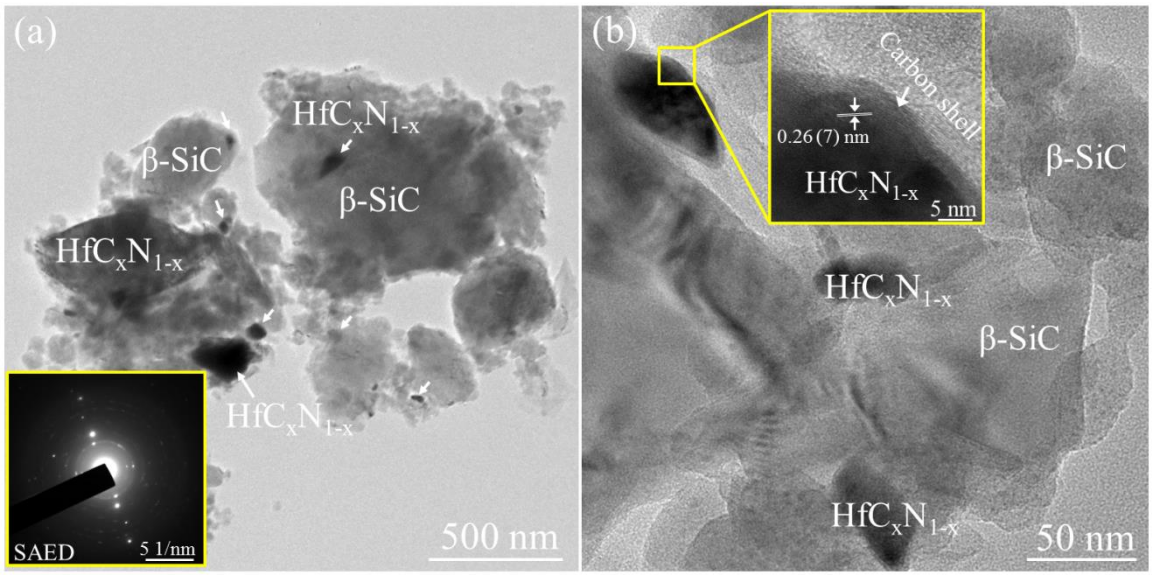

Figure 3. 48 Bright field TEM images of the dense monolithic SiC/30HfC_xN_{1-x}/HfB_2/C ceramics: inset in *(a)* is a SAED image and inset in *(b)* is a high resolution TEM image.

Figure 3. 48 presents the TEM images of dense monolithic SiC/30HfC_xN_{1-x}/HfB_2/C ceramics. Confirmed by EDX and SAED, the particles with dark contrast are HfC_xN_{1-x} grains, and the matrix with bright contrast is β-SiC or amorphous SiHfC(B,N). Nevertheless, HfB_2 grains are too few to be observed. As shown in the TEM images, the grain size of HfC_xN_{1-x} has a wide-range distribution from hundreds of nanometers to around twenty nanometers. This is consistent with the observations on the SEM images and the calculated average diameters of HfC_xN_{1-x} (Table 3. 13). The high resolution TEM image reveals that the HfC_xN_{1-x} grains are encapsulated by a layer of amorphous carbon forming a core-shell structure, which is similar to the dense monolithic SiC/30HfC_xN_{1-x}/C ceramic nanocomposites. The only difference,

as discussed in section 3.3.2, is that the carbon shell should be incorporated with some boron.

As discussed above, the SiC/30HfC$_x$N$_{1-x}$/HfB$_2$/C monoliths show significantly different features from the SiC/30HfC$_x$N$_{1-x}$/C monoliths in terms of enhanced sinterability and improved grain sizes. This difference should be contributed by the introduction of boron into the single-source-precursors. In section 3.3.2, the elemental analysis shows that boron content within the amorphous boron-doped SiHfC(N) ceramics (*i.e.*, SHBC-1000ºC) is around 0.50 wt.%, and after annealing at 1900 ºC (*i.e.*, SHBC-1900ºC) the boron content increases to 0.58 wt.% (Table 3. 5). That means the boron content within the SiC/30HfC$_x$N$_{1-x}$/HfB$_2$/C monolith should be in the range of 0.50 ~ 0.60 wt.%. According to the phase composition, ≈ 0.04 wt.% of B is consumed by the formation of HfB$_2$ (Table 3. 13). Thus, the rest of B should still disperse within the matrix of the monolith. As reported in the literature, boron combined with free carbon is a necessary and promising sintering aid for fabrication of a dense SiC monolith.[242] The boron-carbon sintering aid is able to improve the grain boundary diffusivity (*i.e.*, diffusional mass transport) by reducing the ratio of grain-boundary energy to surface energy but retain the high-temperature strength with essentially covalent bonds at the grain boundary.[243, 244] A case study was conducted on SiC samples containing 3 wt.% carbon (constant) and 0 ~ 4 wt.% boron.[242] The results suggest that at the carbon content of 3 wt.%, the optimum amount of boron for sintering was 0.2 ~ 0.5 wt.%, and moreover the grain size of SiC increased significantly. Elemental analysis indicates that the free carbon within the boron-doped SiHfC(N) ceramics is around 5.5 ~ 6.5 wt.% (Table 3. 5). Thus, the boron content here should be enough for acting as a boron-carbon sintering aid for fabrication of a fully dense SiHfC(N) monolith (Table 3. 13). During sintering, the boron incorporated into the free carbon, forming homogeneously dispersed boron-carbon sintering aids, which significantly enhanced the sinterability of the SiHfC(N) ceramics. Moreover, the grain size of both β-SiC and HfC$_x$N$_{1-x}$ was improved as well.

3.4.3.3 Dense monolithic SiC/30TaC/C ceramic nanocomposites

SEM images of the dense monolithic SiC/30TaC/C ceramic nanocomposites are shown in Figure 3. 49. Similar to the dense monolithic SiC/30HfC$_x$N$_{1-x}$/C ceramic nanocomposites, two kinds of different areas [*i.e.*, area (1) and area (2)] can be observed on the surface. Figure 3. 49c is a BSE image enlarged from the white square in Figure 3. 49a. Thus, the homogeneously dispersed white phase is the *in situ* formed TaC, and the matrix phase is β-SiC (XRD results indicate that the *x* value of TaC$_x$N$_{1-x}$ here is 1; see Table 3. 13). The average diameter of the white phase is around 100 nm with the maximum and minimum diameters of ≈ 150 nm and ≈ 50 nm, respectively. The inset (b) shows that some larger TaC grains aggregated in area (2), but the grain size is not as large as the HfC$_x$N$_{1-x}$ within the dense monolithic SiC/30HfC$_x$N$_{1-x}$/C ceramic nanocomposites (Figure 3. 45).

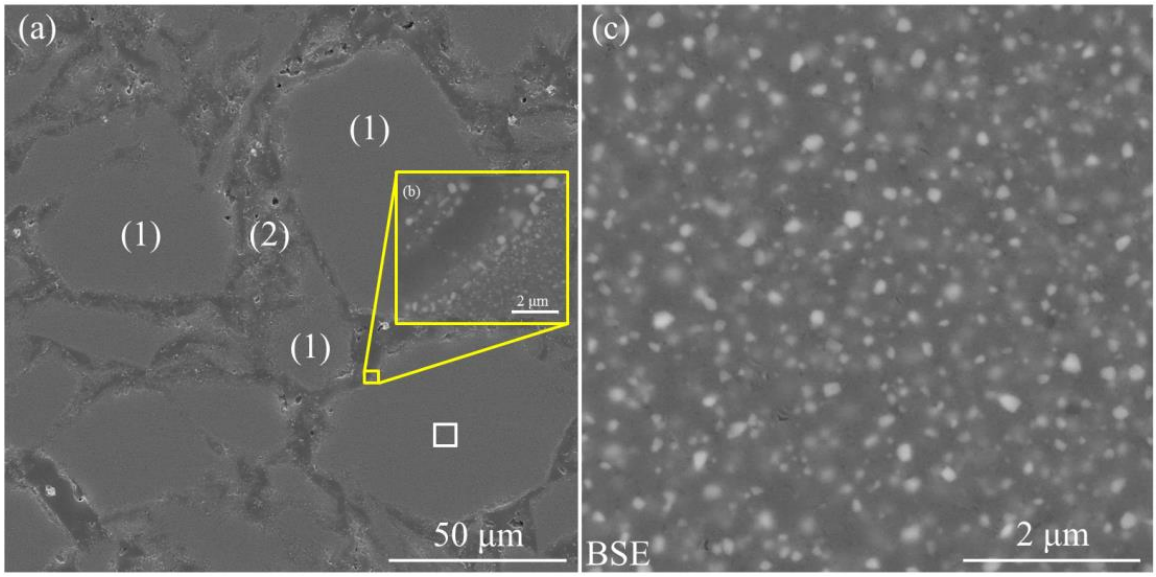

Figure 3. 49 SEM images of dense monolithic SiC/30TaC/C ceramic nanocomposites: *(a)* and inset *(b)* are in SE mode, *(c) is* in BSE mode and is taken from the white square in *(a)*.

Figure 3. 50 shows TEM images of the dense monolithic SiC/30TaC/C ceramic nanocomposites. Confirmed by EDX and SAED, the particles with dark contrast are TaC grains, and the matrix with bright contrast is β-SiC or amorphous SiTaC(N). The TaC grains with different diameters from ≈ 240 nm to ≈ 30 nm (average ≈ 85 nm) can be observed. That is the reason why we observed many large TaC grains in the SEM images, but we calculated the average diameters of TaC grains to be ≈ 75 nm using XRD refinement (Table 3. 13). That means within the monolithic sample, the grain size of TaC has a wide-range distribution from 30 nm to 240 nm, but the average value is less than 100 nm. Besides, there is another reasonable explanation. The larger TaC grains observed in the SEM images might be polycrystalline TaC with smaller grain size instead of TaC single crystals, but this should be further proved. It is not easy to confirm the grain size of β-SiC by TEM, but the XRD refinement indicate that the average grain size is ≈ 75 nm (Table 3. 13). Therefore, the dense monolithic SiC/30TaC/C is a ceramic nanocomposite.

As discussed in section 3.3.3, different from the SiHfC(N) ceramics, the TaC-carbon core-shell structure can only be observed on some larger TaC nanograins (Figure 3. 37d). Within the dense monolithic SiC/30TaC/C ceramic nanocomposites, the core-shell structure can be observed on some large TaC grains as well (Figure 3. 50b). However, the thickness of carbon shell is rather thin, which is different from the SiHfC(N) ceramics.

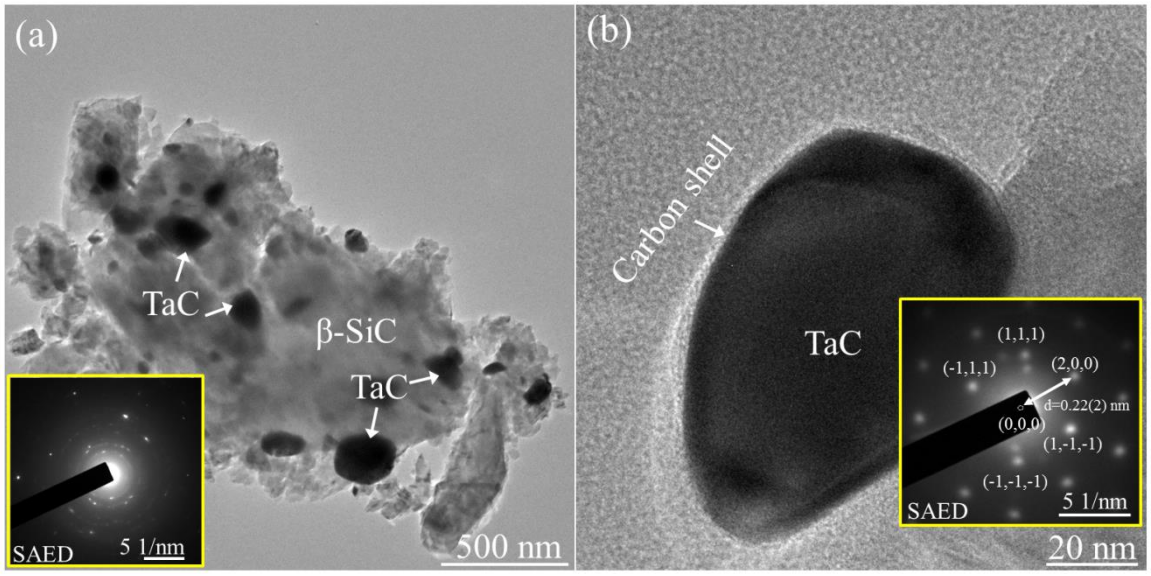

Figure 3. 50 Bright field TEM images of dense monolithic SiC/30TaC/C ceramic nanocomposites (insets are SAED images).

3.4.3.4 Dense monolithic SiC/30$Hf_{0.7}Ta_{0.3}$C/C ceramic nanocomposites

SEM imges of the dense monolithic SiC/30$Hf_{0.7}Ta_{0.3}$C/C ceramic nanocomposites are shown in Figure 3. 51. Similar to the SiHfC(N) and SiTaC(N) monoliths, 2 different area can be observed on the surface: area (1) is fully dense, while some open pores concentrate in area (2). The same as the SiTaC(N) monoliths, some larger $Hf_{0.7}Ta_{0.3}C$ grains aggregated in area (2), whereas the grain size is much smaller than the aggregated HfC_xN_{1-x} grains within the SiHfC(N) monoliths. Figure 3. 51c is a BSE image with high resolution. Thus, the white contrast represents the $Hf_{0.7}Ta_{0.3}C$ phase that disperses homogeneously within the β-SiC matrix (dark contrast). The average diameter of the $Hf_{0.7}Ta_{0.3}C$ phase is around 100 nm with the maximum and minimum diameters of ≈170 nm and 70 nm, respectively.

TEM images of the dense monolithic SiC/30$Hf_{0.7}Ta_{0.3}$C/C ceramic nanocomposites are presented in Figure 3. 52. It clear shows that the $Hf_{0.7}Ta_{0.3}C$ nanograins (dark contrast) disperse homogeneously within the β-SiC matrix or amorphous SiHf7Ta3C(N) phase. The average grain size of the $Hf_{0.7}Ta_{0.3}C$ is ≈ 85 nm with the maximum and minimum diameters of ≈ 160 nm and ≈ 20 nm. The result is consistent with the average grain size (≈ 90 nm) obtained by XRD refinement. Combining the observations on SEM and TEM images as well as XRD patterns, it can be confirmed that the grain size of $Hf_{0.7}Ta_{0.3}C$ phase has a wide-range of distribution from ≈ 20 nm to ≈ 160 nm. But, the average grain size of the $Hf_{0.7}Ta_{0.3}C$ and β-SiC is calculated to be ≈ 90 nm and 80 nm, respectively. Thus, the as-prepared dense SiC/30$Hf_{0.7}Ta_{0.3}$C/C monolith is also a ceramic nanocomposite. The high resolution image reveals that the $Hf_{0.7}Ta_{0.3}C$ grains are encapsulated by an amorphous carbon layer, forming a core-shell structure, which is similar to the SiHfC(N) ceramics. However, the thickness of carbon shell is rather thin, which is slightly different from the SiHfC(N) ceramics.

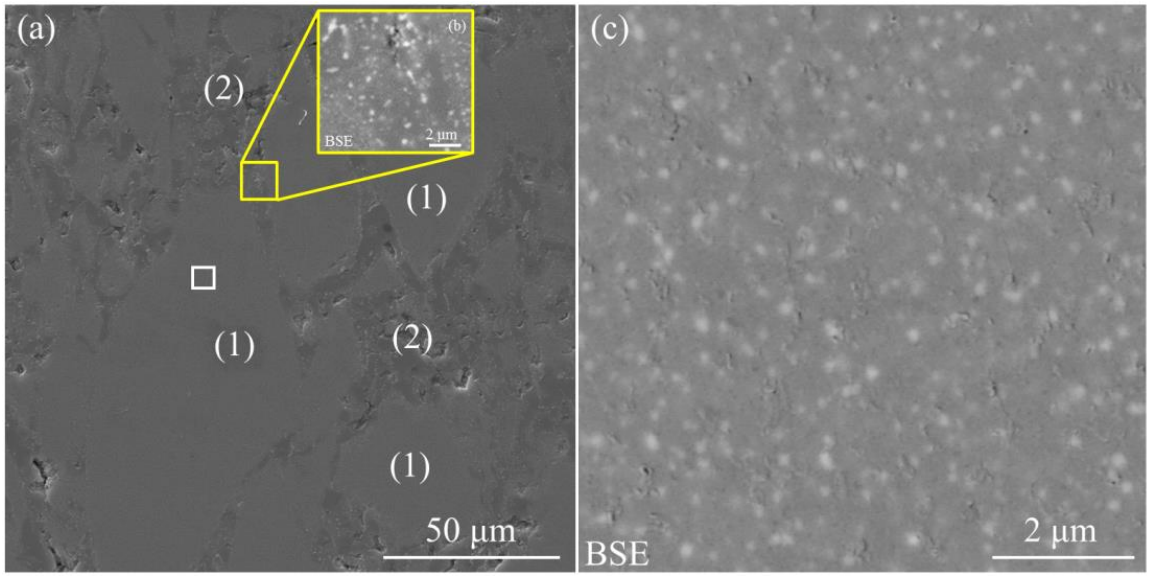

Figure 3. 51 SEM images of dense monolithic SiC/30$Hf_{0.7}Ta_{0.3}$C/C ceramic nanocomposites: *(a)* is in SE mode, inset *(b)* is in BSE mode and *(c)* is also a BSE image enlarged from the white square in *(a)*.

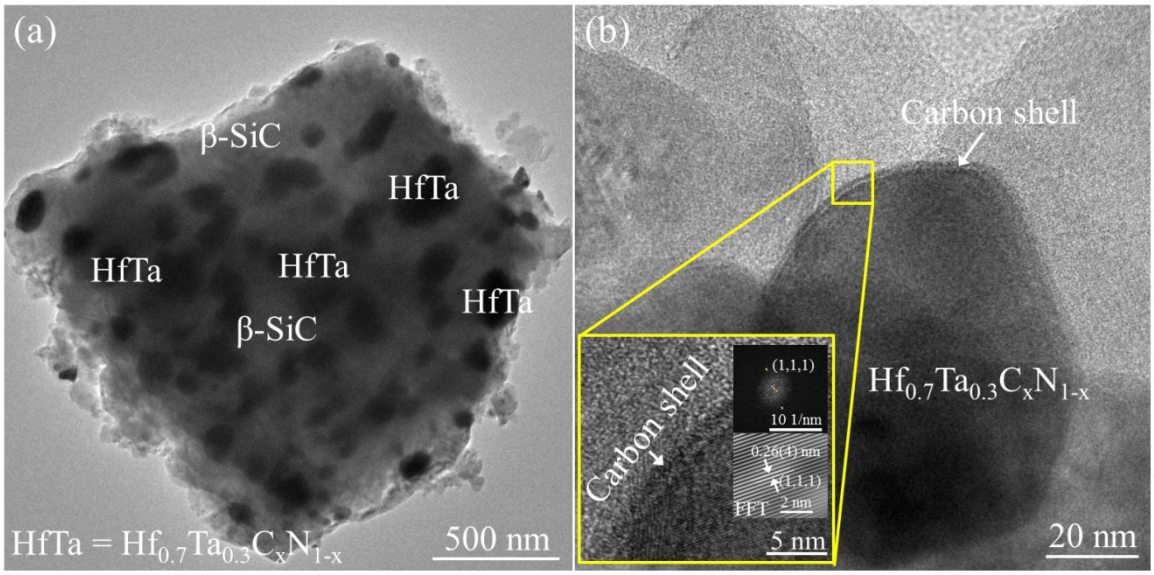

Figure 3. 52 Bright field TEM images of the dense monolithic SiC/30$Hf_{0.7}Ta_{0.3}$C/C ceramic nanocomposites [inset in *(b)* is a high-resolution TEM images].

3.4.3.5 Dense monolithic SiC/30$Hf_{0.2}Ta_{0.8}$C/C ceramic nanocomposites

Figure 3. 53 shows SEM images of the dense monolithic SiC/30$Hf_{0.2}Ta_{0.8}$C/C ceramic nanocomposites. Similarly, two different areas [*i.e.*, area (1) and area (2)] can be observed on the surface. As with the SiTaC(N) monoliths, some larger $Hf_{0.2}Ta_{0.8}C$ grains aggregated in area (2) (Figure 3. 53b), whereas the grain size is much smaller than the aggregated HfC_xN_{1-x} grains within the SiHfC(N) monoliths (Figure 3. 45a). Figure 3. 53c is a BSE image enlarged from the white square in area (1). Thus, the white contrast is the *in situ* formed $Hf_{0.2}Ta_{0.8}C$ phase that homogeneously disperses within β-SiC matrix (dark contrast).

The average diameter of the white phase is around 90 nm with the maximum and minimum diameters of ≈ 160 nm and ≈ 50 nm, respectively.

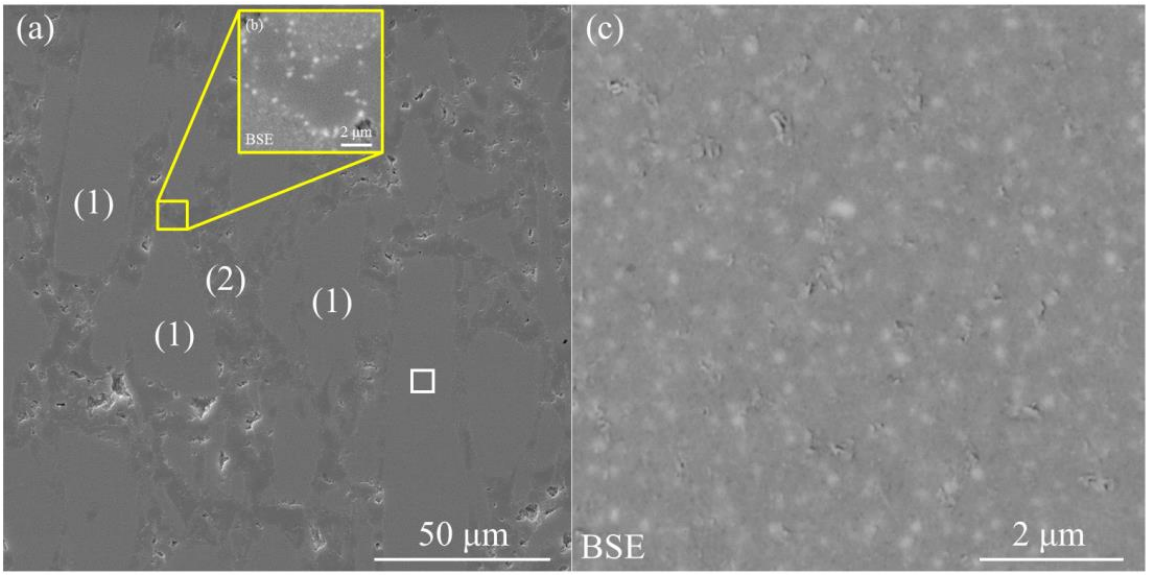

Figure 3. 53 SEM images of the dense monolithic SiC/30$Hf_{0.2}Ta_{0.8}C$/C ceramic nanocomposites: *(a)* is in SE mode, inset *(b)* is in BSE mode and *(c)* is also a BSE image enlarged from the white square in *(a)*.

TEM images of the dense monolithic SiC/30$Hf_{0.2}Ta_{0.8}C$/C ceramic nanocomposites are shown in Figure 3. 54. It clearly shows that $Hf_{0.2}Ta_{0.8}C$ nanograins (dark contrast) homogeneously disperse within β-SiC matrix. The average grain size of $Hf_{0.2}Ta_{0.8}C$ nanograins is ≈ 70 nm with the maximum and minimum grain size of ≈ 125 nm and 30 nm, respectively, which is consistent with the value obtained by XRD refinement (Table 3. 13). The average grain size of β-SiC is ≈ 75 nm (Table 3. 13). Therefore, the dense monolithic SiC/30$Hf_{0.2}Ta_{0.8}C$/C is a ceramic nanocomposite as well. The carbon shell on the $Hf_{0.2}Ta_{0.8}C$ nanograins is also observed on the high resolution TEM images. Similar to the SiTaC(N) and SiHf7Ta3C monoliths, the carbon shell is thinner than that on the HfC_xN_{1-x} nanograins within the SiHfC(N) monoliths.

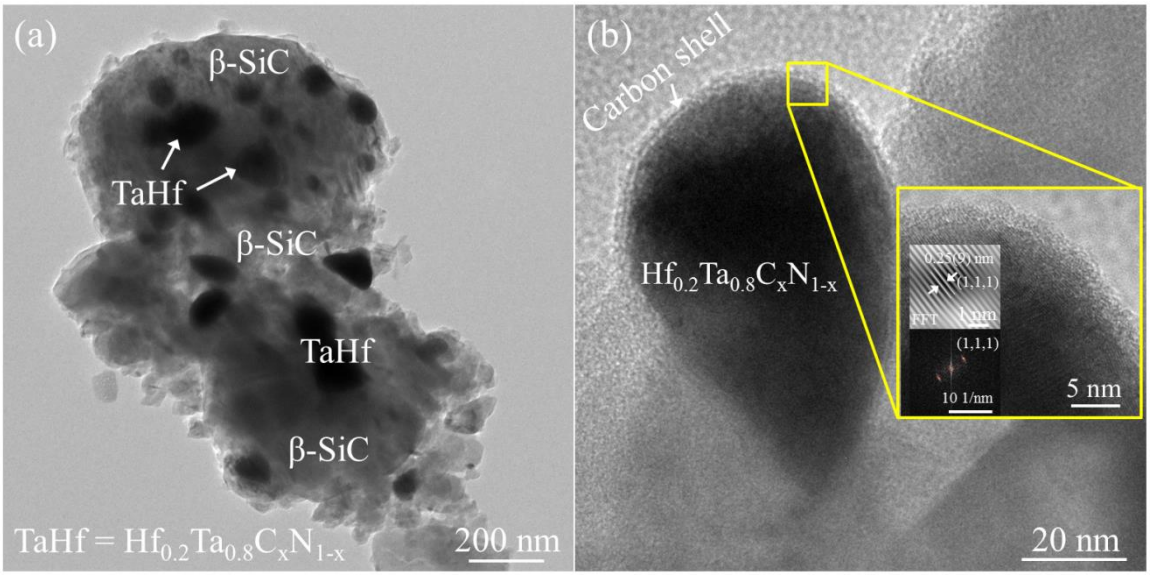

Figure 3. 54 Bright field TEM images of the dense monolithic SiC/30$Hf_{0.2}Ta_{0.8}C$/C ceramic nanocomposites [inset in *(b)* is a high resolution TEM images].

3.4.4 Summary

In this section, a series of dense monolithic SiMC(N) ceramic nanocomposites were successfully fabricated by spark plasma sintering of amorphous SiMC(N) powders (M = Hf, Ta, HfTa), including SiC/30HfC_xN_{1-x}/C, SiC/15HfC_xN_{1-x}/C, SiC/30TaC_xN_{1-x}/C, SiC/30$Hf_{0.7}Ta_{0.3}C_xN_{1-x}$/C and SiC/30$Hf_{0.2}Ta_{0.8}C_xN_{1-x}$/C. For comparison, the SiC/C monoliths were also sintered using amorphous SiC powders coming from pure SMP10. The open porosities (< 1.5%) and SME images prove that the as-sintered monoliths are almost fully dense.

XRD results show that these ceramic monoliths are composed of β-SiC, MC_xN_{1-x} and a small amount of graphite (M = Hf, Ta, Hf_yTa_{1-y}). Similar to the powder ceramic nanocomposites, all of the *x* values of TaC_xN_{1-x}, $Hf_{0.7}Ta_{0.3}C_xN_{1-x}$ and $Hf_{0.2}Ta_{0.8}C_xN_{1-x}$ phases are calculated to be ≈ 1, whereas the *x* value of HfC_xN_{1-x} phase is only 0.83. The $Hf_{0.7}Ta_{0.3}C_xN_{1-x}$ and $Hf_{0.2}Ta_{0.8}C_xN_{1-x}$ solid solutions within the dense monoliths can be observed, and no phase separation occurred on them in spite after being sintered at 2200 ºC. Rietveld refinement of the XRD patterns suggests that the average grain size of both β-SiC and MC_xN_{1-x} are less than 100 nm. The grain size of β-SiC within the SiC/C monoliths is larger than 150 nm, which further proves that the grain growth of β-SiC can be effectively suppressed by introducing of M elements into the single-source precursors.

Interestingly, on the SEM images of the monoliths, a large amount of MC_xN_{1-x} particles with average diameters larger than 100 nm can be clearly observed. This seems to disagree with the results of XRD refinements. The TEM images shows that the MC_xN_{1-x} grains with different diameters from hundreds of nanometers to around twenty nanometers can be observed within the β-SiC matrix, whereas the average grain size is less than 100 nm. This is why we observed many large MC_xN_{1-x} grains in the SEM images,

whereas we calculated the average diameters of the MC_xN_{1-x} grains to be less than 100 nm. Therefore, within the SiMC(N) monoliths, the grain size of MC_xN_{1-x} has a wide-range distribution, but the average value is less than 100 nm. Besides, another explanation is also possible: the larger MC_xN_{1-x} particles observed in the SEM images might be polycrystalline MC_xN_{1-x} with smaller grain size instead of MC_xN_{1-x} single crystals. But, this should be investigated further. Similarly, the MC_xN_{1-x}-carbon core shell structure was observed within all the SiMC(N) monoliths. It clearly shows that the carbon shell on the HfC_xN_{1-x} core is thicker than that on the TaC_xN_{1-x}, $Hf_{0.7}Ta_{0.3}C_xN_{1-x}$ and $Hf_{0.2}Ta_{0.8}C_xN_{1-x}$ cores, which further proves the importance of Hf on the formation of carbon shell.

The boron-doped SiHfC(N) monolith is significantly different from the others. The open porosity (0%) and SEM images reveal that it is already fully dense. Nevertheless, the boron-doped SiHfC(N) monolith is not a nanocomposite in the strictest sense. The average grain size of both β-SiC and HfC_xN_{1-x} are larger than 120 nm. On the SEM image, some HfC_xN_{1-x} grains with diameter even larger than 2 μm can be observed. This is because the boron incorporated into the free carbon forming homogeneously dispersed boron-carbon sintering aids, which significantly enhanced the sinterability of the SiHfC(N) ceramics and the grain size of β-SiC and HfC_xN_{1-x}.

3.5 Laser ablation behavior of the SiHfC(N) ceramics

In this section, the laser ablation results of 2 SiHfC(N) ceramics including the dense monolithic SiHfC(N) ceramic nanocomposites [*i.e.*, SiHfC(N)-SPS] and C_f-reinforced SiHfC(N) CMCs [*i.e.*, C_f/SiHfC(N)] are discussed. The C_f/SiC prepared and ablated under the same condition is discussed as reference.

3.5.1 Dense monolithic SiHfC(N) ceramic nanocomposites

The specific information of the dense monolithic SiHfC(N) ceramic nanocomposites regarding density and open porosity (Table 3. 12), chemical and phase composition (Table 3. 13) as well as surface morphology (Figure 3. 45) and microstructure (Figure 3. 46) is presented in section 3.4.

In the test, the SiHfC(N)-SPS specimens were ablated in air by a CO_2 laser beam (10.6 μm) with a certain ablation time (0.5 ~ 1 s) and power (500~1000 W). Thus, the temperature on the ablated center of the specimens can be estimated to be higher than 3000 ºC according to previously reported ablation experiments on C_f/SiC and C_f/C CMCs under similar testing conditions.[105, 245, 246] During the ablation test, the laser energy was absorbed by the specimens with a certain absorption coefficient, a heat conduction width and a heat penetration depth. Along the heat penetration depth and conduction width, the corresponding temperature decreases progressively from the ablation center to the ablation edge, leading to different ablation mechanisms. In turn, we can estimate the temperature distribution according to the variation of ablation mechanisms.

In air, at temperatures higher than 3000 ºC, some reactions [equation (3- 1) to (3- 5)] as follows can be favorable according to the Ellingham diagram (*i.e.*, temperature dependence of the change in the Gibbs free energy of different possible reactions) reported in Ref[105]. SiC has no melting point, but it decomposes significantly at temperatures higher than 2700 ºC.[167] In addition, the active oxidation of SiC in air starts when the temperature is higher than 3000 ºC; see equation (3- 4).[247] Thus, the loss of β-SiC during laser ablation should be caused by these two processes. The HfC_xN_{1-x} exhibits an ultrahigh melting point (it melts at ≈ 3928 ºC without decomposition) and an ultralow evaporating rate even at 3000 ºC (< 10^{-4} g/(cm^2·s)).[248] Nevertheless, it can be easily oxidized into HfO_2 with relatively lower melting point (≈ 2758 ºC) and higher evaporating rate. Gaseous HfO is the observed products when HfO_2 vaporizes, which has been proved in literature by mass spectrometry.[249] Thus, the loss of HfC_xN_{1-x} in the ablation center should be related to the oxidation and subsequent evaporation process, as described in equation (3- 5). A small amount of free carbon can be observed in the as-prepared SiHfC(N) monoliths. The free carbon can sublimate or be oxidized during laser ablation, as described in equation (3- 1) and (3- 2), respectively.

$$C(s) \rightarrow C(g) \qquad (3\text{- }1)$$

$$2C(s) + O_2(g) \rightarrow 2CO(g) \quad (3\text{- }2)$$

$$7SiC(s) \rightarrow Si(g) + Si_2(g) + Si_2C(g) + 2SiC_3(g) \quad (3\text{- }3)$$

$$SiC(s) + O_2(g) \rightarrow SiO(g) + CO(g) \quad (3\text{- }4)$$

$$HfC_xN_{1-x}(s) + O_2(g) \rightarrow HfO(g) + (1 - x)NO(g) + xCO(g) \quad (3\text{- }5)$$

The photographs and SEM images of the ablated specimens are shown in Figure 3. 55. The specimen ablated at 550 W is denoted as SiHfC(N)-550W, and the one ablated at 840 W is denoted as SiHfC(N)-840W. It clearly shows that, with increasing laser power and exposure time, both the depth and width of the ablation pits increase. After being ablated at 840 W for 1 s, SiHfC(N)-840W—with the thickness of 1 mm—was completely penetrated (Figure 3. 55b). On the rim of ablation pit of SiHfC(N)-550W, some large island-shaped structures can be observed (see the red stars in Figure 3. 55a), while many large bubble-shaped structures can be observed in the ablation pit of SiHfC(N)-840W. The island-shaped structures formed due to the flowing of molten phase, while the bubble-shaped structures should be blown up by the gaseous species. Because the ablation temperature of SiHfC(N)-840W is higher than SiHfC(N)-550W, the viscosity of the molten phase on the SiHfC(N)-840W is lower. Thus, more bubbles can be blown up on the SiHfC(N)-840W sample. The SEM images in Figure 3. 55 are taken in BSE mode in order to identify the distribution of the Hf-containing phase. It reveals that the Hf-containing phase concentrates on the rim of the ablation pit of SiHfC(N)-550W (especially on the island-shaped structures) and on the bubble-shaped structures located in the ablation pit of SiHfC(N)-840W.

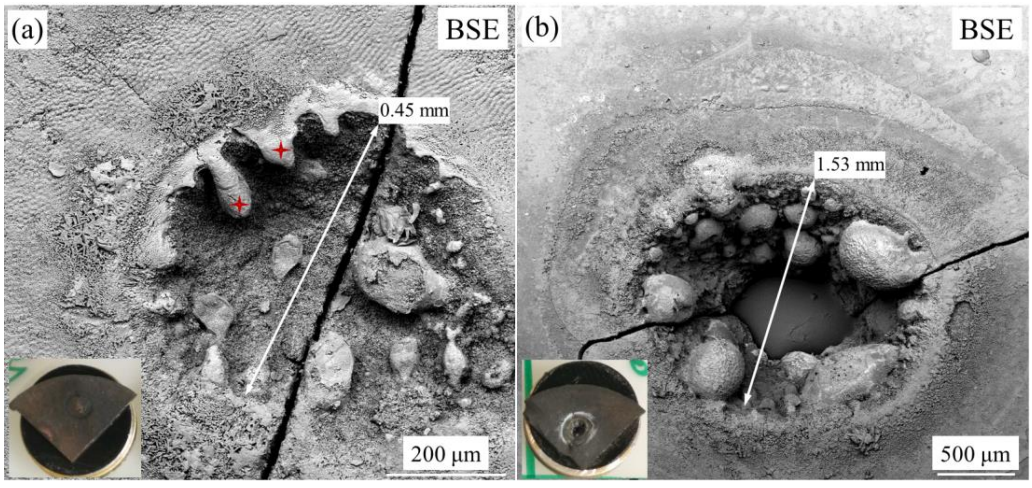

Figure 3. 55 SEM images (in BSE mode) and photographs (insets) of the dense monolithic SiHfC(N) ceramic nanocomposites ablated by a CO_2 laser beam (10.6 µm): *(a)* 550 W, 0.5s; *(b)* 840 W, 1s.

Figure 3. 56 present an enlarged SEM image of a SiHfC(N)-SPS specimen ablated by a 550 W laser beam for 0.5 s [*i.e.*, SiHfC(N)-550W]. Similar to previously reported results[245, 246], three ablation regions can be identified. Region A is the ablation center with a visible pit (see the inside of Cycle 1). Region B is the

transitional zone located between Cycle 1 and Cycle 2. Some deposited crystals can be observed in this region (see B1). Region C is the ablation fringe covered by a glassy layer. Figure 3. 57 are magnified SEM images of different areas within the 3 regions. From the center to the rim of the ablation pit (*i.e.*, Region A), 4 different kinds of surface morphologies (Figure 3. 57, A1 to A4) can be identified.

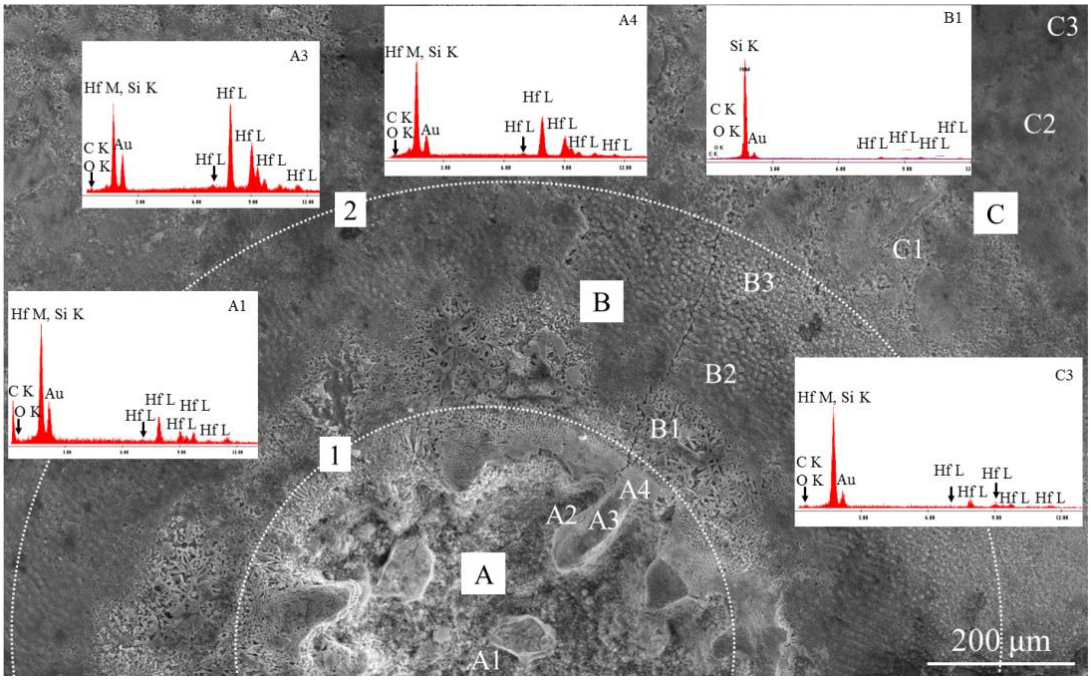

Figure 3. 56 SEM image (in SE mode) of the SiHfC(N)-SPS ablated by a CO_2 laser beam (10.6 µm, 550 W) for 0.5 s.

A1 is the center of the ablation pit and exhibits sheet-like structures with some white depositions. The EDX indicates that A1 is a carbon rich area with ≈ 70 wt.% of carbon, and the rest elements are ≈16 wt.% of Hf, ≈11 wt.% of Si and ≈ 3 wt.% of O. In this area, oxidation, decomposition, sublimation and evaporation takes place during ablation, leading to the formation of sheet-like structures and gaseous species, *e.g.*, C(g), Si(g), Si_2(g), Si_2C (g), SiC_3 (g), SiO (g), HfO (g), CO (g), according to equation (3- 1) to equation (3- 5). The sheet-like structures should be the residual carbon rich phases after decomposition of β-SiC matrix. The gaseous species form immediately and thus lead to a positive gas pressure in the ablation center[245], which can be revealed by the wrinkles in area B1 in Figure 3. 56. Because of the positive gas pressure, the oxygen in ambient atmosphere is not easy to diffuse into the ablation center in a short time. Thus, actually the oxidation mechanism in this region is limited.

Assuming the heat flow of a laser following a Gaussian distribution[105], the temperature of the ablation center goes down in the ending stage. Carbon exhibits the highest sublimation temperature (≈ 3642ºC) among these species; thus, the gaseous carbon should be the first one to deposit. According to the EDX spectrum, the nano-sized white porous phase in A1 (Figure 3. 57) should be the carbon depositions (*i.e.*, graphite). Moreover, the ablation center should be a CO rich atmosphere according to equation (3- 1), (3-

4) and (3- 5). The CO is able to disproportionate into CO_2 and C (graphite) when the temperature cools down (*i.e.*, Boudouard reaction).[250] Therefore, the residual carbon rich phases and deposited carbon in the center of the ablation pit lead to the high carbon content in this area (*i.e.*, A1). Besides, some residual HfC_xN_{1-x}, HfO_2 and SiC may still be in A1 according to the EDX spectrum.

A2 is on the wall of the ablation pit near to an island-shaped structure (Figure 3. 56). The oxidation, decomposition, sublimation and evaporation process must occur as well. The temperature here should be lower than the center during ablation. Thus, the substrate materials are not removed completely, resulting in some island-shaped structures. After ablation, a large amount of white porous graphite similar to that in A1 can be observed. The EDX spectrum suggest that carbon is also the main element (≈ 65 wt.%) in this area, and the rest are ≈ 20 wt.% of Hf, ≈ 9 wt.% of Si and ≈ 6 wt.% of O. Because of the decreased ablation temperature, more residual HfC_xN_{1-x} and HfO_2 can be found according to the EDX results.

A3 is the top of the island-shaped structure (Figure 3. 56). The SEM image in BSE mode (Figure 3. 55) suggests that this area is covered by Hf-containing phase, which is consistent with the EDX spectrum (≈ 83 wt.% Hf, ≈ 4 wt.% of C, ≈ 9 wt.% of Si and ≈ 4 wt.% of O). The magnified SEM image of A3 shows that this area is a rugged Hf-containing scale with some nano-sized particles on the surface (Figure 3. 57). The Hf-containing scale should come from the condensation of HfO_2 from gaseous HfO. Thus, during ablation, the temperature here should be preferable for the condensation of HfO_2 (*i.e.*, the equilibrium vapor pressure of HfO_2 reduced at this temperature) but higher than its melting point (≈ 2758 ºC). Please note that, in the ablation pit (*i.e.*, area A1 and A2), the deposition and condensation processes (including disproportionation, etc.) can only start in the ending stage of ablation when the temperature cools down. However, in the outside areas starting from A3, the deposition and condensation processes can start during ablation because the temperature decreases progressively along the conduction width. That is the reason why we can observe the concentrating of HfO_2 in A3. The liquid HfO_2 intends to flow into the ablation pit, and thus it covers and protects the rim of the ablation pit. It especially concentrates somewhere such as A3 and protects the substrate, leading to the formation of island-shaped structures. The nano-sized particles on the surface of A3 should be partly deposited SiC grains. SiC has no melting point. It starts to decompose at temperatures higher than 2200 ºC and to decompose significantly at temperatures higher than 2700 ºC.[251] In area A3, the temperature is higher than 2750ºC; thus, only a small amount of SiC is deposited.

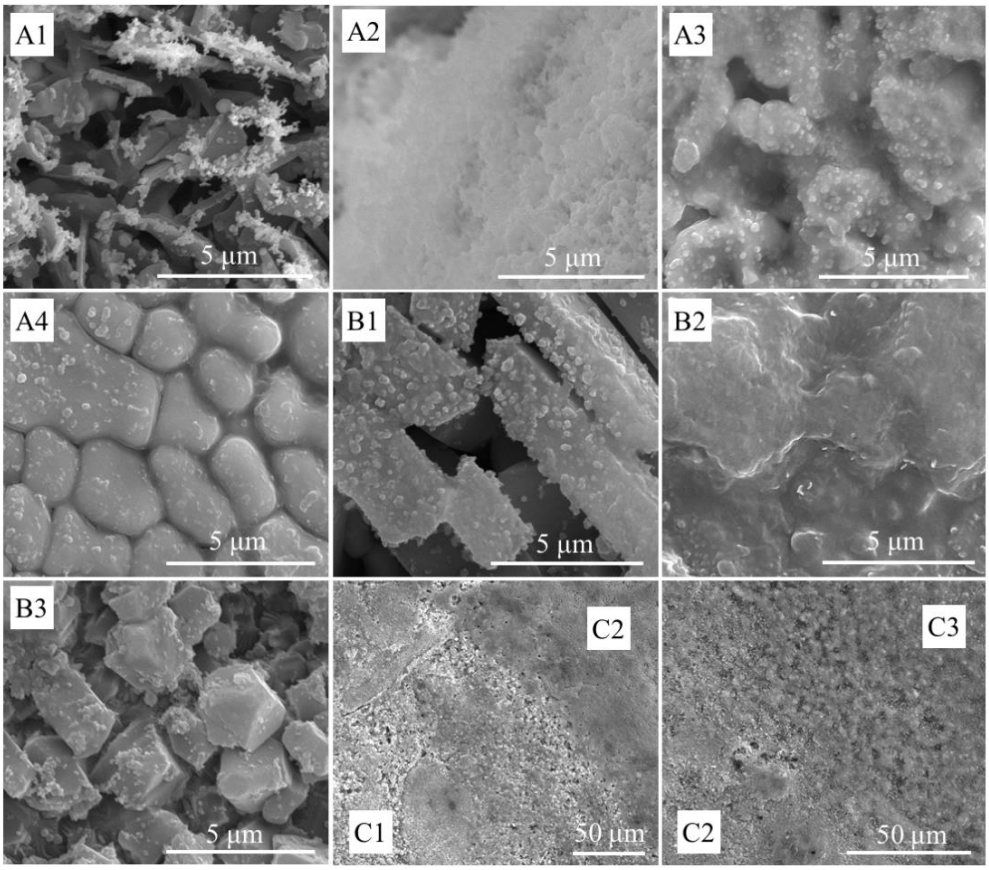

Figure 3. 57 Enlarged SEM images (in SE mode) of the SiHfC(N)-SPS ablated by a CO_2 laser beam (10.6 μm, 550 W) for 0.5 s (A1 to C3 represents the A1 to C3 in Figure 3.51).

A4 is on the rim of the ablation pit. A large amount of bean-like grains (diameter ≈ 2 μm) can be observed in this area. The EDX spectrum (Figure 3. 56) and BSE images (Figure 3. 55) confirm that the grains are HfO_2. A4 is a little far away from the ablation center, and during ablation, the temperature here should be slightly lower than the melting point of HfO_2 (*i.e.*, 2758 ºC). Thus, the HfO_2 grains deposit directly, and they do not completely melt as in A3 (Figure 3. 57). The liquid phase can only be found on the boundary of the HfO_2 grains. The deposition of SiC is limited because of the temperature here is still higher than 2700 ºC.

Region B is the transitional zone where 3 different areas (B1 to B3) can be identified as well. In B1, a lot of flake-like crystals with the thickness of ≈ 2 μm can be observed (Figure 3. 56 and Figure 3. 57). The EDX spectrum shows that Si (≈ 57 wt.%) and C (≈ 31 wt.%) are the main elements in this area. Thus, the flake-like crystals should be deposited SiC. That means the temperature in B1 is lower than the decomposition temperature of SiC (*i.e.,* < 2700 ºC) during ablation, and a majority of SiC deposits in this area. Most of the HfO_2 has deposited in areas A3 and A4. Thus, the Hf content in B1 is very low (see EDX spectrum in Figure 3. 56).

In area B2 and B3, the SiC is also the main phase according to the EDX spectra (not shown). In these

areas, the grain size of SiC is smaller due to the significant deposition of SiC in B1. At the beginning, B2 and B3 should have similar surface morphology. However, SEM images in both Figure 3. 56 and Figure 3. 57 show that the SiC grains in B2 are covered by a glassy layer with wrinkles. The glassy layer should come from the condensation of SiO_2. That means the temperature here should be at least near to the boiling temperature of SiO_2 (*i.e.*, 2230º C). The EDX spectra of the two areas are consistent with the observations (not shown).

Region C is the ablation fringe that can be subdivided into C1, C2 and C3 from inside to outside. Generally, the temperature in region C should be much lower than the ablation center, but due to the heat conduction, the temperature should be sufficient to oxidize the surface of the specimen. Thus, the surface of this region is expected to be oxidized during the ablation test. Interestingly, C1 is not covered by any other species and is not severely oxidized (Figure 3. 56 and Figure 3. 57). It shows similar surface morphology to the as-prepared SiHfC(N) monoliths (Figure 3. 45a). On the contrary, the SEM images taken from C2 and C3 show a glassy layer on the surface of both areas (Figure 3. 57). C1 is not severely oxidized as C2 and C3 should result from the positive gas pressure coming from the ablation center, which prevents the inside diffusion of oxygen. C3 is exposed in the atmosphere with relatively higher oxygen partial pressure. Thus, it shows a SiO_2 glassy layer (Figure 3. 57).

In summary, the laser ablation behavior of the dense monolithic SiHfC(N) ceramic nanocomposites can be described as follows:

In the central region A (*i.e.*, inside Circle 1), decomposition, sublimation, evaporation and oxidation take place during the laser heating, leading to the formation of a visible ablation pit and a large amount of gaseous species, *e.g.*, C(g), Si(g), Si_2(g), Si_2C(g), SiC_3(g), CO(g), SiO(g) and HfO(g). The generation of a large amount of gaseous species leads to a positive gas pressure in the ablation center. Pushed by the positive gas pressure, the gaseous species escape from the ablation center and deposit subsequently from Region A to Region C depending on their phase transformation points (from gas to liquid or solid) and the temperature distribution, forming quite complicated surface morphologies from A1 to C3 (Figure 3. 57).

Carbon has the highest sublimation temperature. Thus, after laser ablation, most of the carbon deposits (*i.e.*, graphite) can be found in the ablation pit (*i.e.*, A1 and A2). In A3, The gaseous HfO condenses near the rim of the ablation pit, forming a liquid HfO_2 phase due to the decreased temperature and corresponding vapor pressure of HfO_2. The liquid HfO_2 flows over the rim of the ablation pit and covers the substrate, protecting the substrate from being directly eroded. Some areas where the liquid HfO_2 concentrates are well protected, resulting in the island-shaped structures (*i.e.*, the HfO_2 covered substrate was not eroded completely). A4 is on the rim of the ablation pit where the temperature is slightly lower than the melting point of HfO_2 (2758 ºC). Thus, the Bean-like HfO_2 crystals can be observed in this area (Figure 3. 57). Because the temperature in this area is still higher than the decomposition temperature of SiC (2700 ºC), only a small amount of SiC particles can be observed in A4.

The rest of the gaseous species come to B1 where the temperature is lower than the decomposition point of SiC. A large amount of SiC deposit here, forming lots of flake-like crystals (Figure 3. 56). After significant deposition, the reset of SiC then deposits in B2 and B3 forming smaller SiC particles. Because the temperature in B2 is approaching the condensation temperature of SiO_2 (≈ 2230ºC), the SiO_2 condenses significantly, forming a glassy layer on the surface of SiC particles. The deposited SiC crystals and condensed SiO_2 seals the surface of substrate, suppressing further oxidation (especially the oxidation of HfC_xN_{1-x}) and erosion during laser ablation. Thus, in region B, the mass loss and erosion of the substrate is limited thanks to the deposited coverings.

In the fringe region (*i.e.*, Region C), the ablation temperatures are much lower than the ablation center, but due to the heat conduction, the temperature should be enough to oxidize the surface of the specimen. Interestingly, the inside part of region C (*i.e.*, C1) is not oxidized as seriously as C2 and C3 due to the positive gas pressure that prevents the inside diffusion of oxygen. The SiO_2 glassy layer formed on the surface of C2 and C3 is able to effectively protect the substrate, especially the HfC_xN_{1-x}.

3.5.2 C_f-reinforced SiHfC(N) ceramic matrix composites

As discussed above, compared with the SiC, the SiHfC(N) exhibits enhanced laser ablation resistant due to the formation of molten HfO_2 that can cover on the rim of ablation pit and hence suppress the ablation process. One practical application of the SiHfC(N) ceramics is to prepare C_f/SiHfC(N) ceramic matrix composites (CMCs) with reduced density, improved fracture toughness and thermal shock resistance. In this part, the C_f/SiHfC(N) CMCs are prepared upon the PIP process. For comparison, the C_f/SiC CMCs are prepared using the same method as well. The photograph and typical load-displacement curves of the as-prepared CMCs are shown in Figure 3. 58. Some general information of the CMCs is given in Table 3. 14. Note that the flexural strength of C_f/SiHfC(N) can be further improved by reducing its open porosity and adjusting the interface between carbon fibers and SiHfC(N) ceramic matrix[104], but this are not discussed in this dissertation. The XRD pattern of the as-prepared C_f/SiHfC(N) is shown in Figure 3. 59. It is almost X-ray amorphous similar to the powder SiHfC(N) ceramics pyrolyzed at 1100 ºC.

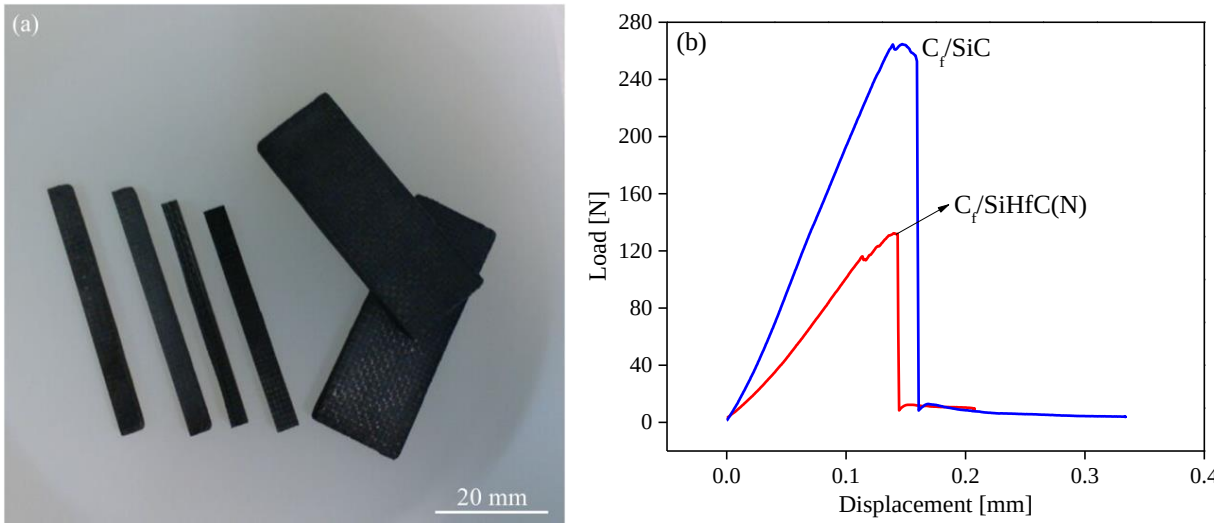

Figure 3. 58 Photograph of the as-prepared C_f/SiHfC(N) and C_f/SiC CMCs (a) and their typical load-displacement curves.

Table 3. 14 General information of the as-prepared C_f/SiHfC(N) and C_f/SiC CMCs.

Name	Processing Temp. [ºC]	Processing Times	Open Porosity	Geometrical Density [g/cm^3]	Percentage of Matrix	Flexural Strength [MPa]
C_f/SiHfC(N)	1100	10	26.0%	1.54	45 wt.%	71.7
C_f/SiC	1100	10	11.8%	1.86	54 wt.%	125.3

The laser ablation test was conducted on both C_f/SiHfC(N) and C_f/SiC CMCs using a 1000 W CO_2 laser beam for 0.5 s. The temperature in the ablation center should be higher than 3000 ºC according to previously reported experiments on the C_f/SiC and C_f/SiHfBCN CMCs.[105, 245, 246] The photographs of ablated specimens are shown in Figure 3. 60. After laser ablation in such a short time, both the specimens retained their integrity, suggesting the high thermal shock resistance of these CMCs. In order to characterize the phase composition of the laser-ablated C_f/SiHfC(N), the ablation spot was cut, ground and characterized using a powder XRD measurement. The XRD pattern is shown in Figure 3. 59. The peaks assigned to β-SiC, HfC_xN_{1-x}, graphite, m-HfO_2 and quartz (SiO_2) can be identified. It is clear that the amorphous SiHfC(N) matrix in the ablation spot almost segregated and crystallized during ablation, forming a SiC/HfC_xN_{1-x}-based composites matrix. Thus, the overall laser ablation of the C_f/SiHfC(N) CMCs might involve two steps: the first step is the phase separation and crystallization of SiHfC(N) matrix, and the second step is the ablation process.

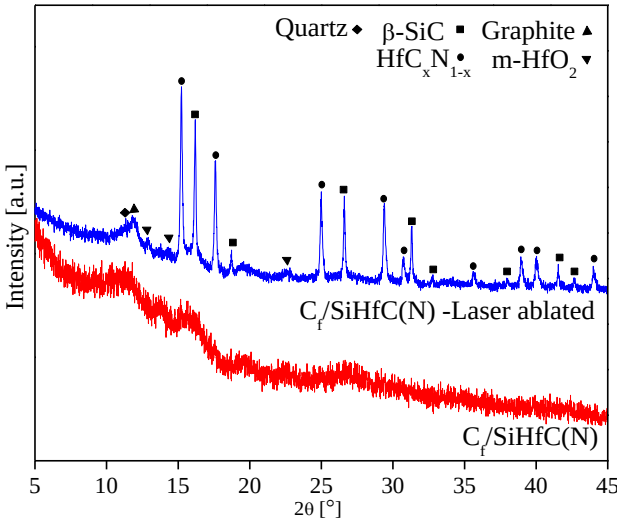

Figure 3. 59 XRD patterns of the as-prepared and laser-ablated C_f/SiHfC(N).

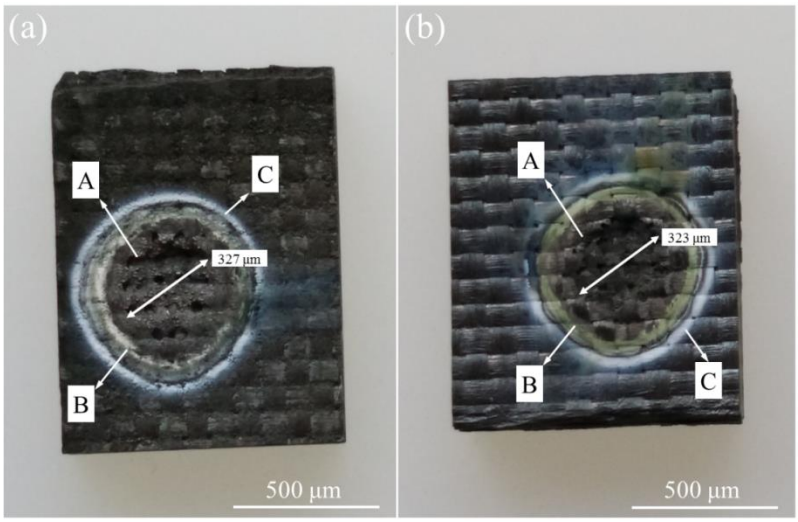

Figure 3. 60 Photographs of the laser ablated C_f/SiHfC(N) (*a*) and C_f/SiC (*b*) CMCs (A, B and C illustrates 3 ablation regions).

Similar to the ablated SiHfC(N) monoliths in section 3.5.1, 3 ablation regions (A, B and C) can be identified clearly on photographs of the laser ablated C_f/SiHfC(N) and C_f/SiC (Figure 3. 60). Region A is the ablation center with an obvious pit. The diameters of the ablation pits on these 2 specimens are almost the same, while the mass ablation rate of C_f/SiHfC(N) and C_f/SiC is 12.6 mg/s and 15.0 mg/s, respectively. That means, the C_f/SiHfC(N) exhibits better laser ablation resistance than C_f/SiC. Region B is a transitional zone where the deposition of gaseous species coming from the ablation center can be observed. On the C_f/SiHfC(N) specimen, 2 kinds of depositions with different color can be found in region B. On the C_f/SiC specimen, only one kind of deposition can be found. According to the color of the deposits and the results of the laser ablation experiments on the dense SiHfC(N) monoliths, the white deposits in region B of C_f/SiHfC(N) should be HfO_2, and the yellowish-green deposits on both specimens are SiC. Region C is the ablation fringe where a white glassy layer can be observed. The glassy layer is

SiO_2 that comes from the condensation of gaseous SiO. Firstly, the gaseous SiO cools down rapidly and condenses to a glassy material, *i.e.*, $(SiO)_n$. Then the air- and moisture- sensitive $(SiO)_n$ is further oxidized in air, forming an SiO_2 layer.

On the photographs of the laser ablated C_f/SiHfC(N) CMCs (Figure 3. 60a) numerous droplet-shaped structures can be observed on the ablation center, which is totally different from the C_f/SiC specimen. The SEM image in Figure 3. 61 shows that the solid droplets adhere to the wall of the ablation pit, encapsulating the ends of the carbon fibers. The EDX spectrum reveals that the surface of the area A1 on a large droplet consists of Si, C, O and Hf, and the Hf content is more than 60 wt.%. The magnified image (Figure 3. 62a) shows that the surface of the solid droplets is covered by a glassy layer with some wrinkles (forming a network). Thus, the composition of the glassy layer might be $HfSi_xO_y$ according to EDX analysis and previously reported results.[105] On the top of some large solid droplets (Figure 3. 62a), a bubble-shaped structure can be observed. The EDX (not shown) and magnified BSE image in Figure 3. 62b reveals that the bubbles possess higher Hf content than the glassy layer. Combined with the significantly cracked surface, the bubble-shaped structures can be assigned to HfO_2.

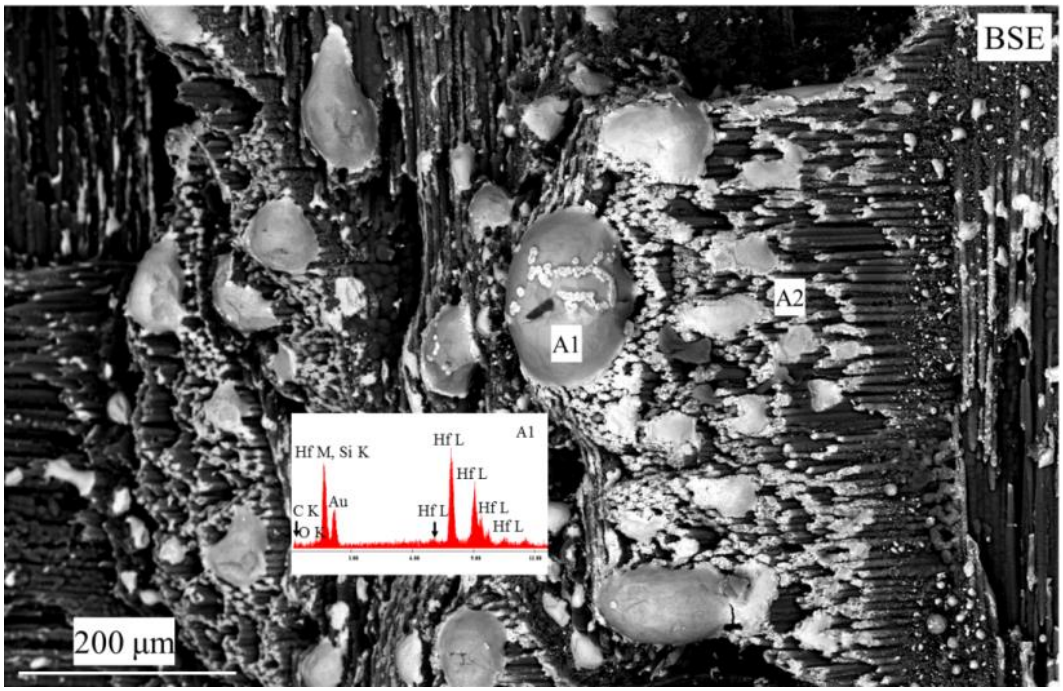

Figure 3. 61 SEM images of the laser ablated C_f/SiHfC(N) CMCs (in BSE mode).

In addition to the droplet-shaped structures, another interesting morphology related to the carbon fibers can be observed. As shown in Figure 3. 62c (*i.e.,* magnification of A2 in Figure 3. 61) and Figure 3. 62d (showing eroded carbon fibers from the ablation center of the ablated C_f/SiC), the morphologies of the carbon fibers in the 2 ablated CMCs are totally different. In case of the C_f/SiC CMCs, the SiC matrix is significantly degraded during ablation and thus the needle-like carbon fibers formed (Figure 3. 62d). In the case of C_f/SiHfC(N), the carbon fibers were covered by some Hf-containing materials similar to the

droplet-shaped structures in Figure 3. 62a and thus retained their original shape. This is likely a result of the presence of Hf within the SiHfC(N) ceramic matrix. Some ablation products of the SiHfC(N) matrix, *i.e.*, HfO_2 or $HfSi_xO_y$, can better protect the carbon fibers than SiC matrix during laser ablation.

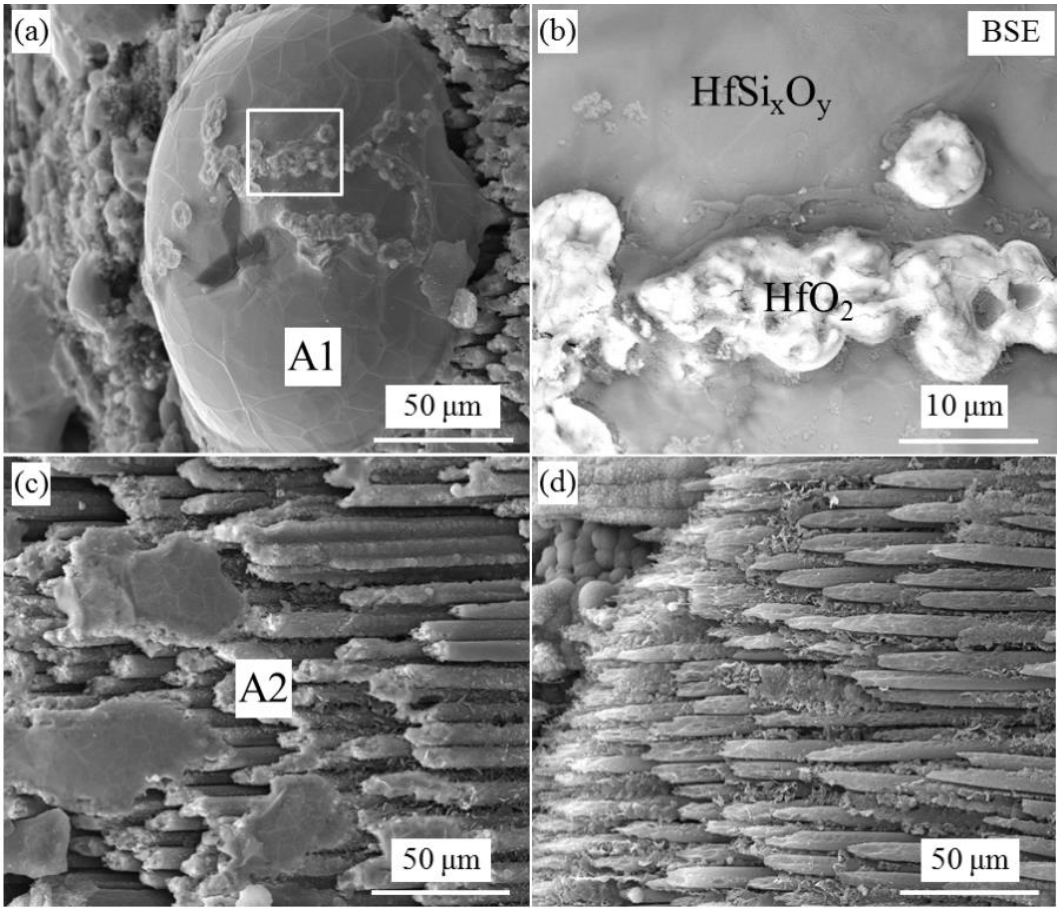

Figure 3. 62 Enlarged SEM images of the laser ablated C_f/SiHfC(N) (*a, b, c*) and C_f/SiC (*d*) CMCs. *(a), (c),* and *(d)* are in SE mode; *(b)* is BSE image magnified from the white square in *(a)*.

3.5.3 Summary

Laser ablation resistance of the bulk SiHfC(N) ceramics was investigated in this section, including dense monolithic SiHfC(N) ceramic nanocomposites and C_f-reinforced SiHfC(N) ceramic matrix composites. The ablation temperature in the center is higher than 3000 ºC. The intrinsic laser ablation behavior was characterized on the dense monolithic SiHfC(N) ceramic nanocomposites. The C_f/SiHfC(N), as a case study for practical applications, was tested and compared with C_f/SiC. During laser ablation, a large amount of gaseous species were generated, leading to a positive gas pressure in the ablation center. Pushed by the positive gas pressure, the gaseous species escape from the ablation center and deposit subsequently from inside of the ablation pit to outside of the ablation spot, depending on their phase transformation points (from gas to liquid or solid) and the temperature distribution; therefore, they form quite complicated surface morphologies. With the addition of the HfC_xN_{1-x} phase, the rim of the ablation pit can be covered by Hf-containing materials (*e.g.*, HfO_2) that are expected to suppress the growth of

ablation pit. The laser ablation tests on C_f/SiHfC(N) and C_f/SiC further prove the positive effect of HfC_xN_{1-x} on enhancing the ultrahigh-temperature performance of SiC-based ceramics. Some ablation products such as HfO_2 and $HfSi_xO_y$ can better protect the carbon fibers than the SiC matrix during laser ablation, which effectively improves their laser ablation resistance.

3.6 Microwave wave absorption performance of SiHfC(N) ceramics

3.6.1 Chemical composition and morphology

The chemical composition and BET specific surface area of SiHfC(N) ceramics used for microwave absorption (MA) are shown in Table 3. 15. In this section, the microwave absorption performance of SiHfC(N) ceramics with different Hf content is discussed. Thus, the amorphous SiC/5HfC_xN_{1-x}/C-1100°C, SiC/15HfC_xN_{1-x}/C-1100°C and SiC/30HfC_xN_{1-x}/C-1100°C ceramics are prepared by pyrolysis of 5Hf-SMP10_80, 15Hf-SMP10_80 and 30Hf-SMP10_80 at 1100 ºC, respectively. The ceramic yield is ≈ 75 wt.%. SiHfC(N) ceramic nanocomposites used for microwave absorption are prepared by annealing of the amorphous ceramics at 1700 ºC for 5 h. For the sake of comparison, SiC/C-1100ºC and SiC/C-1700ºC ceramics are prepared from pure SMP10.

Table 3. 15 Chemical composition and BET specific surface area of SiC/C and SiHfC(N) ceramics.

Name	Elemental content (wt.%)					Atomic ratio	Specific surface area (m^2/g)
	Si	Hf	C	N	O	Hf/Si	
SiC/C -1100°C	61.2	---	32.8	---	6.0	---	3.7
SiC/C -1700°C	68.3	---	31.7	---	0.1	---	7.6
SiC/5HfC_xN_{1-x}/C -1100°C	56.9	3.4	32.8	0.1	6.8	0.01	4.3
SiC/5HfC_xN_{1-x}/C -1700°C	65.8	4.2	30.7	0.0	0.0	0.01	10.5
SiC/15HfC_xN_{1-x}/C -1100°C	53.7	10.1	29.3	1.2	5.7	0.03	5.8
SiC/15HfC_xN_{1-x}/C -1700°C	59.9	11.4	28.6	0.1	0.0	0.03	17.2
SiC/30HfC_xN_{1-x}/C-1100°C[94]	45.8	20.0	25.1	3.9	3.9	0.07	3.2
SiC/30HfC_xN_{1-x}/C-1700°C[94]	51.0	22.9	24.9	0.3	0.1	0.07	23.3

As discussed in section 3.3, there is no loss of Hf during synthesis, and the atomic ratio of Hf/Si does not change during annealing. Thus, the Hf and Si concentration as well as atomic ratio of Hf/Si of SiC/5HfC_xN_{1-x}/C and SiC/15HfC_xN_{1-x}/C can be determined from the weight of the starting materials and the ceramic yield (Table 3. 15). The BET specific surface area of all ceramic powders is small due to the low porosity of the ceramic particles. Figure 3. 63 presents SEM images of SiC/30HfC_xN_{1-x}/C ceramic particles after pyrolysis at 1100°C (a) and after annealing in Ar at 1700°C (b), respectively. All ceramic particles pyrolyzed at 1100°C show a smooth surface morphology, while the ceramic particles annealed at 1700 °C possess some large pores, leading to a slight increase of the BET specific surface area with annealing temperature.

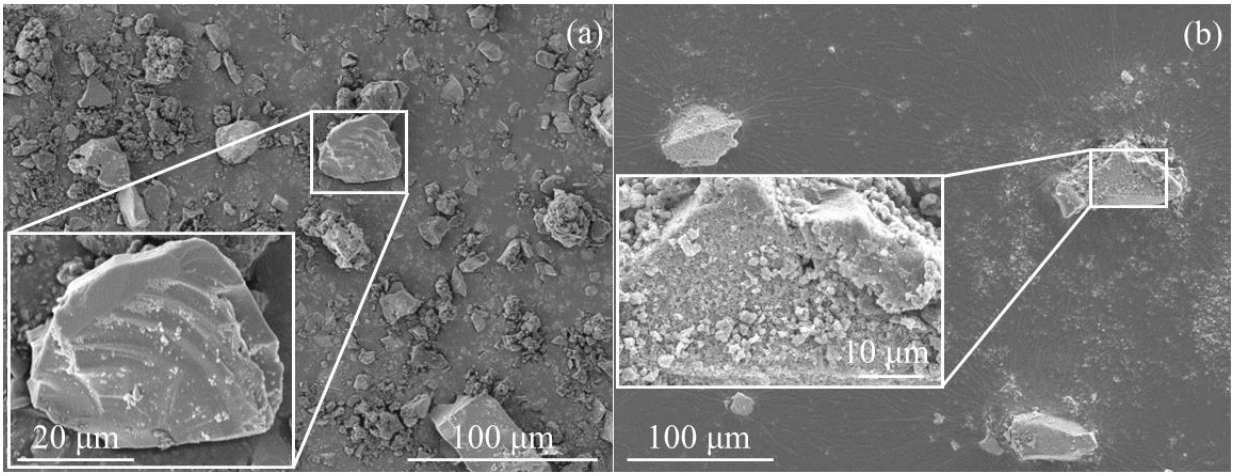

Figure 3. 63 SEM images of SiHfC(N) ceramic particles: SiC/30HfC$_x$N$_{1-x}$/C-1100°C *(a)*; SiC/30HfC$_x$N$_{1-x}$/C-1700°C *(b)*.

3.6.2 Phase composition

X-ray characterization

The X-ray diffraction patterns of SiC/C, SiC/5HfC$_x$N$_{1-x}$/C, SiC/15HfC$_x$N$_{1-x}$/C and SiC/30HfC$_x$N$_{1-x}$/C are shown in Figure 3. 64. After pyrolysis at 1100°C, all of the ceramics are amorphous (Figure 3. 64a). Annealing at elevated temperatures leads to crystallization of β-SiC and HfC$_x$N$_{1-x}$. The reflections of the Hf-containing phase shows slightly higher 2θ values than those of the stoichiometric cubic HfC phase, which indicates that the Hf-containing phase is a solid solution of cubic HfC and HfN (*i.e.*, HfC$_x$N$_{1-x}$). The observed shift of the XRD reflections in Figure 3. 64 (as for the (111) and (200) reflections) can be used to estimate the chemical composition of the HfC$_x$N$_{1-x}$ phase in the as-prepared ceramics via the lattice parameter according to Vegard's law.[218, 219] The average grain size, lattice parameters and volume fraction of crystallized HfC$_x$N$_{1-x}$ and β-SiC were determined by Rietveld refinement of the XRD patterns of the ceramics with the FullProf software (Table 3. 16). The peak shapes were modeled using the Thompson-Cox-Hastings pseudo-Voigt function for average grain size and the pseudo-Voigt function for lattice parameters and volume fraction.[228]

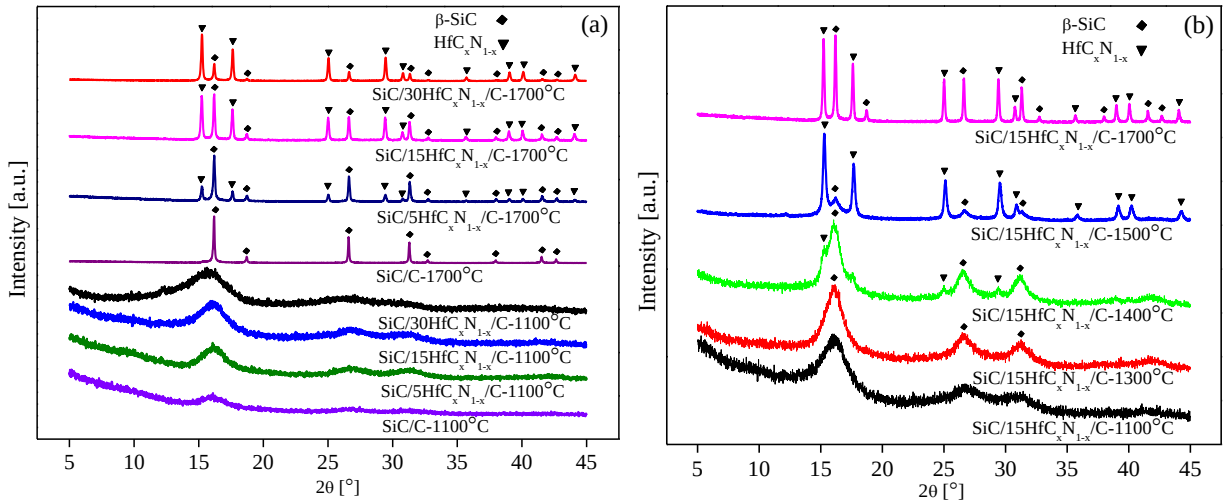

Figure 3. 64 XRD patterns of SiC/HfC_xN_{1-x}/C and SiC/C ceramics *(a)* and of SiC/15HfC_xN_{1-x}/C annealed in the temperature range from 1100 to 1700 °C *(b)*.

Table 3. 16 Average grain size, lattice parameters, volume fractions of HfC_xN_{1-x} and β-SiC as well as the chemical composition of HfC_xN_{1-x} in the β-SiC matrix annealed at different temperatures.

Name	Temp. (℃)	Average Grain Size (nm)		Lattice Parameter a (Å)		Volume Fraction (%)	Chemical composition
		HfC_xN_{1-x}	β-SiC	HfC_xN_{1-x}	β-SiC	HfC_xN_{1-x}	HfC_xN_{1-x}
SiC/C	1700	---	65.5	---	4.3585(5)	0	---
SiC/5HfC_xN_{1-x}/C	1700	77.2	65.1	4.6348(1)	4.3621(0)	1.3	$HfC_{0.97}N_{0.03}$
SiC/15HfC_xN_{1-x}/C	1700	51.2	49.1	4.6304(7)	4.3571(3)	4.2	$HfC_{0.94}N_{0.06}$
SiC/30HfC_xN_{1-x}/C [94]	1700	45.1	33.4	4.6231(1)	4.3518(5)	11.0	$HfC_{0.87}N_{0.13}$
SiC/15HfC_xN_{1-x}/C	1500	18.7	5.4	4.6242(1)	4.3543(9)	3.5	$HfC_{0.88}N_{0.12}$
SiC/15HfC_xN_{1-x}/C	1400	5.1	2.2	4.6013(9)	4.3382(3)	0.2	$HfC_{0.68}N_{0.32}$

Raman spectra

Raman spectra of the ceramics pyrolyzed at 1100°C and annealed at 1300-1700°C are shown in Figure 3. 65. It reveals the presence of sp^2-bonded carbon at all temperatures. After heat-treatment at 1100°C, the D (1350 cm^{-1}) and G (1580 cm^{-1}) bands of carbon are broad due to the high disorder of the segregated carbon.[223] After annealing at 1700 °C, the D and G bands show smaller linewidth, and the intensities of the G and 2D (2700 cm^{-1}) bands grow significantly indicating progressive graphitization (increasing structural ordering). Concerning the concentration dependence we note that the change in the intensities and the width of the Raman lines clearly indicate increasing disorder of carbon with increasing Hf content (Figure 3. 65). The band appearing at 796 cm^{-1} after annealing at 1700 °C is the transverse optical (TO) phonon mode of β-SiC.[222]

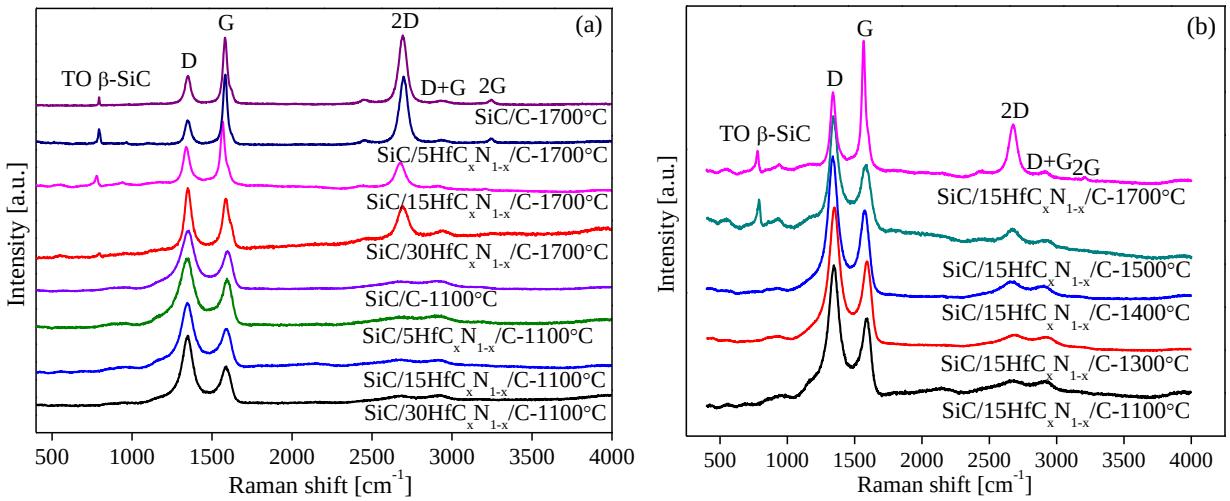

Figure 3. 65 Raman spectra of SiC/HfC$_x$N$_{1-x}$/C and SiC/C ceramics *(a)* as well as of SiC/15HfC$_x$N$_{1-x}$/C ceramics annealed at different temperatures *(b)*.

TEM characterization

The TEM image of SiC/15HfC$_x$N$_{1-x}$/C-1700°C (Figure 3. 66a) reveals the presence of HfC$_x$N$_{1-x}$ precipitations (dark contrast) embedded homogeneously within the β-SiC matrix. The average grain size of the HfC$_x$N$_{1-x}$ particles amounts to ≈ 50 nm, which is consistent with the average grain size estimated via XRD Rietveld refinement (Table 3. 16). As depicted in Figure 3. 66 (b and c), a HfC$_x$N$_{1-x}$-carbon core-shell microstructure is observed, *i.e.*, the nano-sized HfC$_x$N$_{1-x}$ core is encapsulated by a carbon shell with an average thickness of ca. 3~4 nm. The latter consists of disordered carbon (there is no evidence of crystalline structure/graphite planes). The inset in Figure 3. 66a suggests that the β-SiC phase is not encapsulated by a carbon shell (a very thin carbon layer, *e.g.*, few layer graphene, cannot be ruled out, however). Moreover, a network of entangled graphitic carbon ribbons is observed (Figure 3. 66d). Interestingly, part of the carbon ribbons appear to be in close contact with the HfC$_x$N$_{1-x}$-core (Figure 3. 66c, (1)).

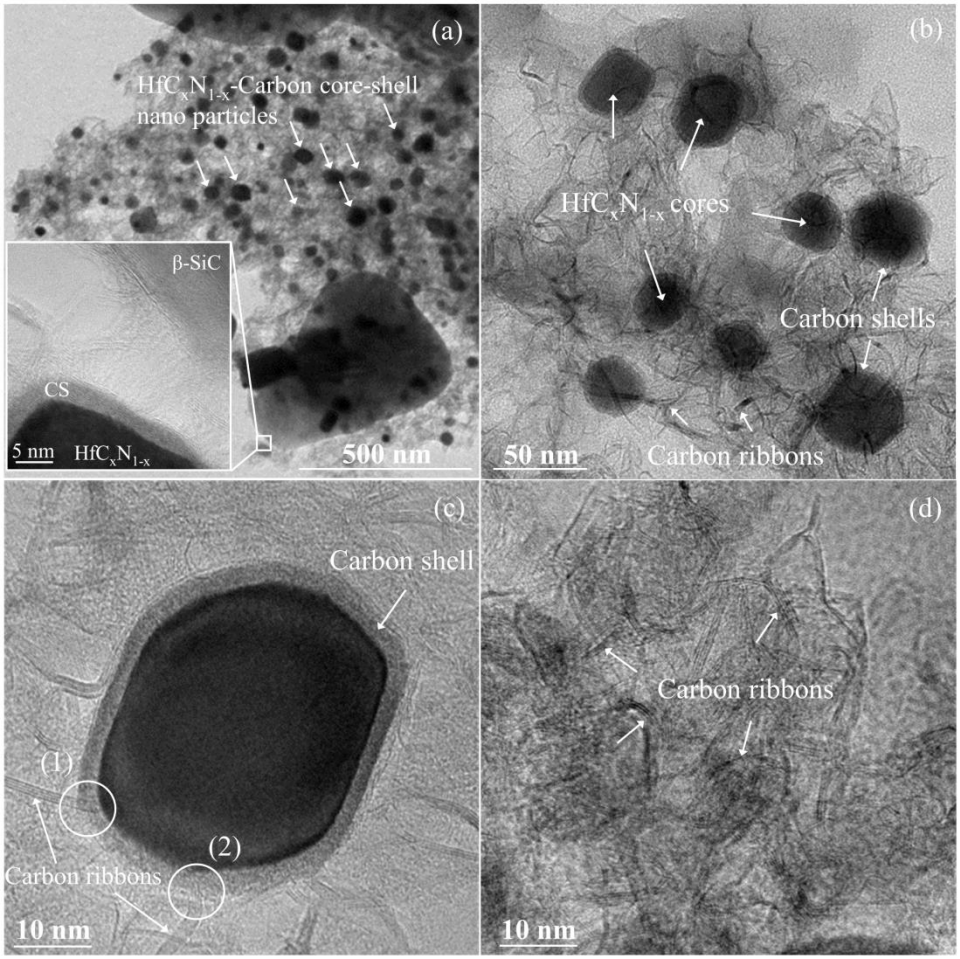

Figure 3. 66 TEM images of SiC/15HfC$_x$N$_{1-x}$/C-1700°C ceramics (*(a), (b) and (c)*) as well as high-resolution image of carbon ribbons *(d)* within the SiC/30HfC$_x$N$_{1-x}$/C-1700°C ceramics. The inset in *(a)* reveals that the β-SiC phase is not encapsulated by carbon shell (CS); the white circles in *(c)* indicate two possible connections between carbon ribbons and HfC$_x$N$_{1-x}$.

3.6.3 Dielectric properties of SiHfC(N) ceramics

Real part of the permittivity

Figure 3. 67 presents the real part of the permittivity ε' of 4:6 mixtures of SiC/HfC$_x$N$_{1-x}$/C-1700°C and of SiC/C-1700°C with paraffin wax in the X-band. The hafnium-free sample (SiC/C-1700°C) shows the highest ε' in the range of 10.3 to 11.5 (average ε' = 10.6), and the SiC/30HfC$_x$N$_{1-x}$/C-1700°C has the lowest value in the range of 5.5 to 6.0 (average ε' = 5.7). The ε' values of the SiC/5HfC$_x$N$_{1-x}$/C-1700°C and SiC/15HfC$_x$N$_{1-x}$/C-1700°C samples are in the range of 9.1 to 9.8 (average ε' = 9.4) and 8.9 to 10.4 (average ε' = 9.6), respectively.

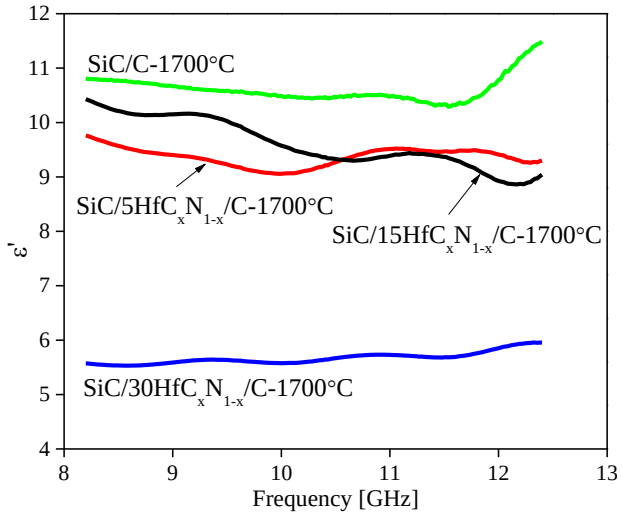

Figure 3. 67 Real part of the permittivity ε' of SiC/HfC$_x$N$_{1-x}$/C-1700°C ceramics and of SiC/C-1700°C.

As reported in the literature, ε' of β-SiC single crystals is around 10.[252] According to the Maxwell Garnett mixing rule[151], ε' of a 4:6 mixture of single-crystalline β-SiC with paraffin wax is estimated to be < 4. Compared to this standard, SiC/HfC$_x$N$_{1-x}$/C-1700°C ceramics and SiC/C-1700°C show enhanced ε'-values (by a factor of < 3) with the enhancement being strongly related to the microstructure.

The SiC/HfC$_x$N$_{1-x}$/C ceramics are characterized by carbon ribbons and HfC$_x$N$_{1-x}$-carbon core-shell nano particles embedded homogeneously within a polycrystalline β-SiC matrix (Figure 3. 66). The enhancement of ε' is due to following three contributions: (i) The grain boundaries between β-SiC nanocrystals give rise to the interfacial polarization.[149] (ii) The graphitic carbon ribbons exhibit high ε' (in the order of 10^2) and also contribute to the enhancement of ε' according to the Maxwell Garnett mixing rule.[253] (iii) The carbon ribbons and HfC$_x$N$_{1-x}$ cores act as conductive fillers and may form a percolative system that can exhibit enhanced real permittivity when the volume fraction of the conductive components approaches the percolation threshold. The enhancement can be described by a power law:[152]

$$\varepsilon' = \varepsilon'_m |x - x_c|^{-s} \qquad (3\text{- }6)$$

where ε'_m is the real part of the permittivity of the matrix, and the exponent s ≈ 1, and x as well as x_c are the volume fraction of the conductive inclusions and the percolation threshold, respectively.

Generally, the percolation threshold strongly depends on the particle size and shape (aspect ratio) of the conductive inclusions. For instance, the percolation threshold was predicted to be less than 5 vol.% when the aspect ratio of the conductive component exceeds 100.[154, 155] For spherical particles with a size below 50 nm the percolation threshold can be lower than 10 vol.%.[156] As shown in Figure 3. 66d, most of the carbon ribbons within the β-SiC matrix possess an aspect ratio < 10, indicating that the percolation threshold x_c is >> 5 vol.%. The actual content of the segregated carbon within SiC/C-1700°C is ≈ 4 vol.%, too low to form a percolative network. Hence, percolation by the ribbon-like carbon part of the composite cannot be responsible for the increase of ε'.

As discussed above for the carbon in SiC/C-1700°C, percolation of HfC_xN_{1-x} particles is unlikely as well. The average particle size of HfC_xN_{1-x} in SiC/5HfC_xN_{1-x}/C-1700°C and SiC/15HfC_xN_{1-x}/C-1700°C is in the range of 50 to 80 nm (Table 3. 16). Accordingly, the percolation threshold for this component is expected to be > 10 vol.%.[156] However, SiC/5HfC_xN_{1-x}/C-1700°C and SiC/15HfC_xN_{1-x}/C-1700°C have rather low HfC_xN_{1-x} contents (1.3 and 4.2 vol. %, respectively), and hence the percolation effect on ε' is irrelevant.

Within the above considerations HfC_xN_{1-x} is taken as a conducting particle. However, the TEM data clearly indicate a core shell structure with a highly conducting HfC_xN_{1-x} core ($\sigma \approx 10^4$ S/cm) covered by a low conducting shell (disordered carbon) with an electrical conductivity $\sigma \approx 10^1$ S/cm.[167, 254] If such core-shell particles form a network, or if a network consisting of core-shell HfC_xN_{1-x}-carbon nanoparticles and carbon ribbons is formed, in both cases the amorphous carbon part acts as a barrier for the electrical transport and consequently shifts the percolation threshold to higher values. The effect is most strong for the composite with the highest HfC_xN_{1-x} concentration (*i.e.*, SiC/30HfC_xN_{1-x}/C-1700°C).

In summary, percolation cannot be of importance for the enhancement of ε' in SiC/HfC_xN_{1-x}/C ceramics reported here since the volume fractions of the conducting particles appear to be well below the respective percolation threshold. Thus, the interfacial polarization of the polycrystalline β-SiC as well as the high ε' of the graphitic carbon ribbons have to account for the increase of ε'.

Imaginary part of the permittivity and loss tangent

The imaginary part of the permittivity (ε'') and the loss tangent ($\tan \delta = \varepsilon''/\varepsilon'$) of dielectric materials are frequently used to describe the dielectric properties in the respective frequency range, here the X-band. Generally, a higher loss tangent implies higher attenuation ability under the condition of impedance match. As shown in Figure 3. 68a, the (average) ε'' of SiC/5HfC_xN_{1-x}/C-1700°C (≈ 3.6) and SiC/15HfC_xN_{1-x}/C-1700°C (≈ 4.8) is remarkably higher than that of SiC/C-1700°C (≈ 1.8) and SiC/30HfC_xN_{1-x}/C-1700°C (≈ 0.7). Further on, the SiC/5HfC_xN_{1-x}/C-1700°C and SiC/15HfC_xN_{1-x}/C-1700°C samples show loss tangent values of ≈ 0.40 and 0.50 which are about 2 and 3 times higher than that of SiC/C-1700°C (loss tan $\delta \approx 0.17$), respectively (Figure 3. 68b).

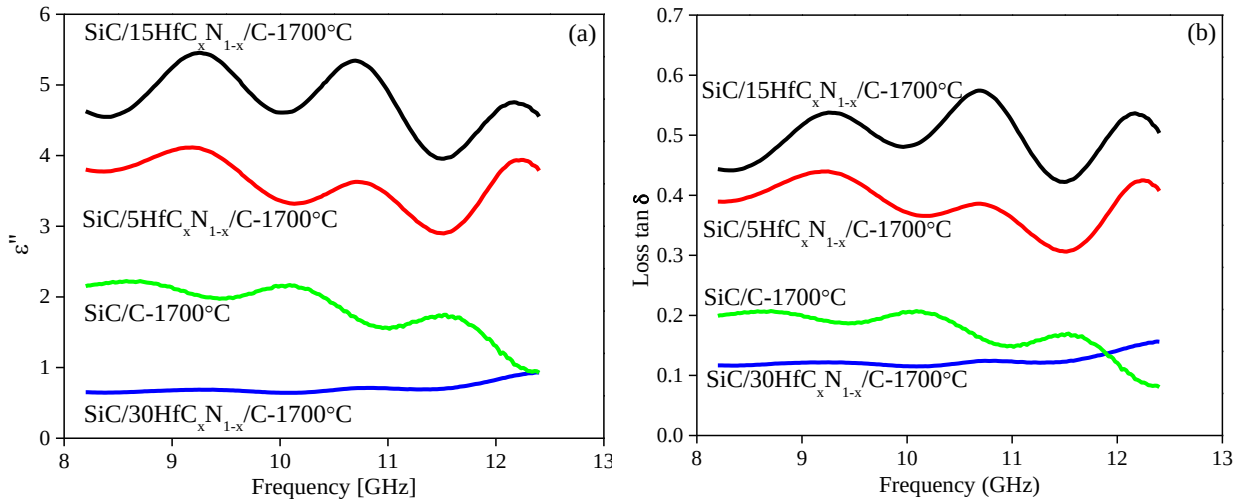

Figure 3. 68 Imaginary part of the permittivity *(a)* and loss tangent *(b)* of SiC/HfC$_x$N$_{1-x}$/C and SiC/C ceramics after annealing at 1700°C.

According to the Debye theory of dielectrics, the ε''can be described by the following equation:

$$\varepsilon'' = \frac{\varepsilon_s - \varepsilon_\infty}{1 + [\omega\tau]^2}\omega\tau + \frac{\sigma}{2\pi f \varepsilon_0} \qquad (3\text{- }7)$$

where ε_s is static relative permittivity, ε_∞ is relative permittivity at high-frequency limit, ω is the angular frequency of incident electromagnetic wave, τ is relaxation time of polarization, σ is electrical conductivity of dielectric materials, f is the frequency of the incident electromagnetic wave, and ε_0 is the permittivity of free space with the value of 8.85×10^{-12} F/m.

In case of composites with carbon (or other highly conducting component) as conductive filler the electronic transport may be approximated by the free electron theory. Equation (3- 7) reduces then to: [130, 140, 255]

$$\varepsilon'' \approx \frac{\sigma}{2\pi f \varepsilon_0} \qquad (3\text{- }8)$$

Accordingly, an increase/decrease of ε''can be directly attributed to the increase/decrease of the electrical conductivity (σ).

As aforementioned, the SiC/C and SiC/HfC$_x$N$_{1-x}$/C ceramics are multiphase composites with an *in situ* formed semiconducting β-SiC matrix and electrically conductive segregations, namely graphite-like carbon ribbons and HfC$_x$N$_{1-x}$-carbon core-shell nano particles. The conductive components can form networks with different connections (Figure 3. 69), which determines the ε''or electrical conductivity of the ceramics, respectively. The electrical conductivity of the graphitic carbon ribbons is of the order of 10^3 S/cm.[254] The conductivity σ_{cs} of carbon coated HfC$_x$N$_{1-x}$ can be approximated by the Maxwell-Garnett equation: [152, 254, 256]

$$\sigma_{cs} = \sigma_s \frac{1+2Y\frac{\sigma_c-\sigma_s}{\sigma_c+2\sigma_s}}{1-Y\frac{\sigma_c-\sigma_s}{\sigma_c+2\sigma_s}} \quad (3\text{- }9)$$

$$Y = \left(\frac{d}{2t+d}\right)^3 \quad (3\text{- }10)$$

where σ_c, σ_s are the electrical conductivity of HfC_xN_{1-x} core and carbon shell, respectively; d is the diameter of the HfC_xN_{1-x} core (40 ~ 80 nm), t the thickness of the carbon shell (3~4 nm), and thus Y is ≈ 0.7 for all the SiC/HfC_xN_{1-x}/C samples. The HfC_xN_{1-x} core exhibits high electrical conductivity with values in the order of 10^4 S/cm. The TEM data (Figure 3. 66) and Raman spectra (Figure 3. 65) clearly indicate that the carbon shell is disordered suggesting σ values of the order of 10^1 S/cm at RT.[257] Taking σ_c = 10^4, σ_s = 10 S/cm and Y = 0.7, a HfC_xN_{1-x}-carbon core-shell nano particle has an electrical conductivity of ≈ 80 S/cm.

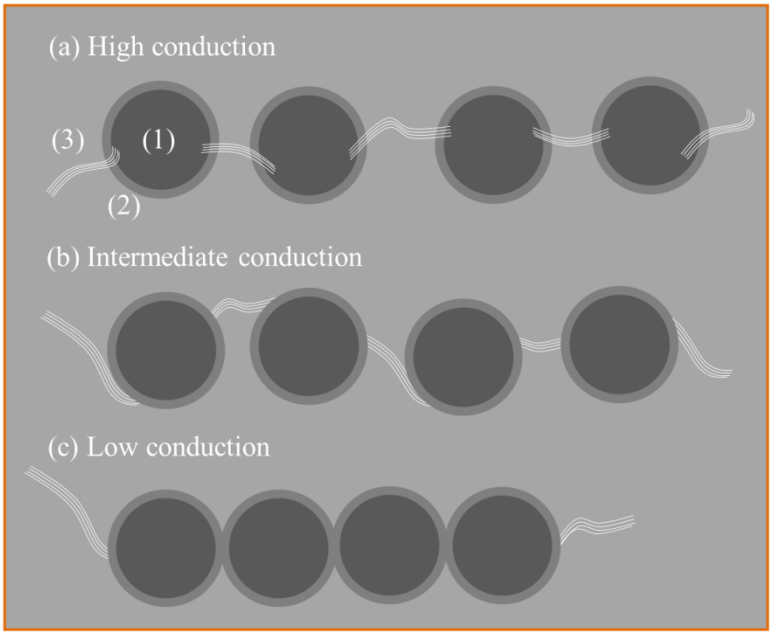

Figure 3. 69 Possible connections of the conductive inclusions in the β-SiC matrix [*(1), (2)* and *(3)* are HfC_xN_{1-x} core, carbon shell and carbon ribbons, respectively].

As depicted schematically in Figure 3. 69, the HfC_xN_{1-x}-carbon core-shell particles can be connected to carbon ribbons in two different ways: forming a direct (highly conductive) core-ribbon connection or a (low conductive) carbon shell-carbon ribbon contact. If several HfC_xN_{1-x} cores are linked via carbon ribbons (Figure 3. 69a), the formation of a network is facilitated where electrons can travel fast over long distances thereby enhancing the electrical conductivity or ε'' respectively. If the carbon ribbons are not bound directly to the core of the HfC_xN_{1-x} particles but form contacts with the carbon shell (Figure 3. 69b and 7c), the conductivity will be significantly reduced because the carbon shell acts as a barrier for the transport. This is similar to other composites with core shell-structured particles, *e.g.*, carbonaceous shell-coated Ag-particles and Al_2O_3-coated Al-particles.[256, 258]

As shown in Figure 3. 68, ε'' and the loss tangent (*tan* δ) increase from SiC/5HfC_xN_{1-x}/C-1700°C to

SiC/15HfC$_x$N$_{1-x}$/C-1700°C, most likely caused by an increase of (highly conductive) direct HfC$_x$N$_{1-x}$ core-carbon ribbon contacts; see Figure 3. 69a. The SiC/30HfC$_x$N$_{1-x}$/C-1700°C with a HfC$_x$N$_{1-x}$ content of ≈ 11.0 vol.%, exhibits the lowest ε' and $tan\ \delta$ values, indicating that in this case the contact between (low conducting) carbon shells (Figure 3. 69c) dominates, in accordance with the clustering of HfC$_x$N$_{1-x}$ particles seen in the TEM data reported in ref.[94] The dc-electrical conductivity (σ_{dc}) of the ceramic-paraffin wax composite samples (Figure 3. 70) further support the discussion above. As can be seen from Figure 3. 70, the σ_{dc}- and ε"- values follow the same trend with Hf-concentration. The σ_{dc} values differ, however, from the respective conductivity values calculated by equation (3- 8). This is to be expected since the electronic transport is not uniform in our materials and comprises very different type of transport mechanisms, notably fast transport along carbon chains and activated inter-chain transport.

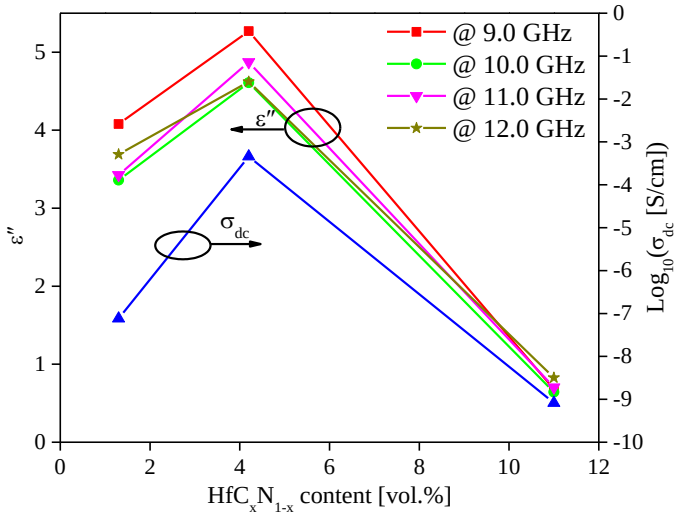

Figure 3. 70 DC conductivity σ$_{dc}$ and imaginary part of the permittivity ε" of the composite samples as a function of the HfC$_x$N$_{1-x}$ content.

3.6.4 Microwave absorption performance at room temperature

Making use of the experimental results for ε', ε'' $tan\ \delta$ and the thickness d of the composite, the reflection loss of the ceramic-paraffin wax mixtures can be calculated by equation (1- 1) in section 1.3.1.

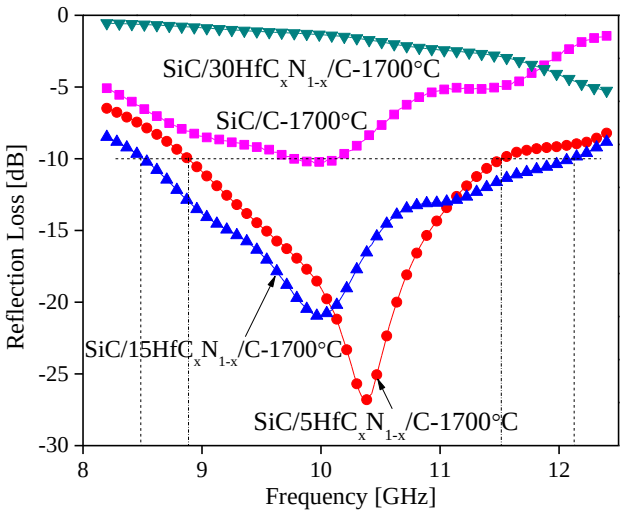

Figure 3. 71 Reflection loss at RT of different SiC/HfC$_x$N$_{1-x}$/C and SiC/C ceramics annealed at 1700 °C (sample thickness: 2.5 mm).

Figure 3. 71 shows the reflection loss of the SiC/HfC$_x$N$_{1-x}$/C-1700°C ceramics for a sample thickness of 2.5 mm. The minimum reflection loss of SiC/5HfC$_x$N$_{1-x}$/C-1700°C and SiC/15HfC$_x$N$_{1-x}$/C-1700°C is -27dB and -21 dB, while that of SiC/C-1700°C amounts to -10 dB. The effective absorption bandwidth (EAB) of SiC/5HfC$_x$N$_{1-x}$/C-1700°C and SiC/15HfC$_x$N$_{1-x}$/C-1700°C are 2.6 GHz and 3.6 GHz which cover 62 % and 85 % of the X-band, respectively. In comparison, the EAB of SiC/C-1700°C is 0.3 GHz or 8 % of the X-band, respectively. SiC/30HfC$_x$N$_{1-x}$-1700°C has rather weak absorption capability in the X-band (RL > -5 dB). As a main result, we note that the 1.3 and 4.2 vol.% HfC$_x$N$_{1-x}$ containing composites show reflection loss superior to the hafnium free sample SiC/C-1700°C.

The MA performance of the SiC/15HfC$_x$N$_{1-x}$/C ceramic (sample thickness 2.5 mm) annealed at different temperatures is shown in Figure 3. 72. Only the SiC/15HfC$_x$N$_{1-x}$/C-1700°C sample shows a distinct reflection loss consistent with the observed ε''(≈ 4.8) and loss tangent value (≈ 0.4). There is a strong correlation between the microwave absorption and the microstructure of the nanocomposites. As explained in section 3.6.2, the intensity ratio of the G band and D band (I(G)/I(D)) in the Raman spectra is a measure of the structural ordering in carbon.[94] The higher I(G)/I(D), the higher the ordering (or conductivity) of carbon. The $\varepsilon'$of SiC/15HfC$_x$N$_{1-x}$/C can be presented as a function of this order parameter (Figure 3. 73). Up to I(G)/I(D) ≈ 0.6 (SiC/15HfC$_x$N$_{1-x}$/C-1500°C) the $\varepsilon''$is only weakly increasing, whereas it is significantly enhanced at higher I(G)/I(D)-value.

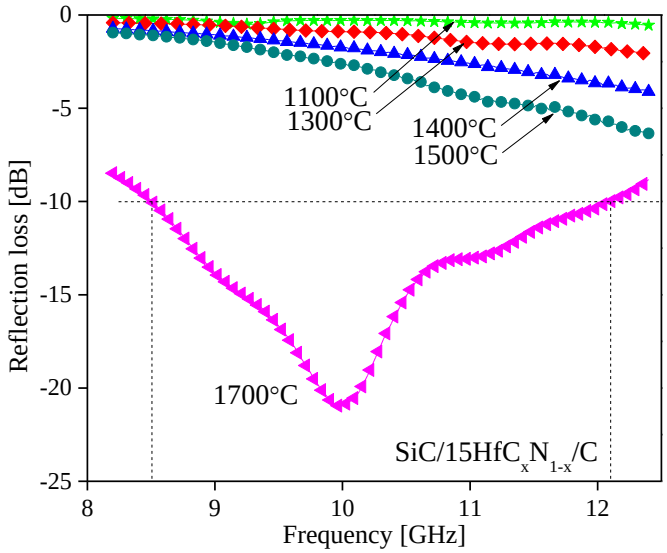

Figure 3. 72 Reflection loss at RT of SiC/15HfC$_x$N$_{1-x}$/C ceramics annealed at different temperatures (sample thickness: 2.5 mm).

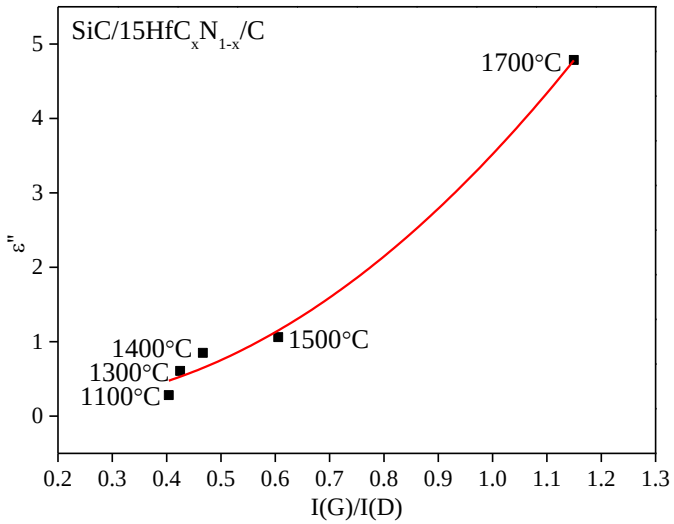

Figure 3. 73 The correlation between the intensity ratio of the Raman G and D bands [I(G)/I(D)] and the imaginary part of the permittivity (ε'') of SiC/15HfC$_x$N$_{1-x}$/C ceramics annealed at different temperatures.

According to equation (1- 1) and the design rules for single-layer radar absorbing coatings, the complex permittivity and the sample thickness *d* determine the reflection loss of dielectric materials.[259] Here, the reflection losses of SiC/5HfC$_x$N$_{1-x}$/C-1700°C and SiC/15HfC$_x$N$_{1-x}$/C-1700°C were calculated with *d* as variable. As shown in Figure 3. 74, both samples exhibit promising MA performances within the thickness range 2.0 - 3.0 mm. Within this range the effective absorption bandwidth (EAB) is broader than 2.0 GHz (Table 3. 17). In the case of SiC/15HfC$_x$N$_{1-x}$/C-1700°C (highest conducting sample), the broadest EAB is observed (3.6 GHz). Among the various samples shown in Figure 3. 74, the minimum reflection loss of SiC/5HfC$_x$N$_{1-x}$/C-1700°C and SiC/15HfC$_x$N$_{1-x}$/C-1700°C are -47 dB and -32 dB, respectively.

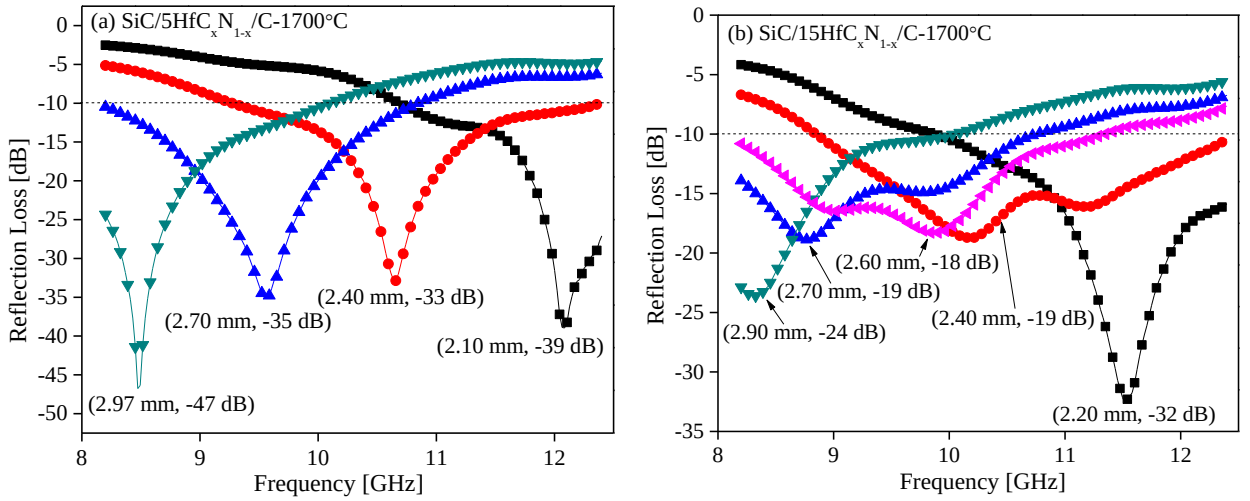

Figure 3. 74 Reflection losses at RT of the SiC/5HfC$_x$N$_{1-x}$/C-1700°C *(a)* and SiC/15HfC$_x$N$_{1-x}$/C-1700°C *(b)* samples in X-band with respect to thickness variation. Sample thickness (in mm) and minimum reflection loss (in dB) are given in brackets.

Table 3. 17 Effective absorption bandwidths (EAB) of SiC/5HfC$_x$N$_{1-x}$/C-1700°C and SiC/15HfC$_x$N$_{1-x}$/C-1700°C for different values of the sample thickness.

Sample 1	**SiC/5HfC$_x$N$_{1-x}$/C-1700°C**										
Thickness (mm)	2.00	2.10	2.20	2.30	2.40	2.50	2.60	2.70	2.80	2.90	2.97
EAB (GHz)	0.90	1.70	2.02	2.42	3.09	2.60	2.60	2.63	2.35	2.08	1.89
Sample 2	**SiC/15HfC$_x$N$_{1-x}$/C-1700°C**										
Thickness (mm)	2.00	2.10	2.20	2.30	2.40	2.50	2.60	2.70	2.80	2.90	3.00
EAB (GHz)	0.41	1.91	2.52	3.19	3.55	3.57	3.13	2.27	2.23	1.83	1.03

3.6.5 Summary

The complex permittivity of SiHfC(N) ceramic nanocomposites is intimately connected with their microstructure formed at the different annealing temperatures (1100-1700 °C). The real part of the permittivity ε' is mainly determined by the dielectric properties of segregated graphitic carbon as well as the interfacial polarization of polycrystalline β-SiC, and the imaginary part ε'' by the increasing graphitization/structural ordering of carbon with temperature. The introduction of HfC$_x$N$_{1-x}$ enhances the dielectric loss of SiC/5HfC$_x$N$_{1-x}$/C-1700°C and SiC/15HfC$_x$N$_{1-x}$/C-1700°C in the X-band. The minimum reflection loss of SiC/5HfC$_x$N$_{1-x}$/C-1700°C and SiC/15HfC$_x$N$_{1-x}$/C-1700°C are -47 dB and -32 dB, and the effective absorption bandwidth amount to 3.1 and 3.6 GHz, respectively. At higher HfC$_x$N$_{1-x}$ contents the disordered carbon shell on the HfC$_x$N$_{1-x}$ core acts as a barrier for the transport and clustering of the HfC$_x$N$_{1-x}$ particles reduces ε'' or the reflection loss, respectively. Adjusting the microstructure by annealing at high temperatures (T >1500 °C) and the chemical composition by the ratio of the precursor materials TDMAH/AHPCS allows for tuning of the minimum reflection loss and absorption frequency range. Combined with their exceptional chemical and oxidation stability, these new nanocomposites are

especially suited for electromagnetic interference shielding in harsh environment (*e.g.*, at high temperatures, in corrosive media).

3.7 EMI shielding performance of dense monolithic SiHfC(N) ceramic nanocomposites

3.7.1 Phase composition, morphology and flexural strength

General information of the dense monolithic SiC/15HfC$_x$N$_{1-x}$/C-35mm ceramic nanocomposite and SiC/C-35mm composite used for EMI shielding measurements including density, open porosity (Table 3. 12), XRD patterns (Figure 3. 43) as well as chemical and phase composition (Table 3. 13) are presented in section 3.4. The SEM images are shown in Figure 3. 75. The open porosity and SEM images prove that the samples are dense monoliths. On the surface of all monoliths, two kinds of different areas [*i.e.*, area (1) and area (2)] can be observed. Area (1) is from the inside of the ceramic particles used for sintering, and area (2) is from the surface-near regions of the ceramic particles. It is clear that the open pores are mainly in area (2), while area (1) is fully dense. Figure 3. 75b is a BSE image magnified from area (1). Thus, the homogeneously dispersed white phase is the *in situ* formed HfC$_x$N$_{1-x}$ grains, and the matrix phase with dark contrast is β-SiC. The average diameter of the white phase is around 180 nm with the maximum and minimum diameters of ≈ 270 nm and ≈ 120 nm, respectively. Moreover, in area (2) of the SiC/15HfC$_x$N$_{1-x}$/C-35mm, some larger HfC$_x$N$_{1-x}$ grains with the diameters of ≈ 2.2 μm can be observed, which is due to the higher diffusion coefficient of Hf in the surface-near regions of ceramic particles.[241] However, the results of XRD refinements indicate that the average grain sizes of the HfC$_x$N$_{1-x}$ and β-SiC are ≈ 78 nm and 70 nm (Table 3. 13), respectively. This is because a large amount of smaller HfC$_x$N$_{1-x}$ grains (< 100 nm) also exist within the matrix, which was proved by TEM images of dense monolithic SiC/30HfC$_x$N$_{1-x}$/C ceramic nanocomposites (Figure 3. 46). Because the average grain sizes of both HfC$_x$N$_{1-x}$ and β-SiC are less than 100 nm, the dense monolithic SiC/15HfC$_x$N$_{1-x}$/C-35mm are ceramic nanocomposites. The average grain size of β-SiC within the SiC/C-35mm is around 160 nm (Table 3. 13), which is much larger than that of β-SiC within the SiHfC(N) ceramics.

The four-point bending flexural test shows that the average flexural strength of the as-sintered dense monolithic SiC/C-35mm and SiC/15HfC$_x$N$_{1-x}$/C-35mm ceramics is 254 ± 22 MPa and 320 ± 25 MPa, respectively. The SiC/15HfC$_x$N$_{1-x}$/C monoliths show that enhanced flexural strength might be due to the reduced grain size of β-SiC matrix (Table 3. 13). Please note that both bulk ceramics are sintered without any sintering aids. Thus, tinny flaws and defects than can act as crack initiators are unavoidable, even though the ceramics are almost fully dense. That means if some sintering aids are added, the flexural strength of the dense monolithic SiHfC(N) ceramic nanocomposites could be significantly improved. Moreover, the flexural strength is measured using a four-point method. More flaws and defects are possible within the loaded area, thus reducing the measured flexural strength values. In this view, the dense monolithic SiHfC(N) ceramic nanocomposites exhibit promising mechanical properties.

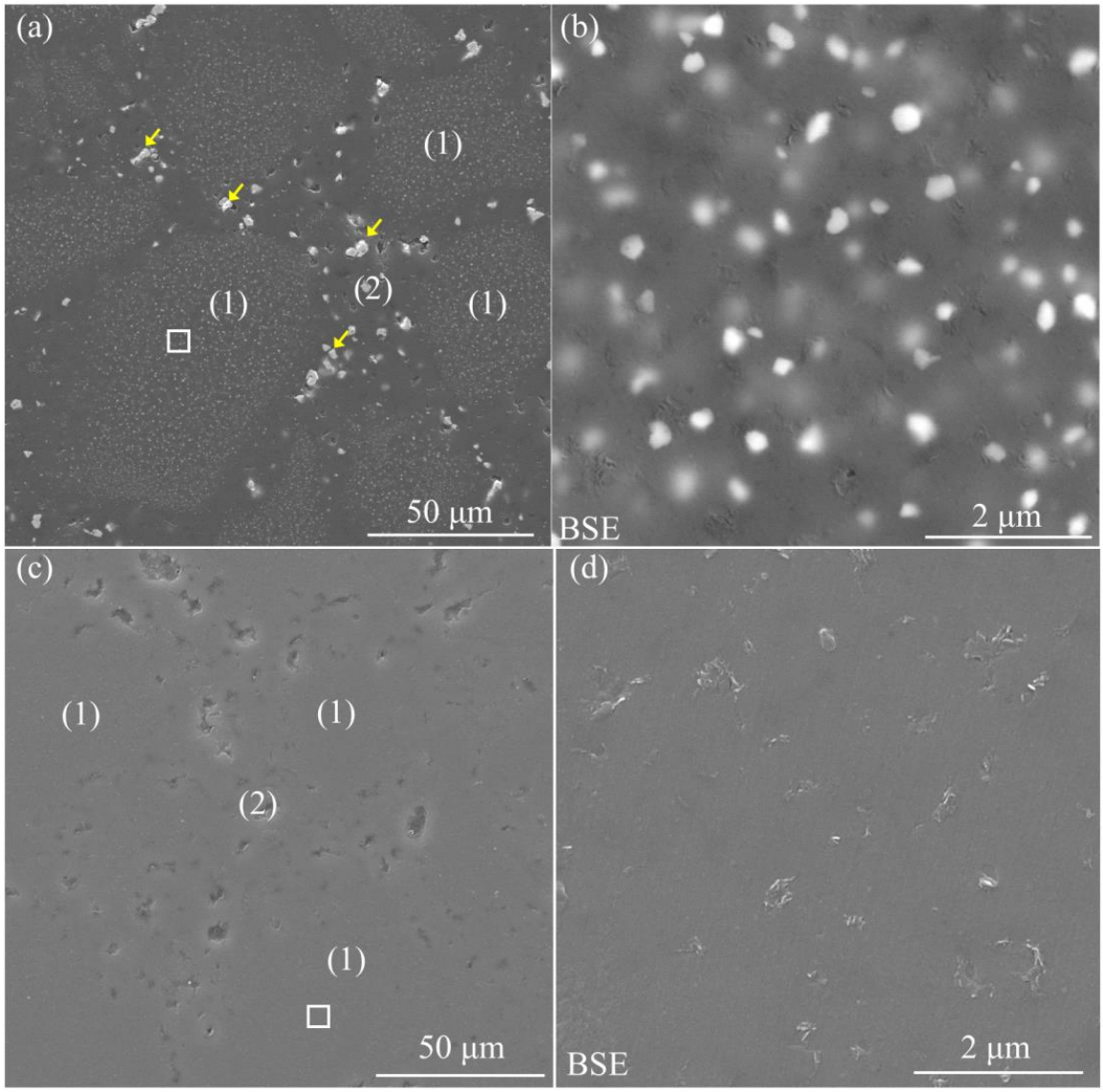

Figure 3. 75 SEM images of the dense monolithic SiC/15HfC$_x$N$_{1-x}$/C-35mm *(a, b)* and SiC/C-35mm *(c, d)* ceramics nanocomposites: *(a)* and *(c)* is in SE mode; *(b)* and *(d)* is in BSE mode.

3.7.2 EMI shielding performance at room temperature

The EMI shielding performance at room temperature was measured on a vector network analyzer (MS4644A; Anritsu, Japan) with a frequency range of 8.2 to 12.4 GHz (X-band) using the waveguide method.[176] As mentioned in section 2.6.7, the total shielding effectiveness (SE_T) and reflection loss (SE_R) can be calculated according to equations (2 - 9) and (2 - 10), respectively. If the thickness of the material is larger than its skin depth, the SE_{MR} value can be negligible. Thus, the SE_A can be obtained by equation (2 - 13).

According to equation (1- 16), the skin depth δ [m] of a metal shield can be calculated according to the following equations:

$$\delta = \left(\sqrt{\pi f \mu_s \sigma_s}\right)^{-1} \quad (3\text{- }11)$$

$$\mu_s = \mu_{sr} * \mu_0 \quad (3\text{- }12)$$

where f is the frequency of incident electromagnetic wave [Hz]; μ_s is the magnetic permeability of the shielding materials [H/m]; μ_{sr} is the relative magnetic permeability of the shielding materials; μ_0 is the magnetic permeability of free space ($\approx 4\pi\times10^{-7}$ H/m) and σ_s is the electrical conductivity [S/m] of the shielding materials. The electrical conductivity of SPS-sintered dense monolithic SiC/C-35mm and SiC/15HfC$_x$N$_{1-x}$/C-35mm are ≈ 1.8 S/cm and ≈ 20.7 S/cm, respectively. In this work, μ_{sr} is taken as 1 due to the weak magnetic properties of SiC/C and SiC/HfC$_x$N$_{1-x}$/C ceramic nanocomposites.[187, 188] Thus, in the X-band (8.2 ~ 12.4 GHz), the skin depths of SiC/C-35mm and SiC/15HfC$_x$N$_{1-x}$/C-35mm are estimated to be in the range of 0.41 ~ 0.33 mm and 0.12 ~ 0.10 mm, respectively. The skin depths of all monoliths are much smaller than their thickness (2.0 mm). Hence, the total shielding effectiveness (SE$_T$) in this work mainly consists of reflection loss (SE$_R$) and absorption loss (SE$_A$), *i.e.*, equation (2 - 12).[176]

Figure 3. 76 shows the shielding effectiveness of the SiC/C-35mm and SiC/15HfC$_x$N$_{1-x}$/C-35mm in the X-band at room temperature. The sample thickness is 2.0 mm. SiC/C-35mm and SiC/15HfC$_x$N$_{1-x}$/C-35mm exhibit an average total shielding effectiveness (SE$_T$) of ≈ 21 dB and ≈ 42 dB, respectively. With addition of a small amount of conductive HfC$_x$N$_{1-x}$ phase (Table 3. 13), the SE$_T$ was greatly improved (by ≈ 100 %). This agrees with the enhanced electrical conductivity of the 2 monoliths from 1.83 S/cm to 22.69 S/cm.

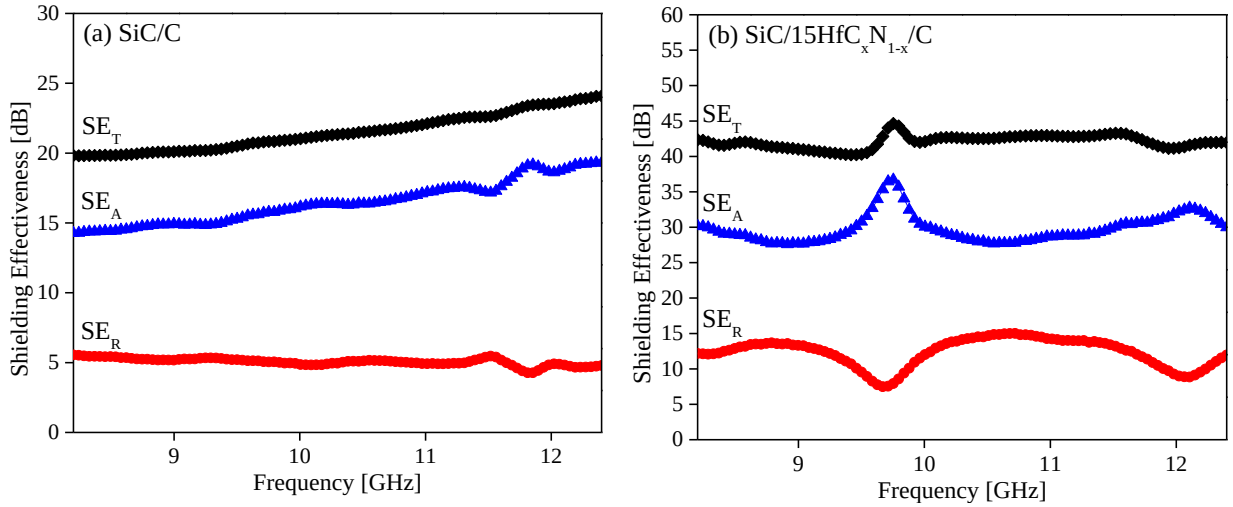

Figure 3. 76 Shielding effectiveness of SiC/C-35mm *(a)* and SiC/15HfC$_x$N$_{1-x}$/C-35mm *(b)* ceramics as a function of frequency in X-band at room temperature (sample thickness: 2.0 mm).

According to equation (2 - 12), the SE$_T$ is composed of reflection loss (SE$_R$) and absorption loss (SE$_A$). The average SE$_R$ of SiC/C-35mm is ≈ 5 dB, indicating that ≈ 68.4% of incident electromagnetic wave is reflected. The SE$_R$ value of SiC/15HfC$_x$N$_{1-x}$/C-35mm is significantly improved to ≈ 12 dB. Thus, ≈ 93.7% of the incident electromagnetic wave is reflected. Therefore, the SiC/15HfC$_x$N$_{1-x}$/C-35mm has a very

strong reflection capability in the X-band due to the enhanced impendence mismatch. According to equation (1- 11), at the same frequency, the impedance value of shielding material is determined by the magnetic permeability, electric permittivity and electrical conductivity of the shield. In the present work, due to the weak magnetic properties of SiC/C and SiHfC(N) ceramics, the effect caused by magnetic permeability can be ignored. According to the Maxwell Garnett mixing rule[151], the electric permittivity of SiC/C-35mm and SiC/15HfC$_x$N$_{1-x}$/C-35mm should be similar due to the small volume percent of HfC$_x$N$_{1-x}$ (< 5 vol.%) within the SiC/15HfC$_x$N$_{1-x}$/C-35mm.[101] Thus, the enhanced of impendence mismatch should be due to the increased electrical conductivity.

After reflection, the rest of the incident electromagnetic wave can be attenuated by absorption. The average SE$_A$ of SiC/C-35mm is ≈ 16.5 dB. Thus, ≈ 97.8% of the rest of the incident electromagnetic wave is absorbed according to equation (2 - 13), allowing for ≈ 0.7% of the incident electromagnetic wave to transmit through the SiC/C-35mm shielding material. The average SE$_A$ of SiC/15HfC$_x$N$_{1-x}$/C-35mm is ≈ 30 dB. That means ≈ 99.9% of the rest of the incident electromagnetic wave is absorbed, allowing for less than 0.006% of the incident electromagnetic wave to transmit through the SiC/15HfC$_x$N$_{1-x}$/C-35mm shielding material. Thus, the absorption loss of the SiC/15HfC$_x$N$_{1-x}$/C-35mm sample is also highly improved. According to equations (1- 17) and (1- 16), at the same frequency, the absorption loss of metallic shield is proportional to the thickness of shield and to the square root of magnetic permeability and electrical conductivity. The SiC/C and SiHfC(N) ceramics are not metal, but the correlation should be similar. Because of the weak magnetic properties of SiC/C and SiHfC(N) ceramics, the absorption loss of these two samples with the same thickness should be proportional to the square root of their electrical conductivity. Thus, the SiC/15HfC$_x$N$_{1-x}$/C-35mm exhibit enhanced absorption loss due to the improved electrical conductivity.

Please note that the measured SE$_T$ values are usually lower than theoretical SE$_T$ values because of the unavoidable gap between the specimen and sample holder that allows electromagnetic fields to leak through the shield, thereby, significantly degrading the measured shielding effectiveness.[175, 260, 261] In spite that the dimension of all the specimens under test is carefully controlled during machining, the electrical contact of the faying surfaces is not ideal. This is also a problem for its practical applications because, in practice, the shield is not continuous but instead contains seams. In this case, conductive sealants are used in the faying surfaces in order to effectively reduce the transfer impedance (or improve the electrical contact) of the seams thereby reducing the penetration of electromagnetic fields through the seams. Thus, a significant portion of the inherent shielding effectiveness of the shield can be retained.[175]

3.7.3 EMI shielding performance at high temperature

The high-temperature EMI shielding performance of SiC/C-35mm and SiC/15HfC$_x$N$_{1-x}$/C-35mm (sample thickness: 2.0 mm) was measured at temperatures varying from 100 to 600 ºC. The results are shown in Figure 3. 77.

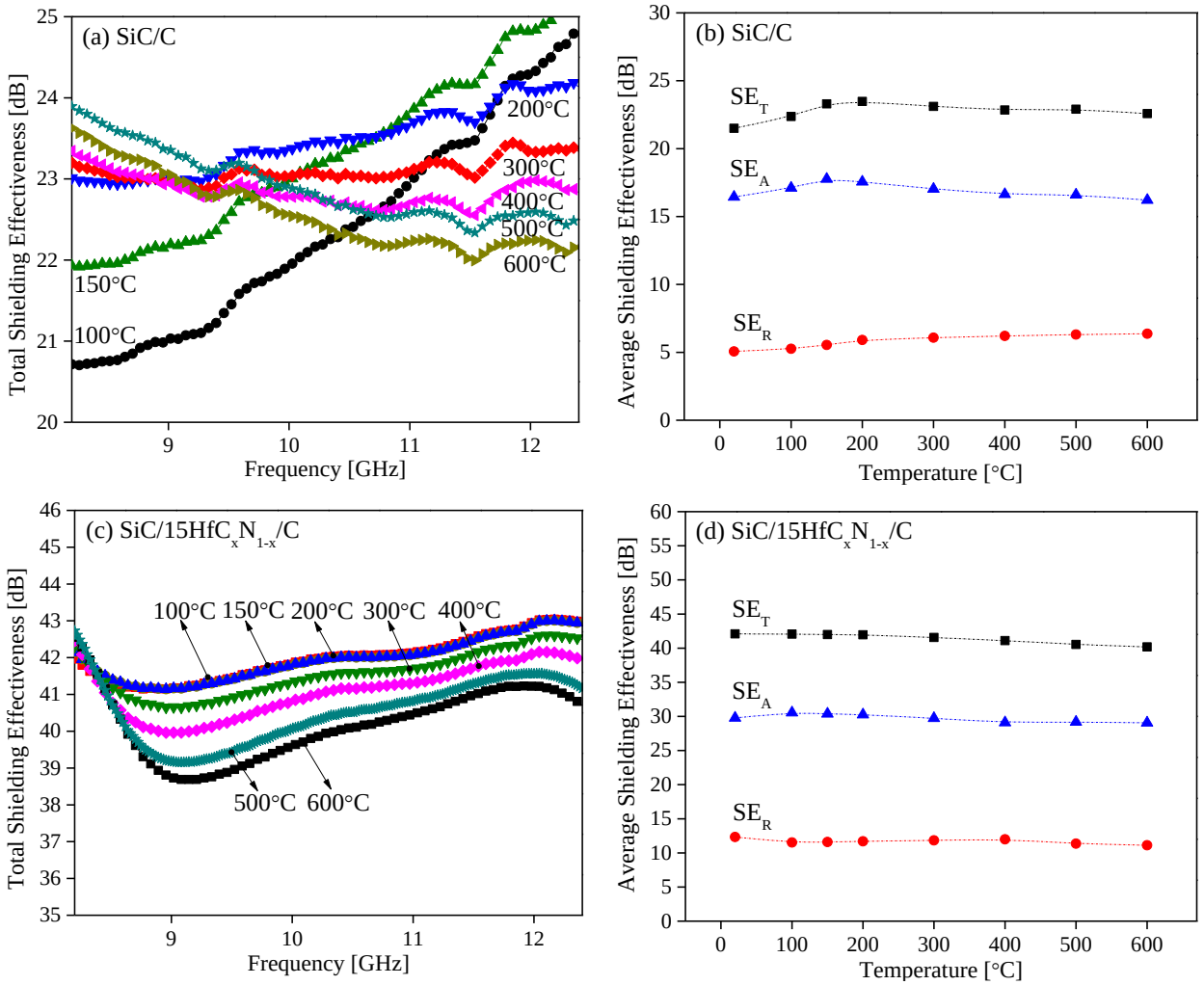

Figure 3. 77 Shielding effectiveness of SiC/C-35mm *(a, b)* and SiC/15HfC$_x$N$_{1-x}$/C-35mm *(c, d)* ceramics at temperatures from 100 to 600 ºC (sample thickness: 2.0 mm).

As shown in Figure 3. 77b, the average SE_T values of SiC/C-35mm increase from 21.5 dB at room temperature to 23.5 dB at 200 ºC and then decrease slightly to 22.6 dB at 600 ºC. Figure 3. 77d presents the average SE_T values of SiC/15HfC$_x$N$_{1-x}$/C-35mm as a function of temperature. This clearly shows that with increasing temperature, the SE_T values decrease from 42.0 dB at room temperature to 40.2 dB at 600 ºC. However, the EMI shielding performance of the SiC/15HfC$_x$N$_{1-x}$/C-35mm at high temperatures is still excellent. More than 99.99% of incident electromagnetic wave can be shielded even at 600 ºC. Figure 3. 77d reveals that both the SE_R and SE_A values decrease with increasing temperature. According to equations (1- 14) and (1- 17), this can be attributed to the variation of electrical conductivity of the SiC/15HfC$_x$N$_{1-x}$/C-35mm as a function of temperature. As mentioned in section 3.4, the SiC/15HfC$_x$N$_{1-x}$/C-35mm comprises β-SiC, HfC$_x$N$_{1-x}$ and free carbon (or turbostratic carbon). The electrical conductivity of both β-SiC and free carbon increases with increasing temperature.[130] However, the electrical conductivity of HfC$_x$N$_{1-x}$ decreases with increasing temperatures due to its metallic feature. Because the HfC$_x$N$_{1-x}$ phase plays a key role in the overall electrical conductivity of the nanocomposite, the electrical conductivity of SiC/15HfC$_x$N$_{1-x}$/C-35mm decreases in the same trend of the HfC$_x$N$_{1-x}$ phase. Thus, the

SE_T of SiC/15HfC_xN_{1-x}/C-35mm decreases at higher temperatures.

3.7.4 Summary

Electromagnetic interference (EMI) shielding performance of the dense monolithic SiHfC(N) ceramic nanocomposites as well as the SiC/C composite were investigated in the X-band (8.2 ~ 12.4 GHz) at room temperature. Incorporation of highly conductive HfC_xN_{1-x} into a SiC matrix substantially enhanced EMI shielding performance of the SiC-based ceramics. Except for some large HfC_xN_{1-x} grains, the average grain size of the HfC_xN_{1-x} is less than 100 nm, which is preferable for reducing the percolation threshold and improving the electrical conductivity of the SiHfC(N) ceramic nanocomposites.

The EMI shielding performance of the SiC/15HfC_xN_{1-x}/C-35mm monoliths and SiC/C-35mm composite at high temperatures up to 600 ºC was investigated as well. At high temperatures, the EMI shielding performance of both SiC/C-35mm and SiC/15HfC_xN_{1-x}/C-35mm decreases slightly. This should be contributed by the variations of electrical conductivity of the composites as a function of temperature. Furthermore, the flexural strength of the 2 monoliths was measured as well. Good mechanical properties, excellent thermal stability and corrosion resistance as well as outstanding EMI shielding performance make the dense monolithic SiHfC(N) ceramic nanocomposite suitable for structural and functional applications in harsh environments (*e.g.*, at high temperatures, in corrosive media).

4 Conclusions and outlook

4.1 Conclusions

Within the scope of the present Ph.D. work, a series of dense monolithic SiMC(N) ceramic nanocomposites (M = Hf, Ta, HfTa) were fabricated successfully from single-source precursors and densified by spark plasma sintering (SPS). The prepared SiMC(N) ceramic nanocomposites were proved to exhibit promising structural and functional properties, including enhanced laser ablation resistance at temperatures higher than 3000 ºC, outstanding microwave absorption performance within a wide bandwidth as well as superior electromagnetic interference shielding capability at high temperatures up to 600 ºC. The nanocomposite formation and unique MC_xN_{1-x}-carbon core shell microstructure dictates the versatile properties of the SiMC(N) ceramic nanocomposites. Thus, several conclusions can be made as follows:

- It is possible to synthesize M-containing single-source precursors upon reaction between SMP10 (AHPCS) and metal compounds, including $Hf(NMe_2)_4$, $Hf(NEt_2)_4$ and $Ta(NMe_2)_5$.
- Single phase amorphous SiMC(N) ceramics can be obtained by pyrolysis of the M-containing single-source precursors (*i.e.*, M-SMP10) at 900 ~ 1100 ºC.
- Powder and dense monolithic SiMC(N) ceramic nanocomposites can be obtained upon annealing and SPS sintering of the amorphous SiMC(N) ceramics, respectively. The SiMC(N) ceramic nanocomposites show promising thermal stability even after annealing at 1900 ºC for 5 h or after sintering at 2200 ºC for 30 min.
- Phase composition and microstructural characterization reveals that the SiMC(N) ceramic nanocomposites comprise three phases, *i.e.*, β-SiC, MC_xN_{1-x} and free carbon. MC_xN_{1-x} and free carbon disperse homogeneously within the β-SiC matrix. The average grain sizes of both β-SiC and MC_xN_{1-x} remain less than 100 nm even after annealing at 1900 ºC for 5 h or sintering at 2200 ºC for 30 min. Additionally, at annealing temperatures lower than 2000 K, nitrogen atoms within the lattice of HfC_xN_{1-x} seem to be more stable than those within the lattice of TaC_xN_{1-x}. It is proved that the $Hf_{0.7}Ta_{0.3}C_xN_{1-x}$ and $Hf_{0.2}Ta_{0.8}C_xN_{1-x}$ solid solutions with an expected Hf/Ta atomic ratio can be controlled precisely by adjusting the mole ratio of metal compounds during synthesis of the M-containing single-source precursors. Within the boron-doped SiHfC(N) ceramics, the high-temperature conversion of boron is clearly thermodynamically controlled, which allows for the preparation of $SiC/HfC_xN_{1-x}/HfB_2/C$ ceramics with tailored phase compositions.
- A unique MC_xN_{1-x}-carbon core shell microstructure is observed within all the SiMC(N) ceramic nanocomposites including powders and monoliths. The carbon shell is able to hinder the coarsening of MC_xN_{1-x} grains during high-temperature annealing and sintering.
- The laser ablation behavior of the bulk SiHfC(N) ceramics was investigated on dense monolithic

SiHfC(N) ceramic nanocomposites and C_f-reinforced SiHfC(N) ceramic matrix composites. With addition of HfC_xN_{1-x} phase, the rim of the ablation pit can be covered by Hf-containing materials (*e.g.*, HfO_2) that are expected to improve the laser ablation resistance of the SiHfC(N) ceramics.

- The dielectric properties and microwave absorption performance of SiHfC(N) ceramic nanocomposites were investigated in the X-band (8.2 ~ 12.4 GHz). The complex permittivity is intimately connected with their microstructure formed at different annealing temperatures (1100-1700 °C). The introduction of HfC_xN_{1-x} substantially enhances the dielectric loss of the SiHfC(N) ceramic nanocomposites in the X-band. The minimum reflection loss and the maximum effective absorption bandwidth amount to -47 dB and 3.6 GHz, respectively. Adjusting the microstructure by annealing at high temperature (T >1500 °C) and the chemical composition by the ratio of the starting materials, *i.e.*, $Hf(NMe_2)_4$/SMP10, allows for tuning of the minimum reflection loss and absorption frequency range.

- Electromagnetic interference (EMI) shielding performance of the dense monolithic SiHfC(N) ceramic nanocomposites were investigated in the X-band (8.2 ~ 12.4 GHz) at temperatures up to 600 ºC. Corporation of highly conductive HfC_xN_{1-x} into a β-SiC matrix substantially enhanced the EMI shielding performance of the SiC-based ceramics. At high temperatures, the EMI shielding performance decreases slightly (< 5 dB). This should be contributed by the variations of electrical conductivity of the composites as a function of temperature. Furthermore, the flexural strength of the SiHfC(N) monoliths is measured to be ≈ 300 MPa. Good mechanical properties, excellent thermal stability and corrosion resistance as well as outstanding EMI shielding performance make the dense monolithic SiHfC(N) ceramic nanocomposite suitable for structural and functional applications in harsh environments (*e.g.*, at high temperatures, in corrosive media).

4.2 Outlook

After investigation of the SiMC(N) ceramic nanocomposites (M = Hf, Ta, HfTa) in the present Ph.D. work, numerous useful information about synthesis, polymer-to-ceramics transformation, microstructural evolution as well as structural and functional properties was collected. With the important information, some challenging work can be conducted in the future.

- Determination of the formation mechanisms of the MC_xN_{1-x}-carbon core shell structure. The core shell structure can be observed in all the as-prepared SiMC(N) ceramic nanocomposites, whereas the thickness of the carbon shell varies on different MC_xN_{1-x} cores, though the reason is not clear. Moreover, physical and chemical properties (*e.g.*, electrical conductivity, hardness) as well as microstructure of the carbon shells should be further characterized.

- Thermal conductivity of UHTC-NCs is also an important parameter for their practical applications. The contributions of MC_xN_{1-x} phase and free carbon as well as MC_xN_{1-x}-carbon core shell structure on the overall thermal conductivity of SiMC(N) ceramic nanocomposites can be investigated.

- Synthesis of single-source precursors with higher concentrations of M elements for fabricating monolithic SiMC(N) ceramic nanocomposites or fiber-reinforced SiMC(N) CMCs with higher MC_xN_{1-x} content should be performed, in order to further enhance the ultrahigh-temperature performance (*e.g.*, laser ablation resistance) of the SiMC(N) ceramics.

- Optimizing microwave absorption and EMI shielding performance of the SiMC(N) ceramic nanocomposites at high temperature should be pursued. The SiTaC(N), SiHf7Ta3C(N) and SiHf2Ta8C(N) ceramic nanocomposites with highly conductive carbides or carbonitrides dispersing within the β-SiC matrix are promising microwave absorption or EMI shielding materials that may be beneficial in harsh environments.

5 References

[1] Riedel, R., Chem. Soc. Rev. **2012,** 41 (15), 5029-5031.
[2] Squire, T. H.; Marschall, J., J. Eur. Ceram. Soc. **2010,** 30 (11), 2239-2251.
[3] Talmy, I.; Zaykoski, J.; Martin, C., J. Am. Ceram. Soc. **2008,** 91 (5), 1441-1447.
[4] Savino, R.; Fumo, M. D. S.; Silvestroni, L.; Sciti, D., J. Eur. Ceram. Soc. **2008,** 28 (9), 1899-1907.
[5] Paul, A.; Jayaseelan, D. D.; Venugopal, S.; Zapata-Solvas, E.; Binner, J.; Vaidhyanathan, B.; Heaton, A.; Brown, P. M.; Lee, W., **2012**.
[6] Patterson, M.; He, S.; Fehrenbacher, L.; Hanigofsky, J.; Reed, B., Mater. Manuf. Process. **1996,** 11 (3), 367-379.
[7] Talmy, I. G.; Zaykoski, J. A.; Opeka, M. M., J. Am. Ceram. Soc. **2008,** 91 (7), 2250-2257.
[8] Sciti, D.; Medri, V.; Silvestroni, L., Scripta Mater. **2010,** 63 (6), 601-604.
[9] Carney, C. M., J. Mater. Sci. **2009,** 44 (20), 5673-5681.
[10] Carney, C. M.; Parthasarathy, T. A.; Cinibulk, M. K., J. Am. Ceram. Soc. **2011,** 94 (8), 2600-2607.
[11] Gleiter, H., Nanostruct. Mater. **1995,** 6 (1), 3-14.
[12] Niihara, K., J. Ceram. Soc. Jpn. **1991,** 99 (10), 974-982.
[13] Ionescu, E.; Kleebe, H.-J.; Riedel, R., Chem. Soc. Rev. **2012,** 41 (15), 5032-5052.
[14] Yan, M.; Li, H.; Fu, Q.; Xie, J.; Liu, L.; Feng, B., Acta. Metall. Sin. **2014,** 27 (6), 981-987.
[15] Chen, Z.-k.; Xiong, X.; Li, G.-d.; Wang, Y.-l., Appl. Surf. Sci. **2009,** 255 (22), 9217-9223.
[16] Wang, Y.; Li, H.; Fu, Q.; Wu, H.; Yao, D.; Li, H., Surf. Coat. Technol. **2012,** 206 (19), 3883-3887.
[17] Wunder, V.; Popovska, N.; Wegner, A.; Emig, G.; Arnold, W., Surf. Coat. Technol. **1998,** 100, 329-332.
[18] Zhang, X.; Xu, L.; Du, S.; Han, W.; Han, J., J. Am. Ceram. Soc. **2008,** 91 (12), 4068-4073.
[19] Yi, W.; Yongdong, X.; Yiguang, W.; Laifei, C.; Litong, Z., Mater. Lett. **2010,** 64 (19), 2068-2071.
[20] Zhang, S. C.; Hilmas, G. E.; Fahrenholtz, W. G., J. Am. Ceram. Soc. **2008,** 91 (1), 26-32.
[21] Carney, C. M.; Mogilvesky, P.; Parthasarathy, T. A., J. Am. Ceram. Soc. **2009,** 92 (9), 2046-2052.
[22] Wu, W.-W.; Zhang, G.-J.; Kan, Y.-M.; Wang, P.-L.; Vanmeensel, K.; Vleugels, J.; Van der Biest, O., Scripta Mater. **2007,** 57 (4), 317-320.
[23] Feng, L.; Kim, J. M.; Lee, S. H.; Park, S. J., J. Am. Ceram. Soc. **2016**.
[24] Patterson, M., **1999**.
[25] Yuan, J.; Hapis, S.; Breitzke, H.; Xu, Y.; Fasel, C.; Kleebe, H.-J.; Buntkowsky, G.; Riedel, R.; Ionescu, E., Inorg. Chem. **2014,** 53 (19), 10443-10455.
[26] Ionescu, E.; Papendorf, B.; Kleebe, H. J.; Poli, F.; Müller, K.; Riedel, R., J. Am. Ceram. Soc. **2010,** 93 (6), 1774-1782.
[27] Papendorf, B.; Nonnenmacher, K.; Ionescu, E.; Kleebe, H. J.; Riedel, R., Small **2011,** 7 (7), 970-978.
[28] Ionescu, E.; Linck, C.; Fasel, C.; Müller, M.; Kleebe, H. J.; Riedel, R., Journal of the American Ceramic Society **2010,** 93 (1), 241-250.
[29] Riedel, R.; Ionescu, E.; Chen, I.-W., Ceram. Sci. Technol. **2011,** 1, 3-38.
[30] Peuckert, M.; Vaahs, T.; Brück, M., Adv. Mater. **1990,** 2 (9), 398-404.
[31] Colombo, P.; Mera, G.; Riedel, R.; Soraru, G. D., J. Am. Ceram. Soc. **2010,** 93 (7), 1805-1837.
[32] Blum, Y. D.; Platz, R. M.; Crawford, E. J., J. Am. Ceram. Soc. **1990,** 73 (1), 170-172.
[33] Yajima, S.; Hayashi, J.; Omori, M., Chem. Lett. **1975,** 4 (9), 931-934.
[34] Yajima, S.; Hasegawa, Y.; Okamura, K.; Matsuzawa, T., **1978**.
[35] Riedel, R.; Passing, G.; Schönfelder, H.; Brook, R., Nature **1992,** 355 (6362), 714-717.
[36] Riedel, R.; Kienzle, A.; Dressler, W.; Ruwisch, L.; Bill, J.; Aldinger, F., Nature **1996,** 382 (6594), 796-798.
[37] Bill, J.; Aldinger, F., Adv. Mater. **1995,** 7 (9), 775-787.
[38] Riedel, R.; Greiner, A.; Miehe, G.; Dressler, W.; Fuess, H.; Bill, J.; Aldinger, F., Angew. Chem. Int. Ed. **1997,** 36 (6), 603-606.
[39] Yu, Z.; Yang, L.; Min, H.; Zhang, P.; Zhou, C.; Riedel, R., J. Mater. Chem. C **2014,** 2 (6), 1057-1067.
[40] Colombo, P., J. Eur. Ceram. Soc. **2008,** 28 (7), 1389-1395.
[41] Eckel, Z. C.; Zhou, C.; Martin, J. H.; Jacobsen, A. J.; Carter, W. B.; Schaedler, T. A., Science **2016,** 351 (6268), 58-62.
[42] Yang, W.; Gao, F.; Wang, H.; Zheng, X.; Xie, Z.; An, L., J. Am. Ceram. Soc. **2008,** 91 (4), 1312-1315.
[43] Hsu, M. T. S.; Chen, T. S.; Riccitiello, S. R., J. Appl. Polym. Sci. **1991,** 42 (3), 851-861.
[44] Zhang, Z. F.; Babonneau, F.; Laine, R. M.; Mu, Y.; Harrod, J. F.; Rahn, J. A., J. Am. Ceram. Soc. **1991,** 74 (3), 670-673.
[45] Hengge, E.; Weinberger, M., J. Organomet. Chem. **1992,** 433 (1-2), 21-34.
[46] Seyferth, D.; Wood, T. G.; Tracy, H. J.; Robison, J. L., J. Am. Ceram. Soc. **1992,** 75 (5), 1300-1302.
[47] Wu, H. J.; Interrante, L. V., Macromolecules **1992,** 25 (6), 1840-1841.
[48] Interrante, L. V.; Whitmarsh, C.; Sherwood, W.; Wu, H.-J.; Lewis, R.; Maciel, G. In High yield polycarbosilane precursors to stoichiometric SiC. Synthesis, pyrolysis and application, MRS Proceedings, Cambridge Univ Press: **1994**; p 595.

[49] Whitmarsh, C. K.; Interrante, L. V., Organometallics **1991,** 10 (5), 1336-1344.
[50] Whitmarsh, C. K.; Interrante, L. V., Carbosilane polymer precursors to silicon carbide ceramics. Google Patents: **1992**.
[51] Interrante, L.; Rushkin, I.; Shen, Q., Appl. Organomet. Chem. **1998,** 12 (10-11), 695-705.
[52] Duperrier, S.; Gervais, C.; Bernard, S.; Cornu, D.; Babonneau, F.; Balan, C.; Miele, P., Macromolecules **2007,** 40 (4), 1018-1027.
[53] Zhu, Y.; Huang, Z.; Dong, S.; Yuan, M.; Jiang, D., Ceram. Int. **2008,** 34 (5), 1201-1205.
[54] Kim, Y.-W.; Park, C. B., Compos. Sci. Technol. **2003,** 63 (16), 2371-2377.
[55] Wilhelm, M.; Adam, M.; Bäumer, M.; Grathwohl, G., Adv. Eng. Mater. **2008,** 10 (3), 241-245.
[56] Otoishi, S.; Tange, Y., J. Cryst. Growth **1999,** 200 (3), 467-471.
[57] Evans, J., J. Eur. Ceram. Soc. **2008,** 28 (7), 1421-1432.
[58] Melcher, R.; Cromme, P.; Scheffler, M.; Greil, P., J. Am. Ceram. Soc. **2003,** 86 (7), 1211-1213.
[59] Yoon, B. H.; Lee, E. J.; Kim, H. E.; Koh, Y. H., J. Am. Ceram. Soc. **2007,** 90 (6), 1753-1759.
[60] Liu, X.; Li, Y. L.; Hou, F., J. Am. Ceram. Soc. **2009,** 92 (1), 49-53.
[61] Cromme, P.; Scheffler, M.; Greil, P., Adv. Eng. Mater. **2002,** 4 (11), 873-877.
[62] Sato, K.; Tezuka, A.; Funayama, O.; Isoda, T.; Terada, Y.; Kato, S.; Iwata, M., Compos. Sci. Technol. **1999,** 59 (6), 853-859.
[63] Sung, I.-K.; Yoon, S.-B.; Yu, J.-S.; Kim, D.-P., Chem. Commun. **2002,** (14), 1480-1481.
[64] Goerke, O.; Feike, E.; Heine, T.; Trampert, A.; Schubert, H., J. Eur. Ceram. Soc. **2004,** 24 (7), 2141-2147.
[65] Colombo, P.; Paulson, T. E.; Pantano, C. G., J. Am. Ceram. Soc. **1997,** 80 (9), 2333-2340.
[66] Smirnova, T.; Badalian, A.; Yakovkina, L.; Kaichev, V.; Bukhtiyarov, V.; Shmakov, A.; Asanov, I.; Rachlin, V.; Fomina, A., Thin Solid Films **2003,** 429 (1), 144-151.
[67] Haug, R.; Weinmann, M.; Bill, J.; Aldinger, F., J. Eur. Ceram. Soc. **1999,** 19 (1), 1-6.
[68] Galusek, D.; Sedláček, J.; Riedel, R., J. Eur. Ceram. Soc. **2007,** 27 (6), 2385-2392.
[69] Zhang, T.; Evans, J.; Woodthorpe, J., J. Eur. Ceram. Soc. **1995,** 15 (8), 729-734.
[70] Walter, S.; Suttor, D.; Erny, T.; Hahn, B.; Greil, P., J. Eur. Ceram. Soc. **1996,** 16 (4), 387-393.
[71] Kim, Y. W.; Eom, J. H.; Wang, C.; Park, C. B., J. Am. Ceram. Soc. **2008,** 91 (4), 1361-1364.
[72] Perale, G.; Giordano, C.; Daniele, F.; Masi, M.; Colombo, P.; Gottardo, L.; Maccagnan, S., Int. J. Appl. Ceram. Tec. **2008,** 5 (1), 37-43.
[73] Bunsell, A. R.; Piant, A., J. Mater. Sci. **2006,** 41 (3), 823-839.
[74] Okamura, K.; Shimoo, T.; Suzuya, K.; Suzuki, K., J. Ceram. Soc. Jpn. **2006,** 114 (1330), 445-454.
[75] Zeschky, J.; Höfner, T.; Arnold, C.; Weißmann, R.; Bahloul-Hourlier, D.; Scheffler, M.; Greil, P., Acta Mater. **2005,** 53 (4), 927-937.
[76] Rocha, R. M. d.; Greil, P.; Bressiani, J. C.; Bressiani, A. H. d. A., Mat. Res. **2005,** 8 (2), 191-196.
[77] Colombo, P.; Sglavo, V.; Pippel, E.; Woltersdorf, J., J. Mater. Sci. **1998,** 33 (9), 2405-2412.
[78] Lewinsohn, C.; Elangovan, S. In Development of Amorphous, Non-Oxide Seals for Solid Oxide Fuel Cells, 27th Annual Cocoa Beach Conference on Advanced Ceramics and Composites: A: Ceramic Engineering and Science Proceedings, Volume 24, Issue 3, Wiley Online Library: **2003**; pp 317-322.
[79] Friedel, T.; Travitzky, N.; Niebling, F.; Scheffler, M.; Greil, P., J. Eur. Ceram. Soc. **2005,** 25 (2), 193-197.
[80] Mott, M.; Evans, J. R., J. Am. Ceram. Soc. **2001,** 84 (2), 307-13.
[81] Nangrejo, M.; Bernardo, E.; Colombo, P.; Farook, U.; Ahmad, Z.; Stride, E.; Edirisinghe, M., Mater. Lett. **2009,** 63 (3), 483-485.
[82] Welna, D. T.; Bender, J. D.; Wei, X.; Sneddon, L. G.; Allcock, H. R., Adv. Mater. **2005,** 17 (7), 859-862.
[83] Shin, D.-G.; Riu, D.-H.; Kim, H.-E., J. Ceram. Process. Res **2008,** 9 (2), 209-214.
[84] Sarkar, S.; Chunder, A.; Fei, W.; An, L.; Zhai, L., J. Am. Ceram. Soc. **2008,** 91 (8), 2751-2755.
[85] Malenfant, P. R.; Wan, J.; Taylor, S. T.; Manoharan, M., Nat. Nanotechnol. **2007,** 2 (1), 43-46.
[86] Wan, J.; Malenfant, P. R.; Taylor, S. T.; Loureiro, S. M.; Manoharan, M., Mater. Sci. Eng., A **2007,** 463 (1), 78-88.
[87] Schulz, M.; Börner, M.; Haußelt, J.; Heldele, R., J. Eur. Ceram. Soc. **2005,** 25 (2), 199-204.
[88] Lee, H.-J.; Yoon, T.-H.; Kim, D.-P., Microelectron. Eng. **2007,** 84 (12), 2892-2895.
[89] Yang, H.; Deschatelets, P.; Brittain, S. T.; Whitesides, G. M., Adv. Mater. **2001,** 13 (1), 54-58.
[90] Bakumov, V.; Schwarz, M.; Kroke, E., J. Eur. Ceram. Soc. **2009,** 29 (13), 2857-2865.
[91] Zheng, J.; Kramer, M. J.; Akinc, M., J. Am. Ceram. Soc. **2000,** 83 (12), 2961-2966.
[92] Yang, W.; Xie, Z.; Li, J.; Miao, H.; Zhang, L.; An, L., J. Am. Ceram. Soc. **2005,** 88 (6), 1647-1650.
[93] Cai, K.; Huang, L.; Zhang, A.; Yin, J.; Liu, H., J. Nanosci. Nanotechnol. **2008,** 8 (12), 6338-6343.
[94] Wen, Q.; Xu, Y.; Xu, B.; Fasel, C.; Guillon, O.; Buntkowsky, G.; Yu, Z.; Riedel, R.; Ionescu, E., Nanoscale **2014,** 6 (22), 13678-13689.
[95] Sawaguchi, A.; Toda, K.; Niihara, K., J. Am. Ceram. Soc. **1991,** 74 (5), 1142-1144.
[96] Zaheer, M.; Schmalz, T.; Motz, G.; Kempe, R., Chem. Soc. Rev. **2012,** 41 (15), 5102-5116.
[97] An, L.; Wang, Y.; Bharadwaj, L.; Zhang, L.; Fan, Y.; Jiang, D.; Sohn, Y.-h.; Desai, V. H.; Kapat, J.; Chow, L. C., Adv. Eng. Mater. **2004,** 6 (5), 337-340.

[98] Hojamberdiev, M.; Prasad, R. M.; Fasel, C.; Riedel, R.; Ionescu, E., J. Eur. Ceram. Soc. **2013,** 33 (13), 2465-2472.
[99] Kaspar, J.; Terzioglu, C.; Ionescu, E.; Graczyk-Zajac, M.; Hapis, S.; Kleebe, H. J.; Riedel, R., Adv. Funct. Mater. **2014,** 24 (26), 4097-4104.
[100] Glatz, G.; Schmalz, T.; Kraus, T.; Haarmann, F.; Motz, G.; Kempe, R., Chem. Eur. J. **2010,** 16 (14), 4231-4238.
[101] Wen, Q.; Feng, Y.; Yu, Z.; Peng, D. L.; Nicoloso, N.; Ionescu, E.; Riedel, R., J. Am. Ceram. Soc. **2016,** 99 (8).
[102] Bakumov, V.; Gueinzius, K.; Hermann, C.; Schwarz, M.; Kroke, E., J. Eur. Ceram. Soc. **2007,** 27 (10), 3287-3292.
[103] Hojamberdiev, M.; Prasad, R. M.; Morita, K.; Schiavon, M. A.; Riedel, R., Microporous Mesoporous Mater. **2012,** 151, 330-338.
[104] Yuan, J.; Luan, X.; Riedel, R.; Ionescu, E., J. Eur. Ceram. Soc. **2015,** 35 (12), 3329-3337.
[105] Luan, X.; Yuan, J.; Wang, J.; Tian, M.; Cheng, L.; Ionescu, E.; Riedel, R., J. Eur. Ceram. Soc. **2016**.
[106] Sorrentino, R.; Bianchi, G., Microwave and RF engineering. John Wiley & Sons: **2010**; Vol. 1.
[107] Yusoff, A.; Abdullah, M.; Ahmad, S.; Jusoh, S.; Mansor, A.; Hamid, S., J. Appl. Phys. **2002,** 92 (2), 876-882.
[108] Wen, F.; Zuo, W.; Yi, H.; Wang, N.; Qiao, L.; Li, F., Physica. B. **2009,** 404 (20), 3567-3570.
[109] Kang, Y.; Chu, Z.; Zhang, D.; Li, G.; Jiang, Z.; Cheng, H.; Li, X., Carbon **2013,** 61, 200-208.
[110] Shen, G.; Xu, Z.; Li, Y., J. Magn. Magn. Mater. **2006,** 301 (2), 325-330.
[111] Meshram, M.; Agrawal, N. K.; Sinha, B.; Misra, P., J. Magn. Magn. Mater. **2004,** 271 (2), 207-214.
[112] Qin, F.; Brosseau, C., J. Appl. Phys. **2012,** 111 (6), 061301.
[113] Micheli, D.; Apollo, C.; Gradoni, G.; Marchetti, M.; Morles, R. B.; Pastore, R., Electromagnetic characterization of composite materials and microwave absorbing modeling. INTECH Open Access Publisher: **2011**.
[114] Sugimoto, S.; Haga, K.; Kagotani, T.; Inomata, K., J. Magn. Magn. Mater. **2005,** 290, 1188-1191.
[115] Gong, Y.; Zhen, L.; Jiang, J.; Xu, C.; Shao, W., J. Magn. Magn. Mater. **2009,** 321 (22), 3702-3705.
[116] Lee, W.-J.; Lee, J.-W.; Kim, C.-G., Compos. Sci. Technol. **2008,** 68 (12), 2485-2489.
[117] Qi, X.; Yang, Y.; Zhong, W.; Deng, Y.; Au, C.; Du, Y., J. Solid State Chem. **2009,** 182 (10), 2691-2697.
[118] Das, C. K.; Bhattacharya, P.; Kalra, S. S., J. Mat. Sci. Res. **2012,** 1 (2), p126.
[119] Zhuo, R.; Qiao, L.; Feng, H.; Chen, J.; Yan, D.; Wu, Z.; Yan, P., J. Appl. Phys. **2008,** 104 (9), 094101.
[120] Ni, S.; Lin, S.; Pan, Q.; Yang, F.; Huang, K.; He, D., J. Phys. D: Appl. Phys. **2009,** 42 (5), 055004.
[121] Kim, S.-S.; Kim, S.-T.; Yoon, Y.-C.; Lee, K.-S., J. Appl. Phys. **2005,** 97 (10), 10F905.
[122] Lu, B.; Dong, X.; Huang, H.; Zhang, X.; Zhu, X.; Lei, J.; Sun, J., J. Magn. Magn. Mater. **2008,** 320 (6), 1106-1111.
[123] Qiu, J.; Gu, M.; Shen, H., J. Magn. Magn. Mater. **2005,** 295 (3), 263-268.
[124] Tabatabaie, F.; Fathi, M.; Saatchi, A.; Ghasemi, A., J. Alloys Compd. **2009,** 470 (1), 332-335.
[125] Zhang, B.; Feng, Y.; Xiong, J.; Yang, Y.; Lu, H., Magnetics, IEEE Transactions on **2006,** 42 (7), 1778-1781.
[126] Cao, M.-S.; Shi, X.-L.; Fang, X.-Y.; Jin, H.-B.; Hou, Z.-L.; Zhou, W.; Chen, Y.-J., Appl. Phys. Lett. **2007,** 91 (20), 3110.
[127] Oh, J.-H.; Oh, K.-S.; Kim, C.-G.; Hong, C.-S., Compos. Part B. Eng. **2004,** 35 (1), 49-56.
[128] Wadhawan, A.; Garrett, D.; Pérez, J. M., Appl. Phys. Lett. **2003,** 83 (13), 2683-2685.
[129] Wang, L.; Huang, Y.; Sun, X.; Huang, H.; Liu, P.; Zong, M.; Wang, Y., Nanoscale **2014,** 6 (6), 3157-3164.
[130] Cao, M.-S.; Song, W.-L.; Hou, Z.-L.; Wen, B.; Yuan, J., Carbon **2010,** 48 (3), 788-796.
[131] Chiu, S.-C.; Yu, H.-C.; Li, Y.-Y., J. Phys. Chem. C **2010,** 114 (4), 1947-1952.
[132] Abbas, S.; Dixit, A.; Chatterjee, R.; Goel, T., Mater. Sci. Eng., B **2005,** 123 (2), 167-171.
[133] Saini, P.; Choudhary, V.; Singh, B.; Mathur, R.; Dhawan, S., Mater. Chem. Phys. **2009,** 113 (2), 919-926.
[134] Truong, V.-T.; Riddell, S.; Muscat, R., J. Mater. Sci. **1998,** 33 (20), 4971-4976.
[135] Wang, T.; Wang, H.; Chi, X.; Li, R.; Wang, J., Carbon **2014,** 74, 312-318.
[136] Qiu, J.; Qiu, T., Carbon **2015,** 81, 20-28.
[137] Goodenough, J. B., IEEE Trans. Magn. **2002,** 38 (5), 3398-3408.
[138] Zhang, X.; Dong, X.; Huang, H.; Liu, Y.; Wang, W.; Zhu, X.; Lv, B.; Lei, J.; Lee, C., Appl. Phys. Lett. **2006,** 89 (5), 3115.
[139] Wen, B.; Cao, M.; Lu, M.; Cao, W.; Shi, H.; Liu, J.; Wang, X.; Jin, H.; Fang, X.; Wang, W., Adv. Mater. **2014,** 26 (21), 3484-3489.
[140] Micheli, D.; Apollo, C.; Pastore, R.; Marchetti, M., Compos. Sci. Technol. **2010,** 70 (2), 400-409.
[141] Battat, J.; Calame, J., J. Mater. Res. **2007,** 22 (12), 3292-3302.
[142] Calame, J. P.; Abe, D. K.; Levush, B.; Lobas, D., J. Am. Ceram. Soc. **2005,** 88 (8), 2133-2142.
[143] Dishovsky, N.; Grigorova, M., Mater. Res. Bull. **2000,** 35 (3), 403-409.
[144] Liu, Z.; Bai, G.; Huang, Y.; Li, F.; Ma, Y.; Guo, T.; He, X.; Lin, X.; Gao, H.; Chen, Y., J. Phys. Chem. C **2007,** 111 (37), 13696-13700.
[145] Li, Q.; Yin, X.; Duan, W.; Hao, B.; Kong, L.; Liu, X., J. Eur. Ceram. Soc. **2014,** 34 (3), 589-598.
[146] Kong, L.; Yin, X.; Ye, F.; Li, Q.; Zhang, L.; Cheng, L., J. Phys. Chem. C **2013,** 117 (5), 2135-2146.
[147] Liu, J.; Cao, W.-Q.; Jin, H.-B.; Yuan, J.; Zhang, D.-Q.; Cao, M.-S., J. Mater. Chem. C **2015,** 3 (18), 4670-

4677.
[148] Song, W.-L.; Cao, M.-S.; Hou, Z.-L.; Lu, M.-M.; Wang, C.-Y.; Yuan, J.; Fan, L.-Z., Appl. Phys. A **2014,** 116 (4), 1779-1783.
[149] Yin, X.; Xue, Y.; Zhang, L.; Cheng, L., Ceram. Int. **2012,** 38 (3), 2421-2427.
[150] Yuan, X.; Cheng, L.; Zhang, L., Ceram. Int. **2014,** 40 (10), 15391-15397.
[151] Sihvola, A., Subs. Sens. Tech. Appli. **2000,** 1 (4), 393-415.
[152] Nan, C.-W., Prog. Mater Sci. **1993,** 37 (1), 1-116.
[153] Pecharromán, C.; Moya, J. S., Adv. Mater. **2000,** 12 (4), 294-297.
[154] Ueda, N.; Taya, M., J. Appl. Phys. **1986,** 60 (1), 459-461.
[155] Cordelair, J.; Greil, P., J. Eur. Ceram. Soc. **2000,** 20 (12), 1947-1957.
[156] Jing, X.; Zhao, W.; Lan, L., J. Mater. Sci. Lett. **2000,** 19 (5), 377-379.
[157] Zhou, Y.; Zhou, W.; Qing, Y.; Luo, F.; Zhu, D., J. Magn. Magn. Mater. **2015,** 374, 345-349.
[158] Song, W.-L.; Cao, M.-S.; Hou, Z.-L.; Fang, X.-Y.; Shi, X.-L.; Yuan, J., Appl. Phys. Lett. **2009,** 94 (23), 233110.
[159] Yuan, J.; Yang, H.-J.; Hou, Z.-L.; Song, W.-L.; Xu, H.; Kang, Y.-Q.; Jin, H.-B.; Fang, X.-Y.; Cao, M.-S., Powder Technol. **2013,** 237, 309-313.
[160] Yang, H.; Cao, M.; Li, Y.; Shi, H.; Hou, Z.; Fang, X.; Jin, H.; Wang, W.; Yuan, J., Adv. Opt. Mater. **2014,** 2 (3), 214-219.
[161] Dou, Y.-K.; Li, J.-B.; Fang, X.-Y.; Jin, H.-B.; Cao, M.-S., Appl. Phys. Lett. **2014,** 104 (5), 052102.
[162] Yang, H.-J.; Yuan, J.; Li, Y.; Hou, Z.-L.; Jin, H.-B.; Fang, X.-Y.; Cao, M.-S., Solid State Commun. **2013,** 163, 1-6.
[163] Song, W.-l.; Cao, M.-s.; Hou, Z.-l.; Yuan, J.; Fang, X.-y., Scripta Mater. **2009,** 61 (2), 201-204.
[164] Yuan, J.; Song, W.-L.; Fang, X.-Y.; Shi, X.-L.; Hou, Z.-L.; Cao, M.-S., Solid State Commun. **2013,** 154, 64-68.
[165] Kong, L.; Yin, X.; Li, Q.; Ye, F.; Liu, Y.; Duo, G.; Yuan, X., J. Am. Ceram. Soc. **2013,** 96 (7), 2211-2217.
[166] Peng, C.-H.; Chen, P. S.; Chang, C.-C., Ceram. Int. **2014,** 40 (1), 47-55.
[167] Pierson, H. O., Handbook of Refractory Carbides & Nitrides: Properties, Characteristics, Processing and Apps. William Andrew: **1996**; p 118.
[168] Li, Q.; Yin, X.; Duan, W.; Kong, L.; Hao, B.; Ye, F., J. Alloys Compd. **2013,** 565, 66-72.
[169] Li, Q.; Yin, X.; Duan, W.; Kong, L.; Liu, X.; Cheng, L.; Zhang, L., J. Eur. Ceram. Soc. **2014,** 34 (10), 2187-2201.
[170] Ye, F.; Zhang, L.; Yin, X.; Zhang, Y.; Kong, L.; Li, Q.; Liu, Y.; Cheng, L., J. Eur. Ceram. Soc. **2013,** 33 (8), 1469-1477.
[171] Ye, F.; Zhang, L.; Yin, X.; Zhang, Y.; Kong, L.; Liu, Y.; Cheng, L., J. Eur. Ceram. Soc. **2014,** 34 (2), 205-215.
[172] Duan, W.; Yin, X.; Li, Q.; Liu, X.; Cheng, L.; Zhang, L., J. Eur. Ceram. Soc. **2014,** 34 (2), 257-266.
[173] Mera, G.; Riedel, R.; Poli, F.; Müller, K., J. Eur. Ceram. Soc. **2009,** 29 (13), 2873-2883.
[174] Riedel, R.; Ionescu, E.; Bansal, N.; Boccaccini, A., Bansal, NP **2012**, 235-270.
[175] Gooch, J. W.; Daher, J. K., Electromagnetic shielding and corrosion protection for aerospace vehicles. Springer: **2007**.
[176] Liu, X.; Yin, X.; Kong, L.; Li, Q.; Liu, Y.; Duan, W.; Zhang, L.; Cheng, L., Carbon **2014,** 68, 501-510.
[177] Luo, X.; Chung, D., Compos. Part B. Eng. **1999,** 30 (3), 227-231.
[178] Yan, D. X.; Pang, H.; Li, B.; Vajtai, R.; Xu, L.; Ren, P. G.; Wang, J. H.; Li, Z. M., Adv. Funct. Mater. **2015,** 25 (4), 559-566.
[179] Liu, P.; Qing, H.; Hou, H.; Wang, Y.; Zhang, Y., Mater. Desi. **2016,** 92, 823-828.
[180] Chen, Z.; Xu, C.; Ma, C.; Ren, W.; Cheng, H. M., Adv. Mater. **2013,** 25 (9), 1296-1300.
[181] Chen, Y.; Zhang, H. B.; Yang, Y.; Wang, M.; Cao, A.; Yu, Z. Z., Adv. Funct. Mater. **2016,** 26 (3), 447-455.
[182] Mohanty, A. K.; Ghosh, A.; Sawai, P.; Pareek, K.; Banerjee, S.; Das, A.; Pötschke, P.; Heinrich, G.; Voit, B., Polym. Eng. Sci. **2014,** 54 (11), 2560-2570.
[183] Chen, Y.; Wang, Y.; Zhang, H.-B.; Li, X.; Gui, C.-X.; Yu, Z.-Z., Carbon **2015,** 82, 67-76.
[184] Li, X.; Zhang, L.; Yin, X., J. Am. Ceram. Soc. **2012,** 95 (3), 1038-1041.
[185] Mu, Y.; Zhou, W.; Wan, F.; Ding, D.; Hu, Y.; Luo, F., Compos. Part A. Appl. Sci. Manuf. **2015,** 77, 195-203.
[186] Ding, D.; Zhou, W.; Zhang, B.; Luo, F.; Zhu, D., J. Mater. Sci. **2011,** 46 (8), 2709-2714.
[187] Zhao, D.; Zhao, H.; Zhou, W., Physica E: Low-dimensional Systems and Nanostructures **2001,** 9 (4), 679-685.
[188] Gusev, A. I.; Rempel, A. A.; Magerl, A. J., Disorder and order in strongly nonstoichiometric compounds: transition metal carbides, nitrides and oxides. Springer Science & Business Media: **2013**; Vol. 47, p 513-516.
[189] Ning, M.-Q.; Lu, M.-M.; Li, J.-B.; Chen, Z.; Dou, Y.-K.; Wang, C.-Z.; Rehman, F.; Cao, M.-S.; Jin, H.-B., Nanoscale **2015,** 7 (38), 15734-15740.
[190] Huang, M.; Fang, Y.; Li, R.; Huang, T.; Yu, Z.; Xia, H., Journal of applied polymer science **2009,** 113 (3), 1611-1618.
[191] Klymko, N., Future Fab International Issue-Metrology Analysis **2004,** 8, 17.
[192] Li, K.; Li, S.; Li, N.; Dixon, D. A.; Klein, T. M., J. Phys. Chem. C **2010,** 114 (33), 14061-14075.

[193] Ionescu, E.; Papendorf, B.; Kleebe, H.-J.; Breitzke, H.; Nonnenmacher, K.; Buntkowsky, G.; Riedel, R., J. Eur. Ceram. Soc. **2012,** 32 (9), 1873-1881.
[194] Brandstadt, K.; Cook, S.; Nguyen, B. T.; Surgenor, A.; Taylor, R.; Tzou, M. S., Hafnium containing hydrosilylation catalysts and compositions containing the catalysts. Google Patents: **2013**.
[195] Woo, H.; Tilley, T. D., J. Am. Chem. Soc. **1989,** 111 (20).
[196] Nghiem, Q. D.; Asthana, A.; Sung, I.-K.; Kim, D.-P., J. Mater. Res. **2006,** 21 (6), 1543-1549.
[197] Rushkin, I.; Shen, Q.; Lehman, S.; Interrante, L., Macromolecules **1997,** 30 (11), 3141-3146.
[198] Schuhmacher, J.; Berger, F.; Weinmann, M.; Bill, J.; Aldinger, F.; Müller, K., Appl. Organomet. Chem. **2001,** 15 (10), 809-819.
[199] Gao, Y.; Mera, G.; Nguyen, H.; Morita, K.; Kleebe, H.-J.; Riedel, R., J. Eur. Ceram. Soc. **2012,** 32 (9), 1857-1866.
[200] Hauser, R.; Nahar-Borchard, S.; Riedel, R.; Ikuhara, Y. H.; Iwamoto, Y., J. Ceram. Soc. Jpn. **2006,** 114 (1330), 524-528.
[201] Sarkar, S.; Gan, Z.; An, L.; Zhai, L., J. Phys. Chem. C **2011,** 115 (50), 24993-25000.
[202] Zhou, C.; Min, H.; Yang, L.; Chen, M.; Wen, Q.; Yu, Z., J. Eur. Ceram. Soc. **2014,** 34 (15), 3579-3589.
[203] Kaur, S.; Mera, G.; Riedel, R.; Ionescu, E., J. Eur. Ceram. Soc. **2016,** 36 (4), 967-977.
[204] Traßl, S.; Suttor, D.; Motz, G.; Rössler, E.; Ziegler, G., J. Eur. Ceram. Soc. **2000,** 20 (2), 215-225.
[205] Su, D.; Li, Y.; Hou, F.; Yan, X., J. Am. Ceram. Soc. **2014,** 97 (4), 1311-1316.
[206] Ohshita, Y.; Ogura, A.; Ishikawa, M.; Kada, T.; Hoshino, A.; Suzuki, T.; Machida, H.; Soai, K., Chem. Vap. Deposition **2006,** 12 (2-3), 130-135.
[207] Berger, F.; Mueller, A.; Aldinger, F.; Mueller, K., Z. Anorg. Allg. Chem. **2005,** 631 (2-3), 355-363.
[208] Lee, J.; Butt, D. P.; Baney, R. H.; Bowers, C. R.; Tulenko, J. S., J. Non-Cryst. Solids **2005,** 351 (37), 2995-3005.
[209] Gérardin, C.; Taulelle, F.; Bahloul, D., J. Mater. Chem. **1997,** 7 (1), 117-126.
[210] Ionescu, E.; Papendorf, B.; Kleebe, H. J.; Riedel, R., J. Am. Ceram. Soc. **2010,** 93 (6), 1783-1789.
[211] Widgeon, S.; Sen, S.; Mera, G.; Ionescu, E.; Riedel, R.; Navrotsky, A., Chem. Mater. **2010,** 22 (23), 6221-6228.
[212] Dirè, S.; Ceccato, R.; Gialanella, S.; Babonneau, F., J. Eur. Ceram. Soc. **1999,** 19 (16), 2849-2858.
[213] Burns, G. T.; Taylor, R. B.; Xu, Y.; Zangvil, A.; Zank, G. A., Chem. Mater. **1992,** 4 (6), 1313-1323.
[214] Kaur, S.; Riedel, R.; Ionescu, E., J. Eur. Ceram. Soc. **2014,** 34 (15), 3571-3578.
[215] Widgeon, S.; Mera, G.; Gao, Y.; Stoyanov, E.; Sen, S.; Navrotsky, A.; Riedel, R., Chem. Mater. **2012,** 24 (6), 1181-1191.
[216] Widgeon, S.; Mera, G.; Gao, Y.; Sen, S.; Navrotsky, A.; Riedel, R., J. Am. Ceram. Soc. **2013,** 96 (5), 1651-1659.
[217] Mizutani, U., Hume-Rothery rules for structurally complex alloy phases. CRC Press: **2010**.
[218] Córdoba, J. M.; Sayagués, M. J.; Alcalá, M. D.; Gotor, F., J. Am. Ceram. Soc. **2007,** 90 (2), 381-387.
[219] Aigner, K.; Lengauer, W.; Rafaja, D.; Ettmayer, P., J. Alloys Compd. **1994,** 215 (1), 121-126.
[220] Cordoba, J. M.; Sayagués, M. J.; Alcala, M. D.; Gotor, F. J., J. Am. Ceram. Soc. **2005,** 88 (7), 1760-1764.
[221] Nemanich, R.; Solin, S., PhRvB **1979,** 20 (2), 392.
[222] Nakashima, S.-i.; Harima, H., Physica Status Solidi (a) **1997,** 162 (1), 39-64.
[223] Mera, G.; Navrotsky, A.; Sen, S.; Kleebe, H.-J.; Riedel, R., J. of Mater. Chem. A **2013,** 1 (12), 3826-3836.
[224] Guron, M. M.; Wei, X.; Welna, D.; Krogman, N.; Kim, M. J.; Allcock, H.; Sneddon, L. G., Chem. Mater. **2009,** 21 (8), 1708-1715.
[225] Lu, Y.; Zhu, Z.; Liu, Z., Carbon **2005,** 43 (2), 369-374.
[226] Gim, J.; Mathew, V.; Lim, J.; Song, J.; Baek, S.; Kang, J.; Ahn, D.; Song, S.-J.; Yoon, H.; Kim, J., Sci. Rep. **2012,** 2.
[227] Chen, Z.; Wu, W.; Chen, Z.; Cong, X.; Qiu, J., Ceram. Int. **2012,** 38 (1), 761-767.
[228] Li, W.; Li, D.; Gao, X.; Gurlo, A.; Zander, S.; Jones, P.; Navrotsky, A.; Shen, Z.; Riedel, R.; Ionescu, E., DTr **2015,** 44 (17), 8238-8246.
[229] Wang, C.; Huang, F.; Jiang, Y.; Zhou, Y.; Du, L., J. Am. Ceram. Soc. **2012,** 95 (1), 71-74.
[230] Pena-Alonso, R.; Mariotto, G.; Gervais, C.; Babonneau, F.; Soraru, G. D., Chem. Mater. **2007,** 19 (23), 5694-5702.
[231] Maldonado, S.; Morin, S.; Stevenson, K. J., Carbon **2006,** 44 (8), 1429-1437.
[232] Marchetti, P. S.; Kwon, D.; Schmidt, W. R.; Interrante, L. V.; Maciel, G. E., Chem. Mater. **1991,** 3 (3), 482-486.
[233] Blum, Y.; Kleebe, H.-J., J. Mater. Sci. **2004,** 39 (19), 6023-6042.
[234] Khyzhun, O. Y.; Kolyagin, V., J. Electron. Spectrosc. Relat. Phenom. **2004,** 137, 463-467.
[235] Urbonaite, S.; Johnsson, M.; Svensson, G., J. Mater. Sci. **2004,** 39 (5), 1907-1911.
[236] Shi, L.; Yang, Z.; Chen, L.; Qian, Y., Solid State Commun. **2005,** 133 (2), 117-120.
[237] Barin, I., Thermochemical Data of Pure Substances, Thermochemical Data of Pure Substances. Wiley-VCH: **1997**.

[238] Pimenta, M.; Dresselhaus, G.; Dresselhaus, M. S.; Cancado, L.; Jorio, A.; Saito, R., PCCP **2007,** 9 (11), 1276-1290.
[239] Jiang, J.; Wang, S.; Li, W., J. Am. Ceram. Soc. **2016**.
[240] Simonenko, E.; Ignatov, N.; Simonenko, N.; Ezhov, Y. S.; Sevastyanov, V.; Kuznetsov, N., Russ. J. Inorg. Chem. **2011,** 56 (11), 1681-1687.
[241] Kleebe, H. J.; Nonnenmacher, K.; Ionescu, E.; Riedel, R., J. Am. Ceram. Soc. **2012,** 95 (7), 2290-2297.
[242] Stobierski, L.; Gubernat, A., Ceram. Int. **2003,** 29 (4), 355-361.
[243] Gu, H.; Shinoda, Y.; Wakai, F., J. Am. Ceram. Soc. **1999,** 82 (2), 469-472.
[244] PROCHAZKA, S.; SCANLAN, R. M., J. Am. Ceram. Soc. **1975,** 58 (1-2), 72-72.
[245] Tong, Y.; Bai, S.; Zhang, H.; Ye, Y., Ceram. Int. **2013,** 39 (6), 6813-6820.
[246] Liu, Q.; Zhang, L.; Jiang, F.; Liu, J.; Cheng, L.; Li, H.; Wang, Y., Surf. Coat. Technol. **2011,** 205 (17), 4299-4303.
[247] Vaughn, W. L.; Maahs, H. G., J. Am. Ceram. Soc. **1990,** 73 (6), 1540-1543.
[248] Deadmore, D., J. Am. Ceram. Soc. **1965,** 48 (7), 357-359.
[249] Nielsen, R. H., Kirk-Othmer Encyclopedia of Chemical Technology **2000**.
[250] Dai, H.; Rinzler, A. G.; Nikolaev, P.; Thess, A.; Colbert, D. T.; Smalley, R. E., Chem. Phys. Lett. **1996,** 260 (3), 471-475.
[251] Tuominen, M.; Yakimova, R.; Vehanen, A.; Janzen, E., Mater. Sci. Eng., B **1999,** 57 (3), 228-233.
[252] Ivanov, P.; Chelnokov, V., Semicond. Sci. Technol. **1992,** 7 (7), 863.
[253] Wang, C.; Han, X.; Xu, P.; Zhang, X.; Du, Y.; Hu, S.; Wang, J.; Wang, X., Appl. Phys. Lett. **2011,** 98 (7), 072906.
[254] Pierson, H. O., Handbook of carbon, graphite, diamonds and fullerenes: processing, properties and applications. William Andrew: **1994**; p 61.
[255] Micheli, D.; Pastore, R.; Vricella, A.; Morles, R.; Marchetti, M.; Delfini, A.; Moglie, F.; Primiani, V. M., Mater. Sci. Eng., B **2014,** 188, 119-129.
[256] Shen, Y.; Lin, Y.; Nan, C. W., Adv. Funct. Mater. **2007,** 17 (14), 2405-2410.
[257] Dasgupta, D.; Demichelis, F.; Tagliaferro, A., Philos. Mag. B **1991,** 63 (6), 1255-1266.
[258] Xu, J.; Wong, C., Appl. Phys. Lett. **2005,** 87 (8), 2907.
[259] Cao, M.; Qin, R.; Qiu, C.; Zhu, J., Mater. Desi. **2003,** 24 (5), 391-396.
[260] Micheli, D.; Morles, R. B.; Marchetti, M.; Moglie, F.; Primiani, V. M., Carbon **2014,** 68, 149-158.
[261] Albano, M.; Micheli, D.; Gradoni, G.; Morles, R. B.; Marchetti, M.; Moglie, F.; Primiani, V. M., Acta Astronaut. **2013,** 87, 30-39.

Acknowledgements

Finally, it comes to acknowledgements, the indispensable part of a Ph.D. thesis. In spite it is impossible to completely express my appreciation to the people who supported me during my Ph.D. period by saying some nice words, I still want to say:

I would like to express the deepest appreciation and respect to Prof. Dr. Ralf Riedel, my doctoral supervisor, who gave me a golden opportunity to work in his group. Many thanks for his constant support, nice suggestions and warm encouragements during my Ph.D. study. I also would like to express my heartfelt gratitude for his financial support that gives me enough time to find a new position. I really appreciate everyday working in his group and every time talking with him. His genius attitude and wisdom in scientific research teaches me how to continue my research career in the future.

I would like to sincerely thank PD. Dr. Emanuel Ionescu who introduced me into the field of single-source-precursor synthesis of ceramic nanocomposites. Warm thanks for his kind supervision and important support on my experiments, manuscripts and Ph.D. dissertation.

I also would like to deeply acknowledge Prof. Dr. Zhaoju Yu for her important contributions to my work, including TEM, MAS NMR and MA measurements, productive discussions and carful revision of my manuscripts. In addition, many thanks for her warm encouragements and concerns on my Ph.D. work and life.

I sincerely thank Prof. Dr. Norbert Nicoloso for revising my manuscript and teaching me how to write scientific paper. I also appreciate that we were working in the same office for half a year.

I sincerely acknowledge Prof. Dr. Oliver Guillon (Forschungszentrum Jülich, Germany), Prof. Dr. James Shen (Stockholm University, Sweden) and Dr. Koji Morita (NIMS, Japan) for allowing me using spark plasma sintering apparatus in their lab.

I would like to thank Dr. Yeping Xu and Prof. Dr. Gerd Buntkowsky for solid state MAS NMR measurements of ceramic powders. I really appreciate the discussions with Dr. Yeping Xu.

I would like to thank Prof. Dr. Xiaowei Yin (Northwestern Polytechnical University, China) for the measurements of EMI shielding performance in his lab.

I sincerely thank Prof. Dr. Xingang Luan (Northwestern Polytechnical University, China) for laser ablation test, hydrothermal oxidation test and providing me 2D carbon fabrics.

I also sincerely thank Dipl. Claudia Fasel for a lot of TG/MS measurements, oxidation measurements as well as her nice supports on all other daily experiments.

I would like to sincerely acknowledge Dr. Jia Yuan for supporting my experiments from using apparatus to analyzing data. I also appreciate that we (including Dr. Yingwei Zhao) are sharing the apartment for almost 3 years.

I would like to thank M.Sc. Daniela Penther (Fachgebiet Werkstofftechnik, Technische Universität Berlin) for revising the abstract (Zusammenfassung) of the dissertation written in German.

I would like to thank Dr. Wenjie Li for elemental analysis and teaching me the FullProf refinement, to thank M.Sc. Cong Zhou for elemental analysis and nice supports on my experiments, to thank Dr. Cristina Schitco for the training of BET measurements, to thank M. Sc. Xingmin Liu for productive discussions and EMI shielding measurements, to thank M.Sc. Yao Feng for microwave absorption measurements and to thank Dipl. Jean Christophe Jaud for XRD measurements.

I also would like to thank Dr. Magdalena Joanna Graczyk-Zajac, PD Dr. Leonore Wiehl, Dr. Bekheet Maged, Dr. Yan Gao, Dr. Jan Kaspar, Dr. Sarabjeet Kaur, Dr. Ravi Mohan Prasad, Dr. Isabel Gonzalo de Juan, Dipl. Dario De Carolis, M. Sc. Benjamin Juretzka, M. Sc. Dragoljub Vrankovic, M. Sc. Szu-Hsuan Lee, M. Sc. Christina Stabler, Dipl. Felix Rosenburg, M.Sc. Hongguang, Wang, M. Sc. Fangtong Xie, Mrs. Su-Chen Chang and all other Dispersive Solids group members who kindly supported my work or my life in different ways.

I really appreciate all my friends in Darmstadt and the time we spend together. We are the best friends forever. “Auld acquaintance will never be forgot, and will always be brought to mind.”

Particularly, I would like to deeply thank my dear parents, Mr. Chunliu Wen (文春六) and Mrs. Yulan Hu (胡玉兰), my brother and all other family members who always love me, trust me and encourage me in my life. Now, I’m missing my parents, my little Niece and Nephew very much. I wish you all the best.

Special thanks to my beloved and beautiful girlfriend, M.Eng. Shasha Tao, who loves me, cares about me, supports me, trusts me, understands me and encourages me. I appreciate every minute we live together. Thus, please allow me to ask her a question. Would you like to marry me?

Importantly, I would like to greatly acknowledge the Chinese Scholarship Council (CSC) for 4-year financial support on my Ph.D. study in Germany. I’m proud of this experience forever.

Curriculum vitae

Qingbo Wen

Nationality: China

Gender: Male

Date of Birth: 14/03/1987

E-mail: wentsingbo@materials.tu-darmstadt.de or wentsingbo@gmail.com
Address: Nieder-Ramstädter Str. 11, 64283 Darmstadt, Germany

Education

- **Ph.D. Candidate of Material Science (Oct. 2012 ~ Feb. 2017)**, Department of Materials and Earth Sciences, Technische Universität Darmstadt, Germany.
- **Master of Environmental Engineering (Sep. 2009 ~ Jun. 2012)**, Department of Environmental Science and Engineering, Hunan University, **excellent graduate.**
- **Bachelor of Environmental Engineering (Sep. 2005 ~ Jun. 2009)**, Department of Environmental Science and Engineering, Hunan University**.**

Research Experience

- **10/2012~ , Supervisor:** Prof. Dr. Ralf Riedel
  - **Program:** Single-source-precursor synthesis, microstructure and high-temperature applications of dense monolithic SiMC(N) ceramic nanocomposites (M = Hf, Ta, HfTa).
- **09/2009 ~ 06/2012, Supervisor**: Prof. Dr. Caiting Li
  - **Program:** Numerical simulation and experimental investigation of selective catalytic reduction (SCR) process for NO removal using MnO_x-CeO_2/Al_2O_3-La_2O_3 supported on honeycomb ceramic at low temperature (100~150ºC).
- **11/2007 ~ 06/2009, Supervisor:** Prof. Dr. Caiting Li
  - **Program:** Adsorption of indoor formaldehyde and computational fluid dynamic (CFD) simulation of the concentration field.

Conferences

- **Qingbo Wen**, Zhaoju Yu, Olivier Guillon, Xingang Luan, Emanuel Ionescu, Ralf Riedel. Preparation of Monolithic SiHfCN-based nanocomposites and of C_f/SiHfCN Ceramic Matrix Composites from Single-Source Precursors. *Materials Science and Engineering Congress (2014), Darmstadt, Germany*. **(Poster)**
- **Qingbo Wen**, Zhaoju Yu, Norbert Nicoloso, Emanuel Ionescu, Ralf Riedel. Single-source-precursor synthesis and microwave absorption behavior of SiC/HfC_xN_{1-x}/C nanocomposites in the X-band. *European Network on Smart Inorganic Polymers (2015), Uppsala, Sweden.* (**Oral presentation)**
- Sarabjeet Kaur, **Q. Wen**, E. Ionescu, R. Riedel. Synthesis and Processing of Dense Metal-Modified Silicon Carbide Monoliths and Their Behavior in Ultraharsh Environments. 8th *International Conference on High Performance Ceramics (2013)*, Chongqing, China. (**Oral presentation)**
- J.Yuan, **Q. Wen**, E. Ionescu, R. Riedel, Single source precursor Synthesis and Properties of Ultra-high-Temperature Ceramic Nanocomposites (UHTC-NCs). *8th International Symposium on Nitrides (2014), Wildbad Kreuth, Germany.* (**Oral presentation)**

Honors and Awards

- Chinese scholarship for 4 years of Ph.D. work in Germany (2012-2016)
- First Prize Scholarship for Excellent Master Students
- National Scholarship for Bachelor Students (the highest prize for Bachelor students in China), Twice
- Outstanding Bachelor Student of Hunan Province
- Outstanding Award of "Sang-De" Excellent Research Paper Prize
- Excellent Student Prize in Graduate School
- Second Prize of International Biology Olympiad (IBO) in Hunan Division

Research Skills

- Chemical synthesis and characterization: Schlenk technique for oxygen and moisture sensitive materials, TG/MS analysis, FI-TR analysis, NMR analysis, etc.
- Microstructure characterization: XRD, Raman, SEM, TEM, N_2 adsorption BET and Elemental Analysis, etc.
- Processing: Spark plasma sintering (SPS), hot pressing, warm pressing and polymer infiltration & pyrolysis.
- Measurements of oxidation/corrosion resistance and mechanical properties (bending strength, hardness and creep resistance).
- Analysis of dielectric properties, microwave absorption and electromagnetic interference shielding performance.

Publications and patents (2011 ~ 2016)

1) **Qingbo Wen**, Yeping Xu, Binbin Xu, Claudia Fasel, Olivier Guillon, Gerd Buntkowsky, Zhaoju Yu, Ralf Riedel, Emanuel Ionescu. Single-source-precursor synthesis of dense SiC/HfC_xN_{1-x}-based ultrahigh-temperature ceramic nanocomposites[J]. ***Nanoscale***, 2014, 6 (22): 13678-13689.
2) **Qingbo Wen**, Yao Feng, Zhaoju Yu, DongLiang Peng, Norbert Nicoloso, Emanuel Ionescu, Ralf Riedel. Microwave absorption of SiC/HfC_xN_{1-x}/C ceramic nanocomposites with HfC_xN_{1-x}-Carbon core-shell particles[J]. ***Journal of the American Ceramic Society***, 2016, 99 (8): 2655-2663.
3) **Qingbo Wen**, Caiting Li, Zhihong Cai, Wei Zhang, Hongliang Gao, Lijun Chen, Guangming Zeng, Xin Shu, Yapei Zhao. Study on activated carbon derived from sewage sludge for adsorption of gaseous formaldehyde[J]. ***Bioresource Technology***, 2011, 102(2): 942-947.
4) Cong Zhou, Hao Min, Le Yang, Meiyu Chen, **Qingbo Wen**, Zhaoju Yu. Dimethylaminoborane-modified copolysilazane as a novel precursor for high-temperature resistant SiBCN ceramics[J], ***Journal of the European Ceramic Society***, 2014, 34 (15), 3579-3589.
5) Wei Zhang, CaiTing Li, XianXun Wei, HongLiang Gao, **Qingbo Wen**, XiaoPeng Fan, Xin Shu, GuangMing Zeng, Wei Wei, YunBo Zhai, YiDe He, ShanHong Li . Effects of cake collapse caused by deposition of fractal aggregates on pressure drop during ceramic filtration[J], ***Environmental Science & Technology***, 2011, 45(10): 4415-4421.
6) Jingke Song, Caiting Li, Pei Lu, **Qingbo Wen**, Qi Zhan, Yapei Zhao. The Combined Action of Surfactant Mixture and Flocculants for Black Carbon Removal[J]. ***Separation Science and Technology***, 2014, 49(3): 424-431.
7) Shasha Tao, Caiting Li, Xiaopeng Fan, Guangming Zeng, Pei Lu, Xing Zhang, **Qingbo Wen**, Weiwei Zhao, Diqiang Luo, Chunzhen Fan. Activated coke impregnated with cerium chloride used for elemental mercury removal from simulated flue gas[J]. ***Chemical Engineering Journal***, 2012, 210: 547-556.
8) ZhiHong Cai, CaiTing Li, **Qingbo Wen**, Pei Lu, ShanHong Li；GuangMing Zeng. Adsorption of formaldehyde in air by modified fly ash[J]. ***Journal of Central South University (Science and Technology***, 2011, 42(7): 2156-2161.
9) CaiTing Li, Wei Zhang, XianXun Wei, HongLiang Gao, **Qingbo Wen**, XiaoPeng Fan, Liu Hai, Shu Xin, Wei Wei. Experiment and simulation of diffusion of micron-particle in porous ceramic vessel[J]. ***Transactions of Nonferrous Metals Society of China***, 2010, 20, 2358-2365.
10) YuJun Xiao, CaiTing Li, ShanHong Li, GuangMing Zeng, **Qingbo Wen**, GuanQing Guo, JingKe Song. Optimal design of a wet-type desulphurization absorber by the numerical simulation method[J]. ***Chemical Engineering Research and Design***, 2014, 92 (7), 1257-1266.
11) Yapei Zhao, Pei Lu, Caiting Li, Xiaopeng Fan, **Qingbo Wen**, Qi Zhan, Xin Shu, Tieliang Xu, Guangming Zeng. Adsorption mechanism of sodium dodecyl benzene sulfonate on carbon blacks by adsorption isotherm and zeta potential determinations[J]. ***Environmental technology***, 2013, 34(2): 201-207.
12) Weiwei Zhao, Caiting Li, Pei Lu, **Qingbo Wen**, Yapei Zhao, Xing Zhang, Chunzhen Fan, Shasha Tao. Iron, lanthanum and manganese oxides loaded on γ-Al_2O_3 for selective catalytic reduction of NO with NH_3 at low temperature [J]. ***Environmental technology***, 2013, 34(1): 81-90.
13) Hongliang Gao, Caiting Li, Guangming Zeng, Wei Zhang, Lin Shi, Xiaopeng Fan, Yanan Zeng, **Qingbo Wen**, Xin Shu. Experimental study of wet flue gas desulphurization with a novel type PCF device[J]. ***Chemical***

Engineering and Processing: Process Intensification, 2011, 50(2): 189-195.

14) Hongliang Gao, Caiting Li, Guangming Zeng, Wei Zhang, Lin Shi, Shanhong Li, Yanan Zeng, Xiaopeng Fan, **Qingbo Wen**, Xin Shu. Flue gas desulphurization based on limestone-gypsum with a novel wet-type PCF device[J]. ***Separation and Purification Technology***, 2011, 76(3): 253-260.

15) Hongliang Gao, Caiting Li, Guangming Zeng, Wei Zhang, Lin Shi, Shanhong Li, Yanan Zeng, Xiaopeng Fan, **Qingbo Wen**, Xin Shu. Prediction and Experimental Validation Studies of Wet Flue Gas Desulphurization with a Novel Type PCF Device Based on Limestone-Gypsum[J]. ***Energy & Fuels***, 2010, 24: 4944-4951.

Cover:

Top-left: a photograph of dense monolithic SiMC(N) ceramic nanocomposites (M = Hf, Ta and HfTa) sintered via spark plasma sintering process;

Top-right: a picture of a new rocket (Long March 5) developed in China. Its maiden launch occurred successfully on 03.11.2016;

The picture is cited from YangGuangJunshi (央广军事);

Bottom-left: TEM images showing the microstructure of SiMC(N) ceramic nanocomposites;

Bottom-right: a figure (Figure 3. 74a) of microwave absorption performance of the SiC/5HfC$_x$N$_{1-x}$/C-1700°C in the X-band (8.2 ~ 12.4 GHz).